



**HAL**  
open science

# SLIP-WEAKENING MECHANISMS AT HIGH SLIP-VELOCITIES: INSIGHTS FROM ANALOGUE AND NUMERICAL MODELLINGS

Sébastien Boutareaud

► **To cite this version:**

Sébastien Boutareaud. SLIP-WEAKENING MECHANISMS AT HIGH SLIP-VELOCITIES: INSIGHTS FROM ANALOGUE AND NUMERICAL MODELLINGS. Tectonics. Université de Franche-Comté, 2007. English. NNT: . tel-00263691

**HAL Id: tel-00263691**

**<https://theses.hal.science/tel-00263691>**

Submitted on 13 Mar 2008

**HAL** is a multi-disciplinary open access archive for the deposit and dissemination of scientific research documents, whether they are published or not. The documents may come from teaching and research institutions in France or abroad, or from public or private research centers.

L'archive ouverte pluridisciplinaire **HAL**, est destinée au dépôt et à la diffusion de documents scientifiques de niveau recherche, publiés ou non, émanant des établissements d'enseignement et de recherche français ou étrangers, des laboratoires publics ou privés.



# THESE

Présentée à

L'UNIVERSITE DE FRANCHE-COMTE

UFR SCIENCES & TECHNIQUES

## SLIP-WEAKENING MECHANISMS AT HIGH SLIP-VELOCITIES: INSIGHTS FROM ANALOGUE AND NUMERICAL MODELLINGS

Par

**Sébastien Boutareaud**

Pour obtenir le grade de

**Docteur de l'Université de Franche-Comté**

**Spécialité : Sciences de la Terre**

### Composition du Jury:

Jean-Pierre Gratier	Physicien d'Observatoire	OSU Grenoble	Rapporteur
Jean Sulem	Directeur de recherche	ENPC-LCPC Marne-la-Vallée	Rapporteur
Jean Schmittbuhl	Directeur de recherche	EOST Strasbourg	Examineur
Christopher Wibberley	Maître de conférence	UNSA Nice	Co-directeur
Akito Tsutsumi	Maître de conférence	Kyoto University	Examineur
Dan-Gabriel Calugaru	Ingénieur de recherche	UFC Besançon	Examineur
Jean-Pierre Sizun	Maître de conférence	UFC Besançon	Examineur
Olivier Fabbri	Professeur	UFC Besançon	Directeur



*La vie ne vaut d'être vécue - Sans amour.*  
*[ La Javanaise ]*  
*Serge Gainsbourg*



*To Aurélie,  
for your sacrifices, your understanding and your patience,  
forgive me please for these four long years of « absence »,  
working on odd experiments...*



# **RESUME**



Cette thèse vise à étudier les propriétés thermo-poro-mécaniques de roches de faille, à partir de l'analyse structurale et microstructurale d'une faille aujourd'hui à l'affleurement et à partir d'expériences menées en laboratoire, en vue de déterminer les processus qui contrôlent l'efficacité de deux mécanismes responsables de l'affaiblissement cosismique : la *pressurisation thermique* et le *mécanisme d'affaiblissement par drainage*. L'étude de terrain a été conduite sur deux affleurements appartenant à une faille décrochante potentiellement active appartenant au système de failles du Chugoku occidental (Japon) : la faille d'Usukidani. Le travail expérimental a quant à lui été mené dans le laboratoire de déformation des roches de l'Université de Kyoto. Les résultats majeurs de ce travail sont exposés ci-dessous.

Les propriétés hydrologiques et poro-élastiques de la gouge et de la brèche de la faille d'Usukidani ont été déterminées à partir d'échantillons prélevés sur le terrain. Ces données hydrauliques ont ensuite été utilisées dans un modèle numérique afin d'évaluer l'importance du phénomène de pressurisation thermique dans le cas d'un glissement cosismique le long de la zone de glissement principale et le long de zones de glissement secondaires. Les résultats de cette modélisation suggèrent que le mécanisme de pressurisation thermique n'est efficace que si la rupture reste localisée le long des zones de glissement contenant de la gouge, avec comme facteur de contrôle l'épaisseur de cette zone de glissement.

Afin d'identifier les processus dynamiques particuliers responsables de l'affaiblissement cosismique dans la zone de glissement, plusieurs essais de friction ont été menés sur une machine à cisaillement annulaire. Ces expériences ont été conduites à des vitesses cosismiques (équivalentes à 0,09, 0,9 et 1,3 m/s) en conditions humides ou conditions sèches. Les données obtenues montrent que quelles que soient les conditions d'humidité initiales, les failles simulées montrent toutes un affaiblissement lors du déplacement. Un examen détaillé des microstructures des gouges cisillées obtenues une fois l'équilibre frictionnel atteint permet de définir deux types de microstructures impliquant deux régimes de déformation : un régime de déformation par roulement avec la formation d'*agrégats argileux*, et un régime de déformation par glissement avec la formation d'une *zone de cisaillement complexe* localisée à l'interface gouge-éponte. L'affaiblissement observé lors des expériences semble être lié à une diminution de la proportion de grains roulants par rapport à celle de grains glissants, et semble être favorisé par le développement des agrégats argileux, lesquels sont contrôlés par la teneur en eau.

A partir d'un modèle numérique (P2 FEM) et des données de contrainte cisailante obtenues lors des essais de friction, il a été possible de calculer l'évolution de la température

de la gouge en fonction du déplacement. Les résultats suggèrent que la distance  $d_c$  pourrait représenter la distance nécessaire à une faille pour produire et diffuser assez de chaleur afin de casser les ponts d'eau capillaire (forces d'adhésion) et ainsi permettre à l'eau contenue dans la gouge d'être libérée. Ce mécanisme est appelé mécanisme d'affaiblissement par drainage.

# **ABSTRACT**



This thesis aims at studying the thermo-poro-mechanical properties of fault rock materials by means of field analysis of an exhumed fault and laboratory experiments, in order to determine the processes responsible of the efficiency of two thermally-activated slip-weakening mechanisms: the thermal pressurization and the moisture-drained weakening mechanism. The field study was conducted on well-exposed outcrops of a potentially active strike-slip fault that belongs to the Western Chugoku fault system (Japan): the Usukidani fault. The experimental work was conducted in the rock deformation laboratory at Kyoto University. The primary results of this research are exposed below.

The hydrological and poroelastic properties of gouge and breccia of the Usukidani fault have been determined on laboratory from retrieved samples. The thermal pressurization process has been investigated in cases of slip along a principal slip zone and along splay faults branching off the principal displacement zone, from a numerical model constrained by these hydraulic data. Modelling results suggest that thermal pressurization is a viable process only as long as the rupture remains located in the central gouge zones or in mature splay fault gouge zones.

To identify the particle dynamic processes responsible of slip-weakening in clay-rich seismic slip zones, several rotary-shear experiments were conducted at coseismic slip-rates (equivalent to 0.09, 0.9 and 1.3 m/s) for different gouge water contents: wet initial conditions or dry initial conditions. The representative mechanical behavior of the simulated faults show a slip-weakening behavior, whatever initial moisture conditions. Detailed examination of gouge microstructures obtained at the residual friction stage in wet and dry initial conditions allows to define two types of microstructure implying two deformation regimes: a rolling regime with formation of *clay-clast aggregates*, and a sliding regime with formation of a *complex shear zone* localized at the gouge-wall-rock interface. The observed slip-weakening behavior of simulated faults appears to be related to a decrease of the proportion of grain rolling to grain sliding with increasing slip displacement and appears to be favored by the development of clay-clast aggregates, which is controlled by water content.

From a numerical model (P2 FEM) based on shear stress data, the temperature rise on the simulated fault gouge with increasing slip displacement is approached. Modelling results suggest that the slip-weakening distance  $d_c$  might represent the necessary slip distance to produce and diffuse enough heat throughout the fault gouge layer to break liquid capillary bridge and to drain off completely pore water and adsorbed water at contact area of gouge particles, that is the thermally-activated moisture-related weakening mechanism.







## Note to the thesis

Chapters *II* and *IVa* are similar to a manuscript submitted at the *Geological Society of London* with C.A.J. Wibberley, O. Fabbri and T. Shimamoto as co-authors. I express my best gratitude to O. Fabbri and C.A.J. Wibberley for their careful reviews in writing this first paper (see references).

Post-experiment microstructures observations in chapter *III* are similar to a manuscript that will be soon submitted to an international journal. Co-authors will be O. Fabbri, R. Han and T. Shimamoto. O. Fabbri is sincerely thanks for his fruitful reviews.

Chapter *IVb* is similar to a manuscript in preparation that will be also submitted to an international journal, with D. Calugaru, K. Mizoguchi, O. Fabbri and T. Shimamoto as co-authors.

I want to inform readers that the numerical model used in chapter *IVa* has been compiled by C.A.J. Wibberley. As for the P2 FEM numerical model used in chapter *IVb*, D. Calugaru is the author of the program (see references).



## Acknowledgments

*First, I would like to express my best gratitude to Pr. Toshihiko Shimamoto who gave to a sedimentologist the outstanding chance to start working in Tectonics with experimental machines in the vanguard of research, in an excellent environment for Faulting research.*

*I am grateful to Dr. Akito Tsutsumi for many critical discussions and effort to encourage ideas presented in this manuscript.*

*I express him my sincere thanks to Shimaken students (Hiroyuki Noda, Hiroki Sone, Raehee Han, Hiroko Kitajima, Yasutaka Aisawa, Wataru Tanikawa and Manabu Komizo) for valuable discussions about Faulting and helpful experimental advises. Special thanks to Hiroyuki Noda and to Hiroki Sone for their kindness and their patience to teach me the concepts of experiential rock deformation.*

*I have appreciated Dr. Christopher Wibberley as a second supervisor for his critical discussions when starting permeability measurements at Kyoto University. I express him my best gratitude to provide me his thermal pressurization numerical model and above all to give me the first opportunity to publish.*

*I am grateful to Dr. Jean-Pierre Sizun for the interest he was the first to express on my work, and to give me the opportunity to learn porosity concept from mercury measurements.*

*I want to thank Dr. Kazuo Mizoguchi for the fruitful discussions we had together about particle dynamics on gouge friction experiments. These give me the idea to develop the conceptual model of gouge deformation regimes presented herein and over several abroad congresses and seminars.*

*I express my best gratitude to Dr. Dan-Gabriel Calugaru for his great kindness and patience by listening to my explanations about incredible high velocity friction experiments. I want to thank him for his effort to give me the opportunity to develop together a modelling approach of gouge frictional heating.*

*Very many thanks to Pr. Didier Marquer, Pr. Martine Buatier and Dr. Philippe Goncalves for their fruitful discussions, help and encouragements during my third and fourth year at the Geoscience department of the University of Franche-Comté. Special thanks to Pr. Didier Marquer who has done his best to allow me taking part to abroad seminars.*

*I am grateful to Pr. Thierry Adate for his collaboration and great help with XRD analyses.*

*Many thanks to H. Tsutsumi for thin section preparation of extremely challenging experimental rock samples.*

*I would like to thank my office mates at Besançon University (Sabine Bodeï, Emilien Oliot, Charles Cartannaz, Latifa Bouragba, François Souquière, Emilien Belle, Cyril Durand, Aurelie Leroux, Brice Lacroix) for their great helpfulness and enjoyable time we had together. Special thanks to Sabine Bodeï for her good humour each morning that enjoyed my long days at the University.*

*I do not forget to thank Dr Charles Cartannaz for his useful advices on thin section gouge microstructure observation.*

*Many thanks to Aurelie Leroux for her extremely patient retouch on the oral presentation of my PhD defence.*

*I express my sincere thanks to my family for their mental and financial support, especially when I was in Japan.*

*I am grateful to my wife Aurélie and Céline Bernard for their investment in cooking during two long days amazing dish for the drinking party following my PhD defence.*

*And last but not least, special thanks to Pr. Olivier Fabbri who accepted me four years ago, on the basis of my general background in Geology. Also, special thanks to him to give me the chance to work on Faulting from a multidisciplinary approach.*





# Contents

<b>INTRODUCTION .....</b>	<b>26</b>
<b>CHAPTER I .....</b>	<b>30</b>
A. Background.....	31
1. Textural classification of fault rocks .....	31
2. Strength of crustal fault zones .....	31
3. Dynamic crack propagation.....	33
4. Static friction .....	34
5. Dynamic friction .....	36
6. Earthquake friction laws .....	37
B. Friction at low slip-rates ( $10^{-1} - 10^3$ $\mu\text{m/s}$ ) .....	37
1. Influence of hold-time (quasi-stationary contact-time) .....	39
2. Influence of temperature.....	41
3. Influence of normal stress .....	43
4. Influence of fault gouge.....	44
5. Influence of adsorbed water and pore water .....	44
6. Summary.....	46
C. Friction at high slip-rates ( $10^{-3} - 10^0$ $\text{m/s}$ ) .....	48
1. Influence of hold-time (quasi-stationary contact-time) .....	50
2. Influence of temperature.....	50
3. Influence of normal stress .....	53
4. Influence of fault gouge.....	56
5. Influence of adsorbed water and pore water .....	58
D. Conclusions .....	58
<b>CHAPTER II.....</b>	<b>60</b>
A. Structural and microstructural analyses.....	61
1. Internal structure of the Usukidani fault .....	61
1.2. Studied outcrops.....	63
1.2.2. Damage zones .....	67
1.2.3. Core zones .....	67
1.2.3.1. Outcrop A.....	67
1.2.3.2. Outcrop B.....	76
2. Summary of fault zone architecture.....	79
B. Petrophysical analysis .....	80
1. Fluid transport properties of Usukidani fault zone .....	80
1.1. Experimental procedure.....	81
1.1.1. Mercury porosity measurements.....	81
1.1.2. Nitrogen porosity measurements .....	82
1.1.3. Nitrogen permeability measurements.....	83
1.2. Results .....	86
1.2.1 Mercury porosity measurements.....	86
1.2.1.1. Outcrop A.....	86
1.2.1.2. Outcrop B.....	86
1.2.2. Nitrogen porosity measurements .....	90
1.2.2.1. Outcrop A.....	90
1.2.2.2. Outcrop B.....	90
1.2.3. Nitrogen permeability measurements.....	94
1.2.3.1. Outcrop A.....	94
1.2.3.2. Outcrop B.....	95
2. Discussion.....	95

3. Conclusions .....	105
<b>CHAPTER III.....</b>	<b>106</b>
A. High velocity friction experiments on the Usukidani fault gouge: experimental procedure .....	107
1. Preparation of the simulated fault .....	107
2. Experimental technique .....	112
B. Experimental results.....	115
1. Mechanical behavior.....	115
1.1. Friction coefficient.....	115
1.2. Dynamic shear resistance .....	120
2. Post-experiment microstructures.....	123
2.1. A-type gouge .....	123
2.2. B-type gouge .....	129
2.3. C-type gouge .....	131
C. Discussion.....	133
1. Interpretation .....	133
1.1. Mechanical behavior.....	133
1.2. Development of microstructures.....	134
2. Comparison of experimental results with reported laboratory and natural fault gouge microstructure studies .....	135
3. Timing apparition of the experimental microstructures at seismic slip-rates .....	137
4. Correlation of microstructures with slip-weakening behavior.....	138
D. Conclusions .....	140
<b>CHAPTER IV .....</b>	<b>142</b>
A. Thermal pressurization mechanism .....	143
1. Numerical analysis of thermal pressurization during shearing .....	143
1.1. General considerations .....	143
1.2. Choice of parameters .....	144
1.3. Modelling approach of thermal pressurization analysis .....	146
2. Results.....	148
3. Discussion.....	150
3.1. Efficiency of the thermal pressurization.....	150
3.2. Rupture path .....	151
4. Conclusions .....	152
B. Moisture-drained weakening mechanism .....	153
1. Finite element analysis of frictional heating during shearing .....	153
1.1. General considerations .....	153
1.2. Modelling approach of temperature rise analysis .....	154
1.3. Estimation of the fracture energy expended during friction experiments .....	155
2. Results.....	158
2.1. Simulated fault gouge temperatures .....	158
2.2. Frictional behavior of simulated faults.....	158
3. Discussion.....	163
3.1. Stress paths followed by the simulated fault gouge.....	163
3.2. Temperature change during slip-weakening .....	165
3.3. Significance of the slip-weakening distance $d_c$ .....	167
3.4. Frictional contacts localizing heating .....	168
3.5. Energy expended in fracturing .....	168
4. Conclusions .....	170
<b>CONCLUSIONS.....</b>	<b>171</b>
<b>REFERENCES .....</b>	<b>176</b>



# **INTRODUCTION**



Exposures of active faults show that, in the shallow crust, coseismic slip occurs within a few millimeter-thick clay-rich layer (0.1 - 10 cm-thick) called the seismic slip zone (Chester & Chester, 1998, 2003) thought to exist down to depths of about 5 to 8 km. This incohesive foliated or random fabric zone is partly composed of phyllosilicate minerals resulting from rock cataclasis and hydrothermal alteration. Observations and laboratory experiments show that thermo-poro-mechanical properties of this slip zone significantly influence the dynamic frictional strength of active faults by controlling the efficiency of slip-weakening mechanisms (Chester et al., 1993; Marone, 1998a; Sibson, 2003; Rice, 2006) responsible of earthquakes (Kanamori, 1994; Scholz 2002). Based on theoretical or experimental studies and analyses of fossil coseismic slip zones exposed at the Earth's surface, several mechanisms have been proposed to account for the dynamic slip-weakening. These mechanisms include frictional melting (McKenzie & Brune, 1972; Sibson, 1980; Cardwell et al., 1978; Kanamori & Heaton, 2000; Hirose & Shimamoto, 2003, 2005), fluid thermal pressurization (Sibson, 1973; Lachenbruch, 1980; Mase & Smith, 1985, 1987; Andrews, 2002; Wibberley, 2002; Wibberley & Shimamoto, 2003, 2005; Noda & Shimamoto, 2005), acoustic fluidization (Melosh, 1979, 1996), elastohydrodynamic lubrication (Brodsky & Kanamori, 2001) and dynamic unloading effects (Weertman, 1980; Brune et al., 1993; Ben-Zion & Andrews, 1998; Bouissou et al., 1998; Mora & Place, 1999).

Among these possible mechanisms, *thermal pressurization* has received a lot of attention in the last few years due to recent findings that narrow, water-saturated gouge zones often delimit the most recent slip boundaries in active faults observed at the surface and in cores (Lockner et al., 1999; Tsutsumi et al., 2004; Noda & Shimamoto, 2005). Thus, frictional heating is likely to efficiently heat up the pore water in the gouge, generating excess fluid pressures which in turn decrease the effective shear strength. Recent permeability measurements of gouge slip zones in active and exhumed faults (Lockner et al., 1999; Wibberley & Shimamoto, 2005; Noda & Shimamoto, 2005) have confirmed the feasibility of this process. Besides, detailed structural mapping of complex fault zones has shown that secondary faults often branch off the principal displacement zone. However, the effect of secondary branch faults on thermal pressurization has not yet been examined, probably because numerical or analogue modelling of splay faulting in fault zones is a complex issue (Poliakov et al., 2002). Nevertheless, fault branches can play a key role either in inhibiting or promoting fluid pressurization. Since secondary branch faults are commonly found along exhumed outcrops of seismogenic faults, their hydraulic properties need to be determined in order to evaluate their effect on dynamic slip-weakening by thermal pressurization. This

thesis presents results of porosity and permeability measurements obtained on the principal and secondary slip surfaces of an active, clay-rich gouge-bearing strike-slip fault, the Usukidani fault of SW Japan. These porosity and permeability values constrain calculations of hydraulic diffusivities of the displacement zones and determine the conditions under which rupture branching off the principal slip zone may or may not significantly inhibit thermal pressurization and dynamic slip-weakening.

Gouge water content in the seismic slip zone, which varies with depth in relation to the nature of clay minerals, permeability properties, geothermal gradient and applied stress (Bolton et al., 1998; Faulkner & Rutter, 1998; Faulkner, 2004), seems to play an important role in frictional mechanical behaviors of the seismic slip zone (Frye & Marone, 2002; Mizoguchi, 2004). Frictional properties of gouge at coseismic slip-rates have been poorly constrained in laboratory up to date. However, Mizoguchi et al. (2006) have recently proposed a new weakening mechanism termed *moisture-related weakening mechanism*, related to the break of liquid capillary bridges (i.e. adhesion force) between gouge particles from frictional heating during the coseismic slip. But the role of initial gouge water content on particle dynamics, which may be determinant on the amount of heat generated by friction and subsequently on the slip-weakening of gouge-filled faults, needs to be addressed. Therefore, we conducted a series of frictional sliding experiments, performed for different slip-velocities on a simulated fault zone (~ 900  $\mu\text{m}$ ) from natural clay gouge, under either dry or fully hydrated conditions with distilled water. This thesis presents correlation of frictional behavior of simulated faults with developed gouge microstructures from optical microscope and scanning electron microscope observations and calculated gouge temperature change. The development of two deformation regimes during experiments appears to be determinant on the slip-weakening behavior of simulated faults.

# **CHAPTER I**

## **Dynamic fault strength and slip-weakening mechanisms: a review**

## A. Background

### 1. Textural classification of fault rocks

A general model for continental fault rock structures has been proposed by Sibson (1977). It is based on rock deformation textures observed in ancient fault zones and on their relationship to faulting style, assuming a granitic protolith (Fig. 1.1). The main textural divisions are between random fabric and foliated types, and between cohesive and incohesive rocks. Subdivisions within each incohesive type are based on the percentage of visible rock fragments, whereas subdivisions within each cohesive type are based on the tectonic reduction of grain size and the fraction of fine-grained matrix relative to lithic fragments.

Deformation mechanisms producing such variety of fault rocks have been classified by Scholz (1988a; Fig. 1.2). His model shows the passage with increasing depth from a seismogenic frictional regime (i.e. discontinuous pressure-sensitive deformation involving cataclasis and frictional sliding) in the upper crust towards a largely aseismic quasi-plastic regime (i.e. continuous shearing localized within mylonite belts), which is allowed by the progressive ductile behavior of quartz (then feldspar) with increasing temperature and deviatoric stress.

### 2. Strength of crustal fault zones

*In situ* stress measurements through drill holes done in the 1970s indicate that ambient stresses in the upper crust of the earth are too low to initiate fractures in intact rock. Moreover, the necessary differential stress required to initiate brittle fracture in granite is higher than to initiate frictional sliding along optimally oriented planes (Fig. 1.3; Scholz, 2002). This suggests that in the earth's upper crust, sliding along any preexisting natural fractures should occur preferentially. Hence, it is commonly accepted that a crustal earthquake is caused by sliding movement along a preexisting fault. Therefore, understanding rock frictional sliding is required to understand earthquake mechanisms.

		Random fabric		Foliated		
Incohesive		Fault breccia (visible fragments > 30% of rock mass)		?		
Incohesive		Fault gouge (visible fragments < 30% of rock mass)		Foliated gouge		
		Glass-devitrified glass	Pseudotachylyte		?	
Cohesive		Nature of matrix		Percent of matrix		
		Tectonic reduction in grain size dominates grain growth by recrystallization and neomineralization		Crush breccia (fragments > 0.5 cm) Fine crush breccia (0.1 < fragments < 0.5 cm) Crush microbreccia (fragments < 0.1 cm)		
		Cataclasite series	Protocataclasite		10-50	
			Cataclasite		50-90	
			Ultracataclasite		90-100	
		Mylonite series		Protomylonite		
				Mylonite		
				Phyllonite varieties		
				Ultramylonite		
		Grain growth pronounced		?		
				Blastomylonite		

Figure 1.1 - Sibson (1977)'s classification of fault rocks as modified in Scholz (1990).

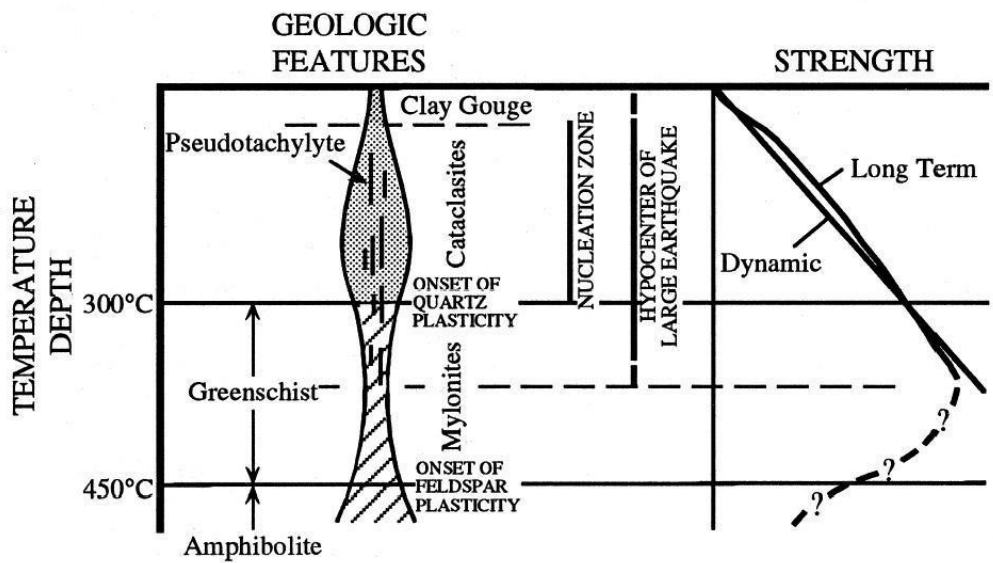


Figure 1.2 - Scholz (1988a)'s synoptic model of a granitic shear zone showing the depth distribution of major fault rocks with the strength profile of the lithosphere (after Kawamoto & Shimamoto, 1998).

On that account, to appreciate the fault rock strength in the upper crust we have to consider firstly bulk strength of rocks, and secondly microcrack frictional strength when slip occurs.

### 3. Dynamic crack propagation

The Coulomb-Mohr failure criterion predicts the stress state at which rock strength is exceeded and a new fracture surface develops in the intact rock, such as:

$$\tau = C + \mu_s \times \sigma_n \quad (1.1)$$

where  $\tau$  is the shear stress at failure,  $C$  is a constant called the cohesion (i.e. the shear stress necessary to initiate sliding under conditions such that  $\sigma_n = 0$  and estimated to range from 0.02 to 0.51 MPa for non-clay gouge and clay-bearing gouge (Bos et al., 2000)),  $\mu_s$  a constant called the static coefficient of internal friction and  $\sigma_n$  the applied normal stress.

While the Coulomb criterion is empirical, the generalized form of the Griffith criterion attempts to predict the complexity of macroscopic failure based on micromechanical description (Griffith, 1924) for identical results. The following discussion is based on Griffith's theory.

Materials naturally contain defects which can be cracks (i.e. surface defects). Considering the crack as a mathematically flat and narrow slit in a linear elastic medium, the macroscopic strength is related to the intrinsic strength of the material through the relationship between the applied stress and the crack-tip stresses (Scholz, 1990). In response to an applied stress, an individual crack can achieve its local propagation conditions when:

$$G_c = \frac{K_c^2}{E} = 2 \times \gamma \quad (1.2)$$

where  $E$  is the Young's modulus,  $\gamma$  is the specific surface energy,  $G_c$  and  $K_c$  represent material properties,  $K_c$  is the critical stress intensity factor (or fracture toughness), depending on the crack propagation mode (Lawn & Wilshaw, 1993) and  $G_c$  is the critical energy release rate (or fracture energy) such as:

$$G = -\frac{\delta(-W + U_e)}{\delta c} \quad (1.3)$$

where  $c$  is the larger semi-axe of the elliptical hole shape of the crack,  $U_e$  is the total energy of the system expended in creating the new surfaces and  $W$  the work done by the external forces.

#### 4. Static friction

Based on low slip-rate experiments ( $V < 0.1$  mm/s), Byerlee (1978) compiled a large quantity of friction data for a great variety of rock types at various normal stresses. He found that rock is strongly dependent on surface roughness at low normal stress, and is nearly independent on rock type at high normal stress. The required shear stress to cause sliding on initially finely ground and interlocked surfaces (i.e. on a preexisting fracture) is given by:

$$\tau = 0.85 \times \sigma_n \quad \text{for } \sigma_n < 200 \text{ MPa} \quad (1.4)$$

$$\tau = 0.5 + 0.6 \times \sigma_n \quad \text{for } \sigma_n > 200 \text{ MPa} \quad (1.5)$$

where  $\tau$  and  $\sigma_n$  are respectively the shear stress and normal stress acting between slip surfaces (Fig. 1.4; see equation 1.1). Hence, the shear stress is defined by the linear law  $\tau = A + B\sigma_n$  where  $A$  and  $B$  are constants. This gives rise to the generally accepted definition of the coefficient of friction  $\mu_s = B + A/\sigma_n$  for which the first term  $B$  is equal to  $\tau/\sigma_n$  and the second term is neglected such as:

$$\mu_s = 0.85 \quad \text{for } \sigma_n < 200 \text{ MPa}$$

$$\mu_s = 0.6 \quad \text{for } \sigma_n > 200 \text{ MPa}$$

A general straight line approximation can be estimated regardless of normal force magnitude (Sibson 1983):

$$\mu_s \approx 0.75$$

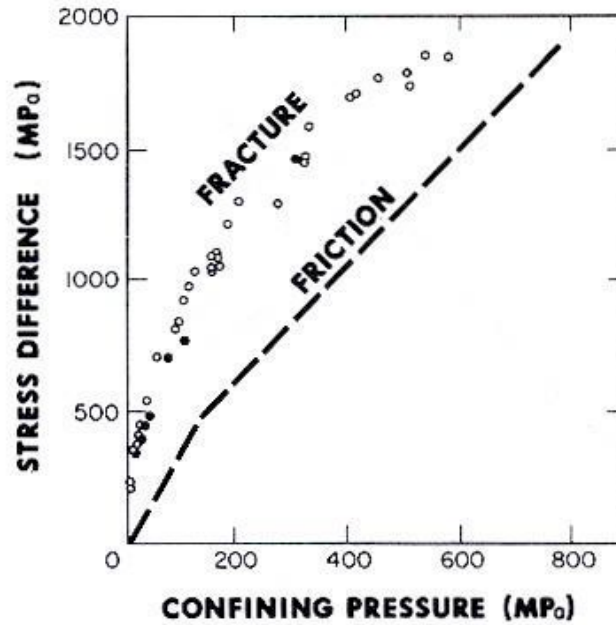


*Figure 1.3 - Strength of Westerly granite as a function of confining pressure with for comparison the referenced frictional strength for sliding on an optimally oriented plane (after Scholz, 1990).*

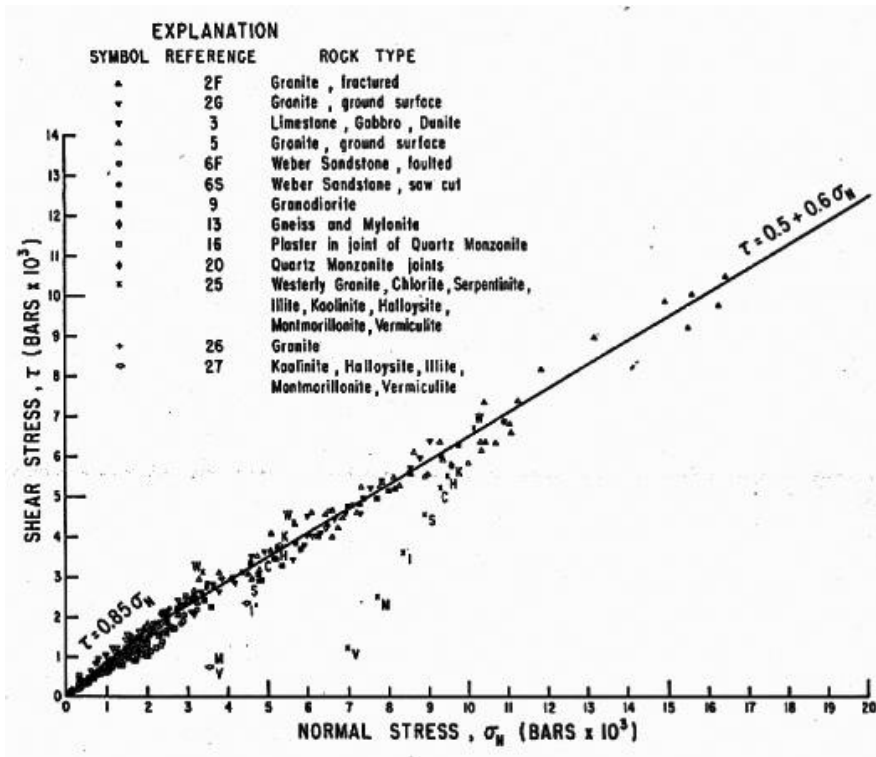


*Figure 1.4 - Frictional strength for a wide variety of rock types plotted as a function of normal load (after Byerlee, 1978).*

This is known as *Byerlee's law* and is consistent with stress measurements in deep boreholes (Zoback & Zoback, 1997). However, friction can be very low ( $\sim 0.2$ ) when sliding surfaces are separated by a layer of clayey gouge (Fig. 1.4).

## 5. Dynamic friction

Laboratory gouge deformation shows that the fabric geometry reflects the geometry of the strain field within the shear zone. Working on granular shear zones, researchers report that in the first millimeters of shear displacement, after a short compaction effect due to closing of preexisting cracks (Scholz, 2002), dilatancy (i.e. non-elastic volume dilation as a result of application of a deviatoric stress) takes place by firstly loosening the interlocking of densely packed grains accounting for clast flaking, transgranular fracturing and distributed microcracking (Brace, 1966; Rawling & Goodwin, 2003), and secondly by initiating the deformation of a narrow shear band of uniform width (Mandl et al., 1977; Marone, 1998b), nearly parallel to the maximum principal stress direction. Refinement of these shear surfaces termed Riedel shears (Mair & Marone, 1999) is accompanied by grain rolling (i.e. erratic dynamic rotation) and grain sliding, as long as clasts prevail with a subangular shape (Mair & Marone, 2000; Mair et al., 2002). The amount of slip on such surfaces is necessarily quite limited, because of their geometry. Thus, to accommodate additional slip displacement, discrete slip surfaces called Y-shears occur parallel to the shear zone and progressively coalesce (Scholz, 2002). With increasing slip displacement, strain is progressively concentrated along the uncoupled contact surfaces, along which asperities (i.e. protrusion between opposite surfaces) interact.

The mechanical behavior of the asperity contacts during the initial slip determines friction: if the adhesive wear mechanism dominates, plastic deformation gives rise to welding of asperities, whereas in the case the abrasive wear mechanism dominates, elastically-brittle interactions give rise to rupture of asperities (Rabinowicz, 1965; Dieterich, 1978; Swanson, 1992).

After an extensive displacement, initial slip surfaces are completely separated by a wear material resulting from abrasion of the two wall-rock surfaces. As a consequence, frictional properties of the fault become more the properties of the wear material than the surface

properties (Scholz, 1990). This fine layer of wear material is thought to control fault strength and related slip instabilities in the shallow crust.

## 6. Earthquake friction laws

Brace and Byerlee (1966) pointed out that earthquakes could be the result of a dynamic frictional instability called stick-slip, resulting in a very sudden slip (1 - 3 m/s) along a preexisting fault, associated to a stress drop termed the *velocity weakening slip* (stick-slip model). To understand the nucleation and the coseismic dynamic of earthquake faulting in the upper crust (including inter-, pre-, co-, and post-seismic processes), we should establish a full frictional constitutive law for rock friction from experimental experiments investigated in a wide range of slip-rates (up to m/s) and slip displacements (up to 10 m).

### **B. Friction at low slip-rates ( $10^{-1} - 10^3 \mu\text{m/s}$ )**

Frictional sliding along a pre-existing surface is initiated once the ratio of shear stress to normal stress exceeds the static coefficient of friction  $\mu_s$ . Then the frictional resistance drops to a lower dynamic friction coefficient  $\mu_d$ . The stiffness of the fault system during this slip-weakening event determines the occurrence of a dynamic instability (Scholz, 2002).

In 1972, Dieterich showed that  $\mu_s$  depended on the history of the sliding surface contact ( $\mu_s$  increases as  $\log t$ ), and that  $\mu_d$  in the steady-state sliding regime depended on the sliding velocity (positive or negative dependence being related to several parameters). The parameter  $D_c$ , which is called the critical slip distance, was proposed to be the necessary slip distance for the coefficient of friction to evolve from  $\mu_s$  to  $\mu_d$  (Dieterich, 1978), i.e. the necessary slip distance for a fault to renew the population of its surface asperity contacts.

Frictional stability of simulated faults during a slip-weakening event was determined from bare rock friction experiments, by empirical heuristic laws called the *slip-rate- and state-variable constitutive laws*. But the version in best agreement with experimental data is the *Dieterich-Ruina's law* (Beeler et al., 1994), which is expressed as:

$$\mu = \left[ \mu_0 + a \times \ln\left(\frac{V}{V_0}\right) + b \times \ln\left(\frac{V_0 \times \theta}{D_c}\right) \right] \quad (1.6)$$

where  $\mu$  is the coefficient of friction without any static or dynamic distinction,  $V$  is the slip-velocity,  $\mu_0$  the steady-state friction for which slip-velocity is equal to  $V_0$ ,  $D_c$  the critical slip distance,  $a$  and  $b$  are material properties, and  $\theta$  is a state variable which evolves with time according to:

$$\frac{d\theta}{dt} = 1 - \frac{\theta \times V}{D_c} \quad (1.7)$$

The second term of the equation 1.6 is a velocity dependent ratio (dependence from a sudden change in sliding velocity), while the third term represents a time dependent ratio (loading time history of the static contact). Hence, in response to an imposed step increase in sliding rate, there is a transient increase in friction, that is the direct effect term  $a$ , followed by a gradual decrease in friction, that is the evolution effect term  $b$  (Fig. 1.5). At the frictional steady-state, the friction is determined by:

$$\mu = \left[ \mu_0 + (a - b) \times \ln\left(\frac{V}{V_0}\right) \right] \quad (1.8)$$

And if  $\mu$  is defined as  $\mu_d$  at the frictional steady-state, equation 1.8 evolves such as:

$$\frac{d\mu_d}{d(\ln V)} = a - b \quad (1.9)$$

From there, two cases can be distinguished: if  $(a - b) \geq 0$ , the frictional behavior is inherently stable and is said to be velocity strengthening (frictional resistance increases with sliding velocity), whereas if  $(a - b) < 0$ , the frictional behavior is said to be velocity weakening and unstable regime can occur under a sufficient strong dynamic loading. Considering a fault system with a stiffness  $k$  and a velocity weakening event, unstable slip instabilities will occur when (Scholz, 1998):

$$\bar{\sigma}_n > \frac{k \times D_c}{-(a-b)} \quad (1.10)$$

Besides, if  $\sigma_n$  is near this critical value, the dynamic coefficient of friction becomes oscillatory. This field is considered to be conditionally stable. Hence, frictional velocity dependence is considered as the most likely explanation for differences between stable sliding (aseismic) and unstable stick-slip (seismogenic) behavior (Marone, 1998b; Scholz, 1998). Meanwhile, one should keep in mind that even earthquakes can only nucleate in the unstable field, they can propagate in both velocity dependence fields (Rice & Ruina, 1983).

This frictional constitutive law has been broadly used in laboratory to reproduce the complex slip-weakening behavior of simulated faults with or without intervening gouge. It is capable of reproducing the entire range of natural fault frictional behaviors during the interseismic and the coseismic slip, by considering the role of several parameters.

Gouge represents the fine-grained incohesive material that underlines the central part (core zone) of mature faults (Fig. 1.1; Sibson, 1977). It is generally assumed that this fault rock is the end-product of a combination of brittle deformation (i.e. cataclasis) and diagenetic processes, with smectite and illite as the most common clay minerals for sedimentary and crystalline host rocks up to at most 8 km depth (Evans & Chester, 1995; Vrolijk & Pluijm, 1999). The dissimilarity in fault maturation implies that corresponding frictional behaviors should be fundamentally different (Marone & Scholz, 1988; Marone et al., 1990). So, the following parameters state the nature of rock contact at the start of friction experiments.

#### 1. Influence of hold-time (quasi-stationary contact-time)

If  $\mu$  in equation 1.8 is defined as  $\mu_s$  at the starting friction of bare rocks, following a long period of time  $t$  in stationary contact, equation 1.8 evolves such as:

$$\frac{d\mu_s}{d(\ln t)} = b \quad (1.11)$$

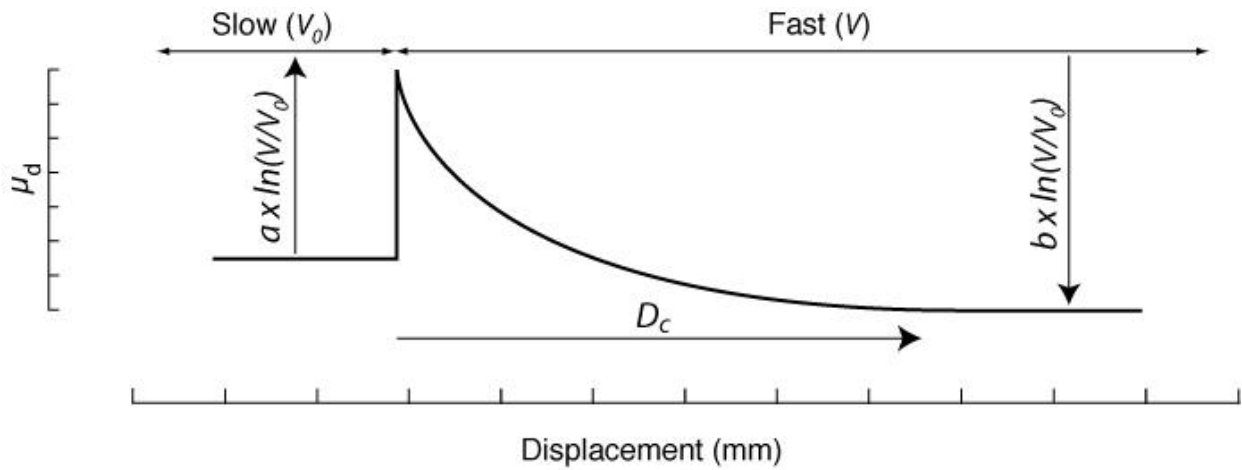


**Figure 1.5** - Schematic diagram showing the significance of the various terms used in the Dieterich-Ruina's law, by the change in the coefficient of friction at a velocity step.

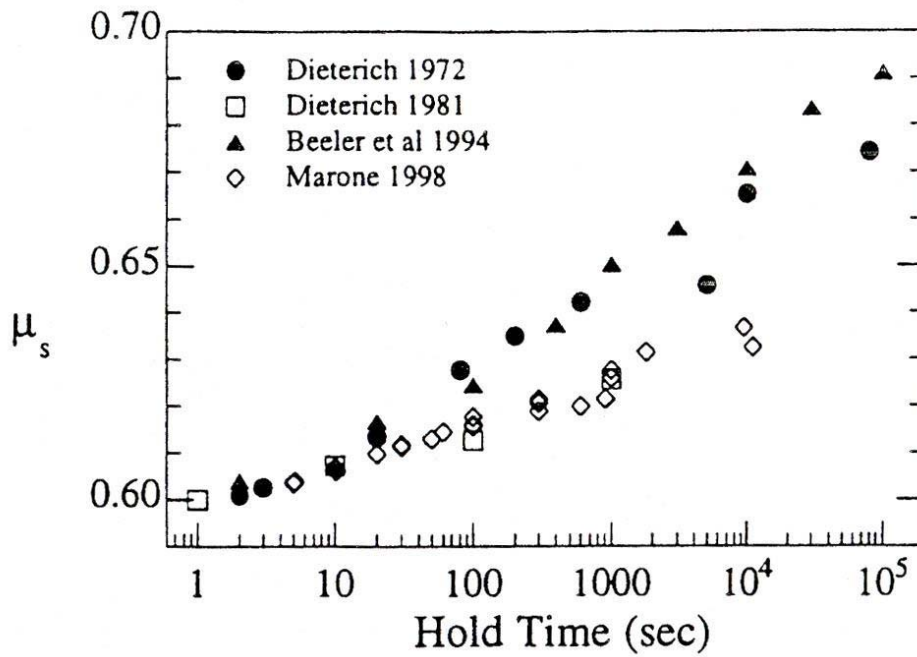


**Figure 1.6** - Dependence of the static coefficient of friction on hold-time for initially bare rock surfaces (solid symbols) and granular fault gouge (open symbols; after Marone, 1998b).

And at the frictional steady-state, the state variable  $\theta$  is proportional to slowness:

$$\theta_{ss} = \frac{D_c}{V} \quad (1.12)$$

$\theta_{ss}$  is then considered to represent an average contact lifetime. Dieterich (1972) showed that static friction increases logarithmically with hold-time (i.e. simulated fault recovers its initial strength), with a rate somewhat higher for bare rock than with intervening fault gouge (Fig. 1.6). This result is related to the physical mechanisms responsible of friction: frictional behavior of bare surfaces can be described as asperity interaction, whereas friction of fault gouge is a more complex issue because it is a granular material. The former is thought to be related to thermally-activated mechanisms that increase the contact area (Scholz, 1990; Dieterich & Kilgore, 1994, 1996) or the contact bonding quality (Hirth & Rice 1980; Rice et al., 2001), whereas the latter is thought to be related to granular particle reorganization, shear localization (Sammis et al., 1987; Wong et al., 1992; Jaeger et al., 1996; Marone, 1998b; de Gennes, 1999) and granular dilation (Morrow & Byerlee, 1989; Marone et al., 1990; Segall & Rice, 1995; Sleep 1997; Mair & Marone 1999). There is however a common parameter between the two frictional cases: physico-chemical mechanisms responsible for the time-dependent strengthening law in static state of sliding surfaces ( $\mu_s$ ) can be simply understood as contact junctions strengthening with age (Rabinowicz, 1951), resulting from both a packing density increase and a contact area/strength increase (Bos & Spiers, 2002).

Hence, friction experiments show that healing mechanism of the hold-time period should play a key role in fault strengthening and subsequently on the fault stress drop magnitude during the coseismic slip.

## 2. Influence of temperature

Studies on the dependence of the friction rate dependence on temperature for bare granite surfaces showed that the friction rate dependence ( $a - b$ ) decreases towards negative values up to 200 °C, but increases towards positive values with increasing temperature above 300 °C (Fig. 1.7, Stesky et al., 1974; Blanpied et al., 1991). This threshold, which corresponds to the onset of quartz plasticity, implies that frictional instabilities below a depth

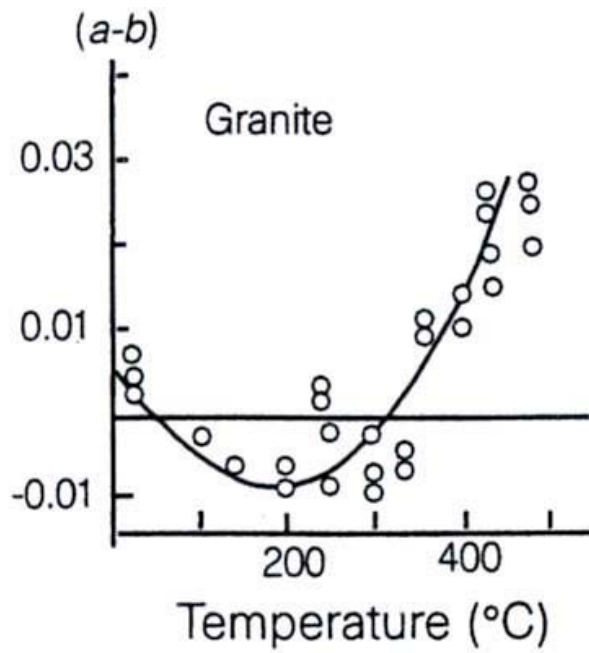


**Figure 1.7** - Dependence of the friction rate dependence ( $a - b$ ) on normal stress for granite (after Marone et al., 1990).

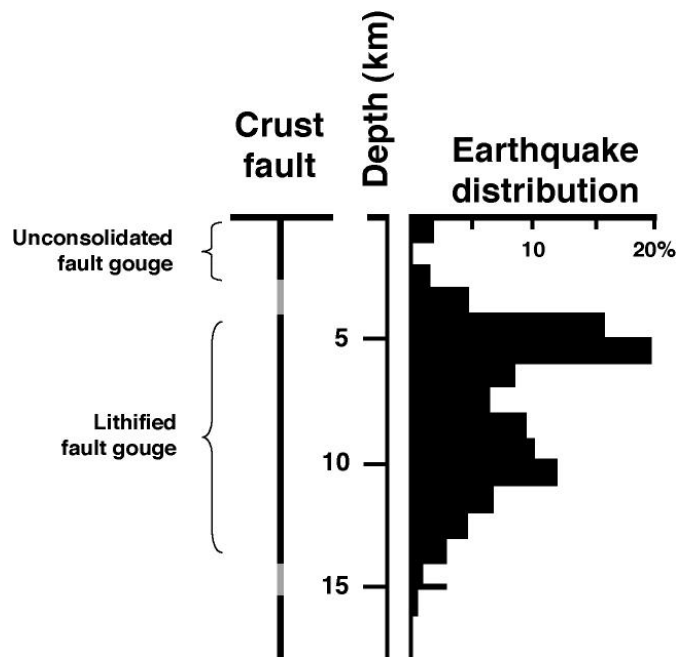


**Figure 1.8** - Depth distribution of earthquakes for a section of the San Andreas fault near Parkfield, California. The evolution of the friction stability parameter with increasing depth is enhanced on the right side of the figure (modified after Scholz, 1998).

of 15 - 20 km for crustal faults in a quartz-rich crust.

Moore et al. (1986) observed a great tendency to stick-slip motion and stress drop for crushed granite gouges, montmorillonite- and illite-rich gouges at 200, 400 and 600 °C, and sliding velocities of  $4.8 \times 10^{-2}$   $\mu\text{m/s}$ . These results are consistent with the concentration of many of the largest earthquakes at the base of the seismogenic zone (Figs. 1.2 & 1.8; Sibson, 1982). This suggests that low slip-rate conditions may be determinant in the earthquake nucleation phase for natural faults at such depths.

Additional work by Moore et al. (1989) in similar experimental conditions as Moore et al. (1986) showed a correlation between sliding behavior and textures: samples showing a frictional stick-slip behavior exhibit well-defined shear bands, whereas samples that slide stably exhibit a pervasively developed deformation fabric, or a localized shear combined with low Riedel shear angles. Therefore, shear bands in natural fault gouge at temperatures higher than 200 °C appear to be a necessary but not a sufficient requirement for stick-slip.

### 3. Influence of normal stress

Experimental shear of fault gouge tends to make the friction rate dependence ( $a - b$ ) more positive because of dilatancy effect, which involves a velocity strengthening behaviour (Marone et al., 1990). But increasing normal stress (i.e. the lithostatic pressure applied on the fault surface) leads to a decrease of the friction rate dependence ( $a - b$ ) (Fig. 1.9; Marone, 1989).

To account for stable behavior of rocks with depth (i.e. with increasing temperature and lithostatic pressure), Scholz (1998) defined from seismological studies a stability parameter  $\xi = (a - b) \times \sigma_n'$ . This latter becomes more negative when the tendency for unstable slip increases, that is between 15 and about 40 km depth (Fig. 1.8). This signifies that there exists a near surface region for which gouge becomes lithified as a result of low-temperature processes (e.g. diagenetic alteration, fluid release from low-temperature dehydration among others), and a depth region for which cataclasite becomes ductile as a result of high-temperature processes.

#### 4. Influence of fault gouge

The weaker component of fault gouge controls the mechanical behavior of a mixed shear zone, even at few percentage per volume (Kawamoto & Shimamoto, 1998). This is related to extreme shearing of the weaker member grains at the zones of strain concentration, which suppresses stick-slip at large shear strains (up to 30). In natural fault gouges, the weakest phase may be constituted by clay phyllosilicates (Vrolijk, 1999), whose volume and degree of alignment lead to fault strength decrease (Shea & Kronenberg, 1993; Vannucchi et al., 2003).

The shear strength of intervening pure clay gouges in drained conditions showed strong variations depending on particle anisotropy and layer charge (Olson, 1974; Rosenquist 1962, 1984; Müller-Vonmoos & Loken, 1989). A review (Warr & Cox, 2001) of clay shear strength shows: kaolinite > illite > chlorite > illite-smectite > chlorite-smectite > vermiculite > smectite. But laboratory experiments report an opposite frictional behavior than the unstable widely expected: a velocity strengthening behavior for illite and an evolution from velocity weakening towards velocity strengthening for smectite over a range of slip-velocities and normal stresses (Saffer & Marone, 2003). No clear explanation has been proposed up to date to account for this apparent inconsistency in the clay frictional behavior.

Blanpied et al. (1992) reported that sealing and compaction of fault gouge under hydrostatic loading and/or during shearing can dramatically increase pore pressure and allow sliding at low shear stress. The process of sealing is thought to appear during the interseismic period of the seismic cycle (Sibson, 1989), because of hydrothermal fluids which flow along the fault zone compartments (Chester & Logan, 1986; Caine et al., 1996) and which seal fault fracture permeability system (Sibson, 1990; Cox, 1995). This process may explain why the San Andreas fault exhibits a lower strength than laboratory friction experiment predictions (Zoback, 1987; Lachenbruch, 1980; Rice, 1992).

#### 5. Influence of adsorbed water and pore water

Shear strength of sheet-structure minerals can be explained in terms of water layers, present within the structure of clay mineral considered: shear of dry montmorillonite gouges leads to abrasion, wear and fractures, whereas shear of water-saturated montmorillonite gouge is concentrated along thin films of water adsorbed onto the (001) planes that line shear

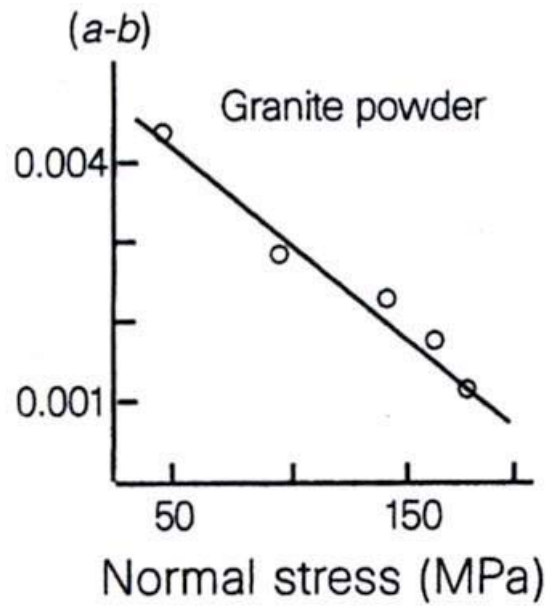


**Figure 1.9** - Evolution of the friction rate dependence ( $a - b$ ) as a function of normal stress for granite (after Stesky et al., 1974 and Blanpied et al., 1991).

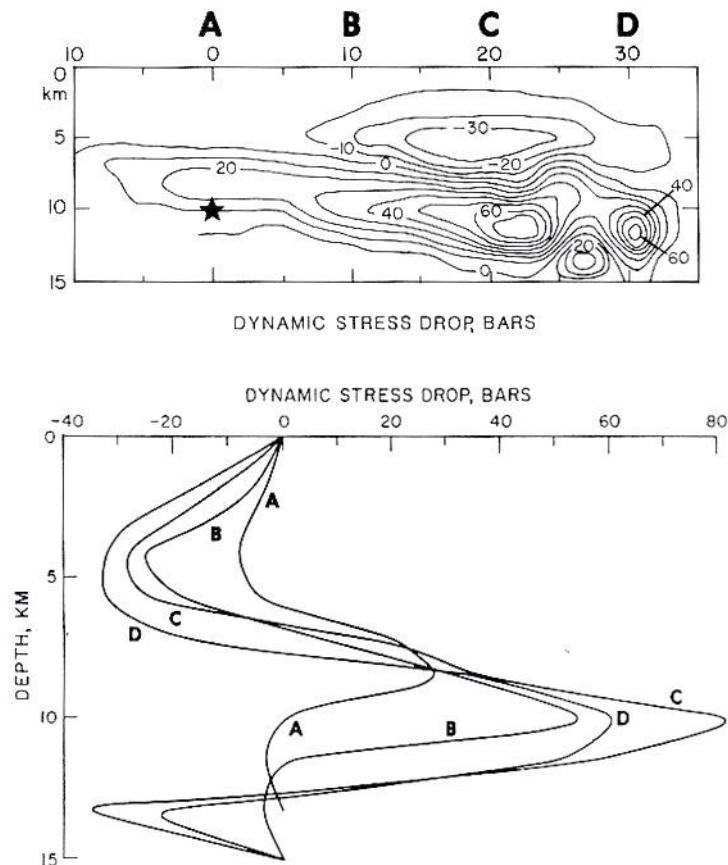


**Figure 1.10** - Results of Quin's (1990) dynamic simulation of Archuleta's result (1984). The upper figure shows dynamic stress drop contoured on the fault. The lower figure shows the depth distribution of stress drop at A-D (after Scholz, 1990).

surfaces (Morrow et al., 2000; Moore & Lockner, 2004a). This provides a low-resistance at slip interfaces by the easy breakage of H<sub>2</sub>O–H<sub>2</sub>O bonds and slip along basal layers (Bird, 1984), which leads water-saturated montmorillonite to exhibit a lower shear strength than dry montmorillonite.

Meanwhile, the shear strength of the adsorbed water film between the (001) surfaces of the platy grains increases as the number of water layers in the film decreases (Israelachvili et al., 1988). In other words, water-saturated sheet silicate strength is inversely related to the water film thicknesses. Hence, the required differential stress to shear water-saturated illite which intrinsically has only one layer of water between the (001) surfaces, is significantly higher than for water-saturated montmorillonite which intrinsically has two layers of water between the (001) surfaces (Wang et al., 1980; Morrow et al., 1984, 1992).

Out of the mineralogical effect of clays, Frye & Marone (2002) have shown that humidity has a significant effect on healing and velocity dependence for quartz and alumina powders at room temperature. They found a transition from velocity strengthening to velocity weakening frictional behavior as the relative humidity (RH) increases, and observed that the healing rate increases with increasing RH. This dependence on RH could be understood as chemically-assisted mechanisms which strengthen contact junctions by increasing the real surface and the quality of contacts. Their work, which is consistent with Dieterich & Conrad (1984) for bare rock friction, suggests that contact junctions of a granular material, depend critically on frictional heating.

As for the presence of pore fluid in fault gouge, it can significantly reduce frictional strength of gouge-filled faults, especially when fluid pressure rises above hydrostatic conditions (Morrow et al., 1992), by facilitating creeping behavior (i.e. stable slip). Indeed, with increasing slip displacement in undrained loading conditions, the presence of fluids can lead to an increase of the total volume of fault gouge, resulting in dilatancy hardening and then velocity strengthening (i.e.  $(a - b)$  more positive; Segall & Rice, 1995).

## 6. Summary

Friction studies at low slip-rates allow to propose a general model for the stability of crustal faults, lined with gouge material as a function of depth, even the role of individual mineral constituent is not clarified. The first transition from stable to unstable slip is localized

around 3 - 4 km of depth (Fig. 1.8). The lower transition is expected to occur at 15 - 20 km depth ( $\sim 350 - 450$  °C), which corresponds to the onset of quartz plasticity and creep behavior (Fig. 1.1). Besides, frictional behavior of clay-rich gouges appear to be controlled by granular material properties and sheet silicate structure, whose shear strength is strongly dependent on initial moisture conditions.

Based on the 1979 Imperial Valley earthquake, results of the dynamic model of Quin (1990) or Favreau & Archuleta (2003), show that the regions of high slip-velocity over 10 km depth correspond roughly to regions of high dynamic stress drop (Fig. 1.10). This result validates the friction model based on the Dieterich-Ruina's law, from which velocity strengthening regions located at around 5 km depth and velocity weakening regions located at around 11 km depth were previously calculated.

However, the Dieterich-Ruina's law (Dieterich, 1978) is inapt to model the early portion of the coseismic slip during which the fault weakens at a faster rate than the release of tectonic stress driving the fault motion (Kanamori, 1994; Kanamori & Heaton, 2000; Scholz, 2002; Jaeger et al., 2007). Therefore, to account for this slip-weakening effect, it is necessary to complement the original Dieterich-Ruina's law by supplementary specific state variables (e.g. Blanpied et al., 1998; Nakatani, 1998; Chambon et al., 2006) developed from laboratory friction studies at high slip-rates. This would allow a better understanding of the dynamic rupture and its mode of propagation, such as the crack-like rupture (Perrin et al., 1995; Andrews & Ben-Zion, 1997; Zheng & Rice, 1998) and the slip pulse rupture (Heaton, 1990; Zheng & Rice, 1998). Moreover, the *D<sub>c</sub> paradox* (Scholz, 1988a; Marone & Kilgore, 1993; Ohnaka & Shen, 1999; Goldsby & Tullis, 2002) and the apparent low coseismic frictional resistance of major faults (Brune et al., 1969; Rice, 1992) can only be solved at present by dynamic weakening mechanisms (based on theoretical or experimental studies and analyses of fossil earthquake rupture zones) such as frictional melting (Jeffreys, 1942; Hirose & Shimamoto 2005), thermal pressurization of pore fluids (Sibson, 1973; Wibberley & Shimamoto, 2004; Noda & Shimamoto, 2005) or silica gel formation (Goldsby & Tullis, 2002; Di Toro et al., 2004). Clarification of newly thermally-activated weakening mechanisms, such as the moisture-related weakening mechanisms of Mizoguchi et al. (2006), which is based on the thermo-poro-mechanical behavior of clay-rich gouge (e.g. Vardoulakis, 2002; Sulem et al., 2004), needs to be addressed to understand the implications of mechanisms such as hydrogen bonding (Rice, 1976; Michalske & Fuller, 1985), water adsorption/desorption (Hirth & Rice, 1980) or capillary bridging (Crassous et al., 1994; Iwamatsu & Horii, 1996) effects at points of contact junctions, on the resistance to slip of

faults in the earth's crust during earthquakes.

### C. Friction at high slip-rates ( $10^{-3} - 10^0$ m/s)

Frictional behavior of bare rocks or gouges at coseismic slip-rates needs to be understood, because it influences the magnitude of strong ground motion (Aagaard et al, 2001), controls the dynamic rupture initiation and propagation (Zheng & Rice, 1998), determines stress evolution during the seismic cycle (Aagaard et al, 2001) and controls the slip-weakening distance  $D_c$  (Ide & Takeo, 1997; Olsen et al, 1997; Mikumo et al., 2003; Fukuyama et al., 2003a).

Frictional properties of bare rocks or gouge at coseismic slip-rates have been poorly constrained in laboratory up to date. The main reason is high velocity frictional apparatus are not able to reproduce the range of earthquake parameters at the same time, such as high slip-rates ( $> 10^{-3}$  m/s), large displacements ( $> 10$  m) or high effective normal stress ( $> 50$  MPa) and to measure simulated fault shear stress behavior.

Frictional data of simulated fault with bare rocks or intervening gouge at high slip-rates show an exponential decrease of the frictional resistance from a peak value ( $\mu_p$ ) towards a steady-state value ( $\mu_{ss}$ ). This slip-weakening behavior can be fitted by empirical laws (Hirose & Shimamoto, 2003; Mizoguchi et al., 2007; Fig. 1.11). But the version in best agreement with experimental data is expressed as (Mizoguchi, 2006):

$$\mu_d = \mu_{ss} + (\mu_p - \mu_{ss}) \times \exp\left(\frac{\ln(0.05) \times d}{d_c}\right) \quad (1.13)$$

where  $\mu_d$  is the dynamic friction coefficient,  $\mu_{ss}$  is the steady-state friction coefficient,  $\mu_p$  is the peak friction coefficient,  $d$  is the displacement and  $d_c$  is the post-peak displacement at which:

$$\mu_d = 0.95 \times (\mu_p - \mu_{ss}) \quad (1.14)$$

The use of  $d_c$  instead of  $D_c$  is justified by the fact that displacement at which frictional

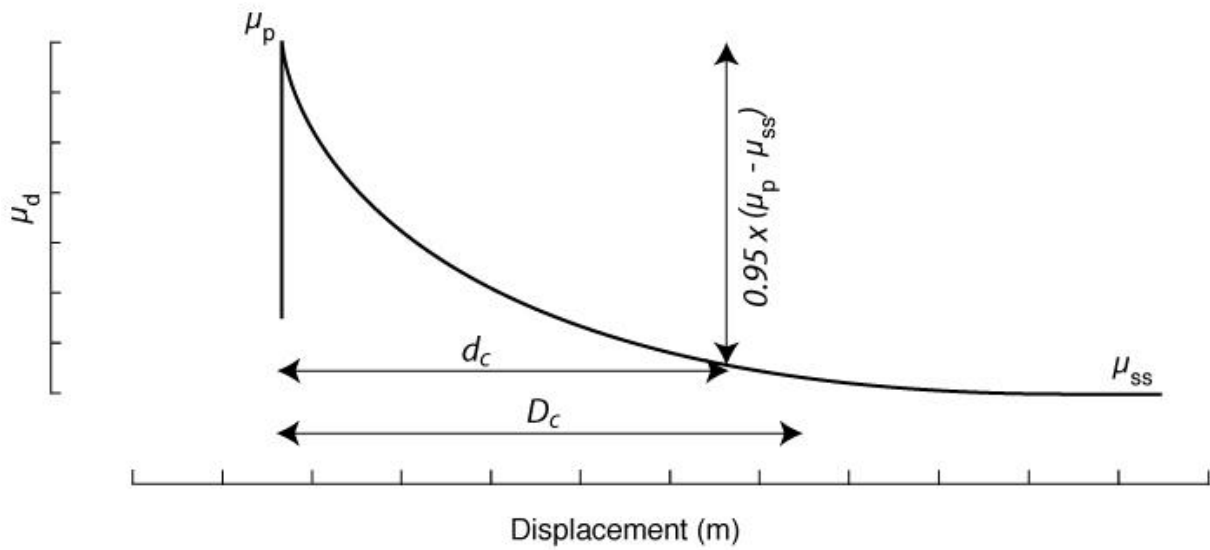


**Figure 1.11** - Schematic diagram showing the significance of the various parameters used in the empirical equation 1.13 to fit the weakening behavior of simulated faults at high slip-velocity.

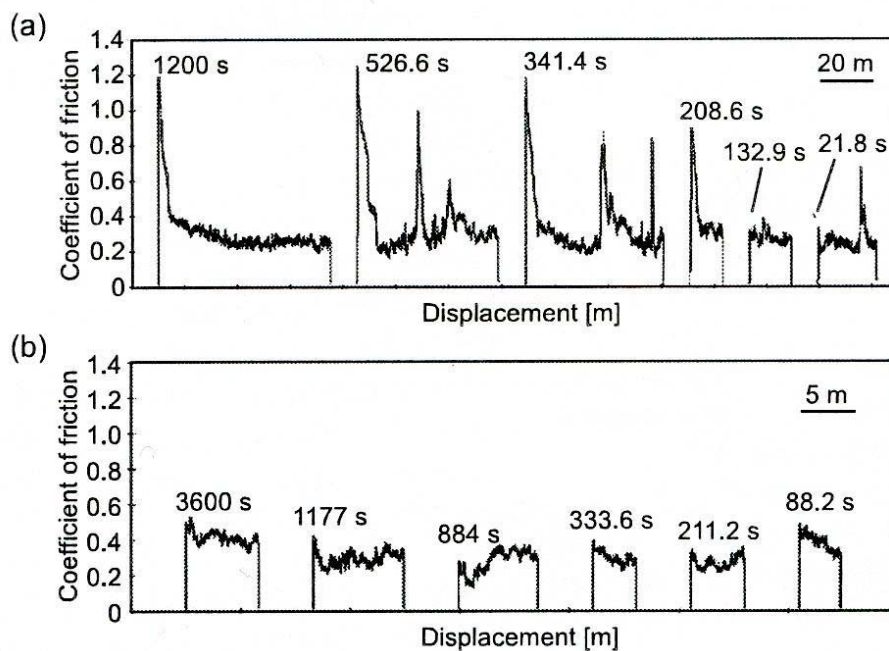


**Figure 1.12** - Representative frictional behavior of a simulated fault at normal stress of 0.62 MPa and a slip-rate of 85 mm/s, containing its own wear material between wall-rocks before each slide test, under (a) room humidity (~43 %) and (b) dry N<sub>2</sub> gas. Numbers at the onset of data represent the pause duration time after previous sliding ended (after Mizoguchi et al., 2006).

steady-state is achieved becomes infinite for the exponential decay of friction. Hence,  $d_c$  can be assumed to represent  $D_c$ . Coefficients of friction ( $\mu_p$  and  $\mu_{ss}$ ) and  $d_c$  are obtained from least square fit curves of experimental data.

Even if this empirical friction constitutive law has not been broadly used to reproduce the complex slip-weakening behavior of simulated faults, some authors (references hereafter) have started to put in an obvious way the role of several fundamental parameters, in order to establish a constitutive law at high slip-rates.

### 1. Influence of hold-time (quasi-stationary contact-time)

From laboratory experiments, Mizoguchi et al. (2006) showed that the strong time-dependent strength recovery of simulated faults containing wear material between wall-rocks is closely related to the moisture conditions (Fig. 1.12). They observed two remarkable trends: firstly, the amount of strength recovery is one order of magnitude higher than that of low slip-rate experiments, and secondly, the steady-state friction is lowered by a factor of three compare to low slip-rate experiments. Mizoguchi et al. (2006) proposed frictional behavior differences to be related to the amount of heat generated by friction, i.e. to be related to the total expended surface energy, which is linearly proportional to slip-velocity, displacement and dynamic stress drop (Lachenbruch, 1980; O'Hara, 2005; Mair et al., 2006).

### 2. Influence of temperature

Reported friction experiments of bare rocks (Westerly granite) at high slip-velocities (up to 2 m/s) revealed that comminution is an essential precursor to melting by friction, with at least 1000 °C reached at the rock interface (Spray, 1987, 1995). Additionally, the author observed that the amount of cataclastic fragments contained within the melt matrix is directly related to the progress of melting, which mainly depends on prevailing rate of strain at the frictional interfaces.

Hirose & Shimamoto (2005) showed that the frictional behavior of simulated bare rock faults (India gabbro) at high slip-velocity (0.85 - 1.49 m/s) could be understood as the association of two stages of slip-weakening separated by a marked strengthening regime (Fig. 1.13). The first weakening stage (which follows an initial peak friction coefficient) is

associated with flash heating at asperity contacts (Rice, 1999), which leads to an increase in the heat production rate with increasing displacement. The incipient formation of melt patches at the tip of asperities, which depends on the melting point of constitutive rock minerals (e.g. Spray, 1992), corresponds to the onset of a selective frictional melting process. It increases shear resistance along the fault (Tsutsumi & Shimamoto, 1997; Koizumi et al., 2004; Spray, 2005) towards a second peak friction coefficient. The subsequent development of a well-defined continuous molten layer affects dramatically the shear resistance of the fault and leads to the second slip-weakening. The  $d_c$  parameter corresponding to the second slip-weakening appears to be determined by two critical factors: the bulk viscosity and shear strain rate of the molten layer. Therefore, melt production at fault interface appears to be a serious candidate to explain the scarcity of natural pseudotachylytes, considering initial melting as a stopping mechanism for fault slip, and to explain the amount of released energy observed for large earthquakes, considering the lubricant effect of a continuous molten layer.

Friction experiments conducted at lower slip-rates (1  $\mu\text{m/s}$  - 100 mm/s) by Di Toro et al. (2004) on bare rocks (Arkansas novaculite) reveals a dramatic decrease in the friction coefficient by more than a factor of 3, once sliding velocity overpasses 1 mm/s, with a maximum average temperature of 150 °C at the rock interface (Fig. 1.14). The slip-weakening behavior is thought to result from the formation of a finely comminuted amorphous silica material on the sliding surfaces. Besides, the authors observed a velocity dependence of friction, which they attribute to the breakdown/formation of bonds between silica particles within a gel layer. This mechanism, acting either as a fault lubricant at coseismic slip-rates or as a viscous brake at low slip-rates, might explain the large dynamic stress drop of earthquakes (Kanamori, 1994), the low stress level of major faults (Brune et al., 1969; Rice 1992) and fault strengthening up to cessation of the coseismic slip observed by seismologists (Koizumi et al, 2004; Fialko & Khazan, 2005).

Numerical studies of thermal pressurization as a slip-weakening mechanism (i.e. drop of fault strength as a result of gouge pore fluid rise by frictional heating during the coseismic slip) show that the heat production rate of a sheared clay-rich gouge layer at seismic slip-rates is far not high enough to melt rock ( $\sim 300$  °C), because of the negative feedback effect of pore pressure rise on the effective fault shear strength (Sibson, 1973; Lachenbruch, 1980; Noda & Shimamoto, 2005). Meanwhile, friction experiments conducted on coal gouge give the evidence that once thermal pressurization operates, the maximum temperature of 900 °C at the rock interface (O'Hara et al., 2006). These results suggest that the temperature at which

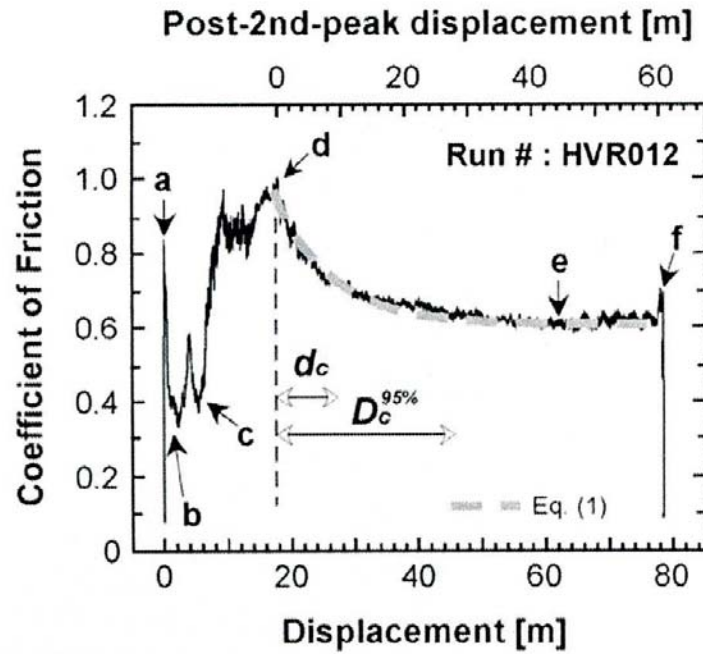


**Figure 1.13** - Representative frictional behavior of a simulated fault at a slip-rate of 0.85 m/s and a normal stress of 1.5 MPa, showing the two weakening stages (a to b and d to e). Dashed line (Eq. 1.13) is a least square fit of the second slip-weakening and  $d_c$  the post-peak displacement value at which  $\mu_d = 1/e \times (\mu_p - \mu_{ss})$  (after Hirose & Shimamoto, 2005).

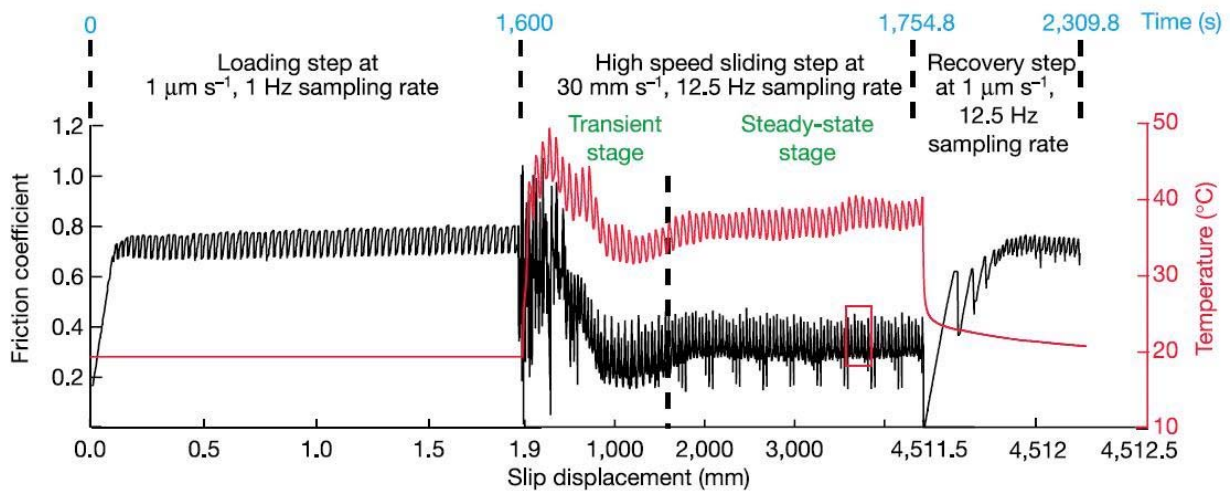


**Figure 1.14** - Representative frictional behavior of a simulated fault at normal stress of 5 MPa with changing slip-velocity as indicated on the figure (after Di Toro et al., 2004).

thermal pressurization is effective depends on the mineral composition of the deformation zone.

Mizoguchi et al. (2006) conducted friction experiments on clay gouge at a slip-velocity of 85 mm/s. They found a moisture-related mechanism which leads to either fault strengthening when moisture is adsorbed on gouge particles (with creation of adhesion forces between particles), or fault weakening when gouge adsorbed moisture is drained off by frictional heating (with break of liquid capillary bridges between contact area of particles) for a maximum average temperature of 380 °C at the rock interface, below the melting point of the main constitutive gouge minerals (e.g. quartz, feldspar and clay minerals; Mizoguchi, 2004). Thus, the moisture-related mechanism is thought to control the friction of the gouge-filled faults in the wet crust, by acting as a fault strength recovering mechanism during the interseismic period, or a coseismic fault lubricant when a sufficient amount of heat is generated by friction during a slip event.

### 3. Influence of normal stress

The load-bearing framework of a fault in the brittle field is governed by the dynamic adhesion of a population of asperities between the sliding surfaces (Rabinowicz, 1965; Scholz, 2002). The localized high stresses at the small asperity contact areas determine the heat production rate of the fault during a coseismic event. Increasing normal stress (and/or slip-velocity and slip duration) leads to extend the stress on individual asperities (Fig. 1.15), which in turn develops abrasive wear mechanism and increases frictional heating on asperities (Fig. 1.16; Scholz, 2002; O'Hara, 2005). It results that thermally-activated slip-weakening mechanisms, such as silica gel lubrication (Goldsby & Tullis, 2002), thermal pressurization (Noda & Shimamoto, 2005; O'Hara et al., 2006) or moisture-drained weakening mechanism (Mizoguchi et al., 2006) are more effective when increasing normal stress (Figs. 1.17 & 1.18).

The  $D_c$  values obtained from laboratory experiments and numerical modelling for thermally-activated slip-weakening mechanisms are of the same order as that determined seismically (Hirose & Shimamoto, 2005; Noda & Shimamoto, 2005). This suggests that this mechanisms can solve the  $D_c$  paradox. And the too large  $D_c$  value obtained by gouge friction experiments approaches the same order of magnitude as seismological studies when increasing normal stress (Fig. 1.19; Mizoguchi, 2007).

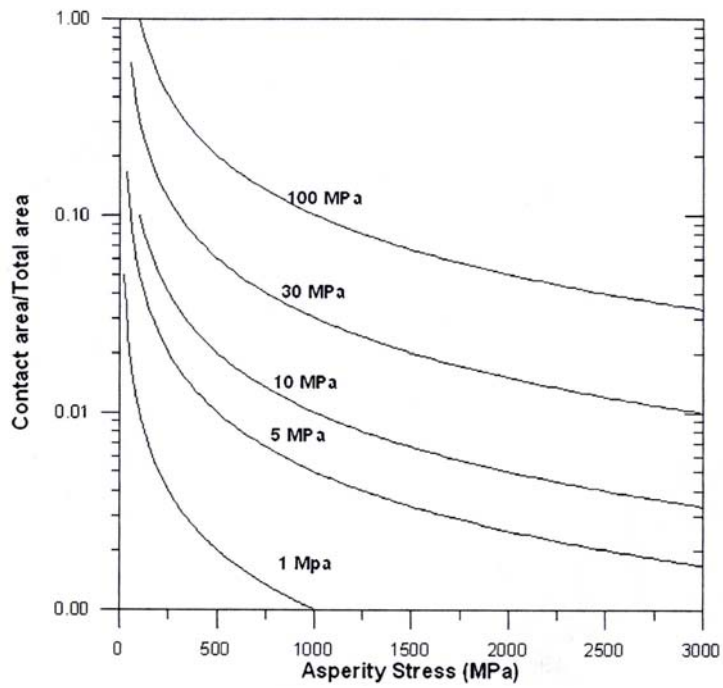


**Figure 1.15** - Plot of asperity stress versus real area of contact/total area for different average fault normal stresses (after O'Hara, 2005).

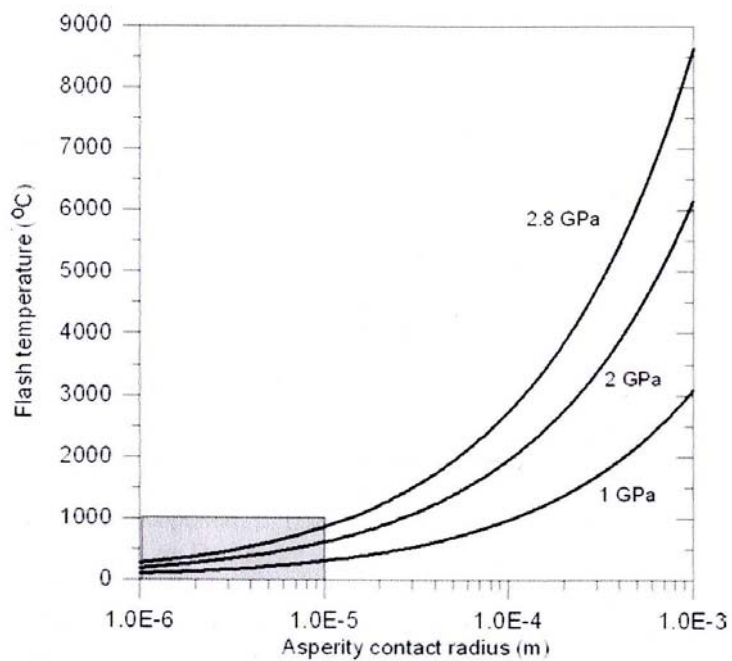


**Figure 1.16** - Flash melt temperatures as a function of asperity contact radius and asperity yield strength (after O'Hara, 2005).

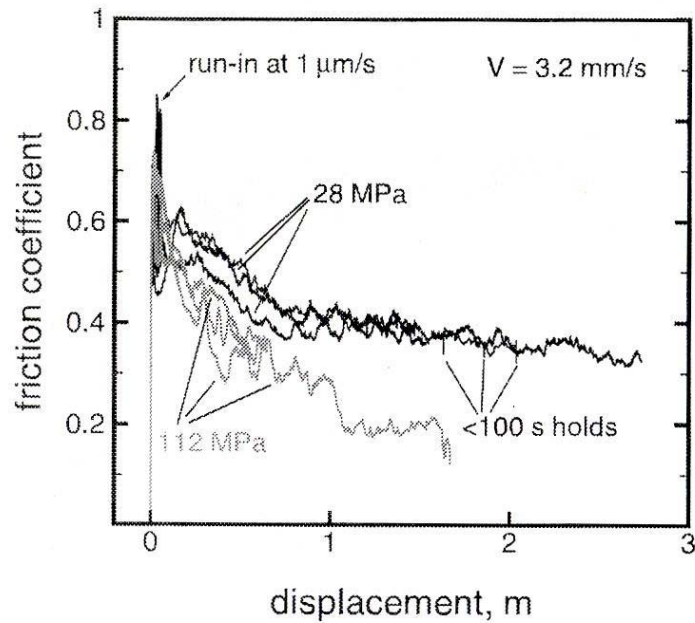


**Figure 1.17** - Plot of friction coefficient versus displacement from high-pressure experiments on confined quartzite samples slid at a normal stress of 28 MPa and 112 MPa (after Goldsby & Tullis, 2002).

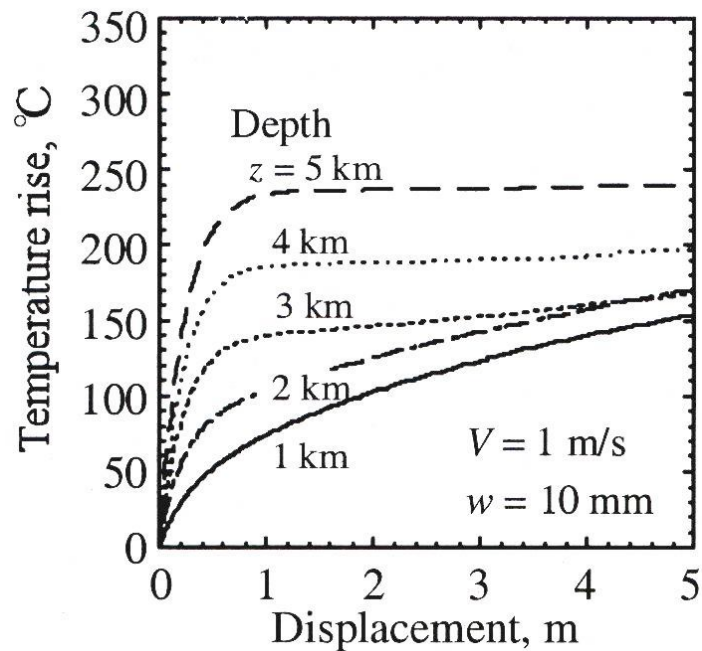


**Figure 1.18** - Temperature rise in the center of a deformation zone plotted against fault displacement during thermal pressurization. The figure shows the numerical effect of depth (after Noda & Shimamoto, 2005).

#### 4. Influence of fault gouge

There are very few friction experiments at high slip-rates on intervening gouge reported in the literature. Mizoguchi et al. (2007) mentioned high velocity friction experiments on fault gouge collected from the Nojima fault. They observed an exponential decrease in friction coefficient from an initial peak friction coefficient ( $\mu_p$ ) towards a steady-state friction coefficient ( $\mu_{ss}$ ) only for slip-velocities higher than 0.09 m/s. This velocity threshold is far higher than the required velocity (1 mm/s) to observe a dramatic weakening on novaculite bare rocks (Di Toro et al., 2004). Additionally, Mizoguchi et al. (2006) reported high velocity friction experiments on bare gabbro rocks. They observed that the necessary distance  $D_c$  for the simulated faults to evolve from  $\mu_p$  to  $\mu_{ss}$  is shortened by about 10 m when friction experiments are conducted without removing the produced gouge on bare rock surfaces from previous sliding. These first results indicate that fault gouge is of primary importance on the occurrence of earthquake during a slip event.

According to Hirose & Shimamoto (2005), the rate of melting and the onset of melt are the primary processes that determine  $D_c$  and the amount of strength reduction. But it is the variation in the mechanical response of minerals (i.e. shear yield strength, fracture toughness and thermal conductivity) that determines the pathway to fusion under conditions of high strain rate deformation. Spray (1992) proposed a hierarchy of friction-melting susceptibilities of the more common rock-forming minerals. A review of the susceptibility to melting is as follows: phyllosilicates > inosilicates (amphiboles > pyroxenes) > tectosilicates > orthosilicates. Considering a mature fault in the upper crust, this suggests that clay minerals should be firstly consumed to form the melt phase, while quartz and feldspar minerals should tend to survive as clasts. But preserved slip zones of exhumed faults rarely exhibit the coexistence of pseudotachylyte and gouge (e.g. Otsuki et al., 2003; Mukoyoshi et al., 2006). This is consistent with friction experiments conducted on clay gouge (Mizoguchi, 2004; Mizoguchi, 2006, 2007) that do not show any melting, contrarily to reported friction experiments of bare rocks under similar high strain rate deformation conditions (Hirose & Shimamoto, 2005). This suggests that additional parameters should determine the fault frictional properties and consecutively the final thermal weakening mechanism. The role of initial gouge water content and scaly fabric development on strain accommodation through localized microshear layers (Vannucchi et al., 2003) needs to be addressed.

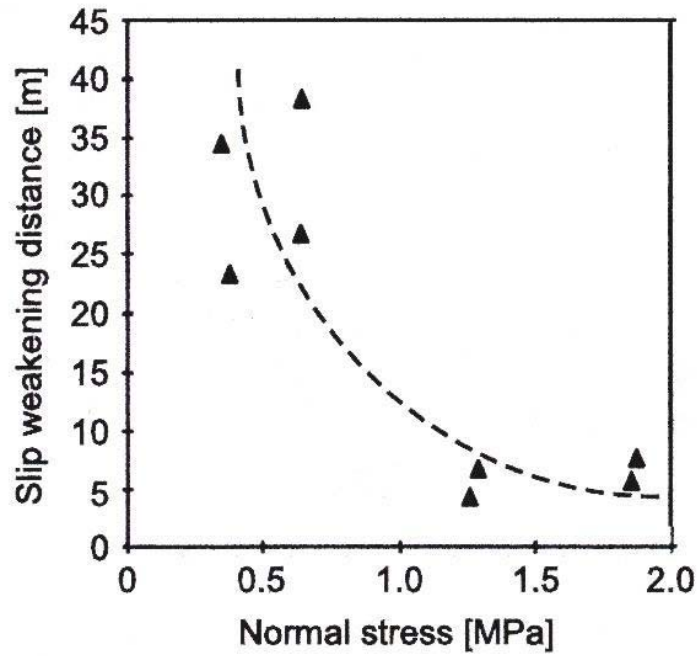


**Figure 1.19** - Slip-weakening distance plotted as a function of normal stress. The figure shows a decrease of  $D_c$  when increasing normal stress (after Mizoguchi et al., 2007).

## 5. Influence of adsorbed water and pore water

Thermally-activated slip-weakening mechanisms, such as thermal pressurization or moisture-drained weakening mechanism do depend on pore fluid-filled conditions of sheared gouge. Indeed, thermal pressurization mechanism is related to the drop of fault strength from gouge pore pressure rise during the coseismic slip, whereas moisture-drained weakening mechanism is related to the break of liquid capillary bridges (i.e. adhesion force) between gouge particles from frictional heating during the coseismic slip. The preferential activation of one mechanism may have important implications on the magnitude of the dynamic fault stress drop and subsequently on the development of frictional instability (Kanamori, 1994; Kanamori & Heaton, 2000). But experimental or numerical consideration of such problem remains unexplored up to date.

## D. Conclusions

Preliminary friction studies conducted at high slip-rates with intervening gouge show a strong slip-weakening behavior and a rapid strength recovery of simulated faults. These first results are consistent with a dynamic rupture propagating as a self-healing slip pulse mode rather than as a shear crack mode. Besides, normal stress and slip-velocity appear to be critical on the determination of the heat production rate during fault sliding and consecutively on the efficiency of thermally-activated slip-weakening mechanisms.

The very slow creeping movements ( $< 1 \times 10^{-3}$  m/s) of initial slip earthquakes over tens of hundred of micrometers can lead in the upper crust to gouge pore fluid heating by shear localization process (Veveakis et al., 2007). This can lead in turn to thermally-activated slip-weakening mechanisms such as thermal pressurization over slip displacement of the order of  $\sim 1$  m (Noda & Shimamoto, 2005). Hence, discrepancy between  $D_c$  obtained from low slip-velocity experiments and seismically inferred  $D_c$  might be reconciled assuming seismic data only detecting the larger  $D_c$  (Goldsby & Tullis, 2002).

Predicting the most likely thermal weakening mechanism for a selected fault from friction experiments and choices conditions would allow to predict in the near future shear fracture energy and earthquake magnitude. Consequently, the new high velocity machine designed by Shimamoto (Shimamoto & Hirose, 2006), which covers slip-rates from 3 mm/yr

to 10 m/s in fluid-rich environments, brings hope to merge experimentally low and high velocity laws with related velocity weakening and slip-weakening behaviors. It aims at exploring the *intermediate strength barrier*, which shows at intermediate velocities (few tenths of mm/s) a change in velocity dependence from velocity weakening to velocity strengthening behavior. This work is of primary importance, because it would state the mechanical and tribochemical conditions along the fault that counteract against the onset large earthquakes, immediately after earthquake nucleation.

## **CHAPTER II**

### **Structure and hydraulic properties of the Usukidani fault (Japan)**

## A. Structural and microstructural analyses

### 1. Internal structure of the Usukidani fault

#### 1.1. Geological setting

The vertical N55°E-striking Usukidani fault is located in the western part of Honshu, Japan, about 50 km north of Hiroshima (Figs. 2.1 & 2.2). It belongs to the Western Chugoku fault system which consists of prominent NE-SW master faults and short second-order NW-SE faults commonly abutting against the previous ones (Kanaori, 1990, 2005; Fabbri et al., 2004). The western Chugoku fault system was formed in Cretaceous to Paleogene times in response to distributed strike-slip deformation between the Median Tectonic Line (MTL) and a poorly-defined fault zone located along the Japan Sea coast, the Southern Japan Sea fault zone (SJSFZ). The formations affected by the Western Chugoku fault system include Permian metamorphic and sedimentary rocks, Jurassic sedimentary rocks and Cretaceous acidic pyroclastic deposits locally intruded by late Cretaceous granites and granodiorites (Yamada et al., 1985).

Several faults of the Western Chugoku system are active today, as attested by shallow earthquakes with magnitudes between 5 and 6.8 and with focal depths ranging from 8 km to 12 - 15 km (Fig. 2.2; Kanaori, 1997, 2005; Okada, 2004). Displaced ridges or valleys testify to an active right-lateral motion along the NE-SW first-order faults. Focal mechanisms of earthquakes generated along these faults also indicate a right-lateral slip along the NE-SW nodal planes (Research Group for Active Faults of Japan, 1991; Fukuyama et al., 2000). Second-order NW-SE faults do not show any clear displaced topographical features. However, in the easternmost part of the Chugoku region, the 2000  $M_w$  6.6 ~ 6.8 Tottori earthquake (focal depth ~ 15 km) nucleated on a NNW-SSE fault without any surface expression (Fukuyama et al., 2003a). The well constrained focal mechanism indicates an almost pure left-lateral sense of slip (Sagiya et al., 2002). Inversion of seismological data further indicates that most of the coseismic displacement occurred in the upper 6 km of the crust (Semmane et al., 2005). Right-lateral slip along NE-SW faults and left-lateral slip along NW-SE faults agree with the directions of the principal components of the present-day stress

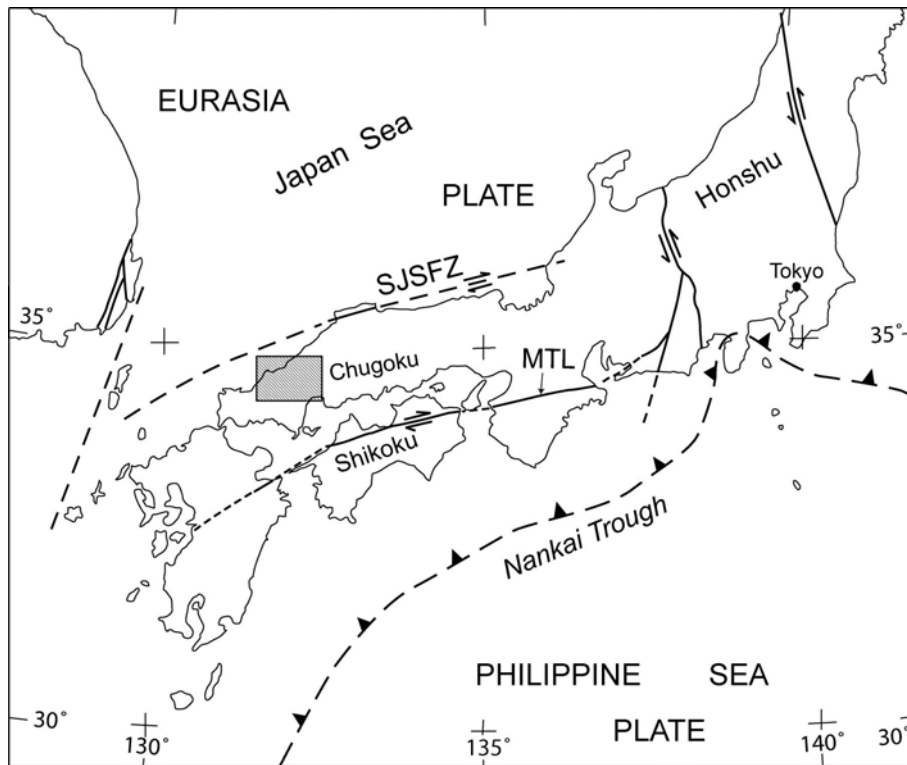


**Figure 2.1** - Geodynamical setting of the Western Chugoku fault system. The area covered by the shaded box indicates the position of Figure 2.2 (after Boutareaud et al., in press).

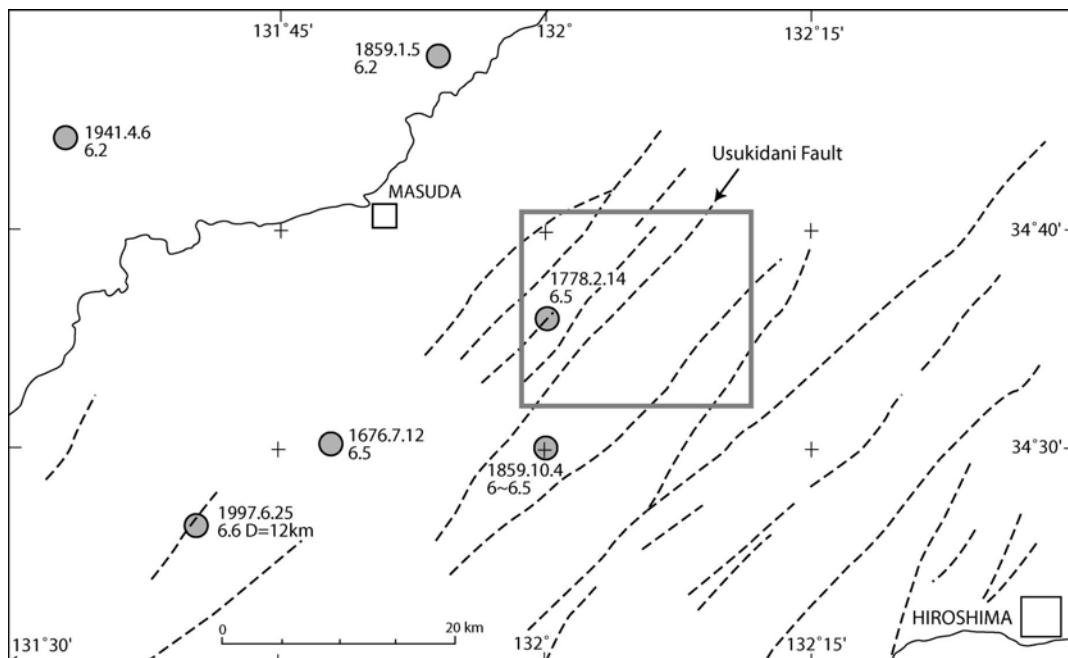


**Figure 2.2** - Seismotectonic context of the study area, with circles corresponding to crustal seismic events. Boxed area indicates the position of Figure 2.3. Labelled circles corresponds to fault rock sampling location (after Boutareaud et al., in press).

field, namely a horizontal E-W-trending  $\sigma_1$  axis and a horizontal N-S-trending  $\sigma_3$  axis (Ichikawa, 1971; Huzita, 1980; Tsukahara & Kobayashi, 1991).

The Usukidani fault cross-cuts late Cretaceous rhyolitic and dacitic secondary silicified tuffs and tuff breccias (Hikimi and Abu Groups; Yamada et al., 1985). It corresponds to an alignment of valleys and depressions which can be followed on aerial photographs along more than 40 km. Based on this pronounced geomorphological expression, the Research Group for Active Faults of Japan (1991) classified the Usukidani fault as potentially active. The epicentres of two magnitude 6 ~ 6.5 historical earthquakes (14 Feb. 1778 and 4 Oct. 1859) are located at about 5 km from the fault trace (Fig. 2.2; Research Group for Active Faults of Japan, 1991), but there is no proven relationship between these events and displacement along the Usukidani fault.

## 1.2. Studied outcrops

The internal structure of the Usukidani fault zone was investigated along two continuous sections where nearly the entire width of the fault zone is exposed: the Shimomichi-kawa-kami exposure (A exposure; Figs. 2.3 & 2.4) and the Jougabashi exposure (abbreviated to B exposure; Figs. 2.3 & 2.6). The fault zone around these localities cut through rhyolitic tuff protolith. At the two localities, the Usukidani fault zone consists of a 10 m wide damage zone which includes three gouge zones (Figs. 2.5 & 2.7).

### 1.2.1. Protolith

The protolith consists of a grey to pink colored coarse secondary silicified tuff with euhedral to subhedral K-feldspar phenocrysts (~ 0.3 mm) embedded in a siliceous matrix inside which rare micas can be recognized (Figs. 2.8a & 2.9a). Flow surfaces are not uncommon in the area, but could not be recognized in the vicinity of the Usukidani fault. Away from the fault, the protolith tuff is moderately jointed, and most of the joints are of cooling type. In the vicinity of the fault, joints become numerous and tectonic joints prevail over cooling joints. Secondary minerals such as quartz or calcite commonly fill the joints. At the microscopic scale, the density of intra- and transgranular cracks increases towards damage zones. The contacts between the protolith and damage zones are always observed to be

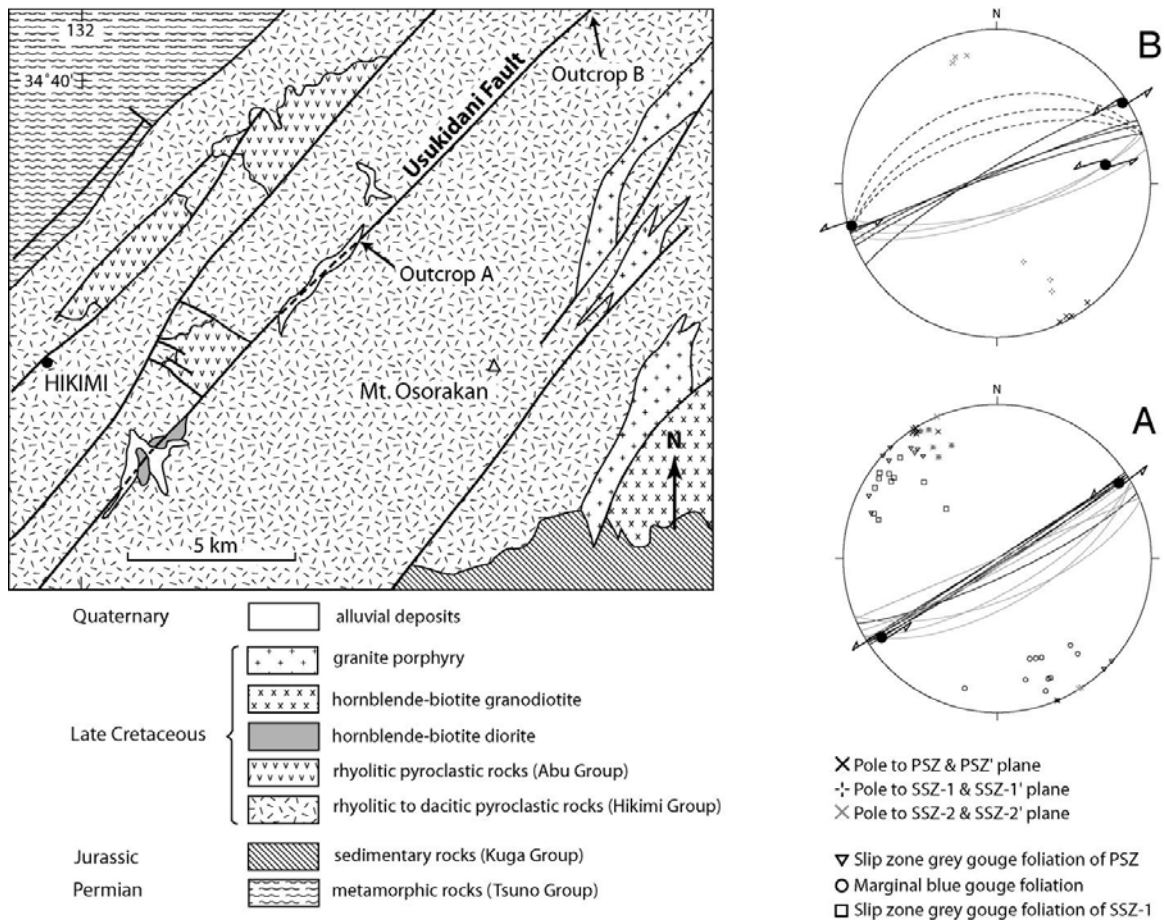


**Figure 2.3** - Simplified geological map of the Usukidani fault and location of the studied outcrops A and B. The stereograms are lower-hemisphere equal-area stereographic projections. Labelled circles corresponds to fault rock sampling location for permeability and/or porosity measurements.

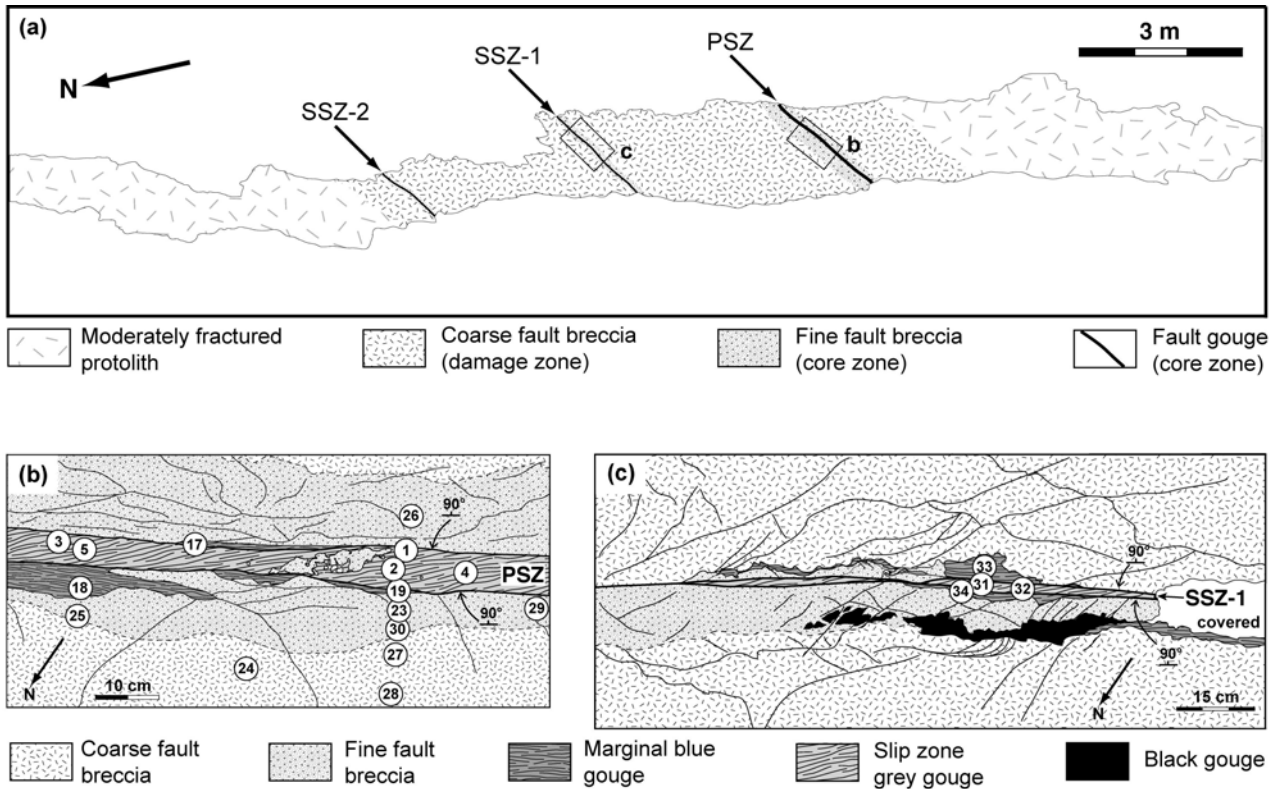


**Figure 2.4** - (a) Structural sketch map of the A exposure, showing the distribution of fault rock types and gouge slip zones. (b) Detail of the principal slip zone PSZ. (c) Detail of the secondary slip zone SSZ-1.

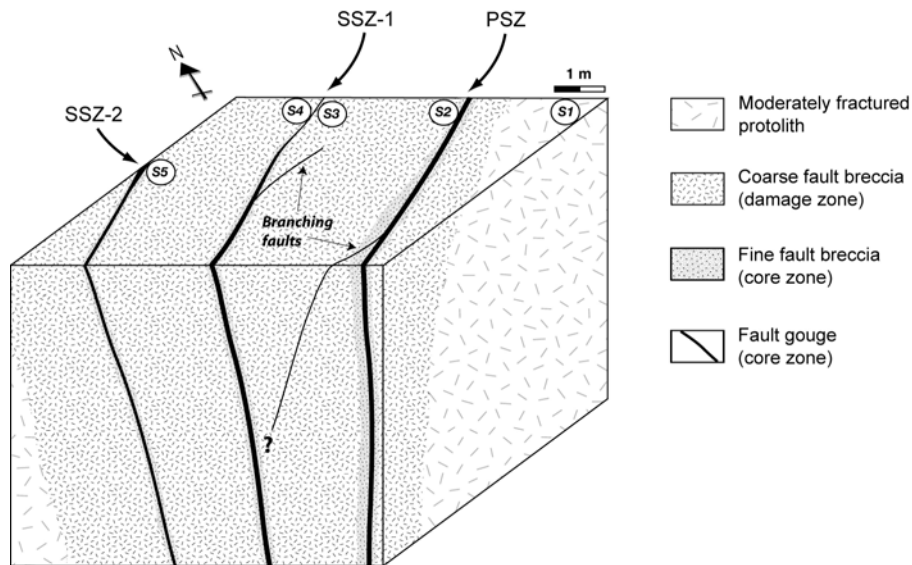


**Figure 2.5** - Summary model of fluid flow behavior around the outcrop A of the Usukidani fault in the shallow crust. Note that gouge slip zones are exaggerated in scale. Labelled circles corresponds to fault rock sampling location for XRD analyses.

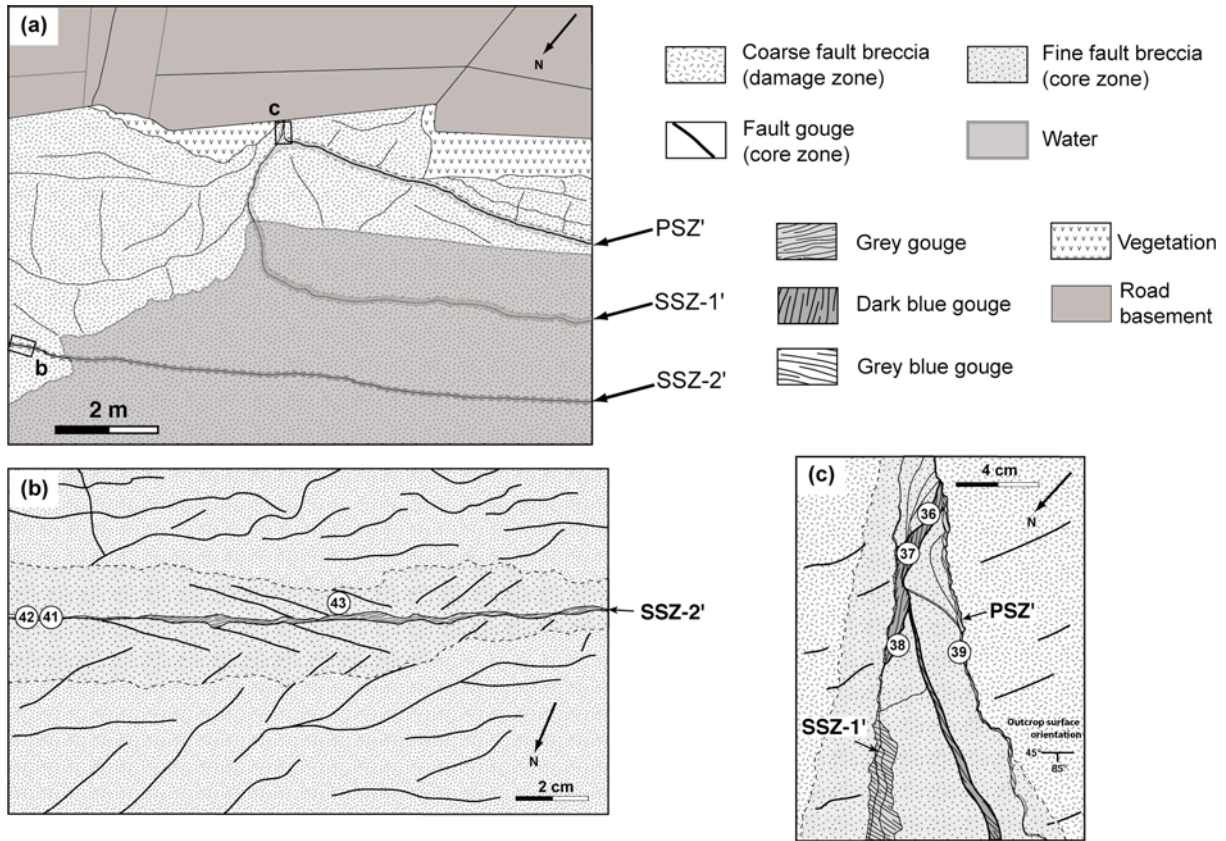


**Figure 2.6** - Structural sketch map of the B exposure, showing the distribution of fault rock types and gouge slip zones. (b) Detail of the merge between the principal slip zone PSZ' and the secondary slip zone SSZ-1'. (c) Detail of the secondary slip zone SSZ-2'. Labelled circles corresponds to fault rock sampling location for permeability and/or porosity measurements. Samples 35 and 40 are out of the scope of the detailed sketch map (c).

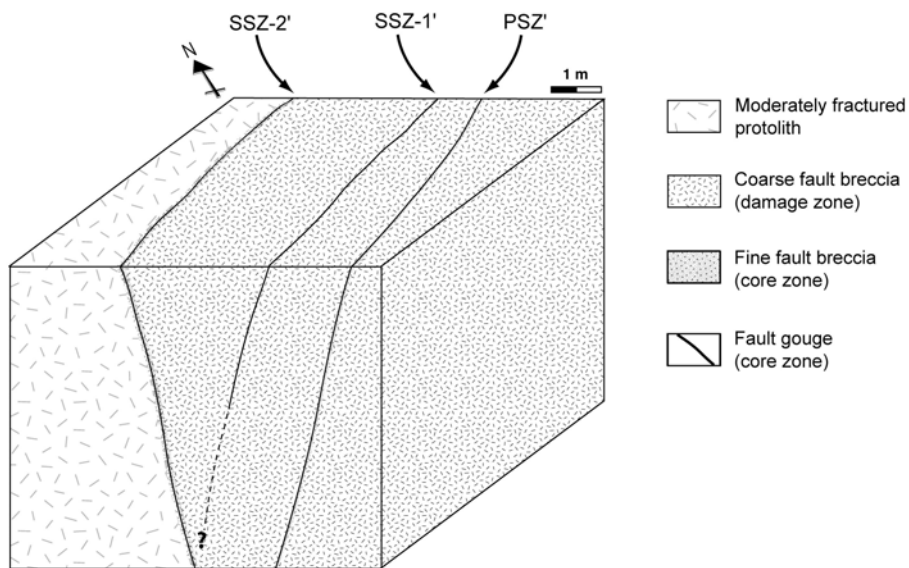


**Figure 2.7** - Summary model of fluid flow behavior around the outcrop B of the Usukidani fault in the shallow crust. Note that gouge slip zones are exaggerated in scale.

gradational.

### 1.2.2. Damage zones

The damage zone consists predominantly of a coarse breccia composed of intensely fractured and strongly altered welded tuff, with clay minerals, quartz, calcite, laumontite and crushed grains of quartz and feldspar filling the fractures (Figs. 2.8b, 2.8c & 2.8d). At the microscopic scale, the altered tuff presents a medium-grained clast-supported matrix composed essentially of fractured quartz phenocrysts showing embayments, anhedral K-feldspars (orthoclase and sanidine) frequently exhibiting a perthitic texture, few intense saussuritized Ca-plagioclases, subordinate amounts of chloritized biotites and hydrothermalized chlorites (Fig. 2.9b). Transgranular cracks in grains of quartz and feldspar are frequently filled by yellowish phylitic minerals. Approaching the core zones, the alteration is more severe, as attested by a decrease in the proportion and size of the clasts, a higher microfracture density, intensely sericitised feldspars, undulatory extension of quartz, cracks filled with carbonate minerals, and clay minerals (mainly smectite) replacing feldspar phenocrysts, especially along fractures. The progressive transition from the damage zones to the gouge core zones is done by a very clayey fine-grained fault breccia, composed of an aphanitic matrix of quartz and feldspar, alteration of mica grains to iron oxides and calcite veins (Figs. 2.8e, 2.8f & 2.9c). The contacts between the fine fault breccia and the gouge core zones are sharp for all the slip zones.

### 1.2.3. Core zones

#### 1.2.3.1. Outcrop A

Three distinct core zones can be distinguished in the section across the fault zone (Figs. 2.4 & 2.5). They consist of unconsolidated or poorly consolidated clay gouge zones flanked by fine fault breccia zones (Fig. 2.8). Among these gouge zones, the one located to the southeast contained the principal slip zone, because its boundaries with the adjacent breccia are sharp and planar, and because of its clear lateral continuity at the scale of the outcrop. Conversely, the two other clay gouge zones display less sharp and less regular

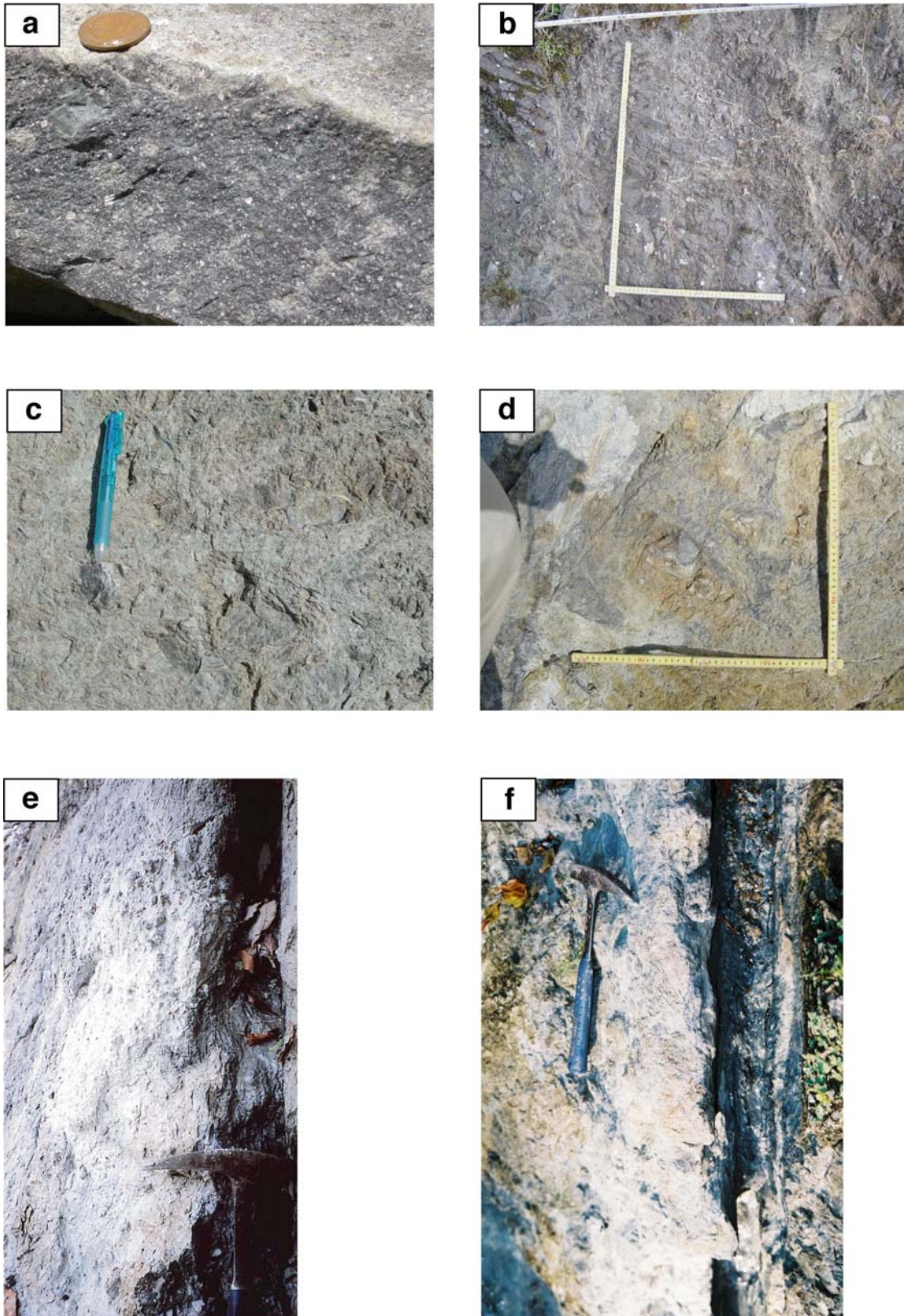


**Figure 2.8** - Photographs of Usukidani fault rocks from A and B exposures. (a) Rhyolitic protolith observed 20 meters away from the SSZ-2'. (b) Coarse breccia located at 25 m to the southeast from the PSZ. (c) Coarse breccia located at 1 m to the southeast from the SSZ-1. (d) Coarse breccia located at 50 cm to the northeast from the PSZ. (e & f) Fine breccia observed along the southwestward side of the PDZ.

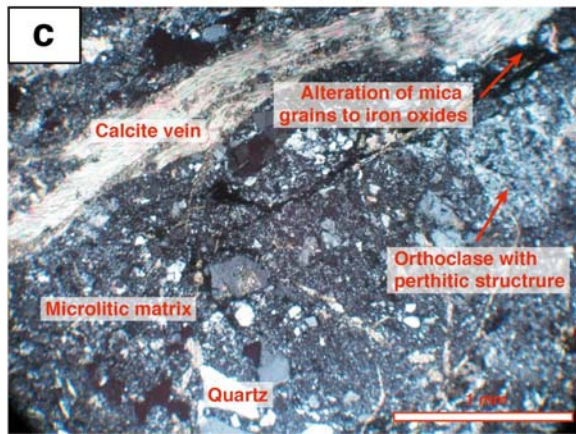
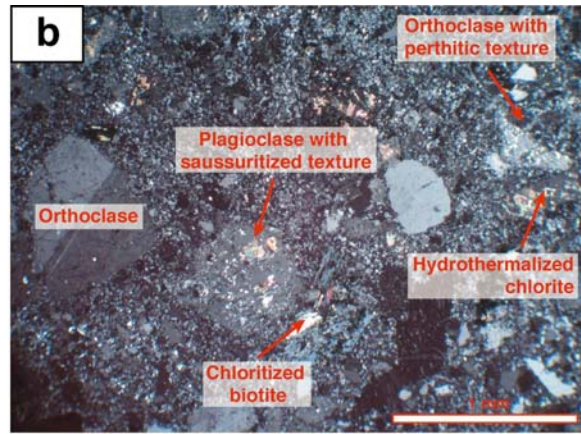
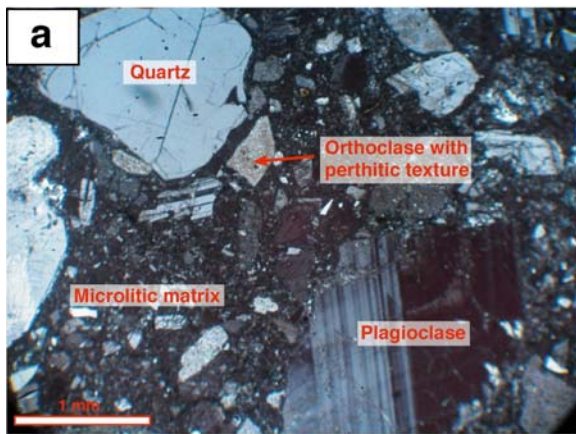


**Figure 2.9** - Microphotographs in polarized light of Usukidani fault rocks from A and B exposures. (a) Moderately fractured protolith. (b) Coarse breccia. (c) Fine breccia.

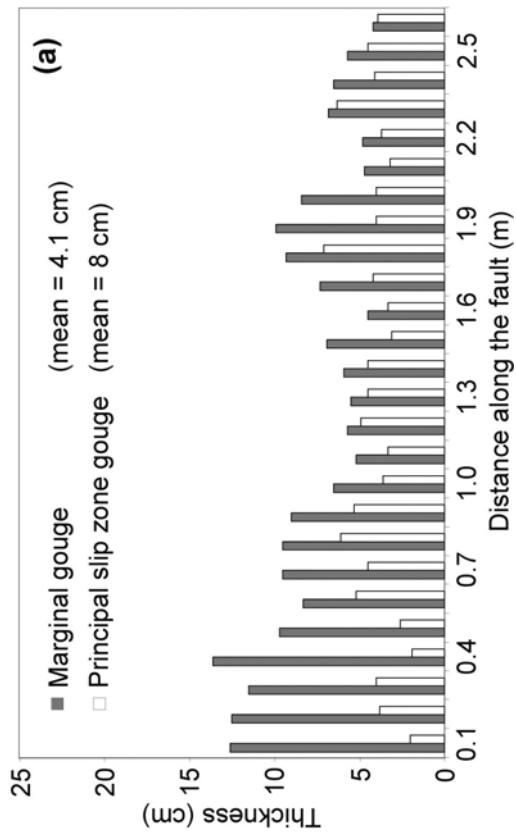
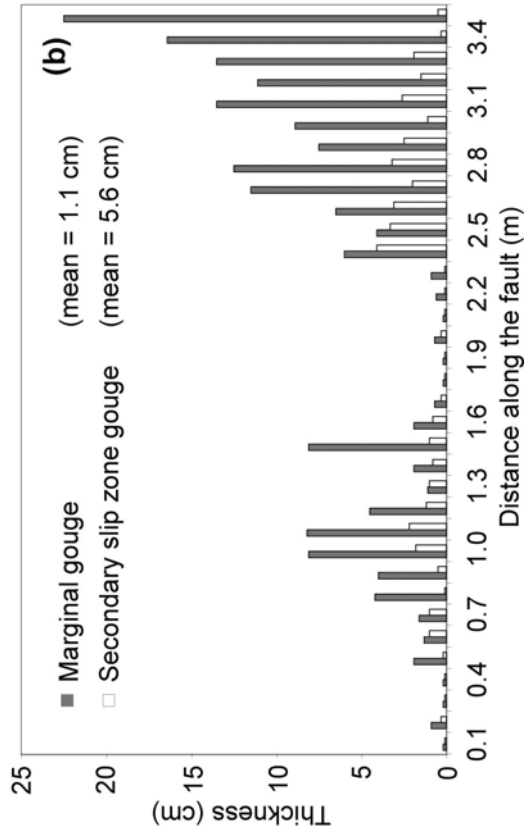


**Figure 2.10** - Along-strike measured variations of the thickness of the PSZ gouge and the marginal gouge (a), and the SSZ-1 gouge and the marginal gouge (b) of the exposure A.

boundaries and their thicknesses show a high variability (Fig. 2.10b). They are considered as secondary slip zones (SSZ) and are presumed to merge laterally, along strike or along dip, with the PSZ. This assumption is supported by the observation at the outcrop B of a secondary slip zone merging with the principal slip zone. Besides, two incipient branching faults of more than 1.5 m in length with few centimeter thick gouge occur at the scale of this outcrop: the first one comes from the SSZ-1 and stops before linking the PSZ over the coarse breccia, and the second one branches from the PSZ towards the SSZ-1 (Fig. 2.5)

The PSZ consists of a planar vertical strip of clay gouge striking N55°E and whose thickness ranges from 4.2 cm to 13.6 cm, with a mean value of 8 cm (averaged on 26 measurements; Fig. 2.10a). It is separated from the adjacent fine fault breccia or from a marginal foliated gouge by two striated vertical planes striking N55°E +/- 2°. The rake of the striation is less than 10° northeastwards. The PSZ gouge, that locally contained large breccia fragments, is composed of incohesive grey clay showing a finely spaced vertical foliation striking 30° or less counterclockwise of the trend of the PSZ, in agreement with the right-lateral sense of slip reported for the Usukidani fault (Kanaori, 1999). XRD analyses (following methods describe by Klug and Alexander (1974) and Kübler (1987)) of grey clay gouge samples show that it is composed of quartz, K-feldspar, plagioclase, calcite, kaolinite, and mixed illite-smectite layers (Fig. 2.11).

The PSZ gouge is flanked by a marginal poorly consolidated blue foliated clayey gouge and by moderately consolidated fine clay-rich fault breccia. The fine breccia likely results from cataclasis and circulation of hydrothermal fluids. Both processes probably contributed to the alteration of the original protolith and its enrichment in clay minerals. Strands of the marginal foliated gouge locally penetrates the fine fault breccia and pinches out along a fracture striking 10 to 20° clockwise to the trend of the PSZ (Fig. 2.4b; area located to the right, or southwest, of sample 18). This pattern suggests that ancient ruptures may have propagated sideways off the line of the main fault.

The zonation of the secondary displacement zone SSZ-1 is similar to that of the PSZ (Fig. 2.4c). It includes a narrow central incohesive grey clay gouge zone bounded by two vertical striated planes striking N55°E +/- 15° and whose thickness ranges from 0.2 cm to 22.5 cm, with a mean value of 5.6 cm (averaged on 35 measurements; Fig. 2.10b). XRD analyses show that the grey clayey gouge is composed of the same minerals as the PSZ gouge (Fig. 2.11). As for the PSZ, the rake of the striation on the bounding planes is between 0 and 10° either northeastwards or southeastwards. Remnants of poorly consolidated foliated blue clayey gouge are observed between the striated planes and the thick marginal clayey fault

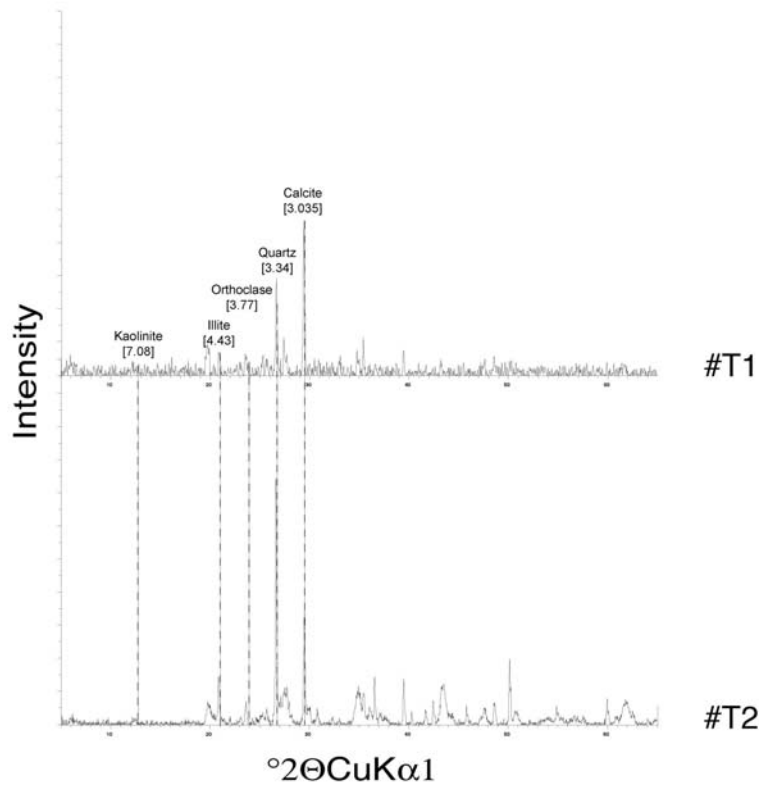


**Figure 2.11** - X-ray diffraction analyses for the T2 sample from PSZ gouge and T1 sample from SSZ-1 gouge, from the all grain-size fractions. Location samples are indicated on the Table 2.1. Sharp peaks are quartz, orthoclase, calcite, kaolinite and illite.

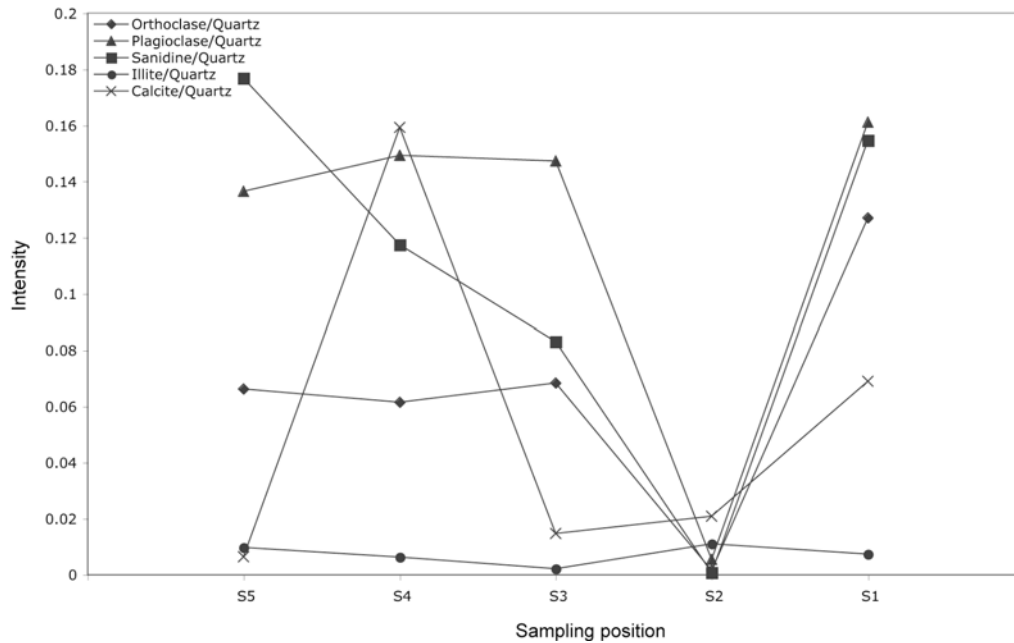


**Figure 2.12** - X-ray diffraction profile across the fault zone of A exposure, with host-rock quartz abundance as normalized component. Location samples are indicated on the Table 2.1 and Figure 2.5.

Sample	Type of gouge	Location
#T1	Grey gouge	SSZ-1
#T2	Grey gouge	PSZ
#T3	Grey gouge	SSZ-1'
#T4	Black gouge	SSZ-1
#T5	Mixed gouges	PSZ

**Table 2.1** - Location of XRD gouge samples referenced on figures 2.11 and 2.13.

Sample	Fault-rock
S1	Moderately fractured protolith
S2	Fine breccia
S3	Coarse breccia
S4	Fine breccia
S5	Fine breccia

**Table 2.2** - Location of XRD fault rock samples referenced on figure 2.12.

breccia zones. Unlike the PSZ, remnants of consolidated black gouge are also found between the fine fault breccia and the coarse fault breccia.

The X-ray diffraction profile done across the fault zone, with host-rock quartz abundance as a normalized component, shows a drop in peak feldspar intensities towards the S2 sampling position, which is located on the northwest side fine breccia of the PSZ (Fig. 2.12). This observation indicates an hydrothermal alteration enhanced along the northwest side of the PSZ, and suggests a spatial variability of the fault-core fluid-flow properties.

X-ray diffraction analyses of mixed grey gouge and marginal blue gouge of the PSZ show the existence of quartz, feldspar, calcite, interstratified smectite/illite, minor amount of kaolinite and pyrite (Fig. 2.13). Grey and blue gouges are clearly matrix-supported and fine-grained for a random fabric (Fig. 2.14). The contact boundary between the fine breccia and the marginal blue gouge is quite regular and sharp, with some fragments of the breccia interfingering and mixing with the bounding part of the blue gouge (Fig. 2.14a). In the matrix, a cataclastic foliation defined as bands of different colors almost parallel to the fault plane can be observed (Fig. 2.14b). This may be related to an alternation of compositional differences in clay minerals. Clasts of quartz or feldspar contained in the matrix are randomly distributed. They are angular to sub-rounded in shape and are well-sorted with a size lower than 28  $\mu\text{m}$  as a mean. Brittle fractures are present in quartz for a small amount of plastic deformation. A wide variety of deformation structures can be observed in the gouge, and may be used as shear sense indicator. Asymmetric structures dissect and offset the foliation, with shear planes or shear bands suggesting a left lateral sense of slip (Figs. 2.14c, 2.14d & 2.14e). Discrete and thin calcite-filled fractures can be locally observed (Fig. 2.14f). Some remain intact, others have undergone deformation subsequent to their development. These microstructural observations indicate that fluid circulation and consecutive cement healing events occurred between past brecciation (slip ?) events (Sibson, 1989).

The gouge matrix of the grey slip zone gouge exhibits a crenulated appearance with locally a wavy-shaped appearance that defines a S-foliation (Fig. 2.15a). This may be related to the intersection of two different fabric orientations. Discrete deformation structures can be observed in the gouge, with shear planes or composite planar fabrics that exhibit patent offsets, or simply dissect the foliation (Figs. 2.15b & 2.15c). But the sense of slip cannot be constrained there. The gouge matrix is very clayey, phylliform and contains few clasts of quartz or feldspar compare to the grey gouge (Fig. 2.15b). This might suggest that this gouge layer has undergone a higher strain rate and a greater clay mineral development compare to the bounding blue gouge. However, coarse elliptical-to-rounded survivor clasts of calcite

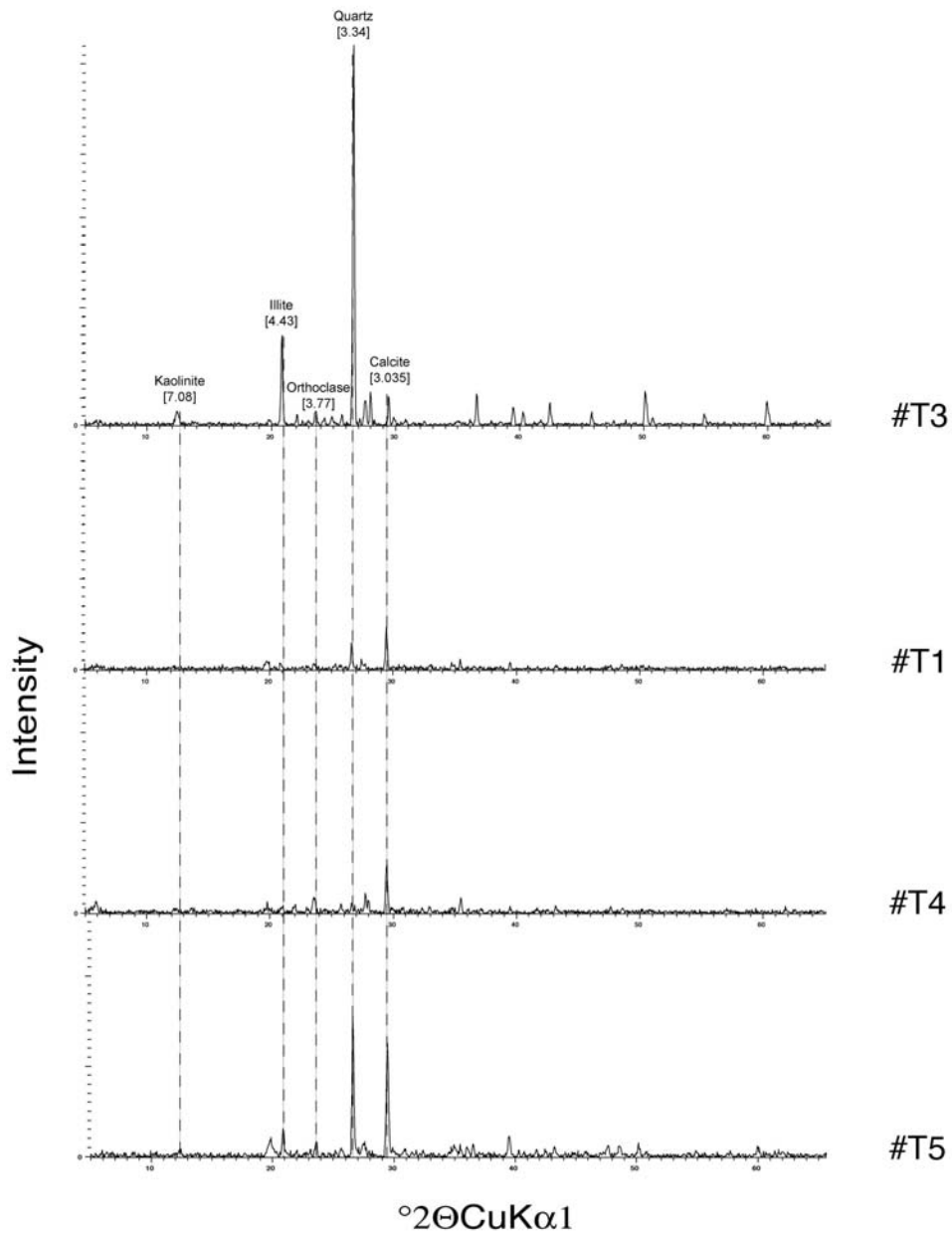


**Figure 2.13** - X-ray diffraction analyses from the all grain-size fractions for the T1 to T5 samples. Location samples are indicated on the Table 2.1. Sharp peaks are quartz, orthoclase, calcite, kaolinite and illite.

veins or breccia can be recognized within the grey gouge (3 mm as a mean; Figs. 2.15d, 2.15e & 2.15f). This suggests that cement healing events were relatively more important for the central grey gouge compare to the bounding blue gouge. This is consistent with the large proportion of opaque minerals observed.

#### 1.2.3.2. Outcrop B

The outcrop B is located 7 km northeastwards from the outcrop A (Fig. 2.3) and shows a similar fault zone architecture (Figs. 2.6 & 2.7): a 10 m wide damage zone which includes three gouge zones, with a continuous sharp and planar gouge slip zone (PSZ') located to the southeast, and two less sharp and less regular gouge slip zones (SSZ-1' and SSZ-2') located northwestwards. But an important difference with the outcrop A should be noted: the principal slip zone merges with the secondary slip zone northeastwards (Figs. 2.6a & 2.6c). And no incipient branching fault comparable to the A exposure could be observed along the B exposure (Fig. 2.7).

The PSZ' consists of a narrow planar vertical strip of clay gouge striking N58°E whose thickness ranges from 0.1 cm to 3.2 cm, with a mean value of 1.3 cm (averaged on 29 measurements). It is separated from the adjacent fine fault breccia or from a marginal foliated dark blue gouge by two striated vertical planes striking N60°E +/- 2°. The rake of the striation is less than 10° northeastwards. The PSZ' gouge is composed of incohesive grey clay showing a vertical foliation striking 40°.

The PSZ' gouge is flanked by a marginal poorly consolidated dark blue foliated clayey gouge and by moderately consolidated fine clay-rich fault breccia. The fine breccia likely results from cataclasis and circulation of hydrothermal fluids, as for A exposure. No evidence of any gouge interfingering could be observed along neither the principal slip zone (PSZ') nor the secondary slip zones (SSZs').

The zonation of the secondary displacement zones SSZ-1' and SSZ-2' is similar, with a narrow central incohesive grey clay gouge zone bounded by the fine breccia (Fig. 2.6b & 2.6c). Corresponding vertical striated planes strike N63°E +/- 15° and N70°E +/- 15° respectively. Their thicknesses ranges from 0.1 cm to 2.7 cm (0.7 cm in average for 34 measurements) for the SSZ-1' gouge and from 0.1 cm to 2.5 cm (a mean of 1.1 cm for 20 measurements) for the SSZ-2' gouge. The foliation of secondary slip zones is not apparent at the scale of the exposure.

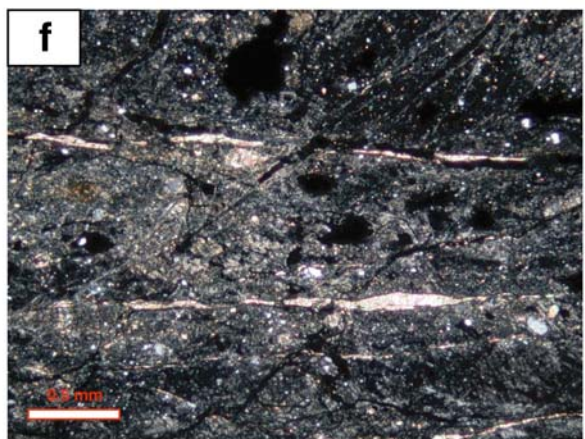
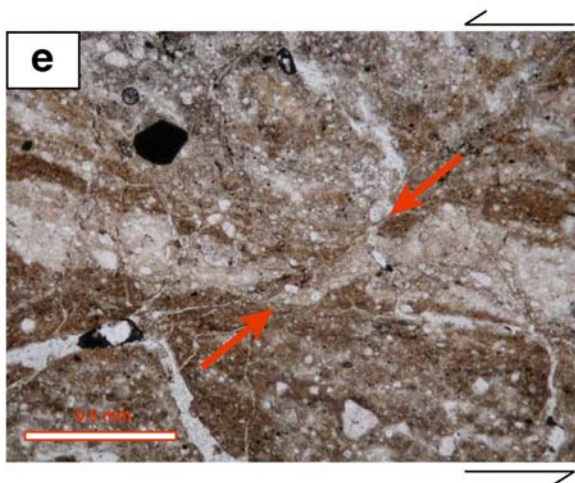
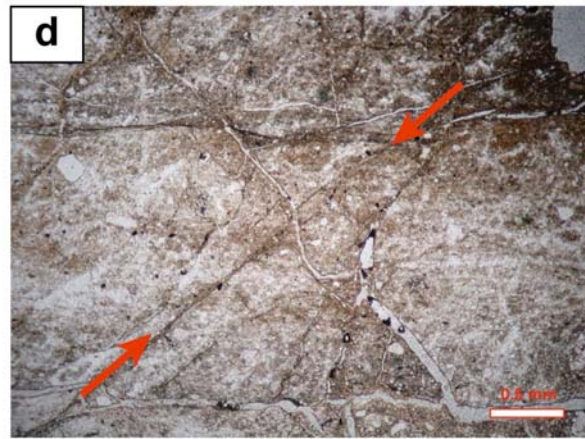
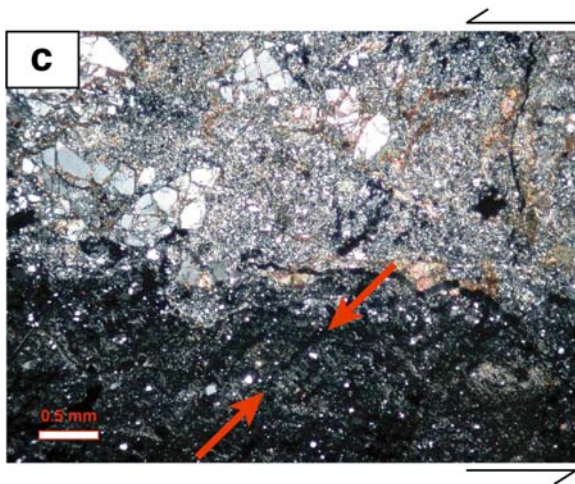
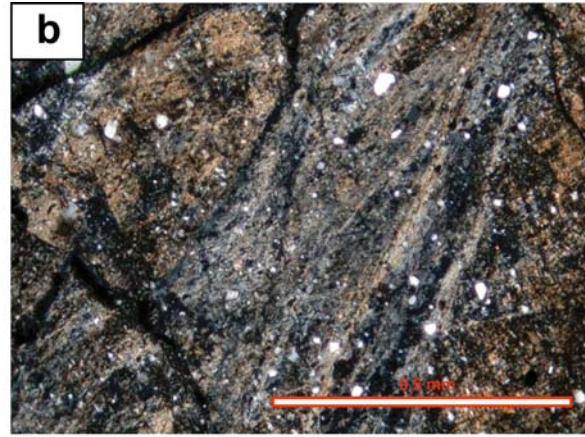
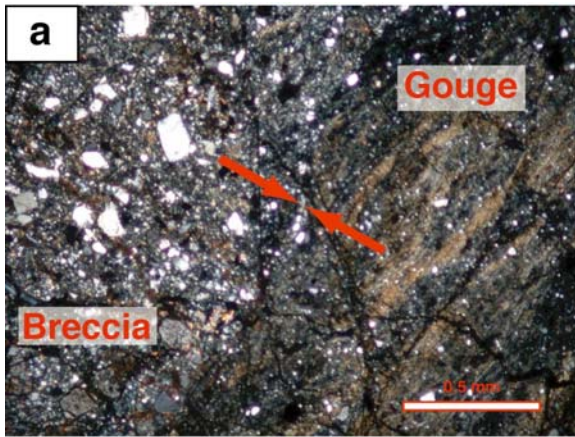


**Figure 2.14** - Microphotographs of the marginal blue gouge (PSZ). (a) Fairly regular boundary between the fine breccia and the fault gouge in polarized light. (b) Gouge cataclastic foliation that may represent clay compositional differences in polarized light. (c) Shear bands (arrow) in polarized light. (d) Shear plane (arrow). (e) Gouge foliation offset along a shear plane (arrow). (f) Discrete thin calcite veins in polarized light.

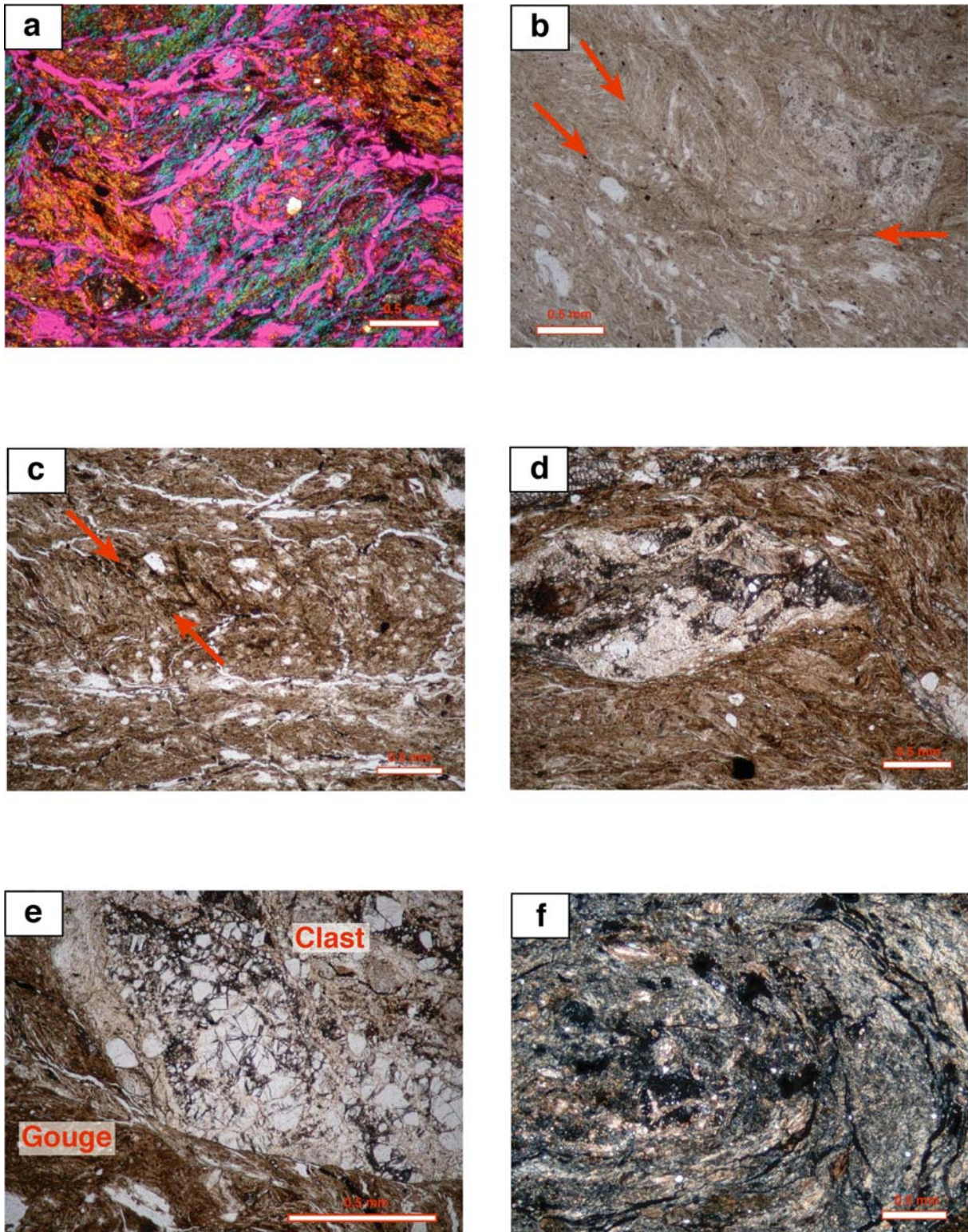


**Figure 2.15** - Microphotographs of the grey slip zone gouge (PSZ). (a) Gouge matrix exhibiting a wavy-shape appearance in polarized light with a added  $\lambda$  lamella. (b) A composite fabric that dissects the gouge texture. (c) Clast showing several shear planes (arrow). (d) Coarse survivor clast showing an elliptical shape. (e) Survivor clast boundary. (f) Re-worked calcite veins.

No microscopic observation could be carried out on gouge slip zones for the B exposure. The main reason is the very low thickness of slip zone gouge that did not allow to retrieve samples without strong damage to the gouge fabric.

## 2. Summary of fault zone architecture

Detailed mapping of the Usukidani fault along two exposures reveals two narrow mm-thick clay-rich gouge slip zones subparallel to a well-developed third one considered as the principal slip zone. The branching off of one of the SSZ' with the PSZ' at the exposure B supports the assumption of their complete lateral merging, along strike or along dip. Flanked by a fine breccia, the principal and secondary faults are included within a coarse breccia composed of intensely fractured and strongly altered welded tuff. The fault zone architecture appears to result from cataclasis and past circulation of hydrothermal fluids, as already reported from other strike-slip faults such as the Punchbowl fault in California (Chester & Logan, 1986), the Carboneras fault in southeastern Spain (Rutter et al., 1986) or the Median Tectonic Line (Wibberley & Shimamoto, 2003).

The principal gouge zones of the two exposures contain a sharp planar central slip zone bordered by irregular marginal gouges which likely stand for relict slip zones. In some places along the PDZ of the exposure A, strands of the marginal gouge locally penetrates the fine fault breccia and pinches out along fractures. This pattern suggests the propagation of ancient ruptures sideways off the line of the principal gouge slip zone. These two considerations suggest that the Usukidani fault is an active fault that has undergone several slip events followed by numerous consecutive fluid-flow episodes (Hickman et al., 1995 ; Scholz, 2002).

Hydraulic fault properties reflect the fault zone component distribution, which can vary greatly in thickness depending on shear strain localization (Caine et al., 1996) and increasing displacement (Micarelli et al., 2006). The size distribution of each component profoundly affects fluid flow regime of the upper crust: faults can act as barrier or conduit systems (Goddard and Evans, 1995; Scholz, 2002). This behaviour, which varies over time and space (Smith et al., 1990; Hickman et al., 1995; Caine et al., 1996; Evans et al., 1997) and seismic cycles (Sibson, 1992; Cox, 1995), influences greatly fluid pressure distribution across the overall fault zone. Thus, determining the general hydrological fault properties (especially

the seismogenic central slip zone gouge layer of the PSZ) is crucial to predict fault mechanical response during earthquake slip (Uehara & Shimamoto, 2004; Rice, 2006).

Investigations on the fault porosity and permeability will allow to constrain the hydrodynamic behaviour of secondary fault branches on excess fluid pressures generated during a coseismic slip event along the principal gouge slip zone.

## **B. Petrophysical analysis**

### **1. Fluid transport properties of Usukidani fault zone**

Cylindrical gouge samples were collected in three mutually perpendicular directions: parallel to both the gouge foliation and the striation ( $// //$ ), parallel to the gouge foliation and perpendicular to the striation ( $// \perp$ ), and perpendicular to both the gouge foliation and the striation ( $\perp \perp$ ). It is important to note that, given the narrowness of each gouge zone, sampling perpendicular to the foliation and the striations ( $\perp \perp$  orientations) was difficult and only a few such samples could be retrieved. Hence the most complete porosity and permeability dataset was obtained for vertical samples ( $// \perp$  orientations) which were the easiest samples to extract from the outcrop with minimum damage to the gouge microfabric. The dataset used in the modelling will therefore correspond to  $// \perp$  orientations.

The samples were obtained by hammering 20 mm-diameter stainless steel or copper tubes into the gouge zones. The 3 to 5 cm long samples were then immediately pushed out into a heat-retractable polyolefin jacket sealed using a hair-drier in order to minimize sample disturbance during transportation. In the laboratory, samples were oven dried at 60 to 80°C for one week to eliminate pore water, cut to the desired length (1 ~ 2 cm) before being further oven dried for a second week. Care was taken to ensure that the original pore structure of the clayey gouge or breccia samples was not significantly modified by sampling nor altered during laboratory preparation and oven drying.

## 1.1. Experimental procedure

### 1.1.1. Mercury porosity measurements

Mercury injection porosimetry is based on the fact that mercury, as a non-wetting fluid, will enter pore spaces when pressure, exceeding capillary pressure, is applied. (Gregg & Sing, 1982). The size of the mercury invaded pore is related to the applied pressure by the Washburn equation, such as:

$$P = \frac{2 \times \gamma \times \cos \theta}{r} \quad (2.1)$$

where  $P$  is the applied pressure,  $\theta$  is the contact angle,  $\gamma$  is the surface tension of the mercury (0.48 N/m) and  $r$  the pore radius. This equation 2.1 can be simplified to:

$$R = \frac{750}{P} \quad (2.2)$$

where  $P$  is the pressure (MPa) and  $R$  pore radius (nm). Equation 2.2 can be applied to cylindrical pores. But in the case where pores are fissure-like, the equation is:

$$P = \frac{2 \times \gamma \times \cos \theta}{D} \quad (2.3)$$

where  $D$  is the distance between both walls of the fissure. The mercury volume intruded into the sample by successive pressure increments allows to determine the *free porosity* ( $N_{Hg}$ ). Mercury ejection curves after reduction of the pressure allows to determine the *trapped porosity* ( $N_p$ ), as mercury withdraws from the smaller to the larger pore spaces. The pore distribution will be referred to pore sizes (i.e. pore diameter) rather than pore radii, because of the undefined pore geometry.

The effective porosity allows to define the porosity distribution as a function of pore diameters by mercury injection up to about 200 MPa for 0.006  $\mu\text{m}$  (De Las Cuevas, 1997). Measurements were performed on the "Autopore IV 9500" device at the University of Franche-Comté (Dehandschutter et al., 2005). Pore size distribution was divided as follows:

micro-porosity ( $\emptyset < 0.1 \mu\text{m}$ ), meso-porosity ( $0.1 \mu\text{m} < \emptyset < 7.5 \mu\text{m}$ ) and macro-porosity ( $\emptyset > 7.5 \mu\text{m}$ ).

### 1.1.2. Nitrogen porosity measurements

The porosities of gouge and breccia samples were measured with the simple pore-pressure decay method (Noda, 2005) with a fixed volume of pore-fluid reservoir, using the intra-vessel deformation fluid-flow apparatus, an oil medium triaxial machine at Kyoto University (Fig. 2.16). This method assumes that mineral grains are rigid and that their compressibility is negligible compared to that of the pores. Nitrogen was used as the pore fluid, and oil used as the confining pressure medium. The nitrogen pressure upstream of the sample did not exceed 1 MPa.

Sample grain volume is first measured using a mini-pressure vessel as follows (white color writing on Figure 2.16). The sample with a grain volume  $V_g$  is placed inside the mini pressure vessel. The volume of this mini pressure vessel added to its connected line (up to the separated valve) is known ( $V_2$ ). A complete line section, that is connected to the separated valve, is defined such as  $V_1$ , with  $V_1$  already known. At the initial state,  $V_2$  is at the atmospheric pressure (0.1 MPa) and  $V_1$  at about 1 MPa. When the separated valve is open, fluid pressure equilibrates at  $P_f$  such as:

$$P_2 \times (V_2 - V_g) + P_1 \times V_1 = P_f \times (V_1 + V_2 - V_g) \quad (2.4)$$

$$\Leftrightarrow V_g = V_2 - \frac{P_1 - P_f}{P_f - P_2} \times V_1 \quad (2.5)$$

Sample pore volume is then measured using a the intra-vessel apparatus as follows (green color writing on Figure 2.16). The sample with a pore volume  $V_p$  is placed inside the intra-vessel apparatus. The volume of the line that is directly connected to the sample (up to the separated valve) is known ( $V'_2$ ). The complete line section, that is connected to the separated valve, is defined such as  $V_1$  with  $V_1$  already known. At the initial state,  $V'_2$  is at the atmospheric pressure (0.1 MPa) and  $V_1$  at about 1 MPa. When the separated valve is open, fluid pressure equilibrates at  $P_f$  such as:

$$P_2 \times (V'_2 + V_p) + P_1 \times V_1 = P_f \times (V_1 + V'_2 + V_p) \quad (2.6)$$

$$\Leftrightarrow V_p = \frac{P_1 - P_f}{P_f - P_2} \times V_1 - V'_2 \quad (2.7)$$

$V_p$  were measured at several confining pressures following first an increasing pressure path (from 10 MPa to 100 MPa by 10 or 20 MPa steps) and then a decreasing path (from 100 MPa to 10 MPa with similar pressure steps). The increasing effective confining pressure paths are assumed to simulate increasing depths and hence increasing lithostatic load from 0.4 km (10 MPa) to 4 km (100 MPa), whereas the decreasing paths are considered to reflect a progressive increase of pore fluid pressure for a given depth.

The sample porosity (%) is then calculated for each confining/deconfining step by the following definition:

$$n = \frac{V_p}{V_p + V_g} \quad (2.8)$$

### 1.1.3. Nitrogen permeability measurements

Permeabilities were measured by steady-flow method, with the same intra-vessel deformation fluid-flow apparatus as for the porosity measurements (Fig. 2.17). A constant differential pore pressure was applied to the top of the specimen with air-drained conditions at the downstream end. The flow rate was monitored by a flowmeter capable of detecting flow rates between 0.05 and 5000 ml/min (corresponding roughly to permeabilities ranging from  $10^{-13}$  to  $10^{-20}$  m<sup>2</sup>). Darcy law is modified to take into account the lower N<sub>2</sub> gas viscosity and higher compressibility compare to water, such as:

$$q = \frac{K \times A \times (P_p^{up} - P_p^{down})}{\mu \times L} \quad (2.9)$$

where  $q$  is the bulk gas flow volume per time (l/min),  $K$  is the permeability (m<sup>2</sup>) of the gas,  $A$  is the area of the cross section of the sample (m<sup>2</sup>),  $\mu$  is the viscosity of the gas (Pas), and  $L$  is

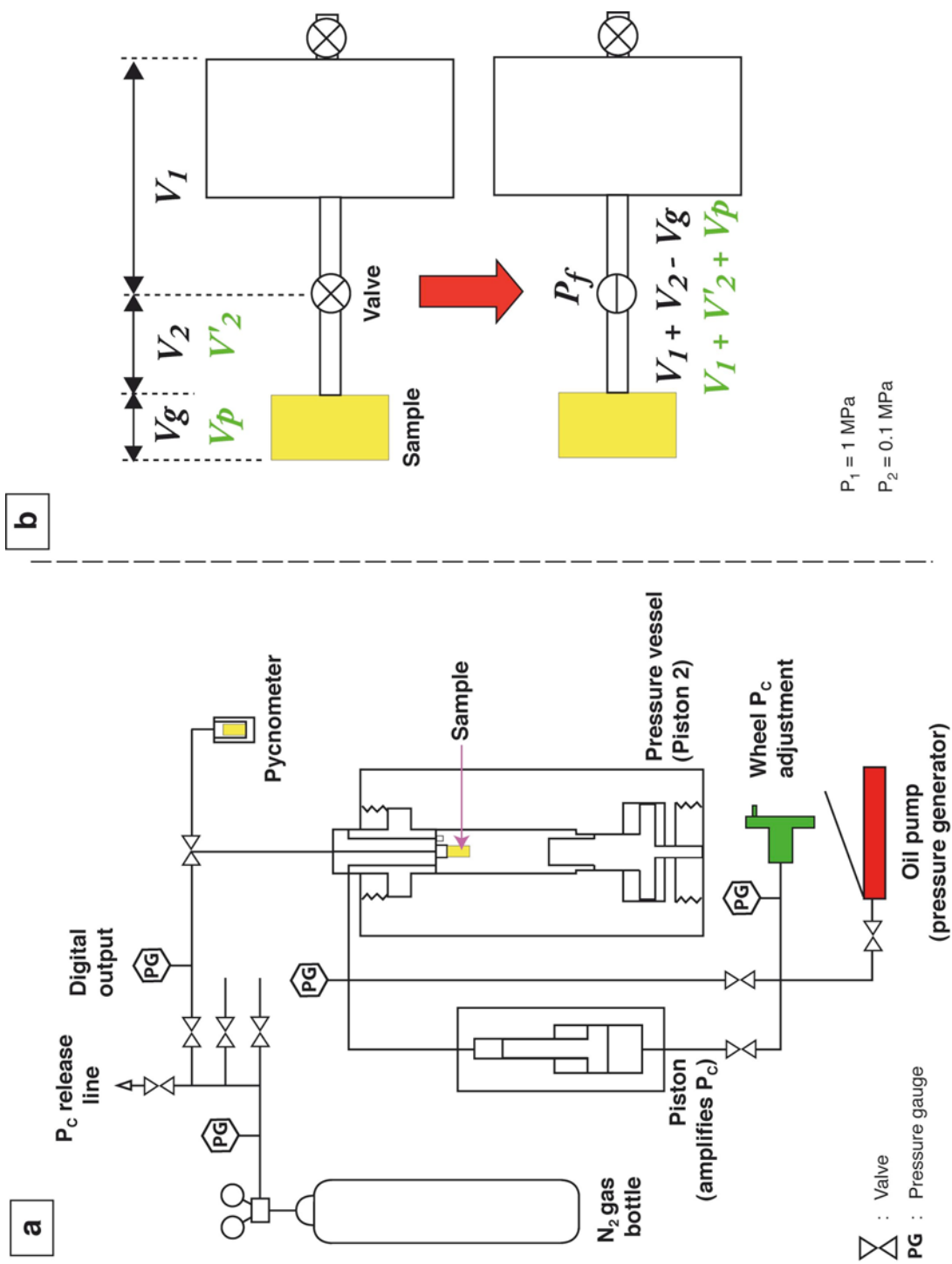


**Figure 2.16** - (a) Diagram of the pressure vessel system used for porosity measurements. (b) Standard procedure is based on the simple pore-pressure decay method combined with pycnometry method (modified after Aisawa, 2005).

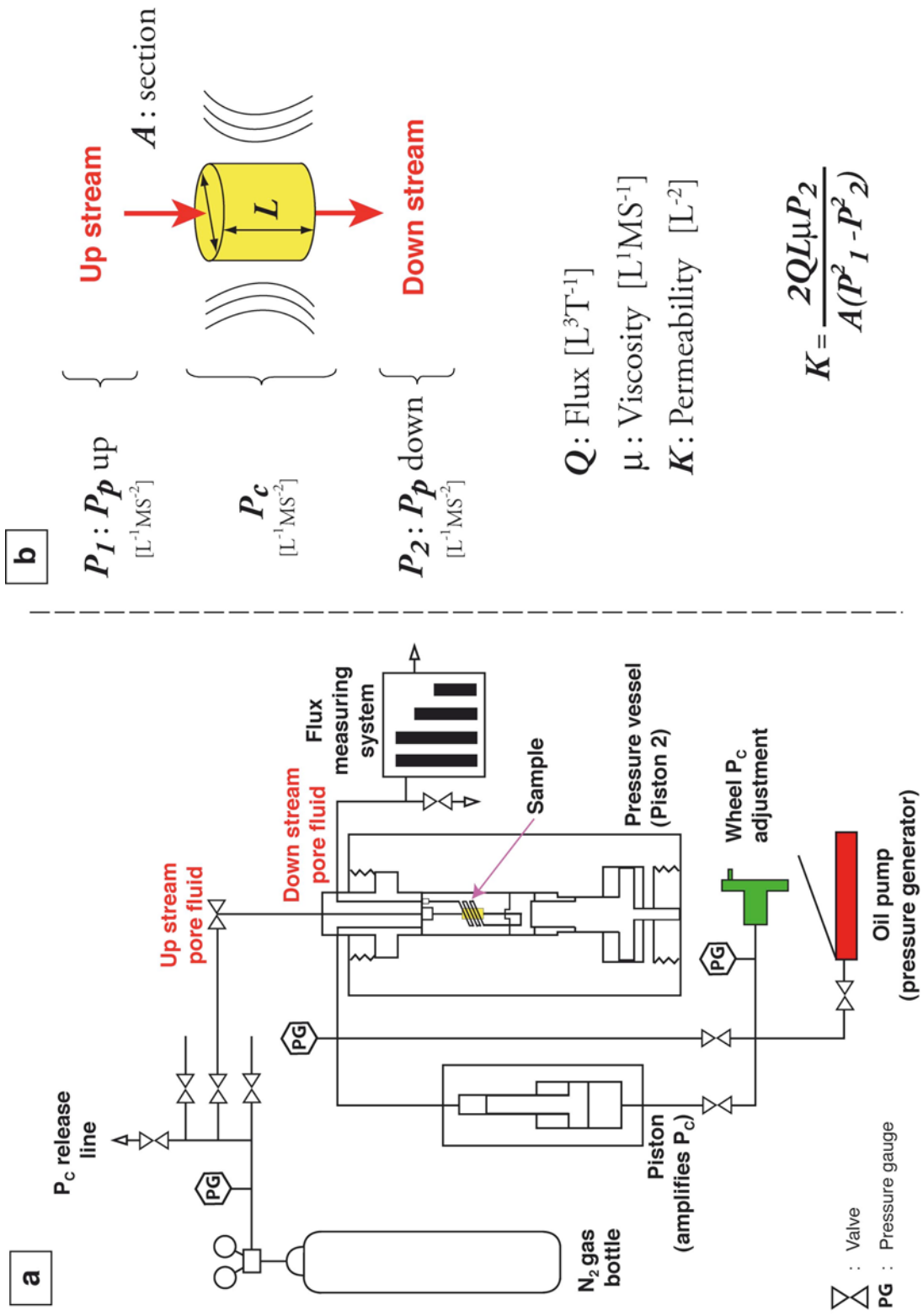


**Figure 2.17** - (a) Diagram of the intravessel deformation fluid-flow gas apparatus used for permeability measurements. (b) Standard procedure is based on the steady-flow method (modified after Aisawa, 2005).

the sample length (m),  $P_p^{up}$  and  $P_p^{down}$  are the upstream and downstream pore pressure, respectively.

As for the porosity measurements, permeabilities were first measured following an increase in effective confining pressure (from 5 MPa to 100 MPa, with 5, 10 or 20 MPa pressure steps) and then following a decrease in effective confining pressure (from 100 MPa to 10 MPa). The maximum effective confining pressure obtained (100 MPa) corresponds to lithostatic load conditions expected at about 6 km depth with a hydrostatic fluid pressure.

## 1.2. Results

### 1.2.1 Mercury porosity measurements

#### 1.2.1.1. Outcrop A

The grey gouge slip zone (H<sub>1</sub> sample) displays a free porosity of 4.28 % (27.90 % of the total porosity) and a trapped porosity of 11.05 % (72.08 % of the total porosity) for a total porosity of 15.33 % (Table 2.3; Fig. 2.18a). This gouge displays a macroporosity corresponding to 25.64 % of the free porosity, a mesoporosity corresponding to 24.7 % and a microporosity corresponding to 50 %. The microporosity domain appears to dominate (Fig. 2.18b).

The blue marginal gouge (H<sub>2</sub> sample) shows a free porosity of 3.89 % (29.84 % of the total porosity) and a trapped porosity of 9.15 % (70.16 % of the total porosity) for a total porosity of 13.05 % (Table 2.3; Fig. 2.18a). This gouge displays a macro-porosity corresponding to 35.4 % of the free porosity, a meso-porosity corresponding to 4.44 % and a micro-porosity corresponding to 60.16 %. The microporosity domain appears to dominate (Fig. 2.18b)

#### 1.2.1.2. Outcrop B

The PSZ' grey gouge (H<sub>3</sub> sample) has a free porosity of 7 % (47.69 % of the total porosity) and a trapped porosity of 7.68 % (52.3 % of the total porosity) for a total porosity of 14.68 % (Table 2.3; Fig. 2.19a). This gouge is characterized a macroporosity corresponding to

Sample	Type of gouge	Cumulative total volume (mL/g)	Total porosity (%)	Cumulative extrusion volume (mL/g)	Trapped porosity (%)	Free porosity (%)	$N_p/N_{Hg}$	Microporosity representativity (%)	Mesoporosity representativity (%)	Macroporosity representativity (%)
#H1	PSZ grey gouge	0.075	15.33	0.0537	72.08	27.92	2.58	49.66	24.70	25.64
#H2	PSZ marginal blue gouge	0.063	13.05	0.0442	70.16	29.84	2.35	60.16	4.44	35.40
#H3	PSZ' grey gouge	0.067	14.68	0.0351	52.30	47.69	1.10	15.35	77.50	7.15
#H4	Junction PSZ'/SSZ-1'	0.070	15.04	0.0427	61.17	38.83	1.58	36.10	45.56	18.34

**Table 2.3** - Summary of porosity measurements by mercury injection on samples from the principal slip zone.  $N_p$  means trapped porosity, and  $N_{Hg}$  means free porosity. %\* means percentage of the total porosity.

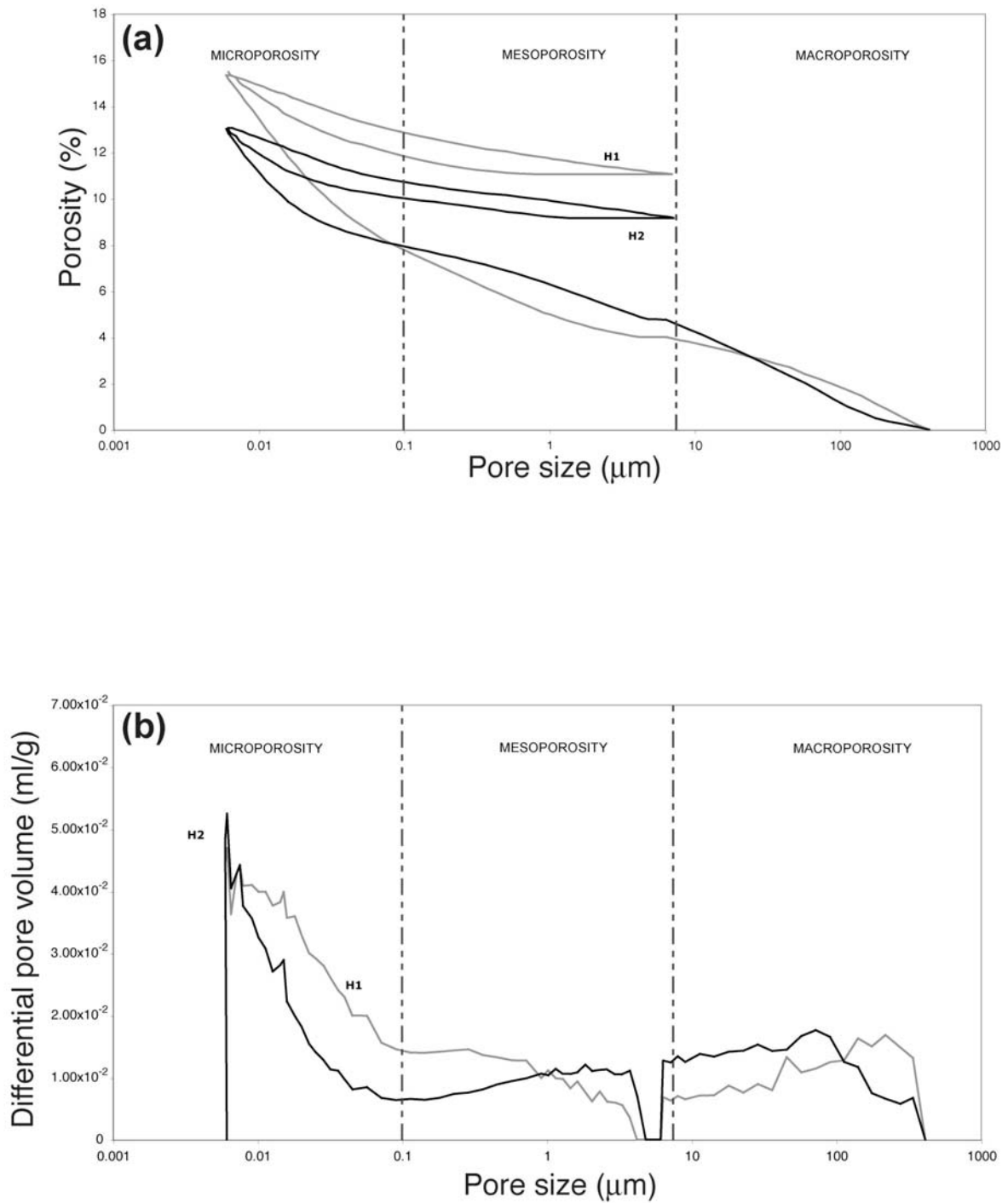


**Figure 2.18** - Pore characterization of the slip zone grey gouge (H1) and the marginal blue gouge (H2) of the principal slip zone, by mercury injection method. (a) Mercury injection curve. (b) Main profile pore size distribution curves. Samples are references on Table 2.3.

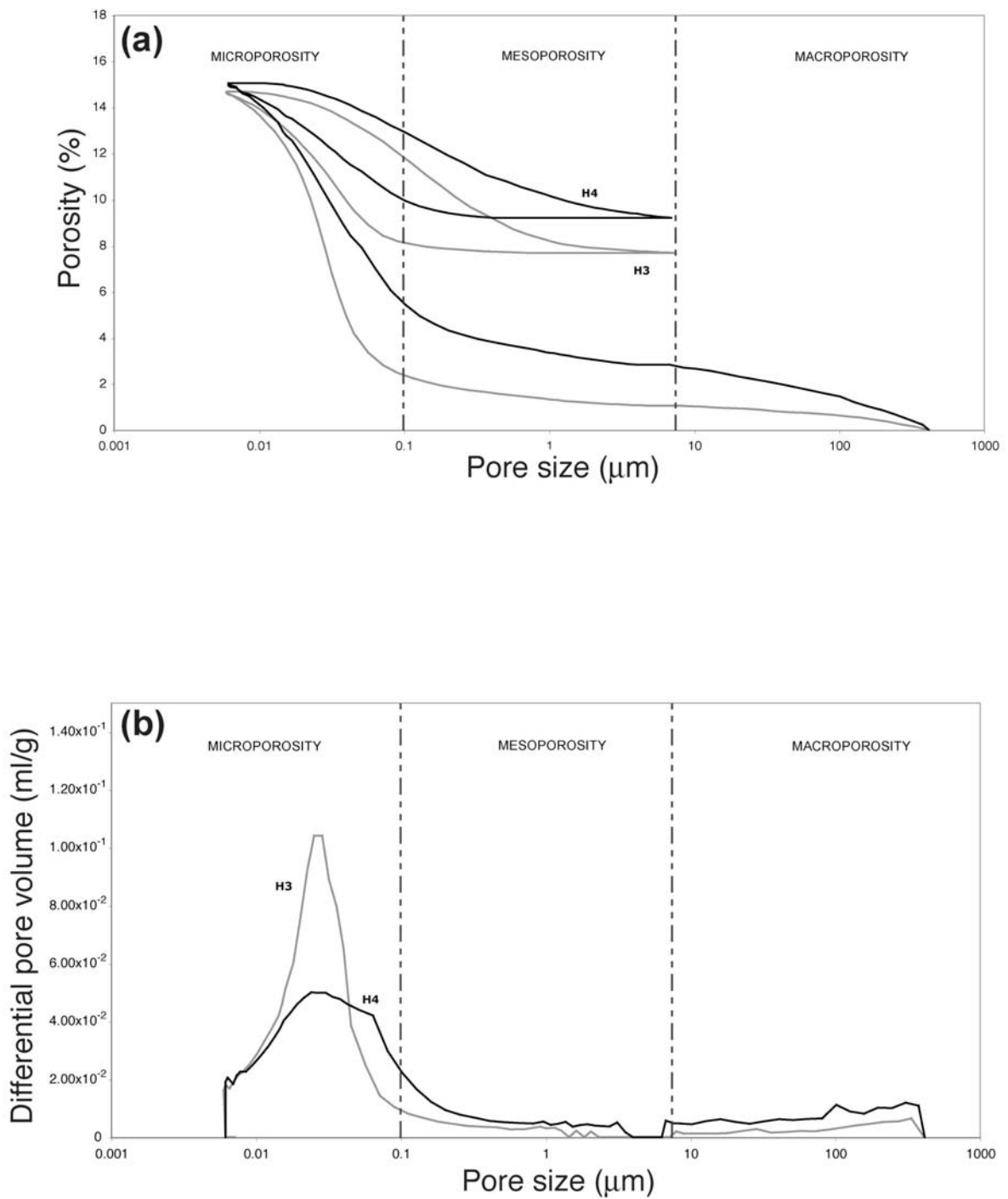


**Figure 2.19** - Pore characterization of the slip zone grey gouge of the PSZ' (H3) and gouge at the junction of PSZ' and SSZ-1' (H4), by mercury injection method. (a) Mercury injection curve. (b) Main profile pore size distribution curves. Samples are references on Table 2.3.

7.15 % of the free porosity, a mesoporosity corresponding to 77.5 % and a microporosity corresponding to 15.35 %. The pore sizes lower than 1  $\mu\text{m}$  appear to dominate (Fig. 2.19b).

The gouge at the junction between PSZ' and SSZ-1' (H<sub>4</sub> sample) shows a free porosity of 5.84 % (38.83 % of the total porosity) and a trapped porosity of 9.2 % (61.17 % of the total porosity) for a total porosity of 15.04 % (Table 2.3; Fig. 2.19a). This gouge has a macro-porosity corresponding to 18.34 % of the free porosity, a meso-porosity corresponding to 45.56 % and a micro-porosity corresponding to 36.1 %. The pore sizes lower than 1  $\mu\text{m}$  appear to dominate (Fig. 2.19b).

## 1.2.2. Nitrogen porosity measurements

### 1.2.2.1. Outcrop A

During increasing pressure paths, porosity values of central and marginal clayey gouges decrease from 25 - 40 % at  $P_e = 10$  MPa to 23 - 34 % at  $P_e = 100$  MPa (Table 2.4 and Fig. 2.20a). During subsequent decreasing pressure paths, the porosity values tend to recover initial values. The porosities of the marginal fault breccia evolve from 10 - 18 % at  $P_e = 10$  MPa to 8 - 9 % at  $P_e = 100$  MPa (Fig. 2.20b). As already noted by David et al. (1994), porosity variations as a function of  $P_e$  generally follow an exponential law of the form:

$$n = n_0 \times \exp[-\alpha \times (P_e - P_0)] \quad (2.10)$$

where  $n_0$  is the porosity at a reference pressure  $P_0$  here fixed at zero. More precisely, for the decreasing confining pressure paths (decreasing effective pressure), the equations in Figure 2.20, derived from best-fit trends, will be used in the modelling to calculate porosity values from given  $P_e$  values.

### 1.2.2.2. Outcrop B

During increasing pressure paths, porosity values of the gouge juncture of PSZ' and SSZ-1' decrease from 17 - 25 % at  $P_e = 10$  MPa down to 20 % at  $P_e = 100$  MPa (Table 2.4

Fault-rock zone	Fault-rock type	Sample number	Sample orientation	Porosity		Reference porosity $n_0$ at $P_e=0$		Porosity-pressure sensitivity coeff. $\alpha$ ( $\text{MPa}^{-1}$ )		Reference compressibility $\beta_0$ ( $\text{Pa}^{-1}$ ) at $P_e=0$		Bulk compressibility-pressure sensitivity coeff. $\chi$ ( $\text{MPa}^{-1}$ )	
				$P_e$ (20 MPa)	$P_e$ (100 MPa)	$n_0$ at $P_e=0$	Deconfining path	sensitivity coeff. $\alpha$ ( $\text{MPa}^{-1}$ )	Deconfining path	$\beta_0$ ( $\text{Pa}^{-1}$ ) at $P_e=0$	Deconfining path	Bulk compressibility-pressure sensitivity coeff. $\chi$ ( $\text{MPa}^{-1}$ )	Deconfining path
PSZ	Central gouge	4	// $\perp$	0.389	0.337	0.375		0.0011		$7 \times 10^{-10}$		$2 \times 10^{-8}$	
"	"	16	$\perp$ $\perp$	0.386	0.237	0.351		0.0041		$1 \times 10^{-8}$		$4 \times 10^{-8}$	
"	Fine fault breccia	24	// $\perp$	0.141	0.089	0.108		0.0022		$7 \times 10^{-10}$		$5 \times 10^{-8}$	
"	"	25	// $\perp$	0.135	0.081	0.120		0.0042		$8 \times 10^{-10}$		$4 \times 10^{-8}$	
"	"	29	// $\perp$	0.146	0.086	0.104		0.0020		$4 \times 10^{-10}$		$4 \times 10^{-8}$	
SSZ-1	Central gouge	31	// $\perp$	0.382	0.319	0.357		0.0012		$6 \times 10^{-10}$		$2 \times 10^{-8}$	
"	"	32	// $\perp$	0.303	0.227	0.270		0.0019		$9 \times 10^{-10}$		$3 \times 10^{-8}$	
Juncture PSZ / SSZ-1'	Undefined gouge	36	// //	0.255	0.200	-		0.0015		$7 \times 10^{-10}$		$3 \times 10^{-8}$	
"	"	37	// //	0.153	-	-		-		-		-	
SSZ-2'	Grey gouge	41	// $\perp$	0.233	0.200	-		0.0009		$3 \times 10^{-10}$		$3 \times 10^{-8}$	

**Table 2.4** - Summary of nitrogen porosity measurements and of estimates of  $n_0$ ,  $\alpha$ ,  $\beta_0$  and  $\chi$  coefficients (for deconfining paths). PSZ is for principal slip zone and SSZ for secondary slip zone (after Boutareaud et al., in press).

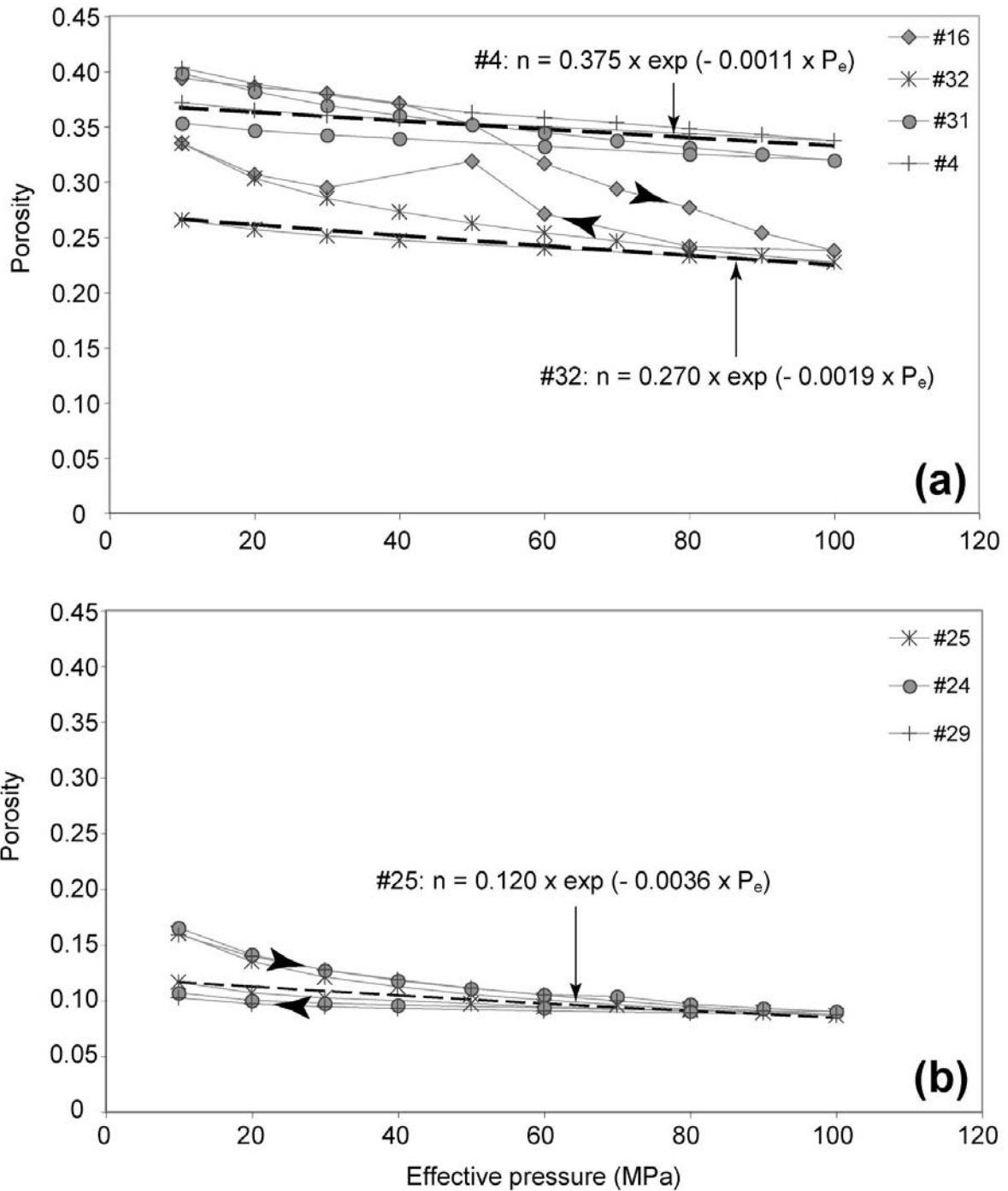


**Figure 2.20** - Evolution of nitrogen porosity with increasing/decreasing effective confining pressures for gouges (a) and fault breccias (b) from the principal and secondary slip zones of the exposure A. All samples except 16 are located on Figs. 2.4b & 2.4c, and are vertical, that is parallel to the gouge foliation and perpendicular to the striation ( $// \perp$  orientations). Sample 16 is perpendicular to the gouge foliation. Also given are the equations of the best-fit curves (dashed lines) for decreasing effective pressure paths for samples 4, 32 and 25. In the equations,  $P_e$  is expressed in MPa. Errors on porosity values are overestimated by 10 % (after Boutareaud et al., in press).

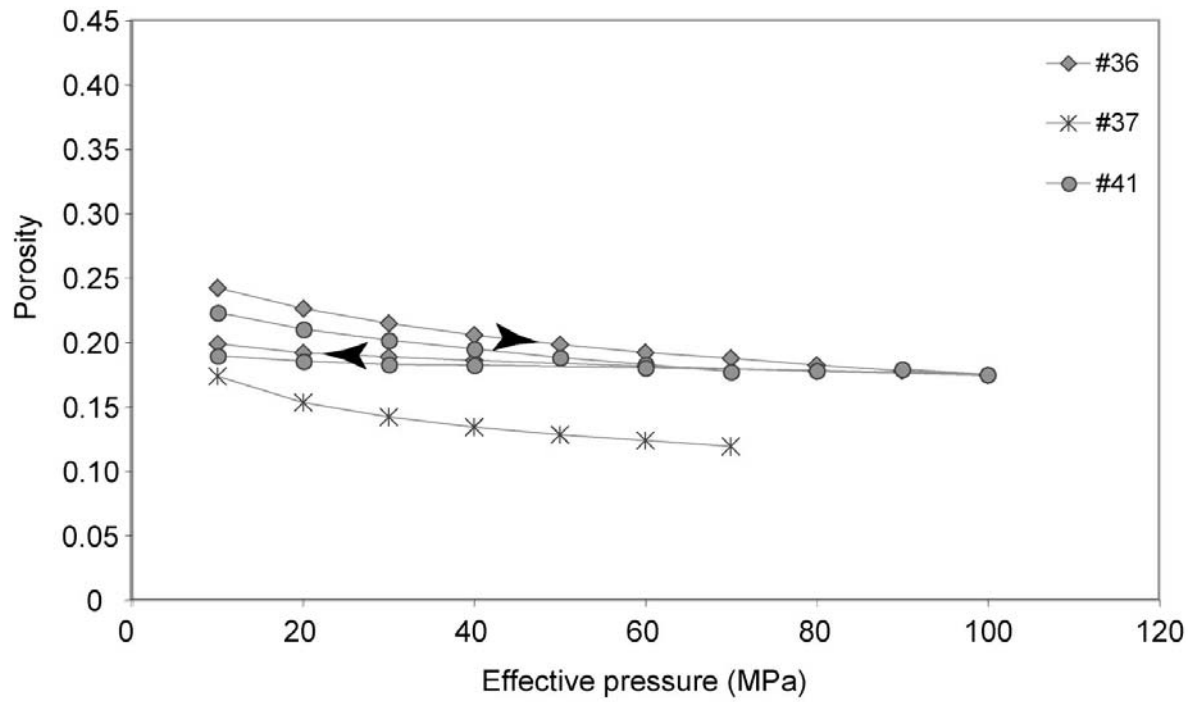


**Figure 2.21** - Evolution of nitrogen porosity with increasing/decreasing effective confining pressures for gouges from the juncture of the principal and secondary slip zones of the exposure B. All samples are located on Fig. 2.6c and 2.6b, and are // //. Sample 41 is //  $\perp$ . Errors on porosity values are overestimated by 10 % .

and Fig. 2.21). During subsequent decreasing pressure paths, the porosity values tend to recover initial values. Following decreasing/increasing paths of sample 37 could not be achieved because sample jacket ruptured at 70 MPa, allowing oil medium to invade the gouge sample. The porosities of the fine fault breccia evolve from 23 % at  $P_e = 10$  MPa to 20 % at  $P_e = 100$  MPa (Fig. 2.21).

### 1.2.3. Nitrogen permeability measurements

#### 1.2.3.1. Outcrop A

During increasing pressure paths (confining paths), permeability values of central and marginal clayey gouges decrease from  $5.5 \times 10^{-17}$  -  $1.06 \times 10^{-14}$  at  $P_e = 20$  MPa down to  $2.95 \times 10^{-19}$  -  $4.16 \times 10^{-16}$  at  $P_e = 100$  MPa (Table 2.5). During subsequent decreasing pressure paths (deconfining paths), the permeability values increase but without returning to their initial values, reflecting the effect of permanent compaction. Indeed, these values at  $P_e = 20$  MPa are one to two orders of magnitude lower than the starting values (Fig. 2.22). With respect to sample orientation, the permeability values show the following hierarchy:  $k_{\perp\perp} < k_{//}$  <  $k_{//\perp}$ , a hierarchy which is particularly clear at  $P_e = 100$  MPa (Fig. 2.22).

In a similar way, during confining paths, the permeability values of the marginal fine clayey fault breccia decrease from  $8.5 \times 10^{-16}$  -  $1.6 \times 10^{-15}$  at  $P_e = 20$  MPa down to  $7.22 \times 10^{-18}$  -  $4.16 \times 10^{-16}$  at  $P_e = 100$  MPa (Table 2.5). During subsequent deconfining paths, the permeability values increase but without returning to their initial values. Their values at  $P_e = 20$  MPa are about two orders of magnitude lower than the starting values (Fig. 2.22e). Given the fact that all samples from the marginal breccia were cored with the same orientation ( $//\perp$  profile orientation), the dependency of permeability with orientation cannot be considered here.

As initially noted by David et al. (1994), the permeability values follow equations of the form:

$$k = K_0 \times \exp[-\gamma \times (P_e - P_0)] \quad (2.11)$$

where  $K_0$  is the permeability at a reference pressure  $P_0$  here fixed at zero. More precisely, for the decreasing confining pressure paths (decreasing effective pressure), the equations in Figure 2.22, derived from best-fit trends, will be used in the modelling to calculate permeability values (in  $\text{m}^2$ ) from  $P_e$  values.

### 1.2.3.2. Outcrop B

During increasing pressure paths (confining paths), permeability values of gouges (i.e. all samples but 43) decrease from  $2.35 \times 10^{-16} - 6.23 \times 10^{-15}$  at  $P_e = 20$  MPa down to  $2.39 \times 10^{-18} - 9.12 \times 10^{-17}$  at  $P_e = 100$  MPa (Table 2.5). During subsequent decreasing pressure paths (deconfining paths), the permeability values increase but without returning to their initial values, reflecting the effect of permanent compaction. Indeed, these values at  $P_e = 20$  MPa are one to two orders of magnitude lower than the starting values (Fig. 2.23). With respect to sample orientation, the permeability values show the following hierarchy:  $k_{\perp\perp} < k_{\parallel\parallel} < k_{\parallel\perp}$ , a hierarchy which is particularly clear at  $P_e = 100$  MPa (Fig. 2.23).

In a similar way, during confining paths, the permeability values of the fine fault breccia (sample 43) decreases from  $1.77 \times 10^{-16}$  at  $P_e = 20$  MPa down to  $4.70 \times 10^{-18}$  at  $P_e = 100$  MPa (Table 2.5). During subsequent deconfining paths, the permeability values increase but without returning to their initial values. Their values at  $P_e = 20$  MPa are about two orders of magnitude lower than the starting values (Fig. 2.23).

## 2. Discussion

Most kilometre-scale mature (long-lived) exhumed faults typically consist of a *core zone* along which the latest displacements occurred, bordered on one or both sides by a fractured *damage zone* passing progressively or abruptly to the non-deformed or weakly deformed *host rock* or *protolith* (Chester & Logan, 1986; Caine et al., 1996; references hereafter). The core zone, whose thickness seldom exceeds 1 m, is commonly composed of highly comminuted material with variable amounts of clay minerals. In the damage zone, the protolith is commonly strongly fractured and altered following extensive fluid-rock interactions. This zonation has also been reported from kilometre-scale active faults. More precisely, several kilometre-scale active faults are characterized by a narrow and continuous

Fault-rock zone	Fault-rock type	Sample number	Sample orientation	Permeability (m <sup>2</sup> )		Permeability-pressure sensitivity coeff. $\gamma$ (MPa <sup>-1</sup> )	
				P <sub>e</sub> (20 MPa)	P <sub>e</sub> (100 MPa)	Confining path	Deconfining path
PSZ	Central gouge	1	// ⊥	3.92 x 10 <sup>-15</sup>	1.24 x 10 <sup>-16</sup>	0.0547	0.0081
"	" "	2	// ⊥	2.14 x 10 <sup>-15</sup>	7.00 x 10 <sup>-18</sup>	0.0738	0.0203
"	" "	3	// ⊥	1.54 x 10 <sup>-15</sup>	5.77 x 10 <sup>-18</sup>	0.0731	0.0162
"	" "	4	// ⊥	1.58 x 10 <sup>-15</sup>	4.74 x 10 <sup>-18</sup>	0.0725	0.0213
"	" "	5	// ⊥	8.39 x 10 <sup>-16</sup>	9.04 x 10 <sup>-19</sup>	0.0843	0.0342
"	" "	6	// //	1.55 x 10 <sup>-15</sup>	2.80 x 10 <sup>-17</sup>	0.0538	0.014
"	" "	7	// //	2.84 x 10 <sup>-16</sup>	1.75 x 10 <sup>-18</sup>	0.0606	0.0222
"	" "	8	// //	6.30 x 10 <sup>-16</sup>	8.49 x 10 <sup>-18</sup>	0.0587	0.014
"	" "	9	// //	2.05 x 10 <sup>-16</sup>	1.83 x 10 <sup>-19</sup>	0.0907	0.0248
"	" "	10	⊥⊥	4.68 x 10 <sup>-16</sup>	3.78 x 10 <sup>-18</sup>	0.068	0.0164
"	" "	11	⊥⊥	3.50 x 10 <sup>-16</sup>	3.18 x 10 <sup>-18</sup>	0.0673	0.0147
"	" "	12	⊥⊥	3.45 x 10 <sup>-16</sup>	2.87 x 10 <sup>-18</sup>	0.0652	0.0151
"	" "	13	⊥⊥	5.66 x 10 <sup>-16</sup>	2.30 x 10 <sup>-18</sup>	0.0733	0.0242
"	" "	14	⊥⊥	7.43 x 10 <sup>-16</sup>	1.99 x 10 <sup>-18</sup>	0.0786	0.0177
"	" "	15	⊥⊥	2.00 x 10 <sup>-16</sup>	1.20 x 10 <sup>-18</sup>	0.0718	0.0211
"	" "	16	⊥⊥	5.50 x 10 <sup>-17</sup>	7.42 x 10 <sup>-19</sup>	0.0503	0.0173
"	Marginal gouge	17	// ⊥	1.06 x 10 <sup>-14</sup>	2.91 x 10 <sup>-17</sup>	0.0779	0.0177
"	" "	18	// ⊥	4.21 x 10 <sup>-15</sup>	1.01 x 10 <sup>-17</sup>	0.0813	0.0207
"	" "	19	// ⊥	5.67 x 10 <sup>-16</sup>	6.64 x 10 <sup>-19</sup>	0.0257	0.0874
"	" "	20	// //	3.13 x 10 <sup>-15</sup>	5.97 x 10 <sup>-18</sup>	0.0862	0.0277
"	" "	21	// //	2.09 x 10 <sup>-15</sup>	1.50 x 10 <sup>-18</sup>	0.0898	0.0217
"	" "	22	// //	4.48 x 10 <sup>-16</sup>	2.95 x 10 <sup>-19</sup>	0.0978	0.0239

**Table 2.5** - Summary of nitrogen permeability measurements and of estimates of  $K_0$  and  $\gamma$  coefficients (after Boutareaud et al., in press).

Fault-rock zone	Fault-rock type	Sample number	Sample orientation	Permeability (m <sup>2</sup> )		Permeability-pressure sensitivity coeff. $\Upsilon$ (MPa <sup>-1</sup> )	
				P <sub>e</sub> (20 MPa)	P <sub>e</sub> (100 MPa)	Confining path	Deconfining path
PSZ	Fine fault breccia	23	// ⊥	5.28 x 10 <sup>-16</sup>	1.14 x 10 <sup>-17</sup>	0.0587	0.016
"	" "	24	// ⊥	2.11 x 10 <sup>-16</sup>	7.22 x 10 <sup>-18</sup>	0.0514	0.0096
"	" "	25	// ⊥	3.03 x 10 <sup>-16</sup>	1.01 x 10 <sup>-17</sup>	0.0535	0.0129
"	" "	26	// ⊥	6.60 x 10 <sup>-15</sup>	4.16 x 10 <sup>-16</sup>	0.0414	0.0078
"	" "	27	// ⊥	8.50 x 10 <sup>-16</sup>	3.07 x 10 <sup>-17</sup>	0.0474	0.0088
"	" "	28	// ⊥	3.29 x 10 <sup>-16</sup>	5.36 x 10 <sup>-18</sup>	0.0585	0.0144
"	" "	29	// ⊥	4.34 x 10 <sup>-16</sup>	1.38 x 10 <sup>-17</sup>	0.0524	0.0137
"	" "	30	// ⊥	1.60 x 10 <sup>-15</sup>	4.64 x 10 <sup>-17</sup>	0.0534	0.0112
SSZ-1	Central gouge	31	// ⊥	4.69 x 10 <sup>-16</sup>	1.04 x 10 <sup>-18</sup>	0.0797	0.014
"	" "	32	// ⊥	8.62 x 10 <sup>-16</sup>	2.65 x 10 <sup>-18</sup>	0.0855	0.014
"	Marginal gouge	33	// ⊥	3.96 x 10 <sup>-16</sup>	3.06 x 10 <sup>-18</sup>	0.0736	0.0149
"	" "	34	// ⊥	7.70 x 10 <sup>-16</sup>	1.15 x 10 <sup>-17</sup>	0.0626	0.0155
PSZ'	Dark blue gouge	35	// ⊥	4.54 x 10 <sup>-15</sup>	8.45 x 10 <sup>-17</sup>	0.0548	0.0146
Juncture PSZ' / SSZ-1'	Undefined gouge	36	// //	1.86 x 10 <sup>-15</sup>	8.56 x 10 <sup>-18</sup>	0.0763	0.0210
"	"	37	// //	3.53 x 10 <sup>-15</sup>	6.18 x 10 <sup>-17</sup>	0.0565	0.0166
"	"	38	// //	6.23 x 10 <sup>-15</sup>	9.12 x 10 <sup>-17</sup>	0.0590	0.0192
SSZ-1'	Grey gouge	39	// //	3.54 x 10 <sup>-16</sup>	1.15 x 10 <sup>-17</sup>	0.0510	0.0130
"	"	40	// ⊥	4.17 x 10 <sup>-15</sup>	4.94 x 10 <sup>-17</sup>	0.0644	0.0180
SSZ-2'	Grey gouge	41	// ⊥	2.42 x 10 <sup>-15</sup>	3.70 x 10 <sup>-17</sup>	0.0599	0.0140
"	Grey blue gouge	42	// ⊥	2.35 x 10 <sup>-16</sup>	2.39 x 10 <sup>-18</sup>	0.0674	0.0200
"	Fine fault breccia	43	// ⊥	1.77 x 10 <sup>-16</sup>	4.70 x 10 <sup>-18</sup>	0.0607	0.0202

*Table 2.5 – Continued*

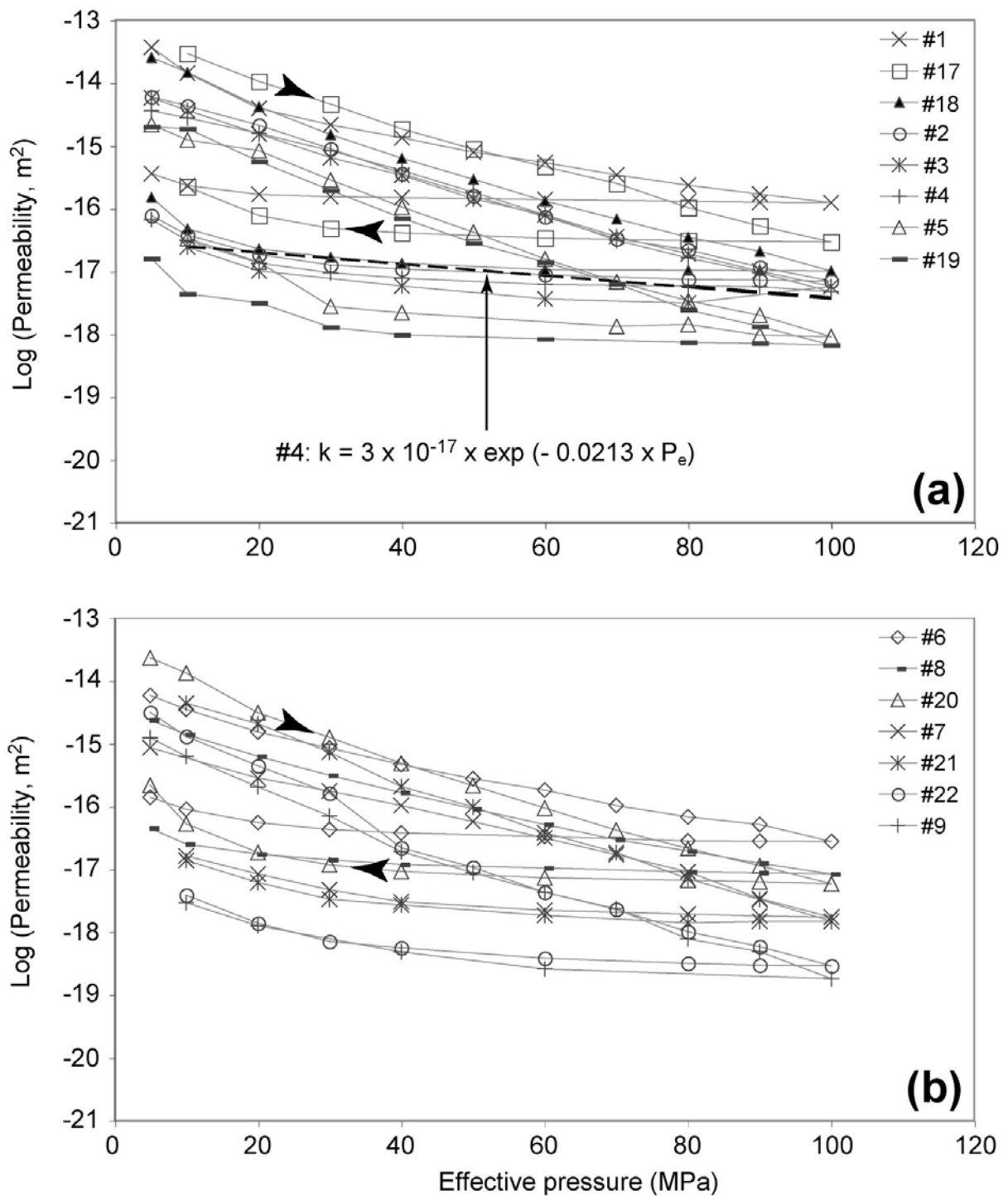


**Figure 2.22** - Evolution of nitrogen permeability with increasing/decreasing effective confining pressures for gouges and breccias from the principal and secondary slip zones of the exposure A. (a) Samples from PSZ gouges with // ⊥ orientations. (b) Same as (a), with // // orientations. (c) Same as (a), with ⊥⊥ orientations. (d) Samples from SSZ-1 gouges with // ⊥ orientations. (e) Samples from PSZ marginal breccias with // ⊥ orientations. Also given are the equations of the best-fit curves (dashed lines) for decreasing effective pressure paths for samples 4, 32 and 25. In the equations,  $P_e$  is expressed in MPa. Errors on permeability values are overestimated by 10 % (after Boutareaud et al., in press).

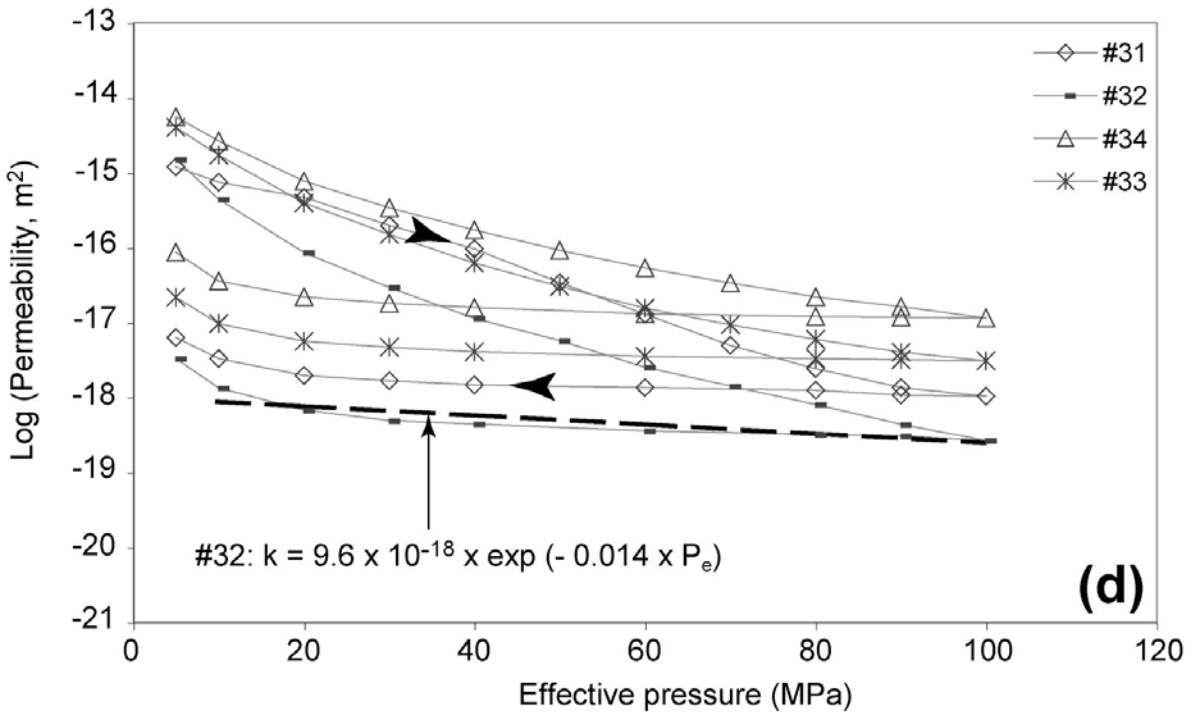
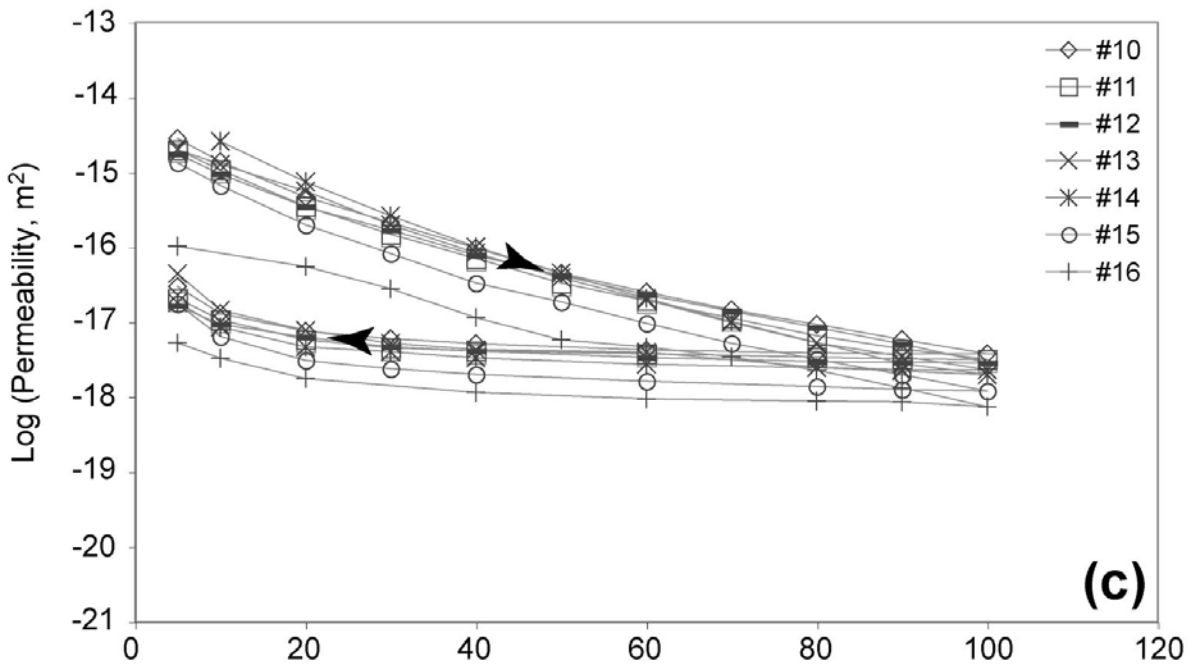


Figure 2.22 – Continued

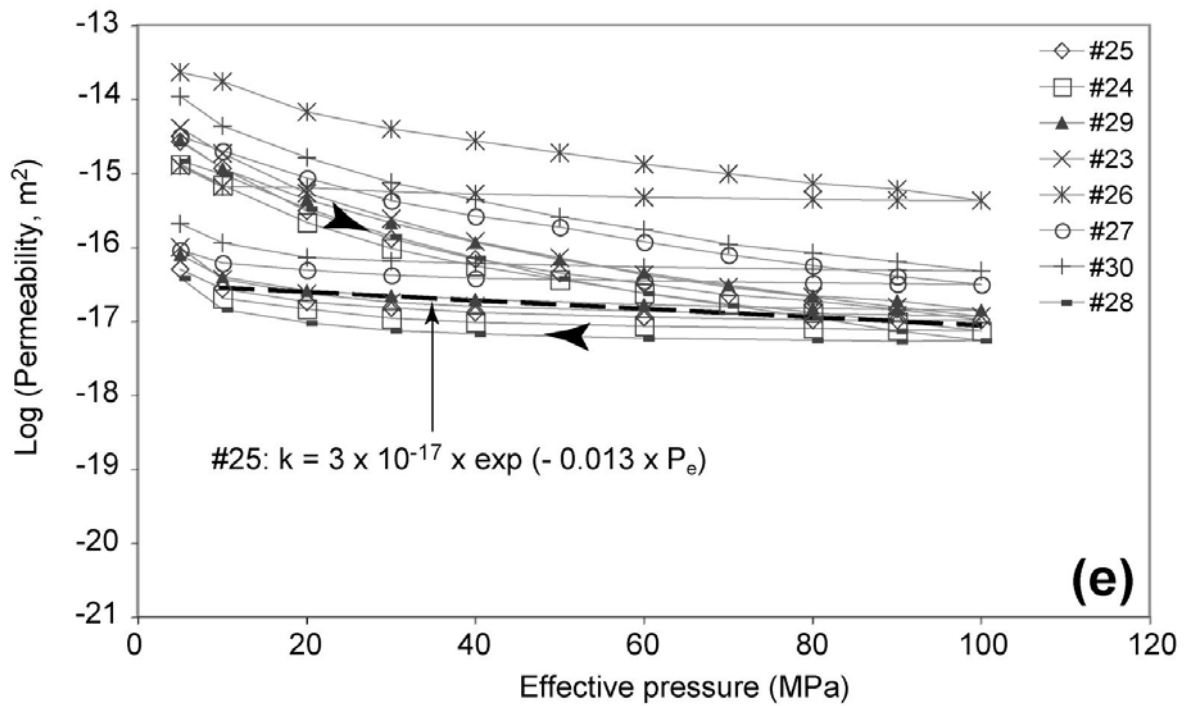


Figure 2.22 – Continued

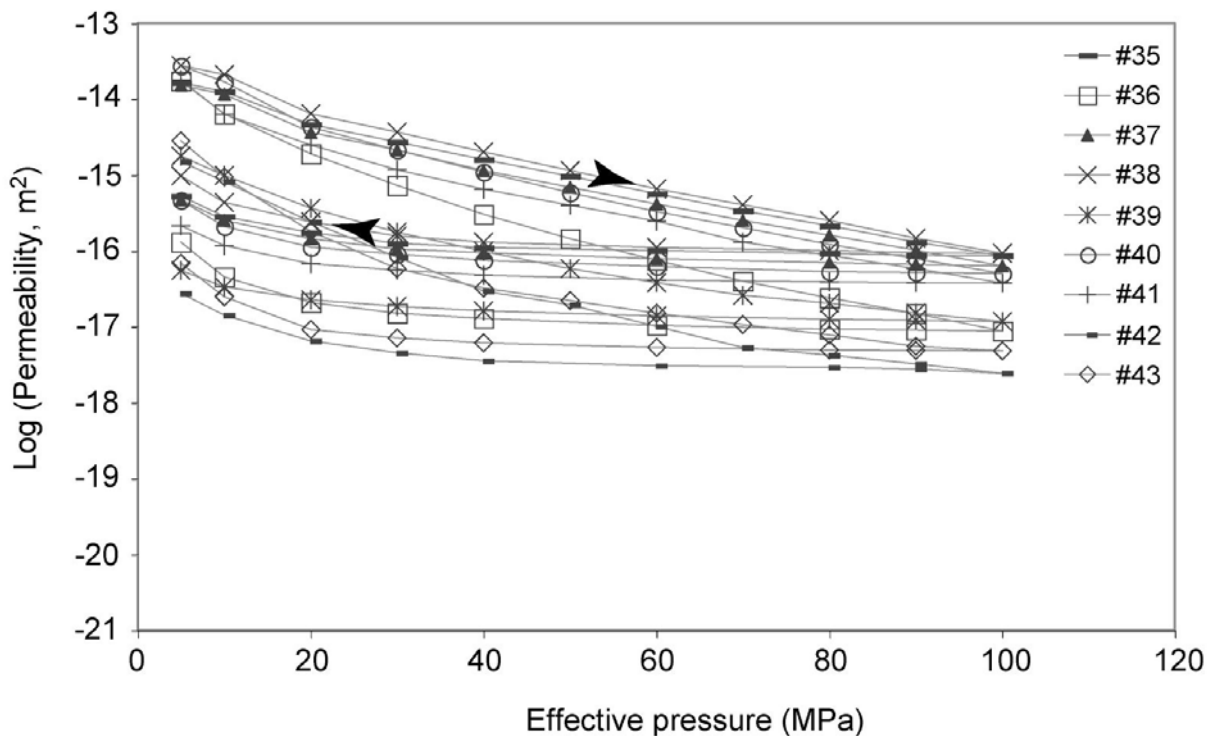


Figure 2.23 - Evolution of nitrogen permeability with increasing/decreasing effective confining pressures for gouges and breccias from the principal and secondary slip zones of the exposure B. All samples are //  $\perp$ , except samples 36, 37, 38 and 39 that are // //. All samples are located on Fig. 2.6b and 2.6c, except samples 35 and 40. Errors on permeability values are overestimated by 10 %.

unconsolidated or poorly consolidated clay-rich gouge layer surrounded by damage zones of variable widths. Indeed, when observed on outcrops, in trenches or through drilling, the uppermost, near-surface, part of seismogenic faults reveals a strong localization of slip along a planar zone consisting of a few centimetre-thick unconsolidated clayey gouge termed the *principal slip zone* (PSZ; Sibson, 2003). The boundaries between the PSZ and the surrounding rocks are sharp surfaces which often bear striations. The PSZ generally maintains good lateral continuity at the scale of the outcrop and between outcrops, typically being between 1 cm and 20 cm thick. In several instances, the gouge is partly or totally foliated, but remains poorly consolidated. Examples have been described in Japan (Lin, 2001; Lin et al., 2001a; Wibberley & Shimamoto, 2003, 2005; Tsutsumi et al., 2004; Noda & Shimamoto, 2005), Taiwan (Lin et al., 2001b) and New Zealand (Sibson, 1981; Warr & Cox, 2001). Such PSZs are interpreted as the location of the most recent displacements, and can thus be considered as the expression of the seismic rupture at or close to the surface of the Earth, between 0 and several kilometres depth (Sibson, 2003).

A review of permeability profiles obtained across inactive or active faults shows that the highest permeability values are typically found in the damage zones (particularly for crystalline rocks), the lowest values are obtained in the core zone and intermediate values come from the protolith (Evans et al., 1997; Seront et al., 1998; Lockner et al., 1999; Faulkner & Rutter, 1998, 2000, 2001; Morrow et al., 1984; Wibberley, 2002; Wibberley & Shimamoto, 2003; Tsutsumi et al., 2004; Uehara & Shimamoto, 2004; Mizoguchi et al., 2000; Mizoguchi, 2004). In addition to the experimental protocols and pressure ranges which vary between studies, the permeability values depend on the clay content, the proportion and size distribution of clasts, the possible sealing of fractures or cracks by secondary minerals and the orientation of the samples with respect to the structural components of the studied faults (open fractures and foliation). In particular, across-fault permeabilities, that is permeabilities of samples oriented perpendicularly to gouge foliation, are one to three orders of magnitude smaller than the permeabilities of samples parallel to the foliation (Evans et al., 1997; Seront et al., 1998; Faulkner & Rutter, 1998, 2000, 2001; Faulkner, 2004).

Measurements carried out on samples from strike-slip active faults in low-porosity host rocks with a clayey PSZ show that, for effective confining pressures in the range 80 - 180 MPa, and for pore pressures of 10 - 20 MPa, the permeability values obtained from the core zone vary between  $10^{-21}$  and  $10^{-17}$  m<sup>2</sup>, those from the damage zones between  $10^{-17}$  and  $10^{-15}$  m<sup>2</sup> and those from the protolith range from  $10^{-18}$  and  $10^{-16}$  m<sup>2</sup> (Fig. 2.24; Morrow et al., 1984; Faulkner & Rutter 1998, 2000, 2001; Mizoguchi et al., 2000; Wibberley 2002; Wibberley &

Shimamoto, 2003; Mizoguchi, 2004; Tsutsumi et al., 2004; Uehara & Shimamoto, 2004; Noda & Shimamoto, 2005).

Concerning the petrophysical properties of the Usukidani fault, we observe that the permeability values obtained for the clay gouges of the A and B exposures at an effective pressure of 100 MPa (Table 2.5, Figs. 2.22 & 2.23) fall mid-way in the range of previously reported data for clay gouges, being closest to those reported for the Neodani and Hanaore faults, Japan (Tsutsumi et al., 2004; Noda & Shimamoto, 2005). At the two exposures, typical values are  $10^{-16}$  -  $10^{-19}$  m<sup>2</sup> for the central clay gouge and  $10^{-15}$  -  $10^{-17}$  m<sup>2</sup> for the marginal fine fault breccia. Nevertheless, a wide range in clay gouge permeability values exists in the literature, which can be explained by: (1) differences in microstructure and clay mineralogy of the gouge zones, influenced by structural history, reworking into the gouge zones of clasts of adjacent material, and strain localization, and/or (2) differences in sampling procedures and experimental methodologies. This is also true for porosity values of clay gouges, although the number of studies reporting porosity data for natural clay gouges is far fewer than for permeability. Besides, others factors can dramatically affect the permeability from laboratory measurements. At low temperatures (< 80 °C), pore fluid chemistry can lead to water adsorption onto very fine-grained clay minerals, which may have important role in affecting the effective pore throat size by reducing natural permeability by about one order of magnitude (Faulkner & Rutter, 2000; Faulkner, 2004). Nitrogen gas is used as pore fluid instead of water. So, this effect does not occur during the permeability measurements. But one should note that the gas permeability data overestimate natural fault rock permeability by one order of magnitude as stated by Faulkner & Rutter (2000). This problem, amplified for very small pore sizes (see II.B.1.2.1) and low differential pore pressure (see II.B.1.1.3), is attributed to the Klinkenberg effect which enhances fluid flow by the collision of gas molecules with the pore wall rather than with other gas molecules (see Sone (2006) for a numerical estimation). At last, if the gas permeability experiments (done at 25 °C) do take into account the geobaric gradient, they do not consider the geothermal gradient, which promotes plasticity, enhances compaction in porous rocks and leads to permeability reduction at temperatures greater than 80 °C (see Faulkner (2004) for a numerical estimation). But this consideration is out of the scope of this work, as permeability measurements correspond to lithostatic conditions at 4 km depth (i.e. at about 80 °C).

Reported nitrogen porosity measurements in the range of 20 - 33 % at effective pressures of 80 - 100 MPa (Table 2.4, Figs. 2.20 & 2.21) are similar to those reported by Noda & Shimamoto (2005) but significantly higher than the porosities of 4 - 9 % measured

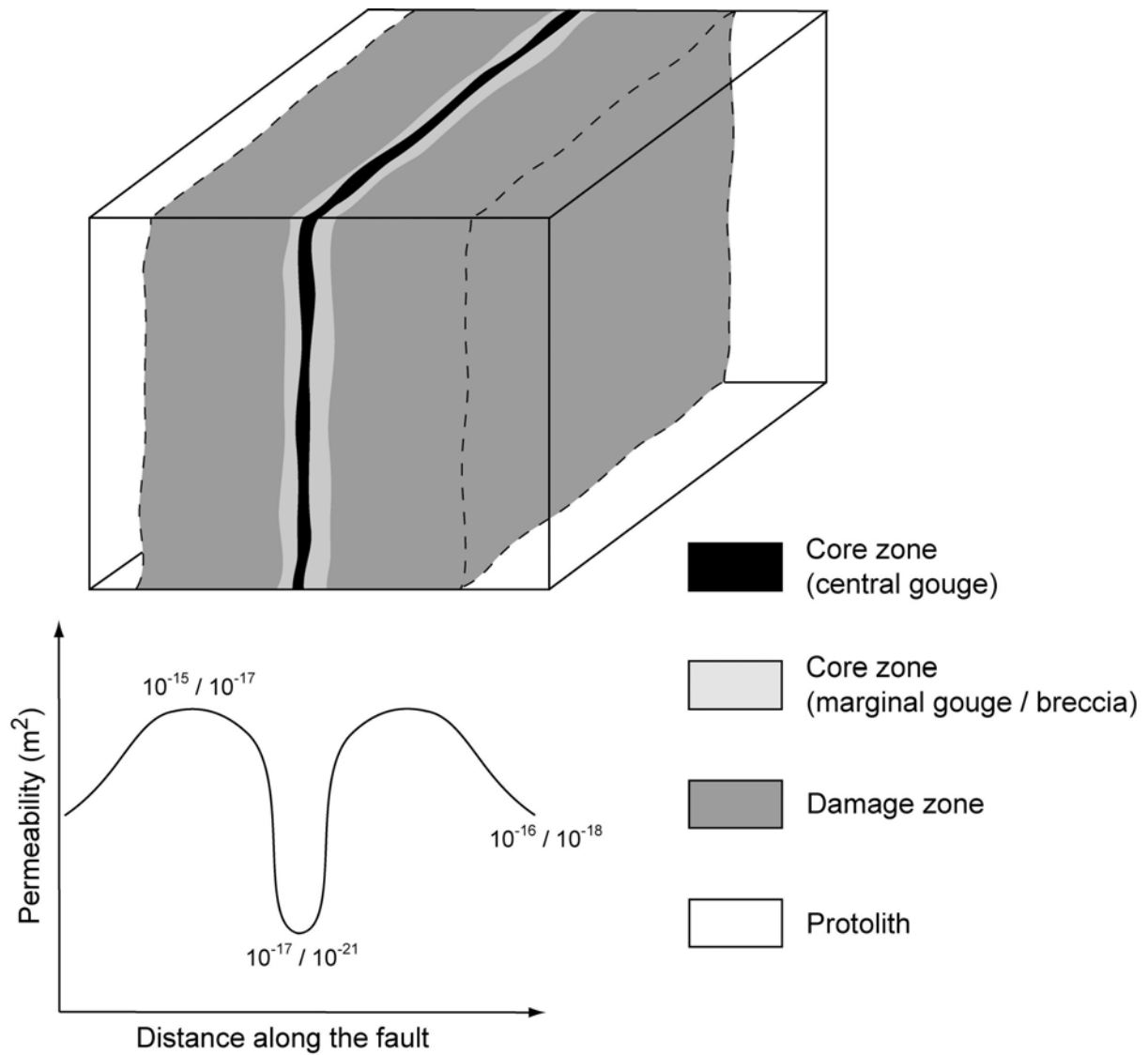


**Figure 2.24** - Schematic permeability profile across an active strike-slip fault after Faulkner & Rutter (1998, 2000, 2001) for mica schists, carbonate sediments and volcanic rocks; Morrow et al. (1984), Wibberley (2002), Wibberley & Shimamoto (2003), Uehara & Shimamoto (2004) for gneisses, mylonitic gneisses rocks and metapelitic schists; Noda & Shimamoto (2005) for pelitic rocks; Mizoguchi et al. (2000) and Mizoguchi (2004) for conglomerates and granitic rocks; Tsutsumi et al. (2004) for sandstone, shale, chert and volcanic rocks. The permeability values are close to values obtained at high effective pressures (of about 100 MPa).

for fault gouges from the Median Tectonic Line (Wibberley & Shimamoto, 2005). Concerning mercury porosities (Table 2.3), measurements show that gouges exhibit free porosities of about 28 - 48 %, trapped porosities of 50 - 70 % and a total porosity of 13 - 15 % at 0.1 MPa (atmospheric pressure) for a dominance of pore sizes lower than 1  $\mu\text{m}$  (Figs. 2.18 & 2.19). This is fewer than measured nitrogen porosities as reported by Yue et al. (2004), but very close to the values of Noda & Shimamoto (2005).

The pore volume of the gouges is tortuous and consists in fact of a network of large pores connected by smaller throats. As pressure increases, accessibility of mercury to gouge internal pores is constrained by the efficiency of mercury to fill completely the external smaller pores. This can lead to an overestimation of the trapped porosity (Ordóñez et al., 1997). But the large pore thresholds observed for the all gouge samples invalidate this assumption. Besides, the macroporosity low values suggest that sample drying does not have significantly influenced gouge microstructures, which appears to be also relevant for the nitrogen porosity and permeability measurements. Furthermore, variations of the  $N_p/N_{Hg}$  ratio, which is mainly controlled by the juxtaposition of enlargements and constrictions in the porous network, correspond to modifications of the clay framework structure (Dehandschutter et al., 2005). Thus, the observed ratio decrease of gouges from A to B exposures can be explained by a relative decrease of gouge pore size compared to pore-throat size. This might suggest variations in gouge matrix strain between A and B exposures, i.e. a higher rate of shearing deformation on gouge slip zones from A exposure compared to gouge slip zones from B exposure.

Individual cores of clay gouge along the Usukidani fault zone (i.e. at A and B exposures) yielded permeability values varying between one and three orders of magnitude, depending on the orientation of the cores (see above: // //, //  $\perp$  or  $\perp$   $\perp$  orientations). More precisely, the permeability values show the following hierarchy, which is quite clear at  $P_e = 100$  MPa (Fig. 2.22):  $k_{\perp\perp} < k_{// //} < k_{//\perp}$ . Similar dependencies between the permeability values and the sample orientations have already been reported by other studies carried out on gouges with internal anisotropies (Seront et al., 1997; Faulkner & Rutter, 1998, 2001; Wibberley & Shimamoto, 2005). These studies have also found the same hierarchy as the one stated above. Comparing A and B exposure permeabilities results, values appear to be quite similar whatever sampling direction (i.e. //  $\perp$  and // //; Table 2.5). Additional samples cored along the fault need to be measured to observe any noteworthy tendency.

Gouge permeability is expected to decrease with depth due to the effect of compaction. For permeability-pressure data matched closely by an exponential decrease law, the compaction coefficient ( $\gamma$ ) illustrates the permeability dependence on pressure. Typical values of  $\gamma$  for Usukidani fault rocks are  $0.05 \text{ MPa}^{-1}$  for fine fault breccia and  $0.1 \text{ MPa}^{-1}$  for clay gouges, whatever sampling direction considered (Table 2.5). Upon deconfinement, permeability recovers values one to three orders of magnitude lower than initial values, illustrating the importance of permanent compaction. This deconfinement represents a decrease in effective pressure, presumed to have a similar effect on permeability as an increase in fluid pressure. Meanwhile, care should be taken with  $\gamma$ , because it may not necessarily reflect the true *in situ* conditions at several kilometers depth (Morrow & Lockner, 1994). Indeed, surface-derived fault rock samples have experienced unloading histories, weathering and hydrothermal alteration, which may have resulted in higher permeability values and higher  $\gamma$ .

### 3. Conclusions

Permeability values of Usukidani fault gouges at 100 MPa fall mid-way in the range of previous studies, cover three orders of magnitude, show a pore size distribution dominated by pore sizes lower than  $1 \mu\text{m}$ , and are ordered according to their internal anisotropies as follows:  $k_{\perp\perp} < k_{//} < k_{//\perp}$ . This hierarchy does not have effect on the compaction coefficient ( $\gamma$ ).

The maximum effective confining pressure obtained in the experiments (100 MPa) corresponds to lithostatic load conditions expected at about 4 km depth. Assuming a geothermal gradient of  $20 \text{ }^\circ\text{C}/\text{km}$ , *in situ* temperatures can be estimated to be around  $80 \text{ }^\circ\text{C}$ . At these temperatures, adsorbed water film effect and thermally-enhanced compaction process can be neglected. Therefore, the fluid transport properties of Usukidani fault rocks measured on laboratory are relevant to be incorporated into any model to predict variations of fault fluid-flow properties.

## **CHAPTER III**

**Frictional experiments carried out on gouge with a high speed  
rotary-shear frictional testing apparatus**

## **A. High velocity friction experiments on the Usukidani fault gouge: experimental procedure**

### **1. Preparation of the simulated fault**

The simulated fault consists of a fine gouge layer of about 1 mm-thick, which is sealed between two solid granite cylinders by a Teflon® sleeve to prevent gouge and liquid water expulsion by centrifugal force during the experiments (Fig. 3.1). The granite comes from the Inada granite and consists of quartz, plagioclase, K-feldspar, hornblende, muscovite and biotite. It is coarse-grained and equigranular, without planar fabrics or fractures. The granite surfaces in contact with the gouge were previously ground with an 80# SiC abrasive powder to obtain rough wall surfaces in order to prevent slip at the gouge-rock interface and to approximate the rough wall rock-gouge boundary conditions in natural fault zones. It should be noted that the sample assembly is consolidated during several hours prior to shearing at the normal force applied during the experiment (Fig. 3.2). During the experiments, one side of the assembly is kept stationary while the other side is rotated.

The experimental gouge comes from the natural clay-rich gouge of the Usukidani fault (see II.B). The natural gouge was disaggregated and then sieved with a #53 mesh cloth (< 37 mm) to obtain a silty to clayey gouge powder. Laser granulometry analyses show a heterogeneous clast-size distribution and a clay fraction of ~ 15.7 % (Fig. 3.3). X-ray diffraction analyses revealed that the gouge powder consists mainly of quartz, calcite, K-feldspar and pyrite, with clay minerals such as kaolinite and randomly interstratified illite-smectite (Figs. 3.4a & 3.4b), with a percentage of illite greater than 40 % (Fig. 3.4c). Optical microscope and Scanning Electron Microscope (SEM) observations of the experimental gouge powder show that it does not contain any aggregated structure (Fig. 3.5a). It consists essentially of 0.3 - 80 µm-thick angular to subangular clasts of quartz, calcite, alkali feldspar, pyrite and oxides. It is matrix-supported, shows a random distribution of clast-size, and does not possess any preferred orientation of matrix clay as well as of clasts (Fig. 3.5b).

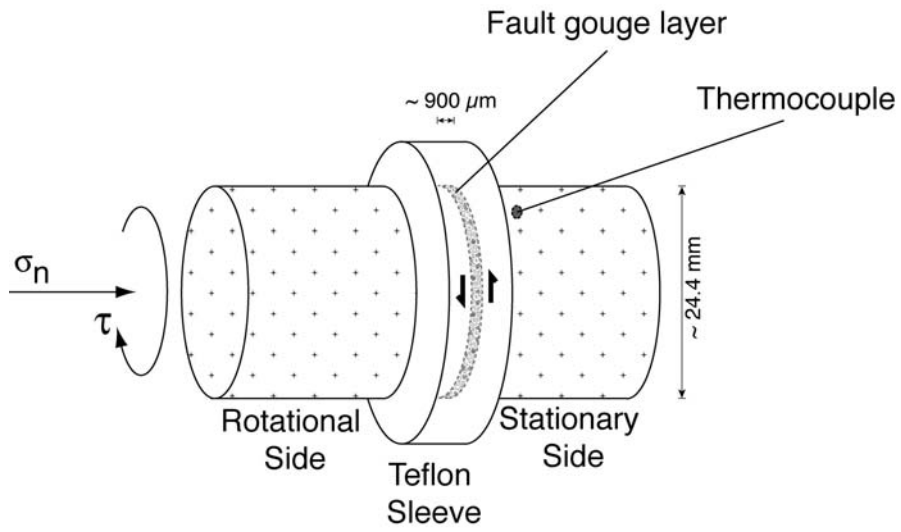


**Figure 3.1** - Schematic sketch showing the specimen assembly illustrating its shear geometry and the location of the thermocouple.

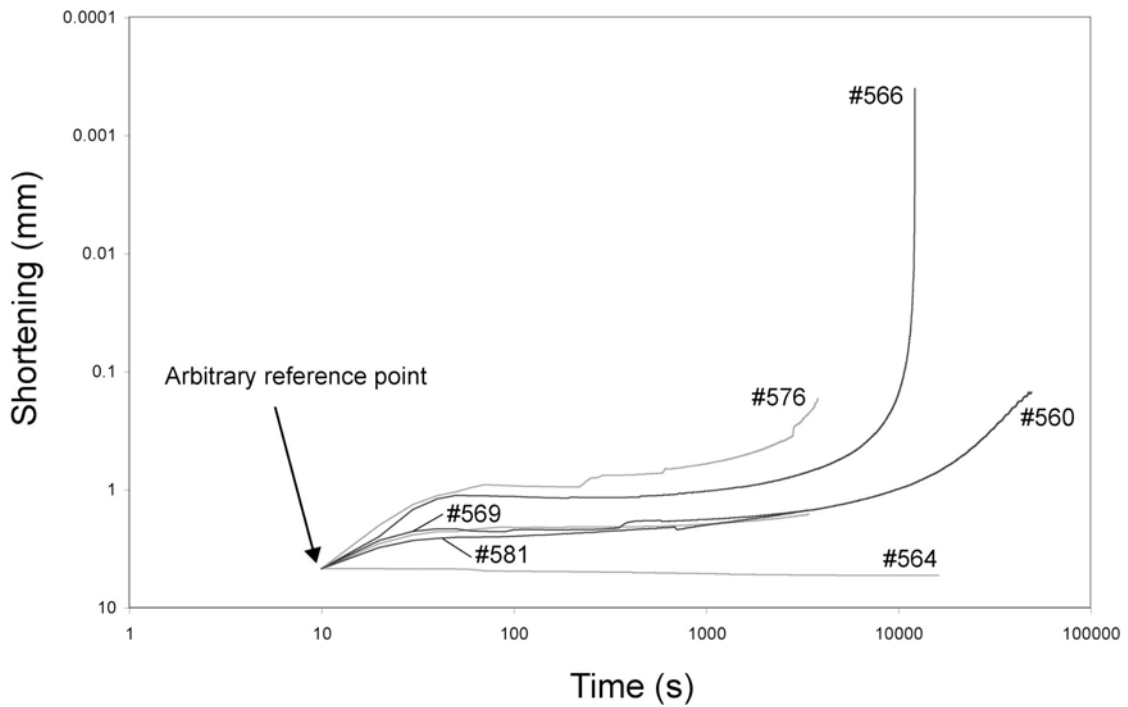


**Figure 3.2** - Evolution of some sample assembly thicknesses, during the pre-compaction period

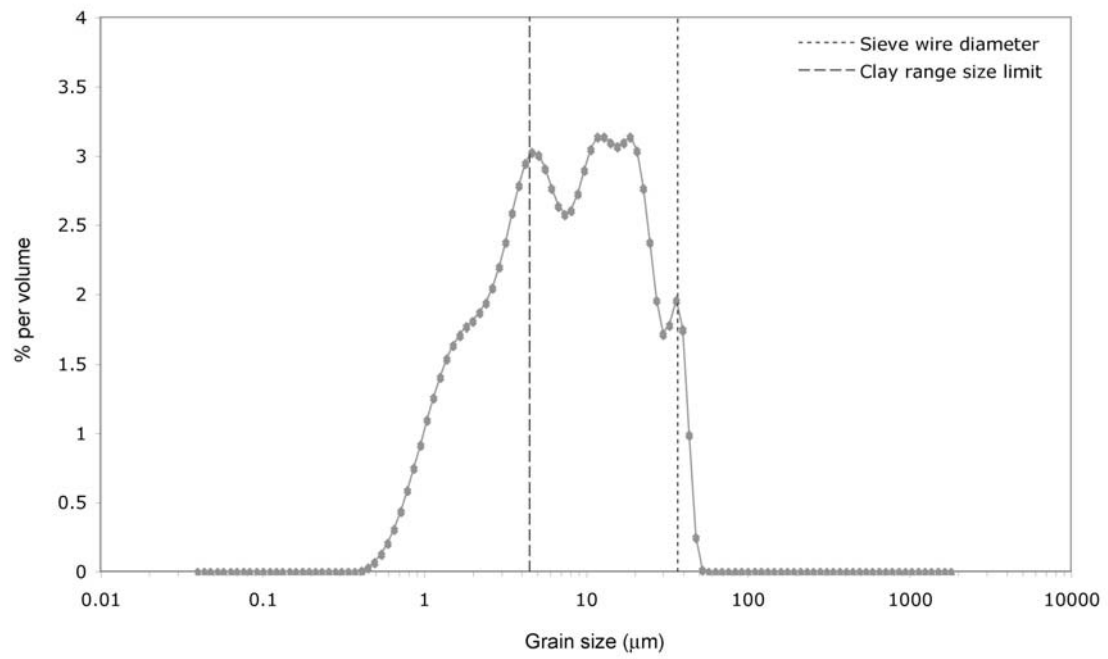


**Figure 3.3** - *Clast-size distribution of the experimental gouge powder.*

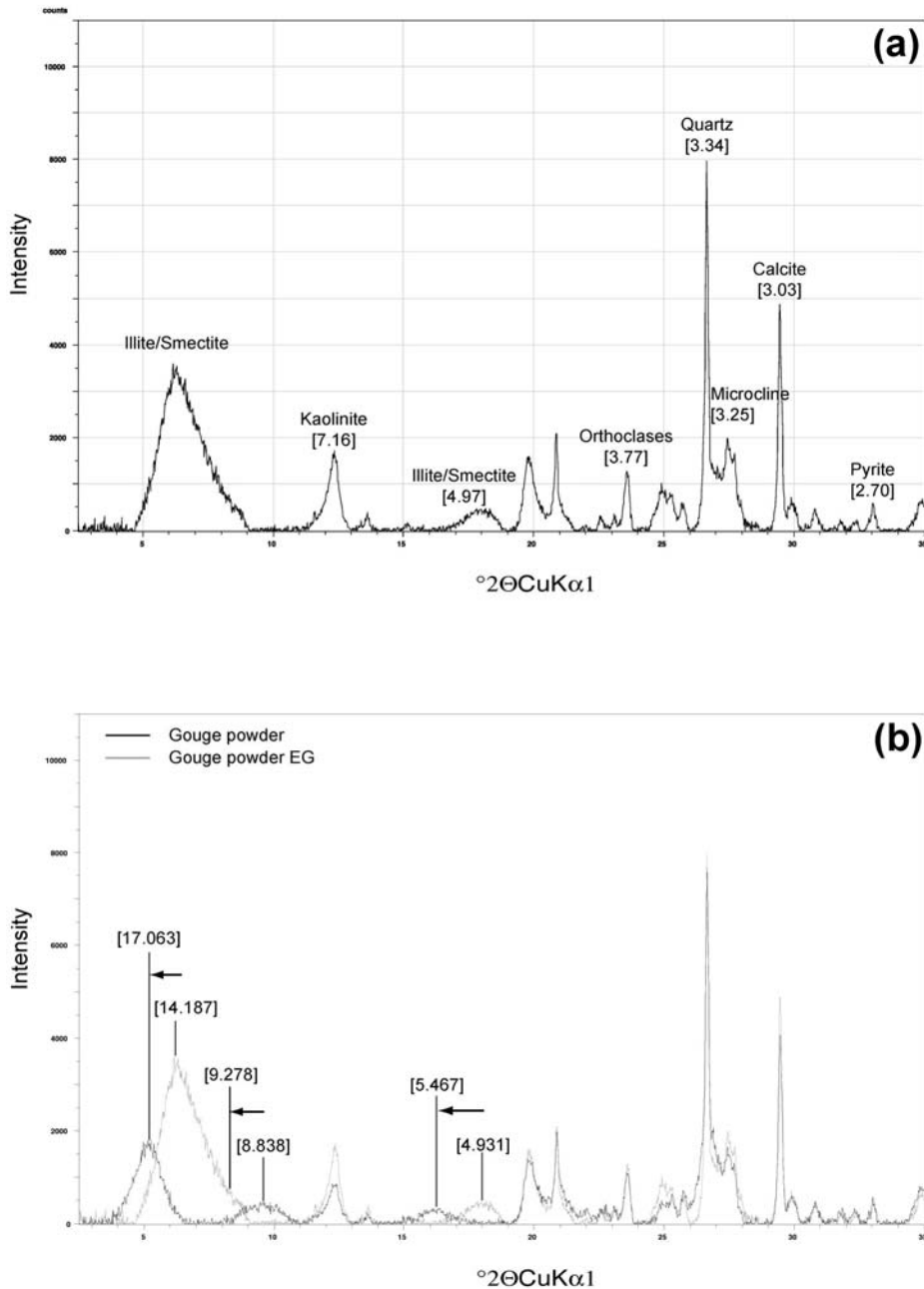


**Figure 3.4** - (a) X-ray diffraction analysis profile of the whole rock fraction from the experimental gouge powder. (b) X-ray diffraction analysis profile of the whole rock fraction of the gouge powder with corresponding profile obtained from the ethylene-glycol solvated preparation. This graph shows a strong escarpment at 17.063 Å. This signifies clay particles are mainly composed of one type of layer (smectite). The two domes observed at 5.467 and 7.19 Å signify that interstratification pattern of clay minerals follows a Gaussian law: 2 types of clay minerals with smectite and illite. Arrows indicate the shift of the 00l reflections (peaks) when gouge powder is glycolated. (c) X-ray diffraction analysis profile of the glycolated whole rock fraction from the experimental gouge powder. Lines named “broad peaks” represent randomly interstratified 60:40 smectite-illite mixed-layer, with solid and dashed lines for the location of the 00l reflections for the pure phases (following the method of Moore & Reynolds, 1989).

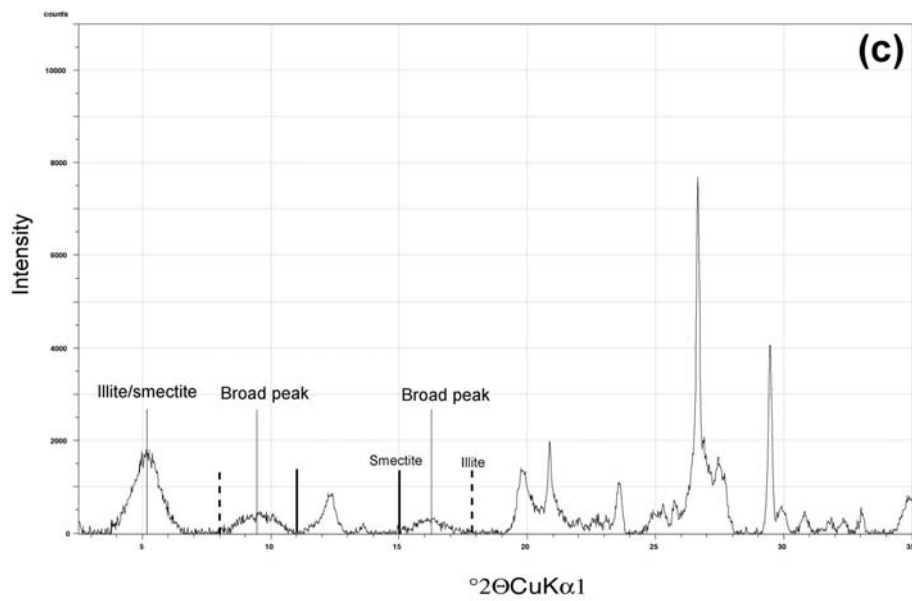


**Figure 3.4 - Continued**

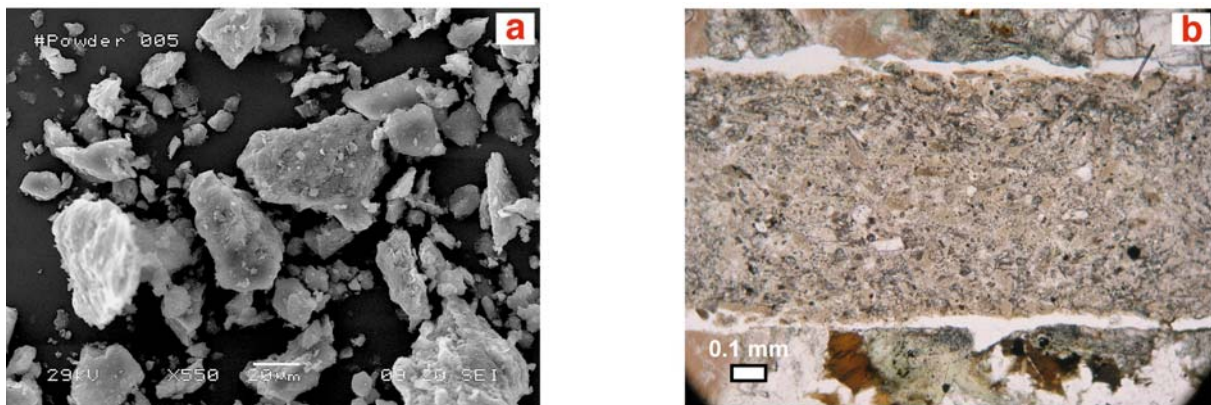


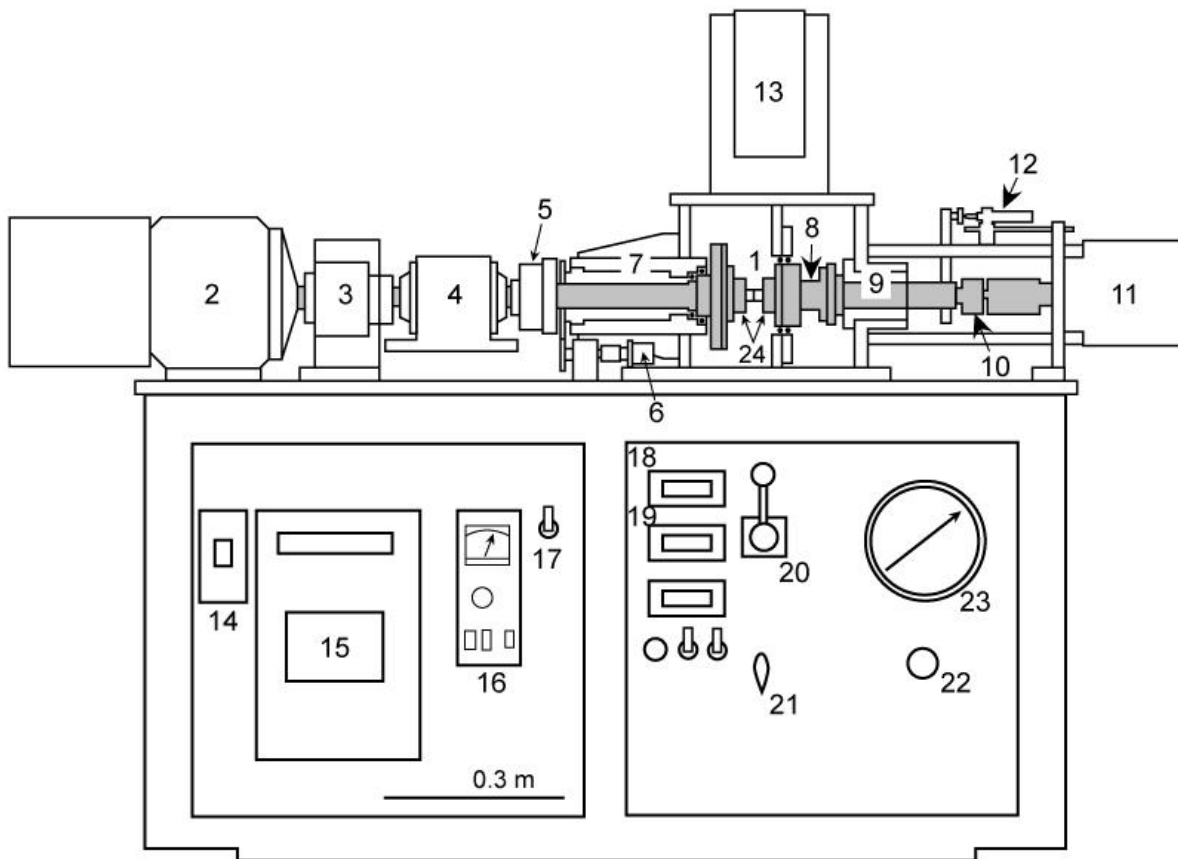
**Figure 3.5 - Photomicrographs of the sieved gouge powder used for sliding experiments. (a) at the SEM scale, no aggregated pattern is observed. (b) at the optical scale, the initial state of gouge before high velocity experiment shows a matrix-supported texture with highly angular clasts.**

## 2. Experimental technique

Experiments were performed at Kyoto University with a rotary-shear high-speed frictional testing machine (Fig. 3.6) described by Hirose & Shimamoto (2005). The maximum revolution rates attained at the periphery of the cylinders by the motor are 1500 rpm, for quasi-infinite displacements (see 2 in Fig. 3.6). The axial force applied to the simulated fault can be increased up to 10 kN, with an air-pressure driven actuator (see 11 in Fig. 3.6). Axial force, torque and axial shortening of simulated fault are measured with a force gauge (see 10 in Fig. 3.6), a torque gauge (see 8 in Fig. 3.6) and a displacement transducer (see 12 in Fig. 3.6), respectively. A thermocouple is fixed at 1 mm from the teflon sleeve on the granite surface in order to measure temperature rise during frictional sliding (Fig. 3.1).

The design of the experiment implies a slip-velocity gradient from the center to the outer part of the cylindrical assembly (Shimamoto & Tsutsumi, 1994). The equivalent slip-velocity ( $V_{eq}$ ) is defined such that  $S \times V_{eq} \times \tau$  gives the rate of total frictional work on a fault area ( $S$ ), assuming no velocity dependence of shear stress ( $\tau$ ), and a constant shear stress over the fault area. The equivalent slip-velocity is always maintained constant until reaching a frictional steady-state, then the motor speed is shut down. Thus, sliding velocity respects natural coseismic slip-velocity. Experiments were conducted at three (equivalent) slip-velocities: 0.09, 0.9 and 1.3 m/s. For all experiments, a constant axial normal force of 294.2 N and 588,4 N (that is 0.6 and 1.2 MPa given the area of the fault) is applied using an air-pressure actuator. Friction experiments on gouge have been conducted at room temperature in water-saturated conditions (*wet initial conditions*), or in room moisture conditions ( $\sim 60\%$  at  $25\text{ }^\circ\text{C}$ , *dry initial conditions*). Table 3.1 summarizes the experimental parameters.

All the post-run thin sections were cut normal to the shearing surface and parallel to the shearing direction at the boundary part of the cylindrical fault assembly (Fig. 3.7).



1: specimen, 2: motor, 3: torque limiter, 4: torque gauge, 5: electromagnetic clutch, 6: rotary encoder, 7: rotary column, 8: torque-axial force gauge, 9: ball spline, 10: axial force gauge, 11: air actuator, 12: displacement transducer, 13: water reservoir, 14: power switch of the motor, 15: controller of the motor, 16: operator of the motor, 17: switch of the electromagnetic clutch, 18~19: displays for axial force and displacement, 20: control valve for the air actuator, 21: inlet valve of air to the actuator, 22: regulator for air pressure, 23: air pressure gauge, 24: specimen holder.

**Figure 3.6** - Schematic diagram of the rotary shear high velocity frictional testing machine (after Mizoguchi, 2004).

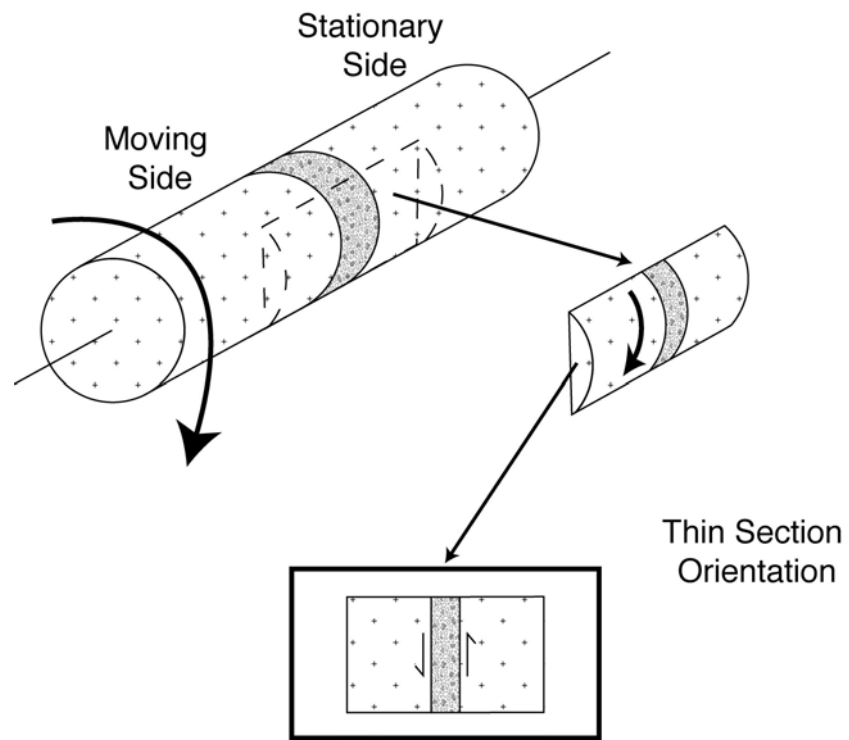


*Figure 3.7 - Schematic sketch showing the way to proceed thin section specimens.*

## B. Experimental results

### 1. Mechanical behavior

#### 1.1. Friction coefficient

The first order trend of the obtained friction curves remains similar (Fig. 3.8). As for the second order trend, the observed periodic fluctuations of the friction coefficient may be due to either distortion of the torque gouge caused by a small misalignment of facing granite cylinders and/or result from dynamic frictional instabilities (stick-slip).

Typically, friction data of simulated faults with intervening gouge performed at equivalent slip-velocities of 0.9 and 1.3 m/s and at a normal stress of 0.6 MPa or 1.2 MPa show a peak of friction immediately after starting the experiment (i.e. after 10 to 100 milliseconds of sliding displacement, depending on experimental conditions), followed by an exponential decay in the frictional resistance over about ten of meters, towards a steady-state friction coefficient (Figs. 3.8c to 3.8f; see I.C). At equivalent slip-velocities of 0.09 m/s, the frictional behavior does not show the dramatic decrease following the peak friction coefficient value, but a gradual decrease over few meters followed by a transient increase (Figs. 3.8a & 3.8b). This succession that occurs several times over ten of meters is most pronounced in dry conditions (Fig. 3.8a).

In dry initial conditions, peak friction coefficient values range from 0.92 to 1.18 at 0.09 m/s, from 1.13 to 1.35 at 0.9 m/s and from 1.15 to 1.31 at 1.3 m/s (Table 3.2). Steady-state friction coefficient values range from 0.75 to 0.98 at 0.09 m/s, from 0.36 to 0.38 at 0.9 m/s and from 0.29 to 0.33 at 1.3 m/s. Slip-weakening distance values range from 0.6 to 0.7 m at 0.09 m/s, from 7.5 to 9.9 m at 0.9 m/s and remain constant at 7.2 m at 1.3 m/s. Thus, changing sliding velocity from 0.09 to 1.3 m/s leads to an increase of the peak friction coefficient, to a decrease of the steady-state friction coefficient and to an increase of the slip-weakening distance. Besides, even if all parameters appear to depend on the velocity in dry conditions, additional experiments are needed to conclude about  $\mu_p$  and  $d_c$  at 1.3 m/s. In wet initial conditions, peak friction coefficient values range from 0.62 to 0.67 at 0.09 m/s, from 0.74 to 0.94 at 0.9 m/s and from 0.64 to 0.76 at 1.3 m/s (Table 3.2). Steady-state friction coefficient values range from 0.35 to 0.38 at 0.09 m/s, from 0.23 to 0.31 at 0.9 m/s and from

Run	Moisture condition	Equivalent Velocity (m/s)	Normal stress (MPa)	Gouge layer thickness after experiment ( $\mu\text{m}$ )	Total displacement (m)
#569	Wet	1.3	0.6	875	64.0
#576	Wet	1.3	0.6	-	33.5
#572	Wet	1.3	0.6	-	28.9
#581	Dry	1.3	0.6	-	34.6
#728	Dry	1.3	0.6	1000	26.6
#571	Wet	0.9	0.6	-	64.4
#564	Wet	0.9	0.6	1000	50.7
#521	Wet	0.9	0.6	750	40.3
#527	Wet	0.9	0.6	1050	48.6
#577	Wet	0.9	0.6	-	30.5
#547	Dry	0.9	0.6	340	42.8
#574	Dry	0.9	0.6	-	23.3
#545	Dry	0.9	0.6	-	36.9
#566	Wet	0.09	0.6	875	4.3
#575	Wet	0.09	0.6	-	4.0
#585	Wet	0.09	0.6	-	3.7
#565	Wet	0.09	0.6	-	3.7
#554	Wet	0.09	0.6	815	2.5
#568	Wet	0.09	0.6	940	2.5
#560	Dry	0.09	0.6	825	5.9
#550	Dry	0.09	0.6	-	4.3
#551	Dry	0.09	0.6	1175	9.6
#583	Wet	1.3	1.2	-	24.6
#579	Wet	1.3	1.2	750	26.0
#582	Dry	1.3	1.2	-	57.5
#580	Dry	1.3	1.2	900	29.3
#586	Wet	0.9	1.2	-	37.1
#587	Dry	0.9	1.2	-	28.8
#549	Wet	0.09	1.2	625	8.3
#548	Wet	0.09	1.2	500	10.6
#584	Wet	0.09	1.2	-	2.8
#567	Wet	0.09	1.2	1150	2.0
#559	Dry	0.09	1.2	-	4.3
#578	Dry	0.09	1.2	1025	2.6
#558	Dry	0.09	1.2	-	1.3

*Table 3.1 - Summary of the main experimental parameters for all the experiments.*

Run	Moisture condition	Equivalent Velocity (m/s)	Normal stress (MPa)	Peak friction coefficient	Steady-state friction coefficient	$d_c$ (m)
#569	Wet	1.3	0.6	0.74	0.17	34.3
#576	Wet	1.3	0.6	0.76	0.14	31.6
#572	Wet	1.3	0.6	0.64	0.29	15.9
#581	Dry	1.3	0.6	1.15	0.29	7.2
#728	Dry	1.3	0.6	1.31	0.33	7.2
#571	Wet	0.9	0.6	0.94	0.23	28.8
#564	Wet	0.9	0.6	0.94	0.27	24.8
#521	Wet	0.9	0.6	0.74	0.31	29.9
#547	Dry	0.9	0.6	1.35	0.38	7.5
#574	Dry	0.9	0.6	1.13	0.36	9.9
#566	Wet	0.09	0.6	0.67	0.35	1.0
#575	Wet	0.09	0.6	0.62	0.38	2.5
#560	Dry	0.09	0.6	1.07	0.75	0.7
#550	Dry	0.09	0.6	1.18	0.98	0.6
#551	Dry	0.09	0.6	0.92	0.80	-

**Table 3.2** - Experimental run conditions and parameters of the most representative friction experiments at 0.6 MPa. The peak friction coefficient values and the steady-state friction coefficient values correspond to bulk friction values. Errors on friction coefficient values are overestimated by 1 %. Slip-weakening distance values result from friction data fitting with equation 1.13, using Kaleidagraph© software. At 0.09 m/s, experiments show a sawtooth frictional behavior.  $d_c$  is calculated from the first friction decrease. Errors on  $d_c$  values are overestimated by 1 %.

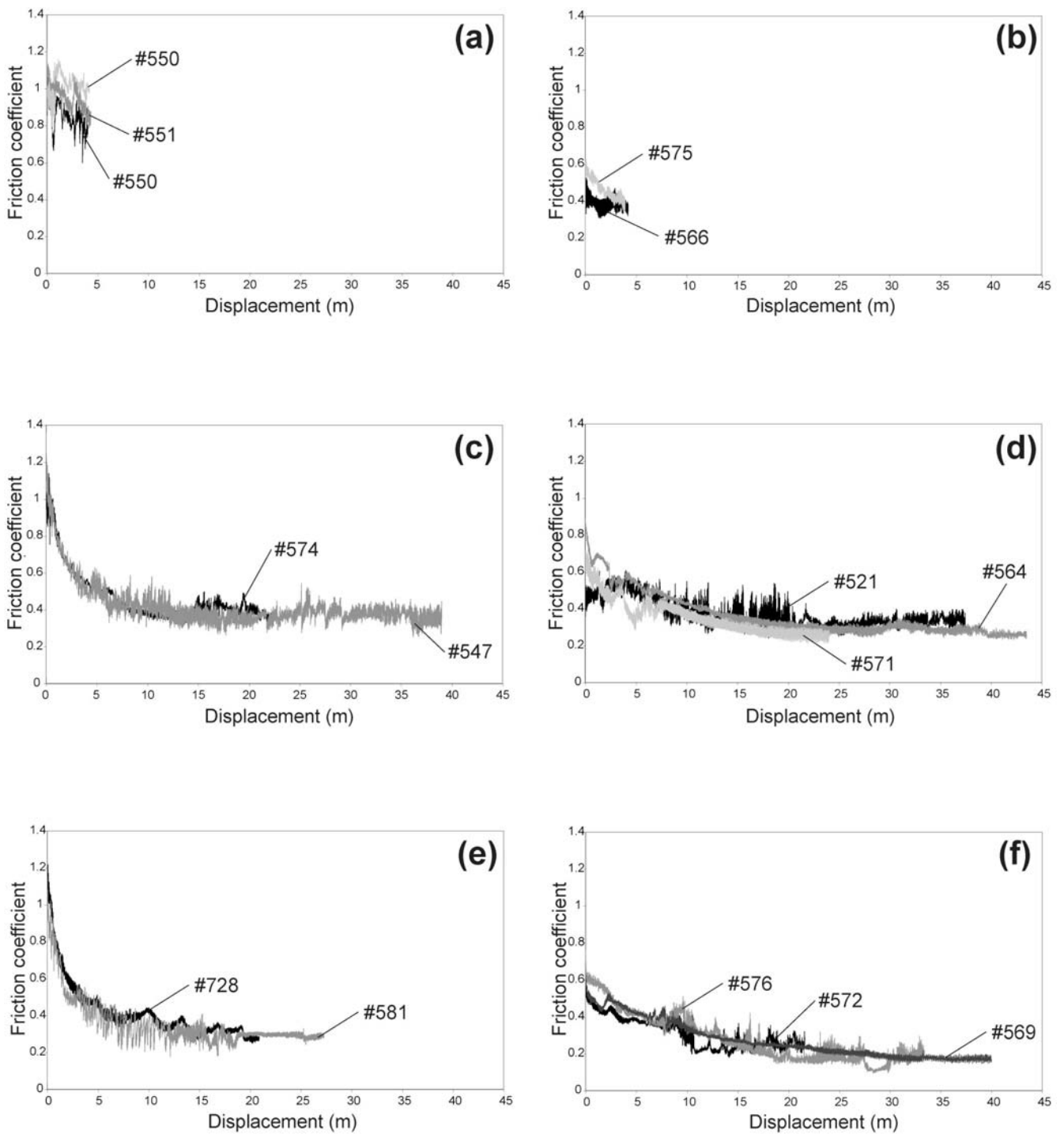


**Figure 3.8** - Most representative mechanical behaviors of gouge simulated faults (a) at 0.09 m/s in dry conditions, (b) at 0.09 m/s in wet conditions, (c) at 0.9 m/s in dry conditions, (d) at 0.9 m/s in wet conditions, (e) at 1.3 m/s in dry conditions, (f) at 1.3 m/s in wet conditions. Experimental parameters are summarize on Table 3.1 (after Boutareaud et al., 2006).

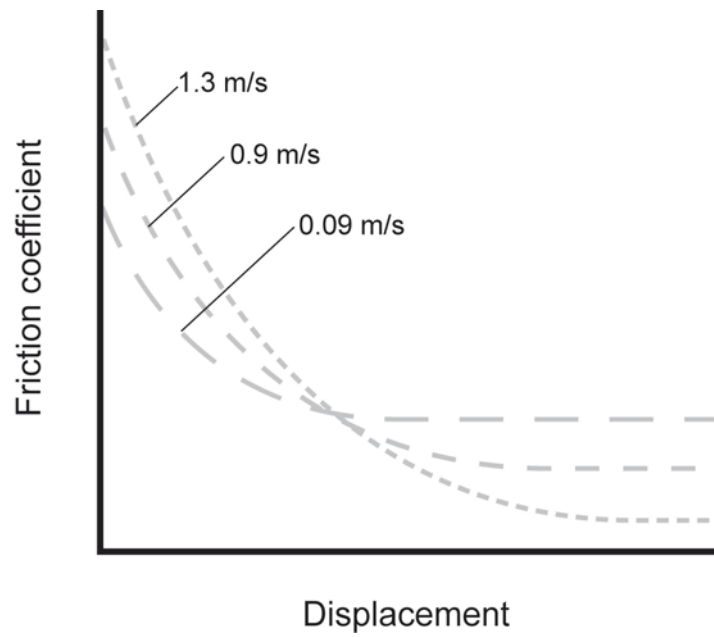


**Figure 3.9** - Typical mechanical behaviors of gouge simulated faults at slip-velocities of 0.09, 0.9 and 1.3 m/s, for wet or dry initial conditions. Changing sliding velocity from 0.09 to 1.3 m/s leads to an increase of  $\mu_p$ , to a decrease of  $\mu_{ss}$  and to an increase of  $d_c$ .

0.14 to 0.29 at 1.3 m/s. Slip-weakening distance values range from 1.0 to 2.5 m at 0.09 m/s, from 24.8 to 29.9 m at 0.9 m/s and from 15.9 to 34.3 m at 1.3 m/s. Thus, changing sliding velocity from 0.09 to 1.3 m/s leads to an increase of the peak friction coefficient, to a decrease of the steady-state friction coefficient and to an increase of the slip-weakening distance. Besides, even if all parameters appear to depend on velocity in wet conditions, additional experiments are needed to conclude about  $\mu_p$  at 1.3 m/s. Hence, friction experiments on simulated faults with intervening gouge show that, whatever initial moisture conditions, changing sliding velocity from 0.09 to 1.3 m/s leads to an increase the peak friction coefficient, to a decrease the steady-state friction coefficient and to an increase of the slip-weakening distance (Fig. 3.9).

## 1.2. Dynamic shear resistance

Figure 3.10 gives the plot of normal stress versus shear stress for initial and residual states (termed *initial friction* and *residual friction*, respectively) for all the experiments.

Best-linear fit lines of initial friction are always above their respective residual friction, whatever slip-velocities and moisture conditions. Additionally, best-linear fit lines of dry initial friction are always above best-linear fit lines of wet initial friction. Similarly, best-linear fit lines of dry residual friction are always above best-linear fit lines of wet residual friction.

Figure 3.11 gives the plot of the slip-weakening distance as a function of normal stress. It should be noted that, even if normal stress is fixed at 0.6 or 1.2 MPa at the beginning of the experiments, axial stress can fluctuate by about 25 % because of a few drawbacks, such as shear dilatancy. In dry initial conditions, changing normal stress from 0.6 to 1.2 MPa leads to a decrease of  $d_c$  by several ten of meters. Similar trend is obtained for wet initial conditions, but the best-fitting curve is shifted by several few MPa towards the Y-axis. Meanwhile, additional friction experiments are needed to conclude about this tendency.

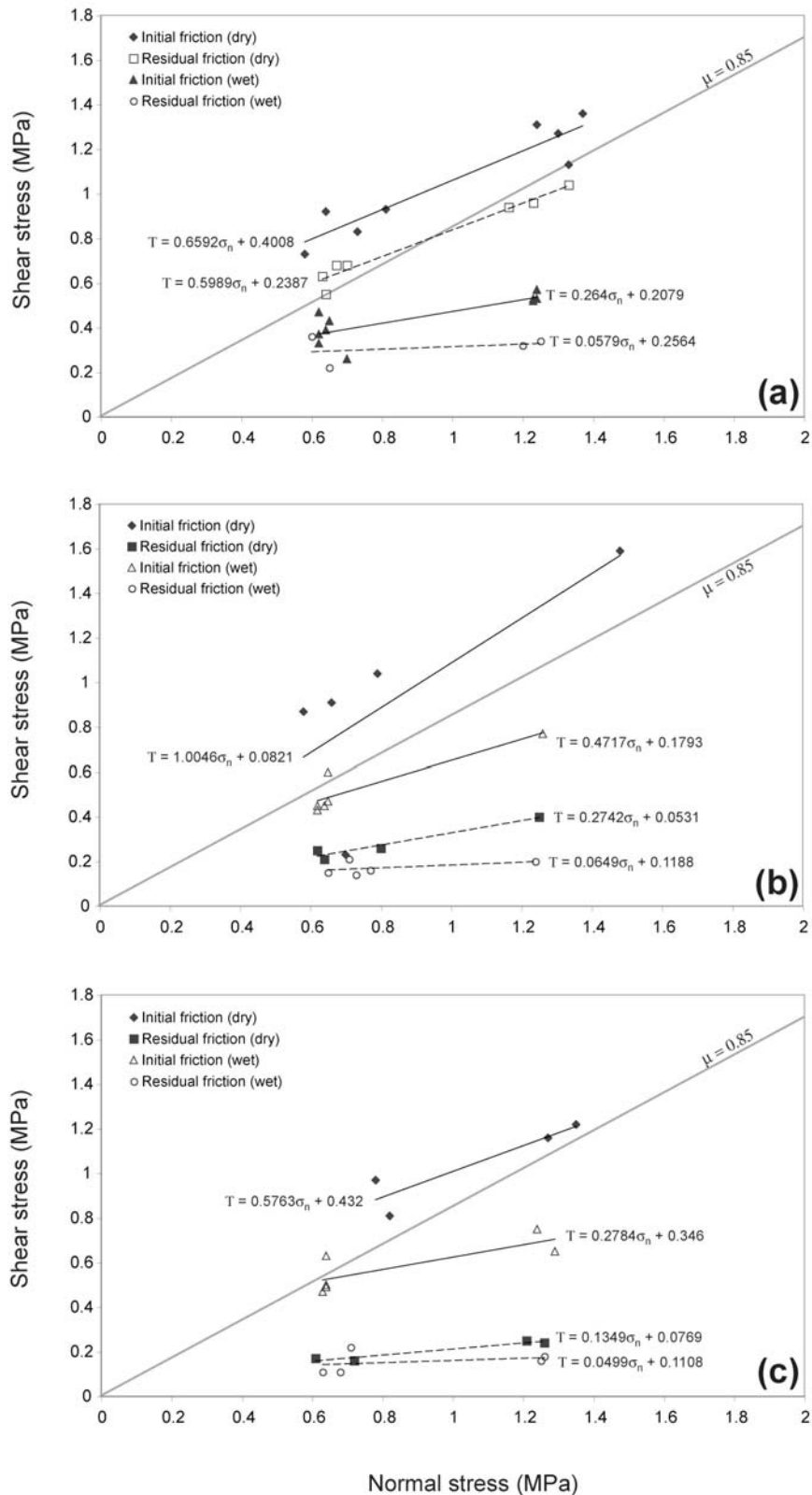


**Figure 3.10** - Shear stress versus effective normal stress for experiments done at (a) 0.09 m/s, (b) 0.9 m/s, (c) 1.3 m/s, with Byerlee's frictional law line in grey color. The solid lines are the best-linear fits for initial friction, and the dashed lines are the best-linear fits for residual friction. All the lines lay below the Byerlee strength, but solid lines in dry conditions.

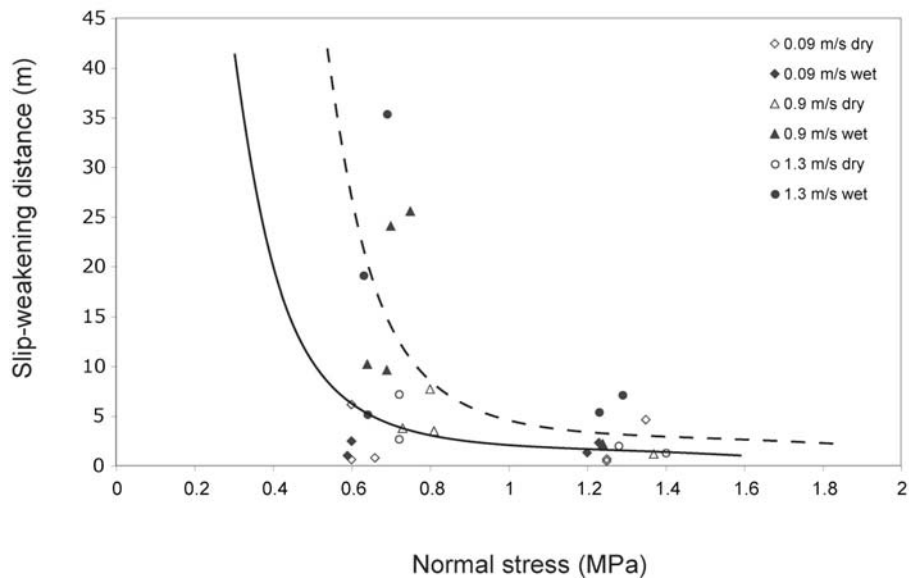


**Figure 3.11** - Slip-weakening distance ( $d_c$ ) plotted as a function of normal stress for the all slip-velocities and moisture conditions. The dashed curve represents the general best-fit trend for wet conditions, and the solid curve represents the general best-fit trend for dry conditions.

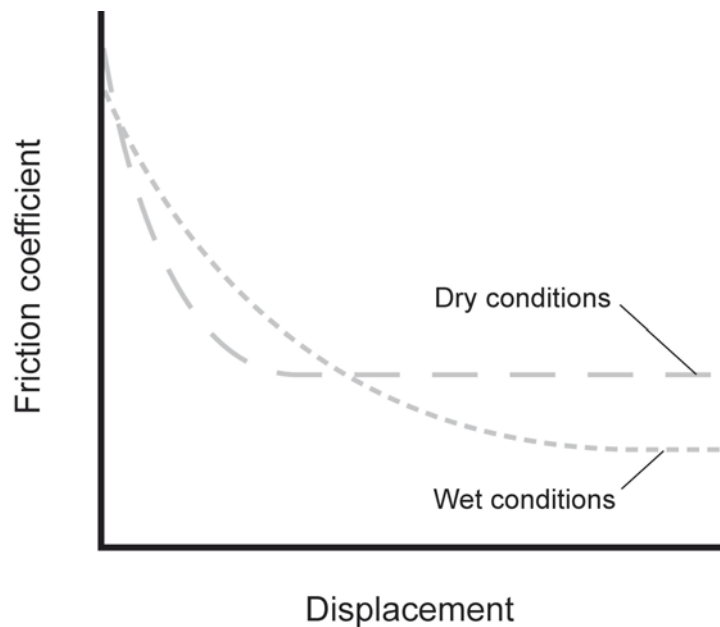


**Figure 3.12** – Typical mechanical behaviors of gouge simulated faults in wet and dry initial conditions. Changing water content from dry to wet initial conditions leads to a decrease of  $\mu_p$ , to a decrease of  $\mu_{ss}$  and to an increase of  $d_c$ .

## 2. Post-experiment microstructures

Microscope and SEM observations of gouge run products allow to distinguish three distinct post-experiment gouges. The presence and the distribution of each gouge depends on initial moisture conditions and slip-velocities.

### 2.1. A-type gouge

The A-type gouge consists of a clay-rich matrix with a random fabric (Fig. 3.13). It is present in all runs, except for the wet runs at slip velocities of 0.09 m/s (Fig. 3.13d) for which a clay-rich matrix with a foliation at 150 - 155° clockwise from the granite interface of the rotational side can be observed (Fig. 3.14a). The A-type gouge is characterized by uniformly distributed rounded clasts of quartz, feldspar or pyrite and spherical clay-clast aggregates distributed throughout the matrix, which is composed of mixed-layer clay minerals (Fig. 3.15b). These clay-clast aggregates exhibit various fabrics and can be composed of several elements, depending on water content and slip-velocities. Four types can be distinguished:

- The first type consists of a single poorly fractured rounded clast of quartz, calcite or feldspar as nucleus, surrounded by a cortex of concentric layers of clays including very-fine fragments of quartz, feldspar or calcite (Fig. 3.16a). This aggregate type can be observed in all runs (Fig. 3.13).

- The second type consists of several concentric layers of clays including fragments of quartz, feldspar or calcite (Fig. 3.16b). This aggregate type can also be observed in all runs (Fig. 3.13).

- The third type consists of a large elliptical nucleus showing a strong preferred orientation and few ultra-fine mineral fragments. It is surrounded by a cortex of concentric layers of clays with very-fine and sparse clasts of quartz, feldspar or calcite (Fig. 3.16c). This type of elliptical aggregate can be observed in all runs, except for the wet runs at 0.09 m/s (Fig. 3.13).

- The fourth type consists of a large elliptical nucleus with one or several large central cracks rimmed by ultra-fine to fine clast layers. The nucleus is surrounded by a cortex of concentric layers of clays with very-fine clasts of quartz, feldspar or calcite (Fig. 3.16d).

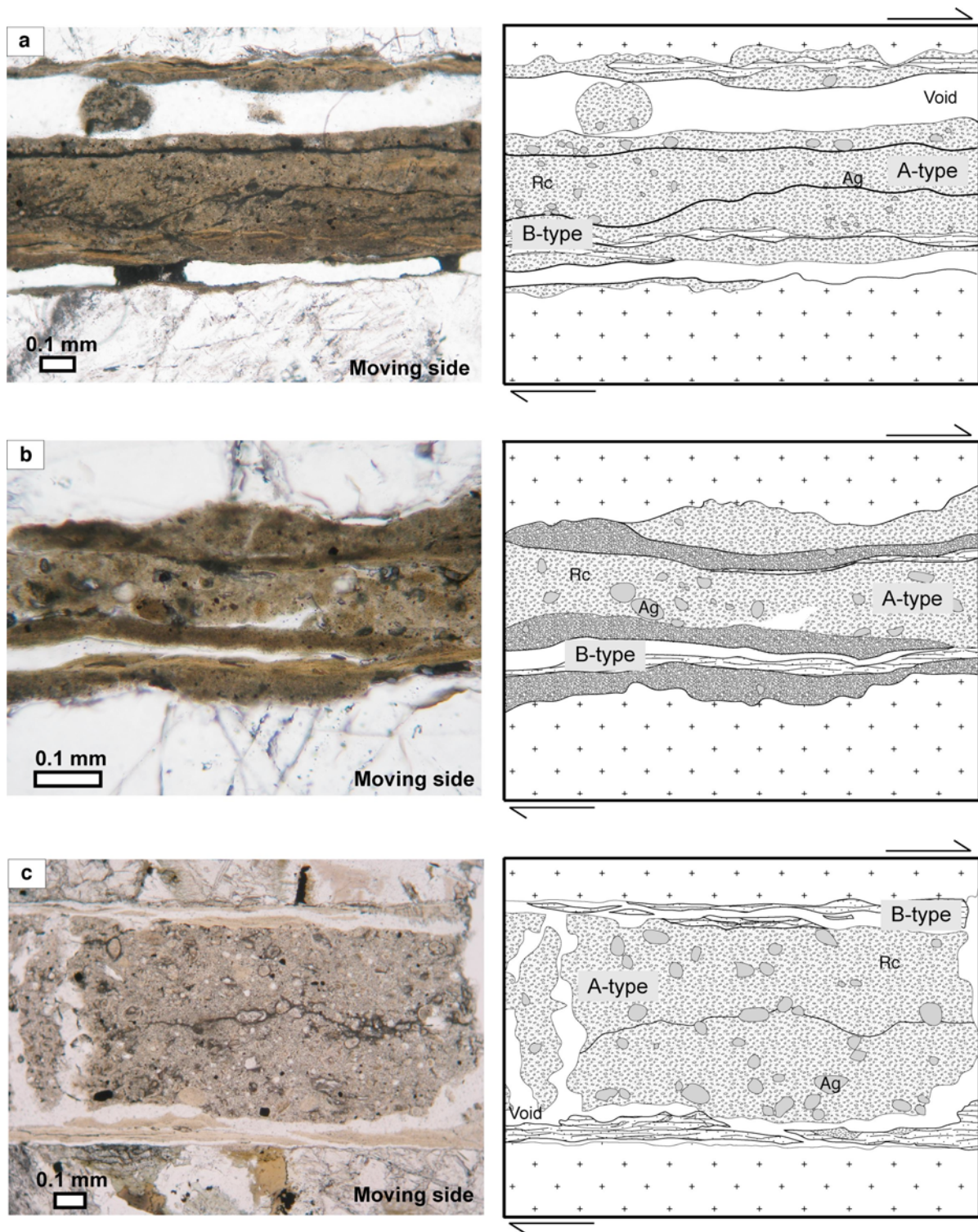


**Figure 3.13** - Optical photomicrographs under plane-polarized light (left) of representative microtextures of simulated fault gouges obtained from frictional sliding experiments, and corresponding sketches. In all figures, shear plane is horizontal and shear sense is top to the right. Rc means rounded clast and Ag clay-clast aggregate. Straight boundary fractures along granite interfaces (voids) correspond to desiccation cracks. (a) at 0.09 m/s for dry initial conditions. (b) at 0.9 m/s for dry initial conditions. (c) at 1.3 m/s for dry initial conditions. (d) at 0.09 m/s for wet initial conditions. (e) at 0.9 m/s for wet initial conditions. (f) at 1.3 m/s for wet initial conditions (after Boutareaud et al., 2006).

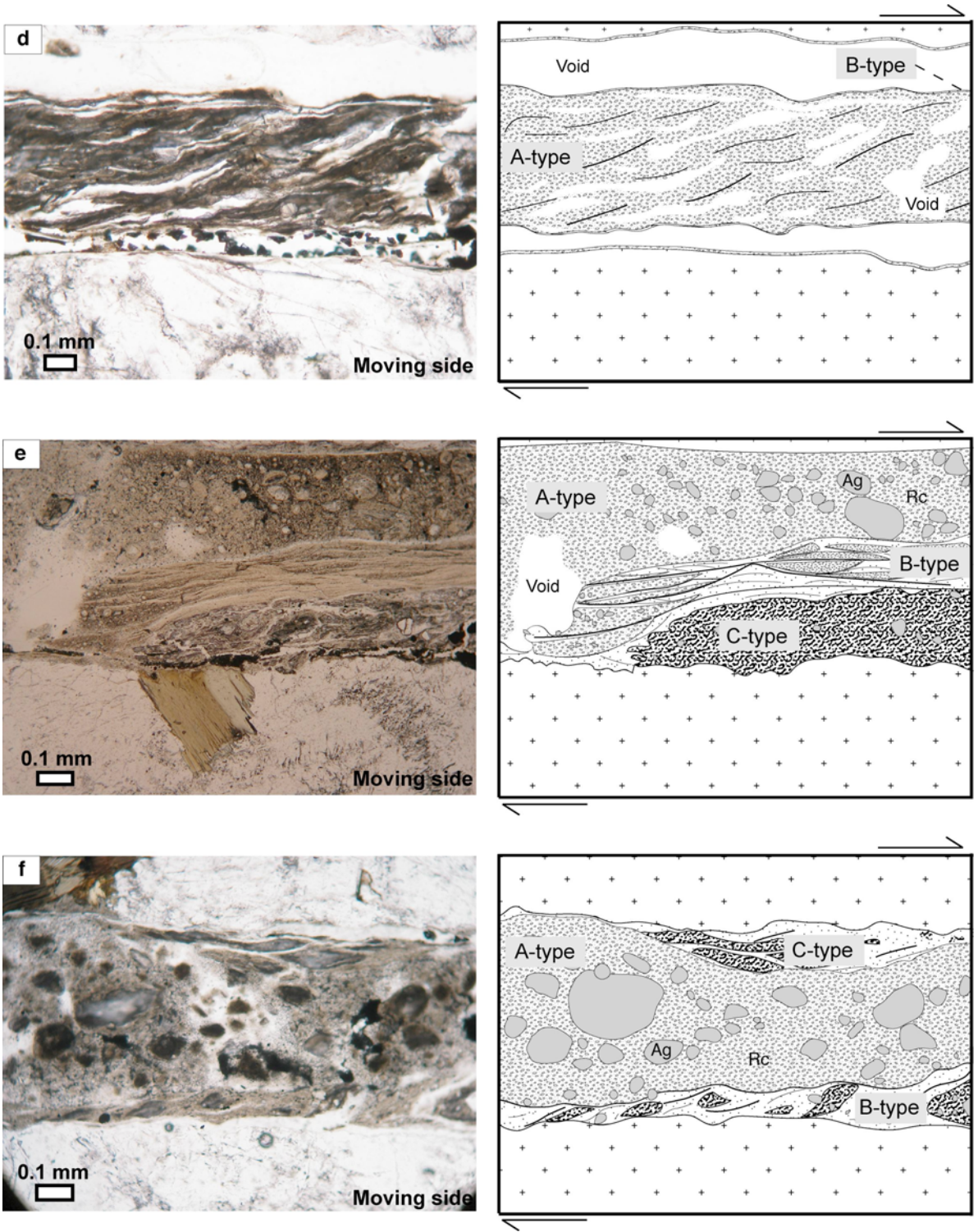
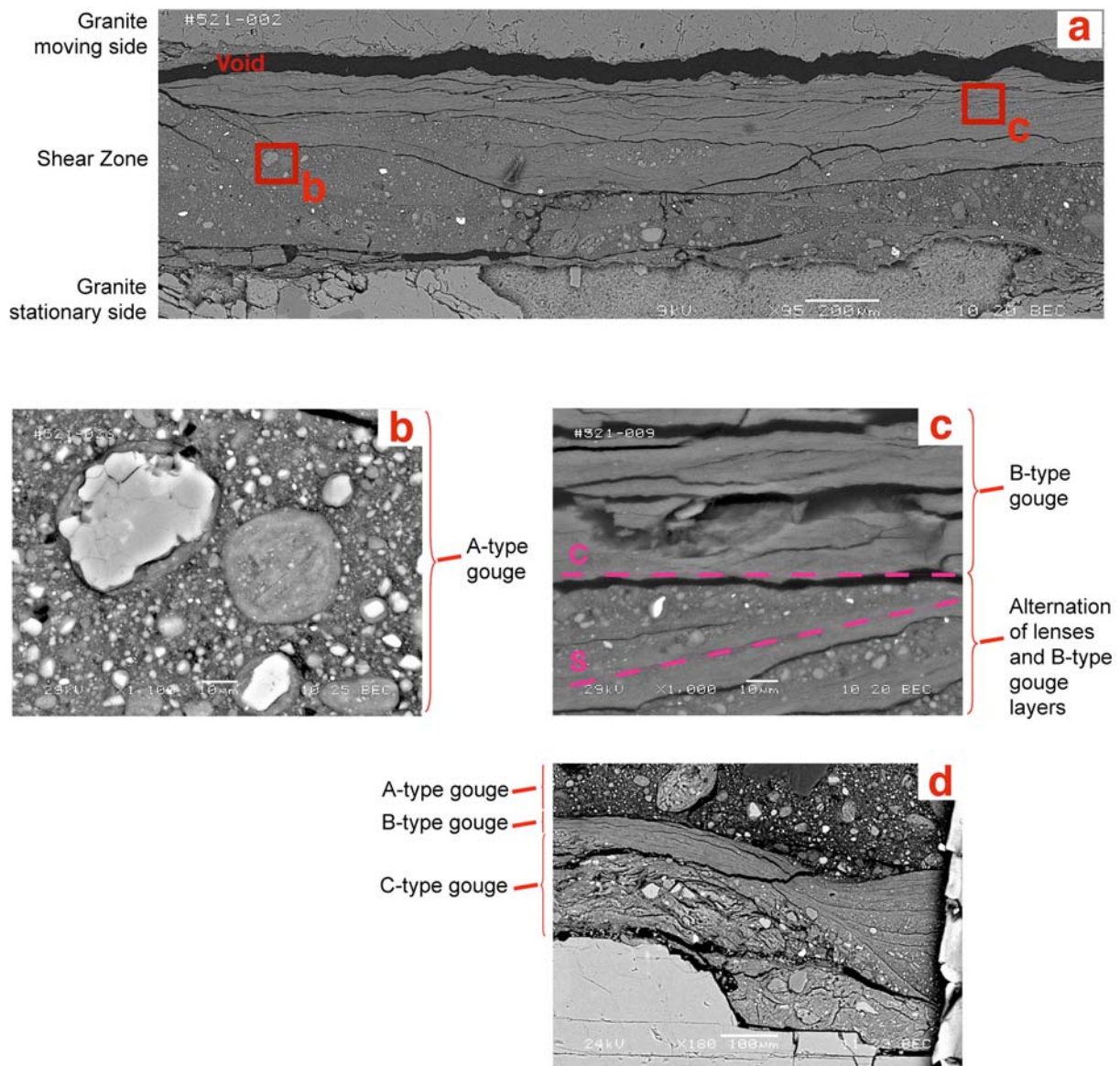
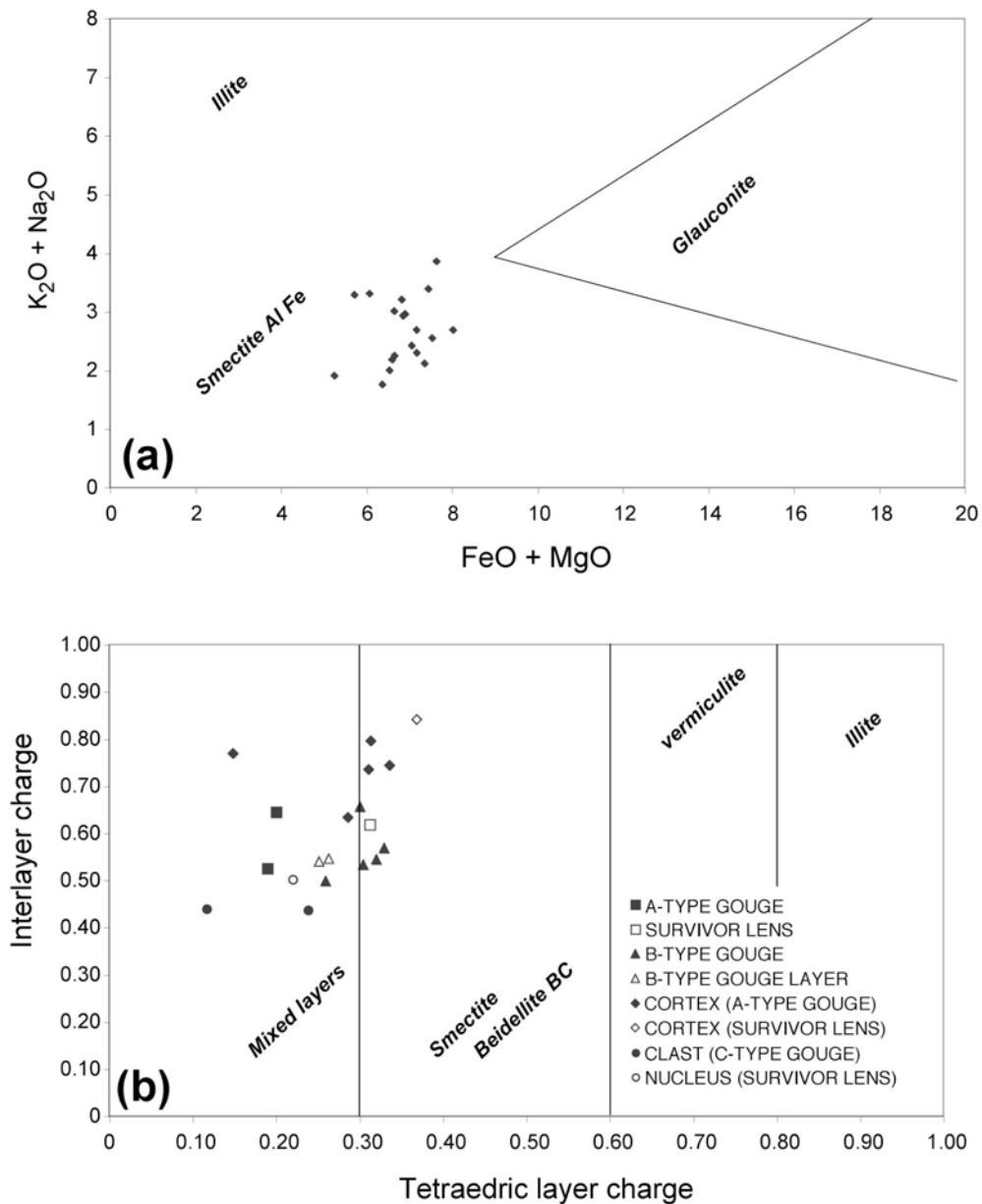


Figure 3.13 - Continued



**Figure 3.14** - Associated SEM images of the sheared gouge for an experiment conducted at 0.9 m/s in wet initial conditions. The gouge layer is limited by the two granite sample boundaries. Shear plane is horizontal and sense of shear is top to the right. Panel (d) is out of the Figure 3.11a, located close to the rotational granite interface (a) General view of gouge microtextures. The upper part concerns the rotational side. (b) First and second aggregate types from the A-type gouge. They display a clast of quartz and a fragment of B-type gouge, both surrounded by a cortex of aggregated clayey material layers. (d) The C-type domain shows an important relief, several sharp cracks and sub-angular clasts of quartz, feldspar and calcite. (c) The upper part of the picture represents the B-type gouge composed of an ultra-fine-grained material. The lower part represents the superimposition of sigmoidal lenses alternating with B-type gouge layers.



**Figure 3.15** - Microprobe data obtained from sheared gouge (run #521). (a) graph showing the prevalence of smectite AlFe. (b) Variation field of tetraedric layer charge for  $Si_4O_{10}$ , with  $Si^{4+}$  substituted by  $Al^{3+}$ . This graph shows the prevalence of mixed-layers and smectite mineral on A- and B-type gouges and cortex of clay-clast aggregates. It should be noted that the beam diameter ranges from 1 to 4  $\mu m$ , which is larger than smectite/illite sheet layer length. This means that the data we obtained from the B-type gouge and the cortex are in fact an "average analyse" of gouge material surrounding the point of analyse.

	Cortex (A-type gouge)	Cortex (A-type gouge)	Cortex (A-type gouge)	Cortex (A-type gouge)	A-type gouge	A-type gouge	B-type gouge	B-type gouge	Cortex (survivor lens)	Survivor lens
FeO	4.18	4.78	4.01	4.21	3.44	4.31	4.91	4.19	4.2	4.2
MgO	2.48	2.76	2.06	2.65	1.81	2.34	3.12	2.98	2.63	2.63
MnO	0.1	0.03	0.02	0.04	0.01	0.01	0.14	0.04	0.11	0.11
CaO	2.14	2.91	2.42	2.59	1.22	1.88	2.42	2.92	1.5	1.5
Na2O	0.09	0.17	0.22	0.18	0.16	0.22	0.3	0.18	0.3	0.3
K2O	2.16	2.38	3.09	2.75	1.75	2.79	2.39	2.51	2.91	2.91
TiO2	0.77	0.51	0.38	0.7	0.52	0.4	0.48	0.9	1.19	1.19
Al2O3	17.11	19.07	16.51	18.72	13.71	17.27	19.51	16.61	17.56	17.56
SiO2	44.03	47.29	47.85	47.19	37.4	47.2	49.69	42.33	44.79	44.79
Total	73.05	79.9	76.55	79.04	60.03	76.43	82.96	72.68	75.19	75.19

	Cortex (A-type gouge)	B-type gouge	Clast (C-type gouge)	Clast (C-type gouge)					
FeO	4.3	4.79	4.1	3.92	4.26	4.38	3.95	3.48	4.6
MgO	2.61	2.57	2.27	2.68	2.92	2.68	2.59	2.24	2.85
MnO	0.01	0.06	0.04	0.13	0.03	0.03	0.08	0.05	0.03
CaO	2.98	1.89	1.83	1.74	1.58	1.52	1.36	0.5	0.71
Na2O	0.19	0.07	0.17	0.2	0.14	0.14	0.1	0.26	0.23
K2O	2.77	2.05	1.59	1.98	2.16	2.28	1.9	3.03	3.16
TiO2	0.61	0.44	0.43	1.01	0.34	0.44	0.32	0.43	0.43
Al2O3	18.86	18.24	16.94	17.34	17.96	17.81	16.19	17.17	20.33
SiO2	47.66	47.24	42.97	42.9	44.42	43.49	41.49	48.01	51.6
Total	80.00	77.34	70.32	71.89	73.81	72.77	67.98	75.16	83.93

**Table 3.4** - Chemical composition of analyzed points in percentage, from the sheared gouge of the run #521.

This second type of elliptical aggregate can be observed in all runs except for the wet runs at 0.09 m/s in wet conditions (Fig. 3.13).

Changing sliding velocities from 0.9 to 1.3 m/s leads to an increase in the size of clay-clast aggregates, which is amplified in wet conditions (Table 3.3), especially for the third and fourth aggregate types. Thus, slip-velocity and water content tend to increase the clay-clast aggregate diameter. However, slip-velocity appears to be the largest controlling effect, as showed by the surface percentage of clay-clast aggregates larger than 50  $\mu\text{m}$  at 0.9 and 1.3 m/s in wet and dry conditions (Table 3.3).

## 2.2. B-type gouge

Located near the gouge-granite interfaces, the B-type gouge is observed in all runs (Fig. 3.13). At the microscope scale, it consists of a fibrous texture of clay minerals, which shows an oblique extinction in polarized light. SEM observations show an homogeneous fabric composed of crystalline fragments lower than 1  $\mu\text{m}$  in diameter (Fig. 3.14c). Preliminary results from EDS analyses (not reported herein) and microprobe analyses show that these fragments consist of quartz, feldspar, calcite, pyrite and clay minerals (Fig ; 3.15; Table 3.4), which is consistent with X-ray analyses done on the initial gouge powder (Fig. 3.4). Microprobe data indicate also that B-type gouge is composed of mixed-layer clay minerals (Fig. 3.15b)

The transition from the B-type gouge to the A-type gouge differs with initial moisture conditions and slip-velocities (Table 3.3):

- Changing sliding velocities from 0.09 to 1.3 m/s in dry conditions leads to the development of stacking lenses of clasts and clay-clast aggregates at the outer rim of the cylinder near the gouge-granite interface of the rotational side (Figs. 3.13a, 3.13b & 3.13c). Each of these lenses are separated by fine layers of B-type gouge which appear to anastomose around them, depicting either shear bands or a S-foliation (Fig. 3.14a). In other places, the transition, underlined by dessication cracks, is done by a continuous layer of fine-grained fragments lower than 5  $\mu\text{m}$ , which can be also present along the wall-gouge granite interface (Fig. 3.13b). These fine-grained layers show locally short and very thin discontinuous layers of B-type gouge.

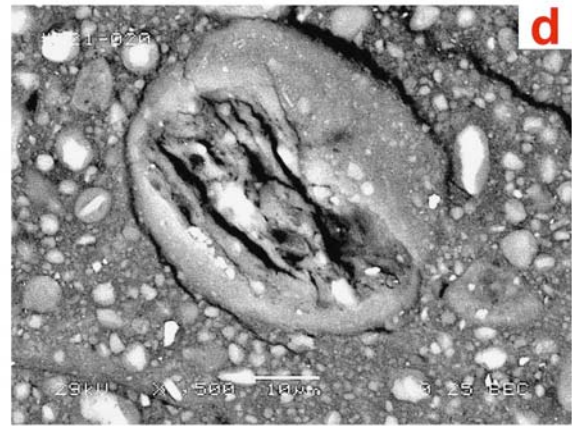
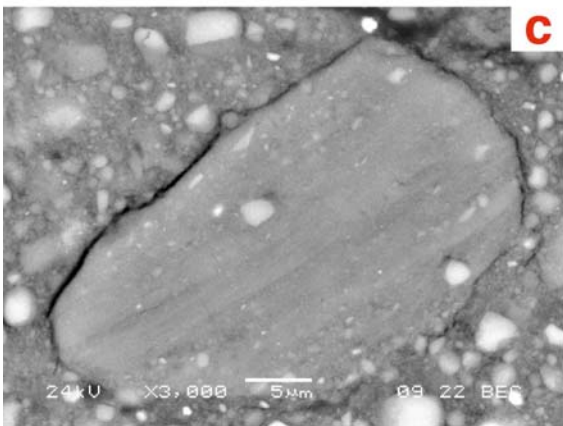
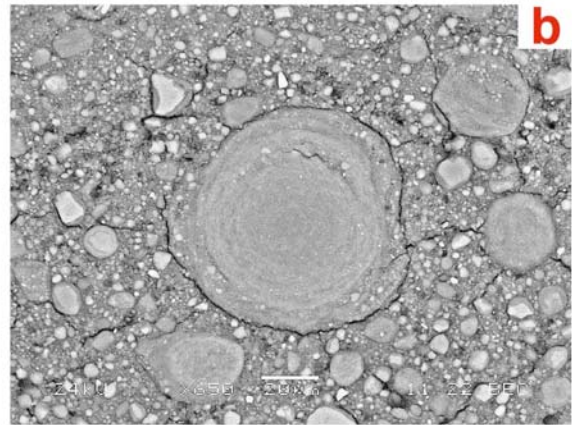
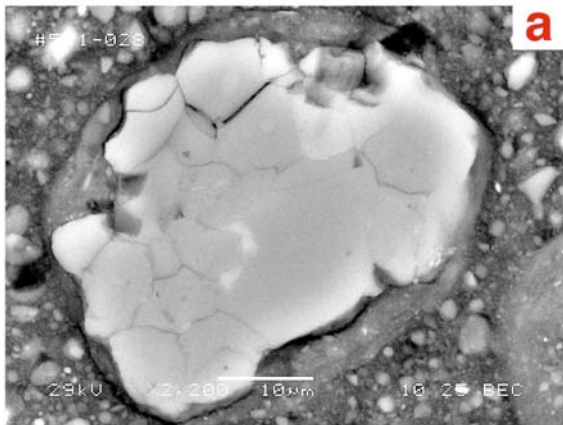


**Figure 3.16** - Clay-clast aggregate types observed in sheared gouge. (a) First type showing a single rounded clast as nucleus, surrounded by a cortex of concentric layers of clay, with very-fine and sparse mineral fragments. (b) Second type showing several concentric layers of clay composed of several fine mineral fragments. (c) Third type showing a large elliptical nucleus with a strong preferred orientation and few scattered ultra-fine mineral fragments, surrounded by a cortex of concentric layers of clay composed of very-fine and sparse mineral fragments. (d) Fourth type showing a large elliptical nucleus with a large central crack rimmed by ultra-fine mineral fragments layers, surrounded by scattered large and fine mineral fragments.

- Changing sliding velocities from 0.9 to 1.3 m/s in wet conditions leads to a significant decrease of lenses and shear bands (Figs. 3.13d, 3.13e & 3.13f). Further examination reveals large stacking sigmoidal lenses increasing in size from the gouge-granite interface of the rotational side towards the center of the simulated fault gouge. These lenses consist of a clay-rich matrix with a random fabric, including uniformly distributed rounded clasts and clay-clast aggregates. Surrounding anastomosed B-type gouge layers do not show any particles larger than 1  $\mu\text{m}$  (Fig. 3.14c). From the rotative gouge-granite interface, transition from a sigmoidal lense to the B-type gouge layer shows a progressive reduction in clast-size, while the contact boundary between the B-type gouge layer and the consecutive sigmoidal lense is sharp, usually underlined by a dessication crack. This *complex shear zone* defines extensional shear bands (Fig. 3.14a).

- At sliding velocities of 0.09 m/s in wet conditions, the transition from the B-type gouge to the A-type gouge is merely defined by a sharp margin (Fig. 3.13d).

### 2.3. C-type gouge

The C-type gouge is found exclusively in wet initial conditions (Figs. 3.13e, 3.13f & 3.14d) and is observed along the interface of the rotational side, essentially in the central part of thin sections (i.e. the central part of the sample assembly). It consists of a matrix of aligned clay minerals in a complex array of variably anastomosing surfaces, with randomly distributed angular clasts of quartz, feldspar or calcite. This scaly fabric does not exhibit any polished or slickensided surfaces, shear zones nor fold hinges. At slip-velocities of 1.3 m/s, a foliated structure at 160° clockwise from the granite interface of the rotational side can be observed in some places.

- At slip velocities of 0.9 m/s and 1.3 m/s, the C-type gouge underlying the B-type gouge layer is bended and thinned.

- At slip velocities of 1.3 m/s, large elliptical clasts of the C-type gouge are locally intercalated with the B-type gouge.

		Clast size	Clay-clast aggregates size ( $\mu\text{m}$ )	Surface percentage (> 50 $\mu\text{m}$ )	Surface percentage (> 100 $\mu\text{m}$ )	Complex shear zone thickness ( $\mu\text{m}$ )	C-Type gouge thickness ( $\mu\text{m}$ )
1.3 m/s	wet	5 (50)	130 (300)	40	10	30 (100)	50 (350)
	dry	5 (45)	70 (250)	40	1	30 (200)	absent
0.9 m/s	wet	5 (50)	50 (250)	5	1	120 (200)	200 (300)
	dry	1 (50)	40 (200)	5	1	20 (50)	absent
0.09 m/s	wet	-	-	-	0	10 (30)	absent
	dry	5 (80)	30 (100)	1	0	50 (80)	absent

**Table 3.3** - Summary of post-experiment gouge characteristics as a function of experimental conditions, for a cross-sectional area of  $\sim 19.8 \text{ mm}^2$ . Note that each reported value is a mean value of all corresponding experiments. Numbers in parentheses correspond to the maximum measured thickness (thickness of microstructures is maximum at the outer part of the cylinders). Dashes indicate that observation was not possible because of the difficulty of thin sectioning process.

## C. Discussion

### 1. Interpretation

#### 1.1. Mechanical behavior

The best-linear fit lines of initial friction and residual friction data do not have the same intercept values at zero normal stress (see equation 1.1; Fig. 3.10). However, these values fall in the range of previously reported values for clay-bearing gouge, that is from 0.02 to 0.51 MPa (see II.3). This suggests that the frictional properties of the clay gouge at high slip-velocities obey the classical frictional law (Coulomb-Mohr equation), with cohesion values interpreted to result from Teflon® friction.

Figure 3.10 shows that the friction coefficient values at the initial and residual states (determined by the best-linear fit lines) are always larger in dry conditions than in wet conditions. This means that frictional strength of simulated faults is controlled by initial moisture conditions.

On Figure 3.10, the experimental data suggest that the shear stress is sensitive to normal stress for initial frictions except in dry conditions, and weakly sensitive to normal stress for residual frictions especially for wet conditions. Additionally, all the best-linear fit lines for residual friction lay below Byerlee's frictional law (except at 0.09 m/s in dry conditions). These results suggest the existence of a dynamic moisture-related weakening mechanism that lowers fault frictional strength at the residual friction (see I.C.2).

All the high velocity experiments show a dramatic decrease of the fault frictional strength with increasing displacement, which is consistent with the decrease in gouge frictional strength reported by Mizoguchi et al. (2006, 2007). This slip-weakening, which plays a key role in determining the degree of fault instabilities, occurs over the slip-weakening distance  $d_c$  (see equation 1.14). In our experiments,  $d_c$  is always larger in wet initial conditions, whatever the slip-velocity and the normal stress (Fig. 3.11; Table 3.2). This results suggest that water content controls the efficiency of the slip-weakening mechanism (Fig. 3.12).

In our experiments, changing sliding velocities from 0.09 to 1.3 m/s leads to an increase of  $d_c$ , which is significantly enhanced in wet initial conditions (Figs 3.9 & 3.11). This

result attests the control of slip-velocity and water content on the efficiency of the moisture-related slip-weakening mechanism that occurs during laboratory friction experiments.

Mizoguchi (2004) conducted dry friction experiments on clay gouge from the Nojima fault (Japan). For slip-velocities of 1.03 m/s and at a normal stress of 0.62 MPa, the peak friction coefficient values he obtained vary between 0.66 and 1.08, the steady-state friction coefficient values range from 0.16 to 0.38, and the slip-weakening distance values vary between 26.7 and 40.1 m. In our experiments, at 1.3 m/s and 0.6 MPa in dry conditions, the peak friction coefficient values we obtained range from 1.15 to 1.31, the steady-state friction coefficient values vary between 0.29 and 0.33, and the slip-weakening distance values range around 7.2 m. Considering that changing sliding velocities from 0.9 to 1.3 m/s leads to an increase of  $\mu_p$ , to a decrease of  $\mu_{ss}$  and to an increase of  $d_c$  (Fig. 3.9), our results appear to be consistent with the previously reported data of Mizoguchi (2004). Besides, even if  $d_c$  obtained in our experiments (0.4 to 35 m) is larger than that of seismically determined (0.01 to 1 m), considering the normal stress dependence observed in the experiments (Fig. 3.11), our experimental slip-weakening distances approach the same order of magnitude as the seismological  $D_c$ .

As for the sawtooth frictional behavior observed at 0.09 m/s in our experiments, it is similar to the one observed by Mizoguchi (2004) at 0.006 m/s in dry conditions. Meanwhile, additional experiments need to be addressed to propose a clear explanation that accounts for this frictional behavior.

## 1.2. Development of microstructures

Table 3.3 shows that whatever slip-velocities or initial moisture conditions, the final size of the rounded clasts contained within the A-type gouge remains similar. This implies that the reduction in size of initial gouge fragments is neither slip-velocity dependent nor water-content dependent.

Changing sliding velocities from 0.09 m/s to 1.3 m/s leads to an increase in clay-clast aggregate diameter regardless of the clay-clast aggregate type. This result is enhanced in wet initial conditions (Table 3.3). This suggests that water content and slip-velocity effects do not imply the same processes in the clay-clast aggregate formation. Changing sliding velocities from 0.9 to 1.3 m/s leads to an expansion of the complex shear zone thickness (composed of B-type gouge layers) in dry initial conditions, whereas it leads to the reduction in thickness of

both the complex shear zone and the C-type gouge in wet initial conditions (Table 3.3). This suggests that the development of the complex shear zone is disturbed by the presence of C-type gouge. The large elliptical clasts of C-type gouge locally intercalated within the B-type gouge at 1.3 m/s in wet initial conditions allows this interpretation.

The B-type gouge layers obtained under wet or dry conditions do not show any amorphous material in polarized light, do not show any increase in irregularity of rock boundaries with sliding velocity, neither reveal injected material into the lower side of host rock cylinders, nor show any flow structure. In addition, preliminary results from microprobe analyses show that B-type gouge consists of quartz, feldspar, calcite, pyrite and clay minerals. And SEM observations does not reveal any interstitial glass. These results suggest that, contrarily to Di Toro et al. (2004) no amorphous silica gel was formed during frictional sliding. This means that the homogeneous texture of the B-type gouge does not result from frictional melting processes.

## 2. Comparison of experimental results with reported laboratory and natural fault gouge microstructure studies

Our high velocity friction experiments allow to produce three main types of microtextures. Two types are comparable to microstructures observed in experimental or natural fault gouges:

- Reported as "soft aggregates", spherical aggregates lower than 100  $\mu\text{m}$  of diameter, composed exclusively of clay and possibly with other minerals such as quartz, have been previously observed in laboratory conditions by Moore et al. (1989) as the product of triaxial friction experiments on illite-rich gouges, conducted at low slip-rates and high temperatures for small slip displacements. Clay-clast aggregates were interpreted as resulting from frictional sliding process.

- An amorphous texture of a continuous layer has been reported by Yund et al. (1990) from frictional sliding experiments conducted on ground surface of granite, at low slip-rates for small slip displacements. This amorphous texture was thought to be constituted by 10 nm-thick crystalline particles, as the result of comminution process rather than by melting.

- Defined as a "deformation zone", an extremely fine-grained layer exhibiting a foliated texture from the strong reorientation of platy clay minerals parallel to the shear direction was also observed by Mizoguchi (2004), on the run products of gouge rotary-shear

experiments, conducted at high slip-rates for large slip displacements. This layer was interpreted to result from localized intense particle size reduction by comminution.

- Defined as "snowballed smectite rims", clay-clast aggregates have been reported by Warr & Cox (2001) from examination of the Alpine fault gouge (New Zealand). The aggregates were composed of a sub-rounded clast of quartz surrounded by compact smectite layers. They were interpreted as resulting from granular flow process (i.e. two-phase flow consisting of clay-clast aggregates as particulates and clay gouge matrix as interstitial fluid).

- Clay-clast aggregates and similar "deformation zones" were also observed by Mizoguchi on the natural gouge of an exposure of the Nojima fault (2004; personal communication, 2006).

Therefore, from microstructural studies on laboratory and natural fault gouges, it appears that the clay-clast aggregates and the B-type gouge are the product of cataclasis through frictional sliding processes. The absence of any melting surface or interstitial glass, from optical & SEM observations and XRD analyses within the post-experiment gouge, suggests that the heat generated through clast comminution did not exceed the amount of heat loss by the system for the highest reached strain rate ( $\sim 10^3$  /s at the outer rim of cylinders at 1.3 m/s). The strong foliation that exhibits the B-type gouge likely results from a passive re-alignment of platy clay particles during shearing. The apparent lack of C-type gouge in natural SSZ gouge may be the result of subsequent clay mineral transformations due to hydrothermal reactions (Rutter et al., 1986; Vrolijk, 1999). Another explanation might be related to the configuration of the experiment, with a C-type gouge interpreted as a portion of the early gouge material stucked at the granite interface, and isolated from the overall gouge matrix by the development of the B-type gouge. Hence, clay-clast aggregates and B-type gouge appear to be related to abrasive wear mechanism (Rabinowicz, 1965; Scholz, 1988b), with water content and slip-velocity as controlling parameters.

The microstructures resulting from gouge friction experiments at coseismic slip-rates are similar to those observed from seismogenic faults. This suggests first a good reliability of the laboratory experiments with natural deformation mechanisms that occur during earthquakes, and secondly that clay-clast aggregates represent potential evidence for past seismic fault sliding, as pseudotachylytes are considered.

### 3. Timing apparition of the experimental microstructures at seismic slip-rates

Previous laboratory works on granular shear zones indicate that in the first millimeters of shear displacement, dilatancy takes place first by loosening the interlocking of densely packed grains accounting for clast flaking, transgranular fracturing and distributed microcracking (Rawling & Goodwin, 2003), and then by initiating the deformation of a narrow shear band of uniform width (Mandl et al., 1977; Marone, 1998b). Grain rolling (i.e. erratic dynamic rotation) and grain sliding (i.e. slippage at the grain boundary contacts) increase abrasion of larger clasts and increase the relative content of finer clasts. These two mechanisms are assumed to come along with dilatancy. However, according to Mair & Marone (2000) and Mair et al. (2002), rolling mechanism is effective only once clasts dominate with a subangular shape. This result suggests that it is only after the initiation of this rolling process that survivor clasts distributed throughout the entire gouge layer can be individually wrapped by the successive concentric layers of clay (Figs. 3.16a & 3.16b). Wrapping process reduces clast fracturing (Fig. 3.14b) and the subsequent size reduction by lowering intense stress contact at the boundaries (Mandl et al., 1977). This process leads to increase the proportion of rounded clasts (i.e. clay-clast aggregates) within the gouge with increasing displacement. Strain is then progressively accommodated by rolling, which reduces the overall bulk frictional strength of the gouge (Mair et al., 2002).

The water content dependence of clay-clast aggregate diameter (Table 3.3) suggests that the quantity and quality of contacts between consecutive concentric clay layers of aggregate cortex are due to adhesion forces, related to purely elastic contacts (Rice, 1976; Michalske & Fuller, 1985) or capillary bridging (Iwamatsu & Horii, 1996; Morrow et al., 2000; Jones et al., 2002; Moore & Lockner, 2004b). The slip-velocity dependence of clay-clast aggregate diameter, particularly observed for the third and fourth types when changing sliding velocities from 0.9 to 1.3 m/s, could be merely associated with the multiplication of grabbed B-type fragments as nuclei. Thus, the efficiency of rolling mechanism does depend on initial gouge water content and slip-velocity.

In the first increments of sliding displacement of sheared argillaceous sediments, clay particles suitably oriented close to the plane of maximum shear strain start to slip once the applied stress overcomes the inter-particle friction, which with increasing displacement leads to the development of discrete slipping zones (Maltman, 1987). This suggests that the discrete  $\mu\text{m}$ -wide B-type layers observed throughout the continuous fine-grained layers can be interpreted as the early stage structure of the complex shear zone formation. Besides,

changing sliding velocities from 0.09 to 1.3 m/s leads to increase the thickness of the complex shear zone (Table 3.3). This suggests that, to accommodate high strain rates, the complex shear zone expands at the expense of the A-type gouge, isolating several portions of the A-type matrix located along wall-gouge interfaces as survivor lenses.

According to Maltman (1987), the ability of clay particles to rotate into the plane of maximum shear strain is greater in high water content gouge. This suggests that the complex shear zone thickness is larger in wet initial conditions than in dry initial conditions. The opposite results obtained at 0.9 and 1.3 m/s (Table 3.3) agree with the interpretation that the complex shear zone development was disturbed during experiments.

At the microscope scale, the narrow B-type gouge layers show a high degree of phyllosilicate reorientation with a well-developed shear band fabric. This means that intense shearing related to large displacement and quasi-infinite shear strain has been locally accommodated by sliding along phyllosilicate slip interfaces (Shea & Kronenberg, 1993; Vannucchi et al., 2003).

In summary, observations of post-experiment microstructures suggest that from initial cataclasis, two deformation regimes occurred during sliding shear, favored by initial wet conditions and high slip-rates: a rolling regime for which strain is accommodated by granular flow with rounded clasts and formation of clay-clast aggregates, and a sliding regime for which strain is accommodated by sliding at particle slip surfaces within  $\mu\text{m}$ -wide B-type gouge layers and formation of a complex shear zone located at the gouge-granite interface of the rotational side. These results are consistent with Mair & Marone (2000) who indicate that shearing deformation is accommodated by a combination of "rolling" and "sliding" mechanisms at low normal stress ( $< 5 \text{ MPa}$ ) and seismic slip-rates.

#### 4. Correlation of microstructures with slip-weakening behavior

The frictional strength of a granular material containing clay particles depends on the volume ratio of plate-like particles to rounded particles (Lupini et al., 1981): a high coefficient of inter-particle friction with no orientation of clay particles implies a rolling regime (reported as "turbulent flow"), while a low coefficient of interparticle friction with a strong orientation of clay particles implies a sliding regime (reported as "sliding behavior"). All the representative mechanical behavior of the simulated faults show a dramatic decrease of the fault frictional strength with increasing displacement (Fig. 3.8). This frictional behavior

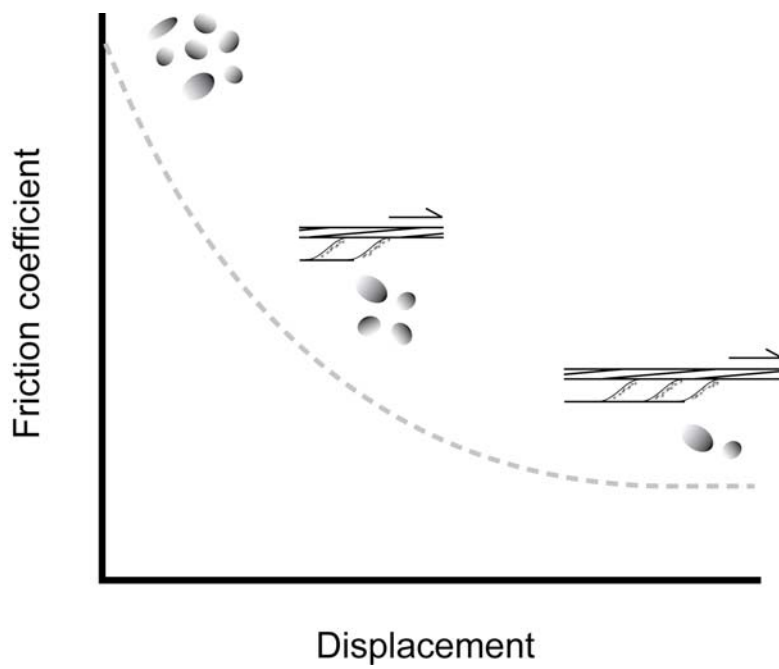


**Figure 3.17** - Possible influence of the rolling regime (illustrated by clay-clast aggregates) and the sliding regime (illustrated by a complex shear zone) on gouge frictional properties, with proportion of grain rolling to grain sliding that decreases with increasing displacement.

suggests firstly that the proportion of grain rolling to grain sliding should decrease with increasing displacement during conducted friction experiments, and secondly that the sliding regime should overtake the rolling regime at the residual friction stage (Fig. 3.17). Therefore, the discrete B-type layers observed along the continuous fine-grained layers do correspond to discrete planes of high shear stress, localizing gradually the slip and decreasing the coefficient of interparticle friction. Subsequent displacement should improve the sliding regime with the complex shear zone development along granite interfaces. And the observed B-type fragments present as nuclei within clay-clast aggregates (Figs. 3.16c & 3.16d) are interpreted to result from wrenching of B-type gouge during the rolling regime stage, after the development of the complex shear zone. This suggests that the rolling regime and the sliding regime coexist at some point during the slip-weakening.

Initial wet conditions and high slip-rates favor the development of clay-clast aggregates, which reduce the overall bulk frictional strength of the simulated faults during the first meters of slip displacement. But in the same time, water content impedes the efficiency of the moisture-related weakening mechanism. These results suggest that in presence of water, extensive development of clay-clast aggregates during the first meters of slip displacement might reduce the heat production rate that is required to break liquid capillary bridge and to drain off moisture at contact area of gouge particles. It follows a retrain of the thermally-activated moisture-related weakening mechanism (Mizoguchi et al., 2006) and a delay of the sliding regime arrival at the frictional steady-state.

## **D. Conclusions**

Considering the normal stress dependence observed in our experiments, all the high velocity experiments show a slip-weakening behavior for a slip-weakening distance that approaches the same order of magnitude as seismological  $D_c$ . Experimental data show that, whatever initial moisture conditions, changing sliding velocity from 0.09 to 1.3 m/s leads to an increase of  $\mu_p$ , to a decrease of  $\mu_{ss}$  and to an increase of  $d_c$ , and that changing water content from dry to wet initial conditions leads to a decrease of  $\mu_p$ , to a decrease of  $\mu_{ss}$  and to an increase of  $d_c$ .

Two main types of microstructures similar to those observed from seismogenic faults can be distinguished at the residual friction stage within sheared gouge layers for all

experiments. The sequence of their development implies two distinct cataclastic processes that coexist at some point during slip-weakening: a sliding regime that follows an initial rolling regime. The observed slip-weakening behavior of simulated faults is related to a decrease of the proportion of grain rolling to grain sliding with increasing displacement. The extensive development of clay-clast aggregates, that is controlled by water content and slip-velocity, might reduce the heat production rate during shearing, which could impede the efficiency of the thermally-activated moisture-drained weakening mechanism.

Our laboratory friction data are relevant to be incorporated into any model to calculate the instantaneous heat production rate during frictional sliding, in order to reconstruct past seismic faulting.

## **CHAPTER IV**

**Numerical analyses: thermal pressurization mechanism and  
frictional heating process at seismic slip-rates**

## A. Thermal pressurization mechanism

### 1. Numerical analysis of thermal pressurization during shearing

#### 1.1. General considerations

The basic condition for thermal pressurization to occur in a slip zone is that the hydraulic diffusion length  $d_h$  of the constitutive material be significantly smaller than the half-width  $w/2$  of the heated zone. The hydraulic diffusion length, which can also be defined as the distance of propagation of a fluid pressure from a source at time  $t$ , can be related to the hydraulic diffusivity by the equation (Lachenbruch, 1980):

$$d_{h(t)} = (4 \times D_h \times t)^{1/2} \quad (4.1)$$

The hydraulic diffusivity,  $D_h$ , depends on the permeability,  $k$ , and the storage capacity per unit sample volume,  $\beta_c$ , of the material constituting the fault zone and on the fluid viscosity,  $\eta$ , according to the equation:

$$D_h = \frac{k}{\eta \times \beta_c} \quad (4.2)$$

The values of  $k$  at a given effective pressure  $P_e$  can be derived by using the equations relating  $k$  and  $P_e$  obtained by best-fit trends (see II.B.1.2.3; Figure 2.22). The storage capacity per unit sample volume  $\beta_c$  is related to the porosity  $n$  of the material, to the compressibilities  $\beta_f$  of the fluid and  $\beta_s$  of the mineral grains, and to the sample bulk framework compressibility  $\beta_b$  by the following equation:

$$\beta_c = n \times (\beta_f - \beta_s) + (\beta_b - \beta_s) \quad (4.3)$$

The compressibilities of liquid water (Table 4.1) and mica ( $1.2 \times 10^{-11} \text{ Pa}^{-1}$ ) will be taken for  $\beta_f$  and for  $\beta_s$  respectively. The values of  $\beta_b$  for different effective pressures  $P_e$  were derived by finding the volume change per unit confining pressure decrease and dividing this

change by the sample volume at the start of the confining pressure step (see details in Wibberley, 2002). The calculated  $\beta_b$  are then plotted as a function of  $P_e$  and a linear extrapolation is made in order to obtain equations relating theoretical  $\beta_b$  values to  $P_e$  for each sample (Fig. 4.1). These equations are of the form:

$$\beta_b = \beta_0 \times \exp[-\chi \times (P_e - P_0)] \quad (4.4)$$

where  $\beta_0$  is a compressibility at a reference pressure  $P_0$  here fixed at zero. More precisely, for the decreasing confining pressure paths (decreasing effective pressure), the equations in Figure 4.1 derived from best-fit trends will be used in the modelling to calculate compressibility values from given  $P_e$  values.

## 1.2. Choice of parameters

In addition to physical constants given in Table 4.1, the following parameters are needed for the modelling: porosity and permeability, fault zone thickness and depth of deformation.

Ideally, the permeability values to be used for modelling should be the ones corresponding to samples oriented perpendicularly to the slip zones. However, as stated above, the data obtained on samples with that ideal orientation are incomplete. The most complete dataset corresponds to samples oriented vertically, i.e. parallel to the slip zones and perpendicular to the striation ( $// \perp$  orientations). Representative samples for each zone are sample 4 (PSZ gouge), 25 (PSZ marginal fine breccia) and sample 32 (SSZ-1 gouge). For each sample, the porosity and permeability at a given effective confining pressure  $P_e$  will be calculated by using the equations corresponding to these samples as determined above.

Although the most complete dataset collected corresponds to samples cored in the  $// \perp$  orientation, in the case of clay gouges, these data show permeabilities one to three orders of magnitude higher than the  $\perp \perp$  samples. Hence the best-fit equation, based on data from the  $// \perp$  direction, will overestimate the permeability perpendicular to the foliation, which is the suitable direction of fluid pressure dissipation from the heated slip zone towards adjacent high permeable breccia. We therefore selected gouges in the centre of the slip zones (#4, #32) as the most representative ones, and reduced their permeability values by one order of magnitude

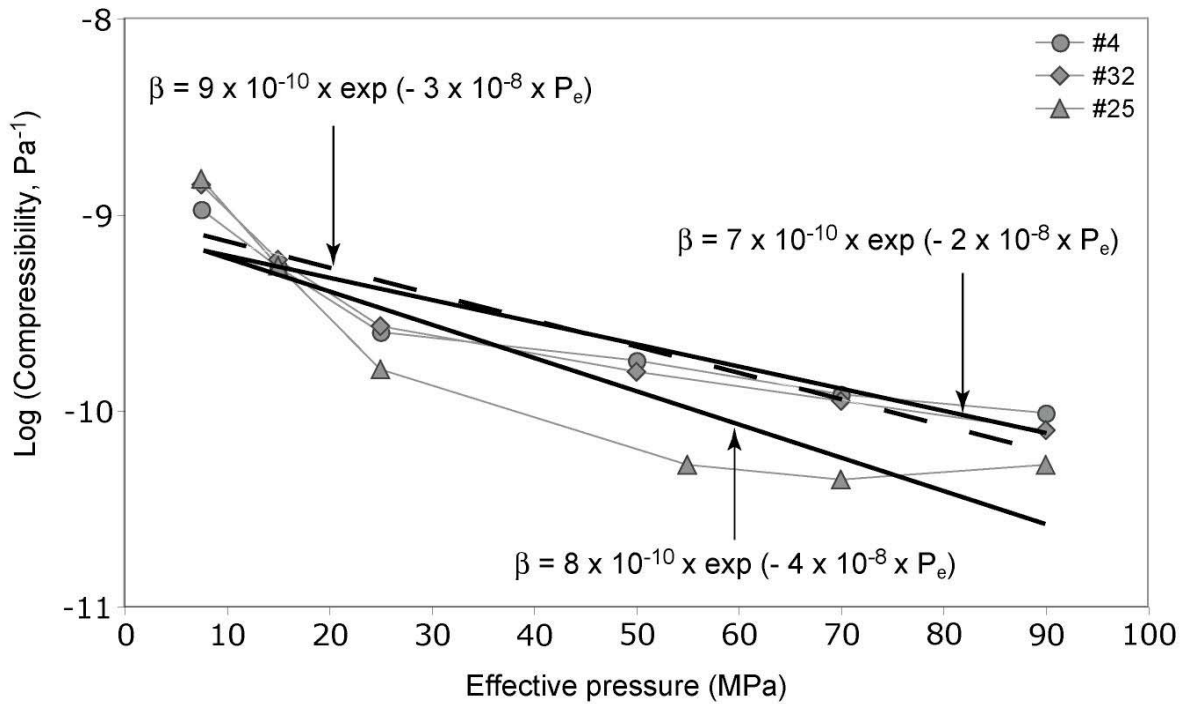


**Figure 4.1** - Calculated sample bulk framework compressibility  $\beta_b$  as a function of the effective confining pressure  $P_e$  and best-fit equations (continuous and dashed lines) for the three samples representative of PSZ gouge (4), SSZ-1 central gouge (32) and PSZ marginal fine breccia (25) of the exposure A. In the equations,  $P_e$  is expressed in MPa.

Water expansivity	$\alpha_w$	0.0015	1 / K
Water specific heat capacity	c	1000	J / kg / K
Water compressibility	$\beta_w$	$4.3 \times 10^{-10}$	1 / Pa

**Table 4.1** - Water properties used in the thermal pressurization modelling.

for the modeling in order to account for this anisotropy. For the breccia permeabilities, we chose an average permeability trend.

The equations relating  $P_e$  to  $n$ ,  $k$  or  $\beta_b$  were obtained by best-fitting of experimental data pertaining to the deconfining path (decrease of  $P_e$  from 100 MPa to 10 MPa; Figs. 2.20, 2.22 & 4.1), as described above, in order to simulate effective pressure decrease. We assume the effective pressure law in its simplest form in order to model pore fluid pressure increase, corresponding to the phenomenon expected to occur during thermal pressurization.

The thickness of the fault zone, either gouge or breccia, is another parameter which needs to be taken into consideration. The values used for the PSZ and SSZ-1 gouges are average values derived from direct measurements carried out on the outcrop (Fig. 2.8). They are 80 mm for the PSZ central gouge and 56 mm for SSZ-1 central gouge. The thickness of the marginal fine breccia is difficult to measure with accuracy on the outcrop because the limits between this breccia and the surrounding coarse breccia are unclear. Estimates range from 50 to 700 mm. In order to test the possible effects of a rupture propagating from the PSZ into the marginal fine breccia, modelling of breccia pressurization will be done for a 50 mm thick zone, which may correspond to a mean thickness of the zone supposed to accommodate the slip.

The 2000 Tottori earthquake, whose hypocentral depth is estimated at 10 - 15 km (Semmane et al., 2005) can be considered as a representative event of the Chugoku region. Modelling of strong motion displacement records and GPS coseismic data reveal two areas of large slip amplitudes: a shallow one, between 0 and 2 km, and a deeper one, between 4 and 6 km (Semmane et al., 2005). The thermal pressurization process will be tested at 6 km, that is the depth at which the rupture propagating upward from depth starts to induce a significant amount of slip.

### 1.3. Modelling approach of thermal pressurization analysis

Our modelling assumes a planar slip zone (thickness  $2w$ ) of finite hydraulic diffusivity,  $D_h$ , surrounded by a material of infinite hydraulic diffusivity, so that the fluid pressure can be assumed to remain hydrostatic at all times at the limits of the shear zone. Our second assumption is to ignore the effect of heat loss, justified because for typical thermal diffusivities, the thermal diffusion length scale is much smaller than the thickness of the gouge central slip zone (Lachenbruch, 1980; Mase & Smith, 1987). A third assumption is that

dilatancy does not occur in the slip zone: for poroelastic dilatancy to occur during pore fluid pressure rises, the low matrix compressibility in comparison to that of water will inhibit dilatancy (Wibberley, 2002); for shear dilatancy, dilatancy angles measured in clay materials are typically very small, and dilatancy in coarse granular materials decreases to zero at shear strains of about 0.1 - 0.5 (e.g. Mandl et al., 1977), i.e. after only a small amount of the total shear strain suffered during seismic slip on a narrow zone.

The modelling approach balances the rate of fluid pressure increase by frictional heating with the rate of fluid pressure decrease by excess pressure dissipation, to determine the net change in fluid pressure through time. The rate of frictional heating ( $dT/dt$ ) of the pore water in the slip zone is determined by the shear stress,  $\tau$ , the relative slip-velocity,  $2V$ , (assumed constant in this modelling at 0.5 m/s) and the width of the shear zone, assuming that all the frictional work is transformed into heat:

$$\frac{dT}{dt} = \frac{\tau \times V}{\rho \times c \times w} \quad (4.5)$$

where  $\tau = \mu \times (\sigma_n - P_{(t)})$ ,  $\rho$  is the density of the material (assumed to be constant at 2500 kg/m<sup>3</sup>),  $c$  is the specific heat capacity (assumed to be constant at 1000 J/kg/K),  $\mu$  is the coefficient of friction (assumed to remain constant at 0.4),  $\sigma_n$  is the normal stress (assumed to equal the overburden pressure) and  $P$  is the fluid pressure in the slip zone. Starting with the "undrained" extreme case of no fluid escape, the water pressure will rise at a rate related to the thermal expansivity of the gouge,  $\alpha$ , and the storage capacity per unit sample volume,  $\beta_c$ :

$$\frac{d\Delta P}{dt} = \frac{\alpha}{\beta_c} \times \frac{dT}{dt} = \frac{\alpha}{\beta_c} \times \frac{\mu \times (\sigma_n - P_{(t)}) \times V}{\rho \times c \times w} \quad (4.6)$$

where  $\alpha = [n \times \alpha_w + (1 - n) \times \alpha_m - \alpha_s]$ ,  $n$  is the porosity of the material (see II.B.1.2.2),  $\alpha_w$  is the thermal expansivity of water assumed to be constant (Table 4.1),  $\alpha_m$  is the mineral thermal expansivity (assumed to be constant at  $2 \times 10^{-5}$  /K),  $\alpha_s$  is the porous medium thermal expansivity (assumed to be constant at  $1 \times 10^{-5}$  /K).

Following classical solutions for heat diffusion as an analogue for fluid pressure diffusion (Carslaw & Jaeger, 1959), the rate of fluid pressure dissipation in the centre of the shear zone can be estimated as:

$$\frac{d\Delta P}{dt} = -D_h \times \Delta P \times \left(\frac{\pi}{2w}\right)^2 \times e^{-D_h \times \left(\frac{\pi}{2w}\right)^2 \times t} \quad (4.7)$$

The rate of thermal pressurization is the difference between the rate of pressure build-up due to frictional heating and the rate of pressure dissipation due to fluid flow and is obtained by subtracting equation 4.7 from equation 4.6. Integration of the result with respect to time allows calculation of the fluid pressure evolution. Note that the rate of thermal pressurization depends upon the actual excess fluid pressure at any one point in time (equation 4.7), and hence the effective normal stress. As thermal pressurization occurs, the effective normal stress will decrease; hence the rate of frictional heating will decrease (equation 4.5). The fluid pressure can therefore never exceed lithostatic pressure in the model.

The modelling calculates, as a function of time, the increase of pore fluid pressure inside a slip zone of given width due to coseismic frictional heating of the pore fluid in the gouge zone, and the corresponding shear stress evolution through time, assuming Amonton law with the effective normal stress being the difference between normal stress and fluid pressure. Thermal pressurization is considered to be fully efficient in the cases for which the effective normal stress is reduced to zero in a short span of time (of the same order as the earthquake duration).

## 2. Results

We calculate the evolution through time of the shear stress expected for three representative rock types of the Usukidani fault: PSZ central gouge (sample number 4), SSZ-1 central gouge (sample 32) and PSZ marginal fine fault breccia (sample 25) at depths of 6 km (Fig. 4.2).

Thermal pressurization appears to be efficient for the two PSZ and SSZ-1 gouges, and dynamic stress drop is predicted to occur to 1/e of its initial value over timescales of the order of one second. For small widths, for instance of 5 mm (Fig. 4.3), the thermal pressurization is less efficient, yet the dynamic shear stress is nevertheless reduced by one order of magnitude, although it does not reach zero.

Unlike the PSZ or SSZ-1 gouges, the hydraulic properties of the PSZ marginal breccia do not allow the pore fluid pressure to rise sufficiently to counteract the normal stress, at least for the 50 mm thickness used in the modelling (Fig. 4.2b). For larger thicknesses (1 m or

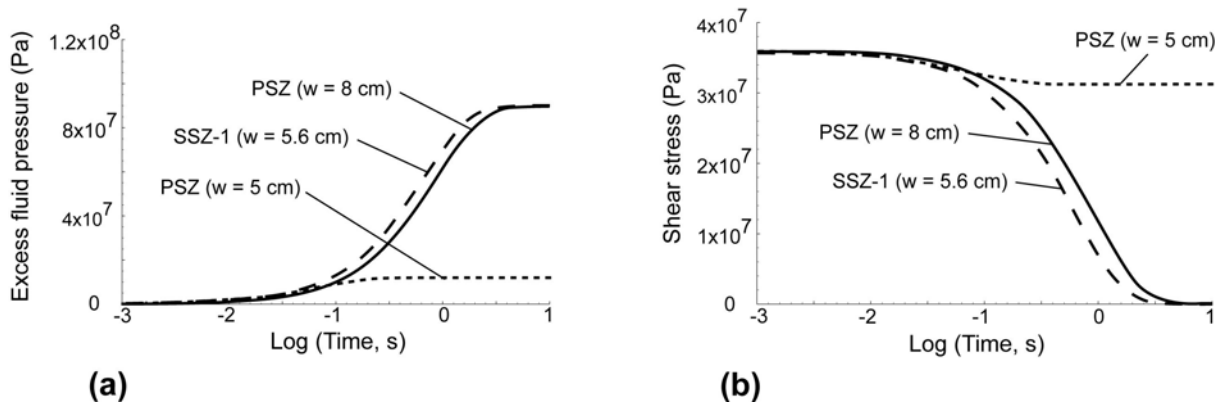


**Figure 4.2** - Results of modelling of the thermal pressurization process for gouge or breccia showing the effects of frictional heating during seismic slip at a depth of 6 km, for respectively PSZ gouge ( $w = 8$  cm), SSZ-1 gouge ( $w = 5.6$  cm), PSZ marginal fine fault breccia ( $w$  estimated at 5 cm). (a) predicted fluid pressure against time. (b) corresponding shear stress variation with time.

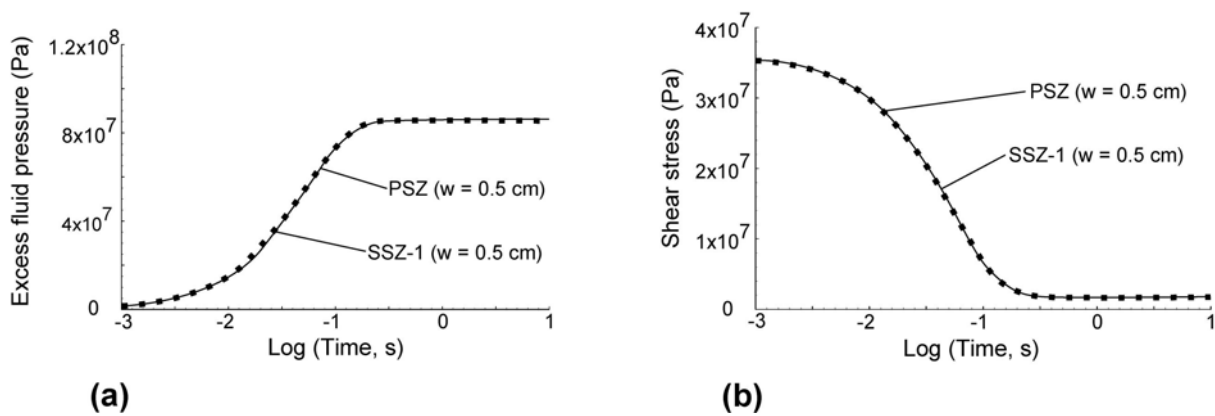


**Figure 4.3** - Same as Figure 4.2 for a 0.5 cm thickness value of PSZ and SSZ-1 gouge zones.

more), the effective normal stress (and hence shear stress) would decrease to zero, but only after significantly longer periods of time than typical earthquake slip durations.

Calculations carried out on the same samples with the same thicknesses at a depth of 4 km show that thermal pressurization is less efficient than at 6 km. In particular, the pore pressure rise for the PSZ and SSZ-1 gouges is not sufficient to counteract the normal stress. Conversely, at a depth of 8 km, if thermal pressurization does still not occur for the marginal breccia samples, it becomes efficient for the thin PSZ and SSZ-1 gouges.

### 3. Discussion

#### 3.1. Efficiency of the thermal pressurization

Previous investigations of the thermal pressurization process as a slip-weakening mechanism have shown that it is highly affected by several factors such as the slip-rate, the depth and the width of the deformation zone (Andrews, 2002; Noda & Shimamoto, 2005; Wibberley & Shimamoto, 2005). The slip-rate determines the rate of frictional heating and the rate of fluid pressure build-up. However, in order to compare the different modelling cases, the relative sliding velocity in our models is fixed at 0.5 m/s, which is in the range of seismological studies (Scholz, 2002).

The depth determines the hydraulic transport properties and controls the normal stress. Calculations performed for parameters appropriate to a depth of 6 km yielded estimates for the amount of shear stress drop on the fault of around 36 MPa for both the PSZ and the SSZ-1 for fully effective thermal pressurization (Figs. 4.2a & 4.2b), slightly larger (half an order of magnitude) than that considered typical for large earthquakes (in the order of 10 MPa). When the microbreccia properties are used as the parameters in the thermal pressurization modeling, pressurization and consequent shear stress drop occur to a much lesser extent, and over much longer time scales, than those compatible with significant coseismic stress drop. This difference in hydrodynamical behaviour is directly related to the contrast in material hydraulic properties, which depends on the clast-size supported framework, clast-size distribution and amount of clay.

The width of the slip zone controls the rate of frictional heating and the rate of thermal pressurization. Calculations carried out on the same samples for different deformation zone widths show that thermal pressurization is not effective for  $w < 1$  mm (see the representative

cases for PSZ and SSZ-1 on Fig. 4.3a & 4.3b), which implies that the half-width of the slip zone is lower than the hydraulic diffusion length (Lachenbruch, 1980), and that pressurized fluid loss can no longer be neglected. This suggests that the variation in slip zone width can lead to an important heterogeneity in fluid pressure distribution along the fault, which could result in critical variations in the degree and rate of slip-weakening, and hence could dramatically affect the way in which thermal pressurization progresses, influencing the dynamic fault motion (Wibberley & Shimamoto, 2005).

### 3.2. Rupture path

A fault is expected to be less stable for a small slip-weakening distance  $D_c$  (Scholz, 2002), which is seismically estimated between 0.01 and 1 m (Ide & Takeo, 1997; Fukuyama et al., 2003b). This implies that earthquake instabilities should appear for a slip-weakening duration between 0.02 and 2 seconds if we assume a constant slip-velocity of 0.5 m/s. The numerical analyses presented in this paper suggest that thermal pressurization would lead to a stress drop on PSZ or SSZ-1 to 1/e of its initial value over time scales of the order of one second, this timescale being consistent with seismological data.

The results of our modelling predict fault stress drops and slip-weakening durations in broad agreement with seismological studies. Based on a constant slip-rate and constant mean width values of the gouge zones (80 mm for PSZ central gouge, and 56 mm for SSZ-1 central gouge), our numerical analyses suggest that the thermal pressurization should be effective at 6 km depth, regardless of the path (PSZ or SSZ-1) followed by the rupture. However, rupture branching off these zones into adjacent high-permeability fine breccia will lead to fluid pressure decrease and inhibition of thermal pressurization as a slip-weakening process (as must have once happened when SSZ-1 was initially generated).

Although it is difficult to incorporate the along-strike difference in properties from the PSZ to the high-permeability fine breccia into modeling the overall slip response in such a case of branching, we speculatively suggest that the fault will be locally controlled by the strongest points, i.e. such high-permeability branch structures, which may act as seismic asperities. Along with the control exerted by the width of the slip zone on the feasibility of thermal pressurization, this mechanism may explain why complete dynamic stress drop is unlikely to occur in natural earthquakes.

#### 4. Conclusions

Based on porosity and permeability data obtained from the principal and secondary slip zones of the Usukidani fault, our modelling shows that thermal pressurization is a viable process to account for dynamic slip-weakening, as long as the rupture remains located within the PSZ and SSZ-1 gouges and these gouge zones maintain good lateral continuity along the fault. If the rupture splays from the gouge slip zone and propagates through the marginal fine fault breccia, as could happen along small faults branching off the PSZ (e.g. Figure 2.4b, NW side), coseismic excess fluid pressure will no longer be trapped, and will rapidly bleed off into the breccia, thus cancelling dynamic weakening.

The possibility of thermal pressurization to occur along secondary as well as along principal slip zones is probably a common feature of many crustal earthquakes. A notable example of such a complex propagation could be represented by the 1992 Landers event in California in which the rupture of the earthquake first propagated along a major fault, then shifted along a secondary fault before jumping to a third fault (Sowers et al., 1994). Indeed, if rupture propagates into an "immature" branch fault or microbreccia zone characterized by a hydraulic diffusivity higher than that of the principal slip zone, excess fluid pressure can dissipate from this main zone, thus inhibiting pressurization. On the contrary, transfer of slip to "mature" branching faults (such as SSZ-1 in the case of the example presented here), with a hydraulic diffusivity similar to or lower than the main slip zone, will not impede fluid pressurization unless the branching faults are significantly narrower than about 5 - 10 mm.

Partial inhibition of thermal pressurization by propagation of the rupture into an adjacent fine breccia or into an immature splay fault may explain why coseismic stress drops do not generally reach zero. This implies that a complete investigation of the hydraulic behaviour of active faults should also include secondary or higher order faults, if the geological exposure conditions permit.

## B. Moisture-drained weakening mechanism

### 1. Finite element analysis of frictional heating during shearing

#### 1.1. General considerations

In the case of a strike-slip fault, the work against gravity during faulting can be neglected and the energy balance for the work done can be written as (Scholz, 1990):

$$W_f = Q + E_s + U_s \quad (4.8)$$

where  $W_f$  is the mechanical work done in faulting,  $Q$  is produced heat,  $U_s$  is surface energy for rupture propagation and subsequent gouge formation, and  $E_s$  is the energy radiated in earthquake. Following the discussion of Scholz (1990),  $E_s$  and  $U_s$  are negligible compare to  $W_f$  and all frictional work is assumed to be converted into heat. The amount of heat generated during coseismic slip for a unit area of the fault is then (Price & Cosgrove, 1990):

$$Q \approx W_f = \mu_d \times (\sigma_n - P_p) \times d \quad (4.9)$$

where  $\mu_d$  is the dynamic friction coefficient,  $\sigma_n$  is the normal stress applied during experiments,  $P_p$  is pore fluid pressure and  $d$  is the sliding distance. Considering the time derivative of equation 4.9, the heat generated per unit area of the fault is (McKenzie & Brune, 1972):

$$q = \mu_d \times (\sigma_n - P_p) \times V \quad (4.10)$$

$$\Leftrightarrow q = A \times w \quad (4.11)$$

where  $V$  is the applied sliding velocity,  $w$  is the width of the deformation zone and  $A$  is the heat generated per unit volume (Noda & Shimamoto, 2005).

To estimate temperature change of the clay-granite system during friction experiment, we neglect pore fluid pressure (i.e.  $P_p = 0$ ) and we use the mathematical model of

Lachenbruch (1980): temperature change is given by the sum of a heat production term and a heat transfer term, such as:

$$\frac{\partial T}{\partial t} = \frac{A}{\rho \times c} + \frac{\kappa}{\rho \times c} \times \left( \frac{\partial^2 T}{\partial x^2} + \frac{\partial^2 T}{\partial y^2} \right) \quad (4.12)$$

where  $t$  is time,  $T$  is temperature rise,  $\kappa$  is thermal conductivity,  $\rho$  is fault rock density,  $c$  is heat capacity of fault rock,  $x$  is the radial position from the center of the cylinder assembly and  $y$  the corresponding cartesian position. From there, the frictional heat generation per unit surface can be calculated from the measured shear stress  $\tau$  as follows:

$$\frac{A}{\rho \times c} = \frac{A \times a}{K} \quad (4.13)$$

$$\Leftrightarrow \frac{A \times a}{K} = \frac{V}{w} \times \mu \times \sigma_n \times \frac{a}{K} \quad (4.14)$$

$$\Leftrightarrow \frac{V}{w} \times \mu \times \sigma_n \times \frac{a}{K} = \tau \times V \times \frac{a}{w \times K} \quad (4.15)$$

where  $a$  and  $K$  are the thermal diffusivity and the thermal conductivity of the material, respectively (Table 4.3).

## 1.2. Modelling approach of temperature rise analysis

The fault gouge layer is idealized as a narrow deformation zone  $w$  with a constant and uniform rate of shearing deformation dependent on measured  $\tau$  (see III.A.2) and radial position  $x$  (equation 4.12), surrounded by a matrix which does not deform during experiment (Fig. 4.4c; Table 4.2). This method does not take into account the progressive development of microstructures previously presented in chapter III (see C.3), but simplifies the calculation procedure for similar results.

For the numerical simulation of the heat transfer in the clay-granite system, we adapted an already existing software called SETMP (Calugaru, 2006), which has been initially developed for the simulation of flow and mass transport in porous media. Because heat transfer and mass transport are governed by similar partial differential equations, the

adaptation of this code essentially consists in considering no flow in the domain and in replacing mass transport parameters (molecular diffusion and mass source term) by heat transfer parameters (thermal conductivity and heat production term). Specimen assembly is axis-symmetric (Fig. 3.1). Thus, it is appropriate to consider the clay-granite system as a 2 dimensions domain (Fig. 4.4b).

From the point of view of numerical methods, a full implicit Euler scheme is used for time discretization and a P2 FEM (finite element method) is used for the space discretization. The advantage of the interpolation of degree 2 is that it allows a better approximation of the heat flux. Indeed, the heat flux being proportional to the temperature gradient, it is approximated by a polynomial of degree one in each element. Therefore, locally, heat conservation at discrete level is preserved better than in a classical P1 FEM.

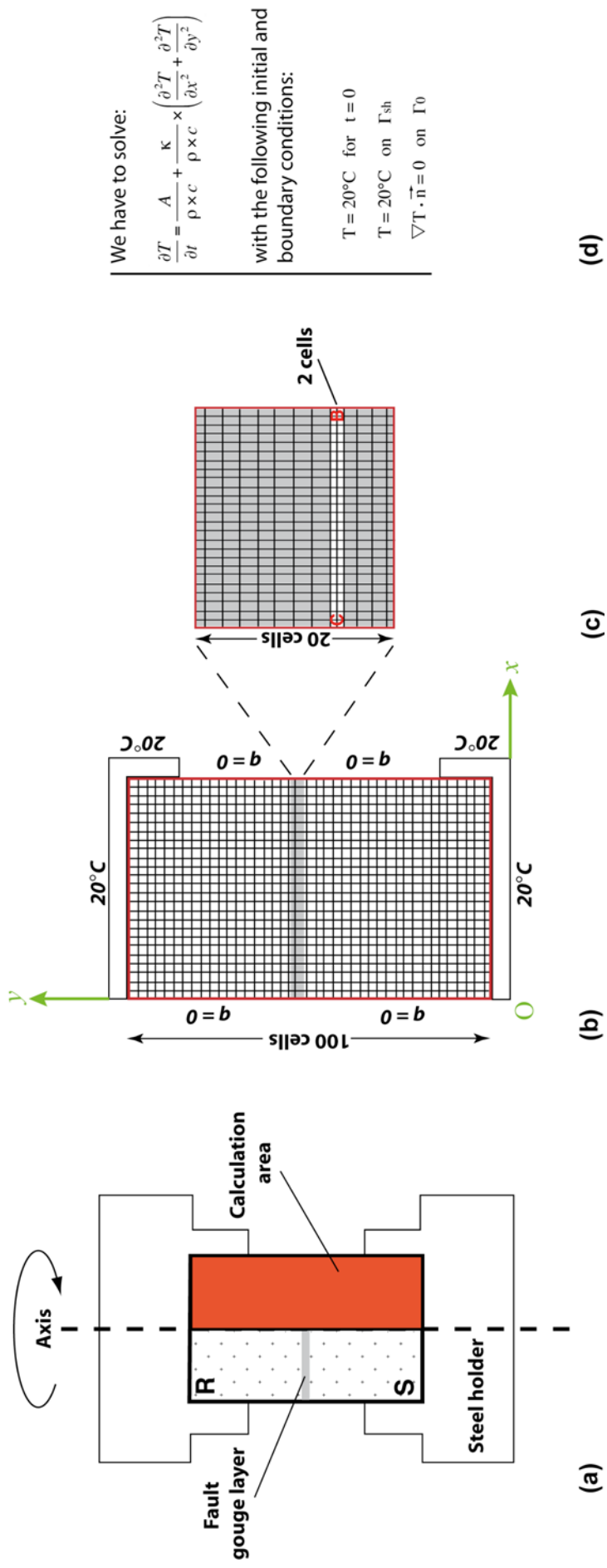
This P2 FEM calculation is then applied to the cells of the calculation area, which is subdivided by 2500 cells, with 1000 vertical cells for the clay gouge and only 100 cells for the heat production gouge zone (Figs. 4.4b & 4.4c). Time step is fixed at 0.05 s for the all experiments. Because the thermal conductivity is different in clay and granite samples (Table 4.3), a non-overlapping domain decomposition method is used (Calugaru & Tromeur-Dervout, 2004) to ensure heat conservation on the two interfaces (i.e. clay-rotational side and clay-stationary side).

We assume initial temperature in the calculation area at 20 °C, and we fixed boundary temperature of the steel holder during the all duration of the experiments at 20 °C. Considering the axis-symmetry of the clay-granite system (Fig. 4.4a) and the very low thermal diffusivity of the ambient air, the other surfaces of the clay-granite system are assumed to represent adiabatic boundaries (Fig. 4.4b).

In the following work, to take into account the range of slip-rate in the radial direction over the circular fault surface, we report temporal evolution of the calculated temperature at two points of the clay-granite system (Fig. 4.4c): a point (*C*) located in the middle of the fault gouge layer at  $x = 0$  mm (i.e. in the *central gouge*), and a point (*B*) located in the middle of the fault gouge layer at  $x = 24$  mm (i.e. in the *boundary gouge*).

### 1.3. Estimation of the fracture energy expended during friction experiments

The fracture energy is the work done in the rupture breakdown in excess of that done against the steady-state friction. Assuming a simple slip-weakening model for stress



We have to solve:

$$\frac{\partial T}{\partial t} = \frac{A}{\rho \times c} + \frac{\kappa}{\rho \times c} \times \left( \frac{\partial^2 T}{\partial x^2} + \frac{\partial^2 T}{\partial y^2} \right)$$

with the following initial and boundary conditions:

$T = 20^\circ\text{C}$  for  $t = 0$

$T = 20^\circ\text{C}$  on  $\Gamma_{sh}$

$\nabla T \cdot \vec{n} = 0$  on  $\Gamma_0$

**Figure 4.4** - Sketch of the clay-granite system used for numerical simulation. (a) geometry of the specimen sample. *R* means rotary side and *S* means stationary side. (b) enlarged sketch of the total calculation domain showing assumed boundary conditions. (c) enlarged sketch of the heat production gouge zone. Only 20 X 50 cells are used to calculate the heat generation rate. (d) calculation procedure.  $\Gamma_{sh}$  is the granite-steel holder boundary surface and  $\Gamma_0$  is the remainder of the calculation area boundary .

		Run	Deformation zone thickness ( $\mu\text{m}$ )	Total fault gouge thickness ( $\mu\text{m}$ )
1.3 m/s	wet	#569	40	875
	dry	#581	40	800
0.9 m/s	wet	#564	120	1000
	dry	#547	40	340

**Table 4.2** - Clay system characteristics used in the P2 FEM analysis from post-run thin section measurements.

Thermal diffusivity	a	Clay	$7.5 \times 10^{-7}$	$\text{m}^2 / \text{s}$
		Granite	$9.6 \times 10^{-7}$	
Density	d	Clay	2000	$\text{kg} / \text{m}^3$
		Granite	2600	
Heat capacity	$C_p$	Clay	1000	$\text{J} / \text{kg} / \text{K}$
		Granite	800	
Thermal conductivity	K	Clay	1.5	$\text{W} / \text{m} / \text{K}$
		Granite	2.0	

**Table 4.3** - Physical material properties used in the P2 FEM analysis.

breakdown (Andrews, 1976), the fracture energy that is expended during our friction experiments is approximated such as:

$$E_f = \frac{1}{2} \times (\tau_p - \tau_{ss}) \times D_c \quad (4.16)$$

where  $d_c$  is substituted to  $D_c$  in the calculation (see equation 1.14),  $\tau_p$  corresponds to the peak shear stress value and  $\tau_{ss}$  corresponds to the steady-state shear stress value.

## 2. Results

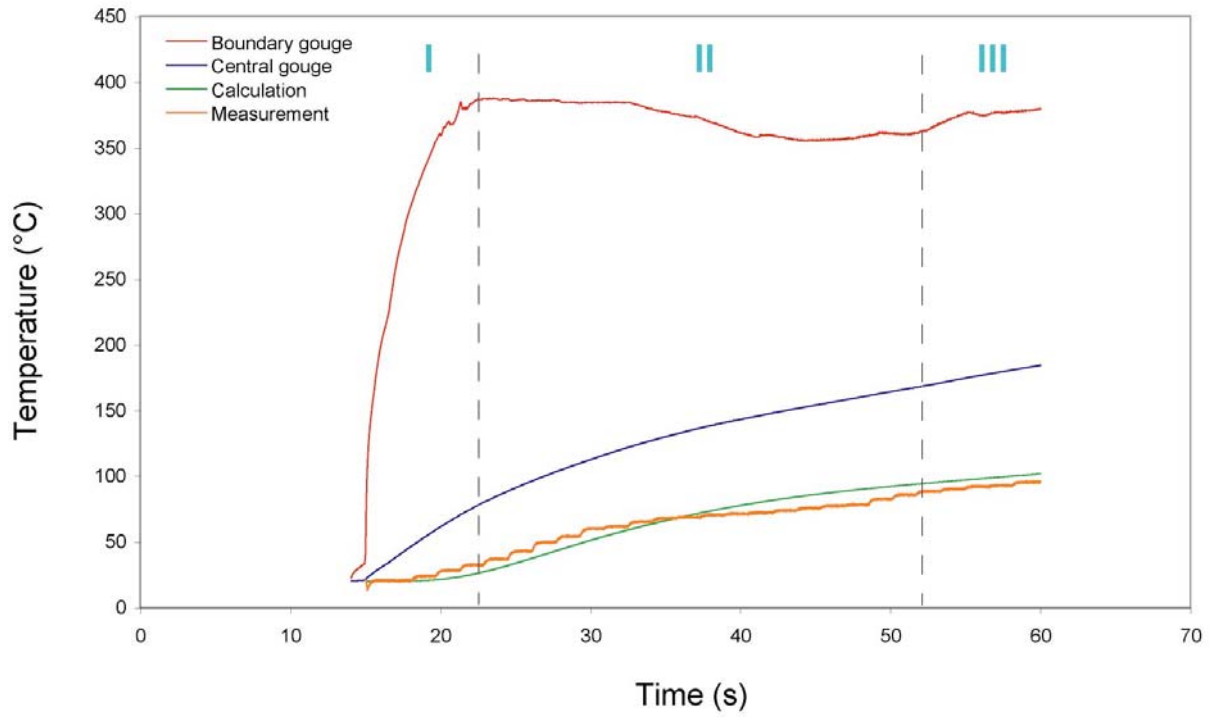
### 2.1. Simulated fault gouge temperatures

Figure 4.5 shows temperature rise measured at the thermocouple location (Fig. 3.1) and corresponding temperature rise calculated from the numerical model, against time. The curve of the calculated temperature approaches accurately the curve of the measured temperature, with errors on  $T$  values lower than 10 degrees. This result validates our numerical model and allows us to consider calculated temperature rise from heat dissipation through the clay-granite system as relevant for the other friction experiments.

Time evolution of the boundary gouge temperature reaches a peak after a logarithmic increase (*part I*), then weakly decreases over a long sliding displacement (*part II*) and finally weakly increases with small fluctuations about the mean (*part III*). To the contrary, time evolution of the central gouge temperature increases monotonically with no apparent fluctuation.

### 2.2. Frictional behavior of simulated faults

Figure 4.6 shows four graphs of the most representative gouge frictional behavior ( $\mu$ ) of simulated faults at 0.9 and 1.3 m/s for dry and wet initial conditions, respectively. The concomitant evolution of axial shortening ( $S$ ), boundary gouge temperature ( $T_b$ ) and central gouge temperature ( $T_c$ ) are reported on the same graphs. All the friction coefficients show a



**Figure 4.5** - Validation of the numerical model. "Measurement" and "Calculation" temperatures are effective at 13 mm from the gouge-granite interface for the run #569. Parts I, II and III correspond to temperature rise sequences of the boundary gouge.

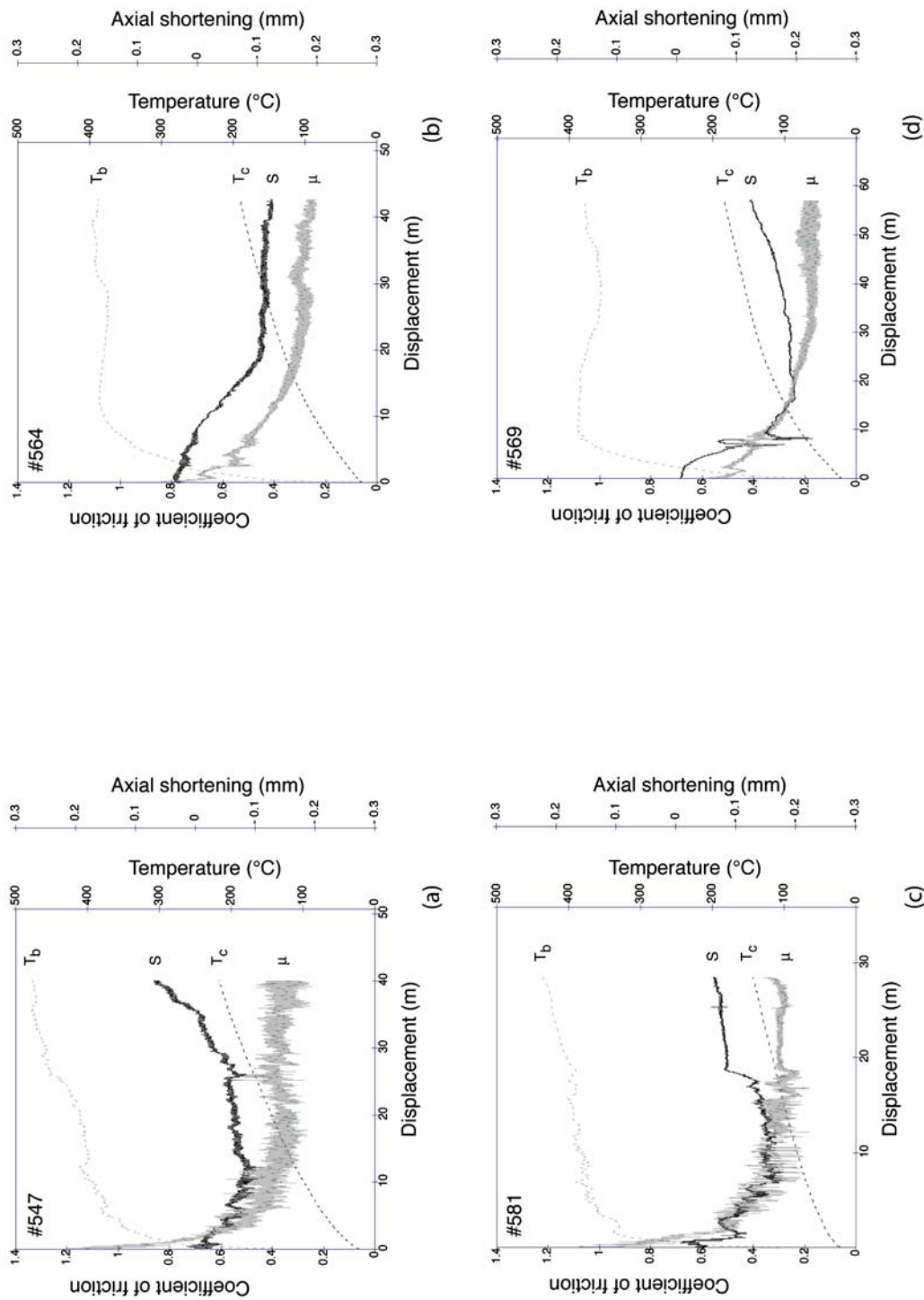


**Figure 4.6** - Representative gouge frictional behavior of simulated faults (a) in dry conditions at 0.9 m/s, (b) in wet conditions at 0.9 m/s, (c) in dry conditions at 1.3 m/s, (d) in wet conditions at 1.3 m/s. Graphs show the concomitant evolution of the friction coefficient with corresponding axial shortening (S), boundary and central gouges.  $\mu$  is friction coefficient, S is shortening,  $T_b$  is the boundary gouge temperature and  $T_c$  is the central gouge temperature.

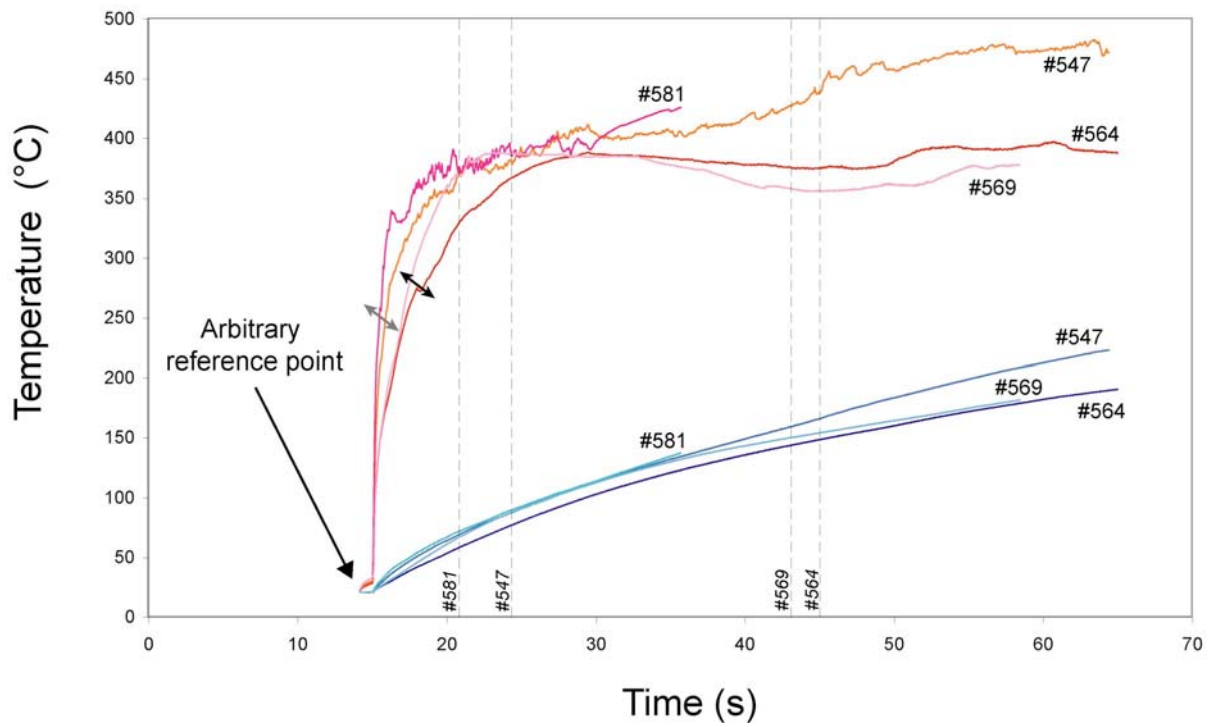


**Figure 4.7** - Evolution of boundary gouge temperatures and central gouge temperatures against time, for the four representative friction experiments presented on Figure 4.6. Vertical dashed lines corresponds to the time location of the run slip-weakening distances. Double black arrow indicates wet initial experiments and double grey arrow indicates dry initial experiments.

Run	Equivalent velocity (m/s)	Initial moisture conditions	$d_c$ (m)	$T_b$ (°C)	$T_c$ (°C)	$E_f$ ( $10^6$ N/m)
#547	0.9	Dry	7.7	375	83	1.6
#564	0.9	Wet	25.5	375	142	3.6
#581	1.3	Dry	7.2	372	72	1.4
#569	1.3	Wet	35.3	360	149	4.1

**Table 4.4** - Summary of high-velocity friction results of four representative runs.  $d_c$  means critical slip distance,  $T_b$  and  $T_c$  are respectively boundary and central gouge temperatures once  $d_c$  is reached, and  $E_f$  indicates the corresponding fracture energy. Slip-weakening distance values and shear stress values used in  $E_f$  calculation result from friction data fitting with equation 1.13, using Kaleidagraph© software. Errors on  $T$  values lower than 10 degrees, errors on  $d_c$  values are overestimated by 1 %, and errors on  $E_f$  values are overestimated by 5 %.

dramatic decrease from a peak friction coefficient value ( $\mu_p$ ) towards a steady-state friction value ( $\mu_{ss}$ ) over a slip-weakening distance  $d_c$  (see I.C). In dry conditions, axial shortening decreases up to 10 m of slip displacement, then increases up to the initial value. In wet conditions, axial shortening decreases up to 20 m of slip displacement, then increases but does not reach the initial value. The graphs show that whatever initial moisture conditions, the central gouge temperature increases logarithmically with slip displacement, whereas the boundary gouge temperature increases logarithmically, at a higher rate in dry conditions than in wet conditions. At least, at 1.3 m/s in wet initial conditions, two drops in axial shortening (0.09 mm and 0.16 mm, respectively) corresponding to two dramatic drops in  $\mu_d$  (0.03 and 0.1, respectively) can be observed at 6.5 and 7.5 m of slip displacement.

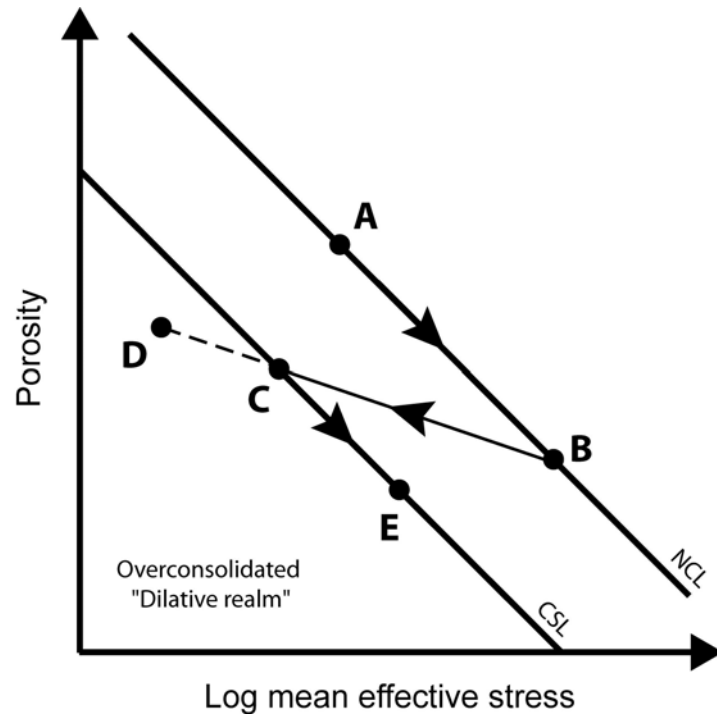
Figure 4.7 shows the evolution of boundary gouge temperatures and central gouge temperatures of these four representative runs. During *part I*, the boundary gouge temperature increase is lower in wet initial conditions than in dry initial conditions (see arrows). From *part I* to *part III*, whatever slip-velocity, boundary gouge temperatures and central gouge temperatures are lower in wet initial conditions than in dry initial conditions.

Table 4.4 reports the measured  $T_b$  and  $T_c$  and calculated fracture energy  $E_f$  once the slip-weakening distance  $d_c$  is reached, for the four representative gouge frictional behaviors. At 0.9 and 1.3 m/s, the Table 4.4 shows firstly that  $T_b$  is similar whatever initial moisture conditions, secondly that  $T_c$  is larger in wet conditions than in dry conditions, for a  $d_c$  larger in wet conditions than in dry conditions. Additionally, whatever slip-velocity,  $E_f$  is larger in wet conditions than in dry conditions. Besides, it is remarkable that all these parameters do not appear to depend on slip-velocity. Additional results from experiments done at 0.09 m/s (i.e. one order of magnitude lower than at 1.3 m/s) are needed to conclude about this tendency.

### 3. Discussion

#### 3.1. Stress paths followed by the simulated fault gouge

Simulated fault is consolidated during several hours prior to shearing at the normal stress applied during the experiment (see III.A.1). As a response to this load, the axial shortening decreases significantly (Fig. 3.2), which corresponds to a reduction of gouge porosity. This suggests that stress path of gouge follows the normal consolidation path (NCL) from A to B (Fig. 4.8). Subsequently, the gouge is sheared at a constant slip-velocity. It



**Figure 4.8** - Diagrammatic representation of stress paths for sheared gouge deformed during high velocity friction experiments plotted versus porosity. NCL means Normal Consolidation Line, and CSL means Critical State Line.

follows an increase in gouge volume for all the slip-velocities and initial moisture conditions (Fig. 4.6). This corresponds to an increase in porosity and indicates first that shear dilatancy occurs, and secondly that the normally consolidated gouge evolves towards the critical state line (CSL) from B to C.

Two rises (and consecutive drops) in axial shortening can be observed on the representative experiment conducted at 1.3 m/s in wet initial conditions (Fig. 4.6d). They are correlated with a drop and a rise of the shearing resistance, for a central gouge and a boundary gouge define at 70 °C and at 380 °C, respectively. They correspond to an abrupt increase followed by a collapse in gouge porosity and indicate the occurrence of pore fluid pressure rise and pore fluid pressure escape during shearing (Fig. 4.9). This suggests a reduction of the mean effective stress which leads the stress path of the consolidated gouge to move briefly into the overconsolidated realm along the line CD during pore fluid pressure rise timescale.

Afterwards, the axial shortening increases significantly in dry initial conditions but weakly in wet initial conditions. This indicates a higher porosity collapse of gouge in dry conditions, and suggests that whatever initial moisture conditions, stress path of gouge follows the CSL from C to E.

### 3.2. Temperature change during slip-weakening

The logarithmic increase of  $T_b$  along *part I* suggests firstly that the heat production rate is considerably higher than the heat diffusion rate over the first 7 meters of slip displacement, and secondly that the ratio of heat production on heat diffusion decreases progressively from an initial peak value. Then,  $T_b$  evolves rapidly towards a steady level with a marked decrease after 18 meters of slip displacement (*part II*). This indicates that the heat diffusion rate balanced the heat production rate, and that the ratio value of heat production on heat diffusion is lower but close to the value of 1. Finally, *part III* shows a weak increase of  $T_b$  towards a steady level. This suggests that the heat diffusion rate balanced the heat production rate, and that the ratio value of heat production on heat diffusion overpasses the value of 1.

Thence, according to the gouge temperature evolution curves, heat generated by frictional sliding during *part I* represents the major contribution to the total energy budget produced during the slip-weakening.

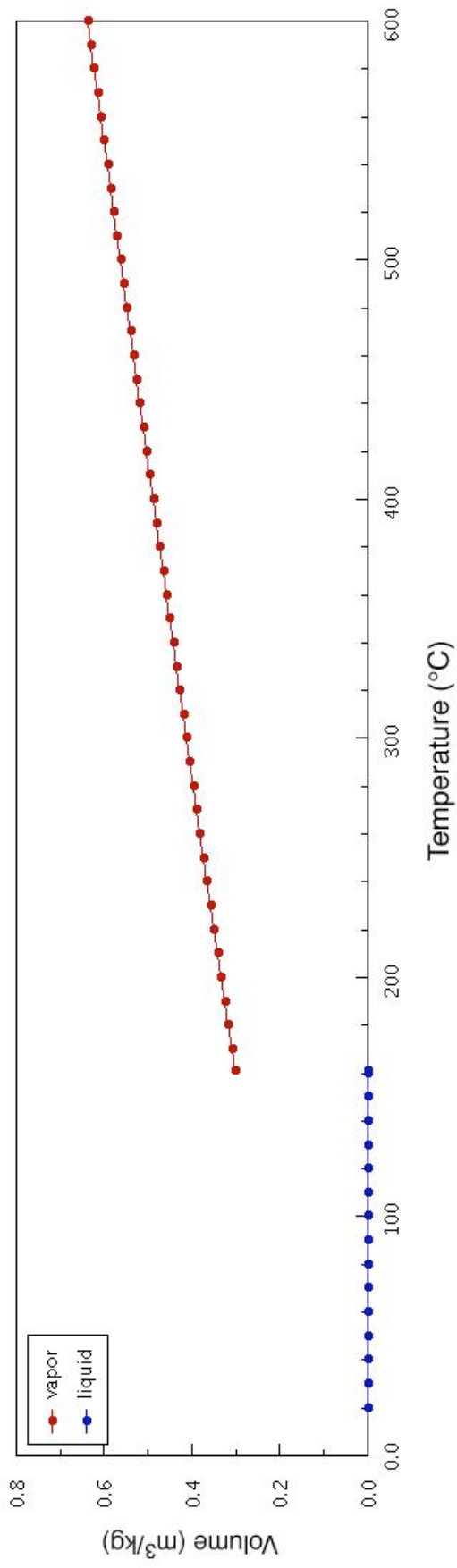


**Figure 4.9** - Isobaric data of water for  $\sigma_n = 0.6 \text{ MPa}$ . This graph shows the relative state evolution of water from liquid to vapor with increasing temperature, and consecutive volume expansion (data are available at <http://webbook.nist.gov/chemistry>).

### 3.3. Significance of the slip-weakening distance $d_c$

Table 4.4 shows firstly that the slip-weakening distance  $d_c$  is larger in wet initial conditions than in dry initial conditions, and secondly that whatever initial moisture condition, once  $d_c$  is reached the boundary gouge temperature is close to 375 °C, whereas the central gouge temperature turns around 85 °C in dry initial conditions and around 145 °C in wet initial conditions. These results suggest that simulated faults have the opportunity to achieve  $d_c$  only once boundary and central gouges have reached a temperature threshold which depends on gouge water content.

Two main types of microstructures implying two distinct particle dynamics have been previously reported (see III.C.3). The observed slip-weakening behavior of simulated faults has been interpreted to be related to a decrease of the proportion of grain rolling to grain sliding with increasing displacement, with water content (and slip-velocity) as controlling parameter of clay-clast aggregate development, which lowers the friction coefficient during displacement. Figure 4.7 shows that the boundary gouge temperature increase during the *part I* is lower in wet initial conditions than in dry initial conditions. This result suggests that clay-clast aggregates, whose development is favored by water content, reduce dramatically the heat production rate during the first meters of slip displacement. But the pore pressure rise observed in wet initial conditions suggests that excess fluid pressure has also contributed to the reduction of the heat production rate, by reducing dynamic fault shear stress (see equation 4.10).

From *part I* to *part III*, the heat production rate of boundary gouges and central gouges is lower in wet initial conditions than in dry initial conditions, for a slip-weakening distance  $d_c$  that is always larger in wet initial conditions than in dry initial conditions (Fig. 4.7; table 4.4). It results that once  $d_c$  is reached in dry initial conditions, the corresponding temperatures of the central and boundary gouges for similar displacement are lower in wet initial conditions, whatever slip-velocities (Fig. 4.7). Additionally, once  $d_c$  is reached, the central gouge temperature is higher in wet initial conditions than in dry initial conditions, for similar boundary gouge temperatures, whatever slip-velocities. These results suggest that the slip-weakening distance  $d_c$  might represent the necessary slip distance to produce and diffuse enough heat throughout the fault gouge layer, to break liquid capillary bridge and to drain off completely pore water (in wet initial conditions) and adsorbed water (in both wet and dry initial conditions) at contact area of gouge particles.

### 3.4. Frictional contacts localizing heating

The load-bearing framework of a fault in the brittle field is governed by the dynamic adhesion of a population of asperity contact between the sliding surfaces (Rabinowicz, 1965; Scholz, 2002). Physical mechanisms responsible of frictional behavior of fault containing clay gouge is more complex than bare faults because it is a granular material (Mair et al., 2006).

According to microstructural observations, the concept of asperity interactions during shearing can be described as the interaction of two distinct particle dynamics (see III.C.3). Thus the localized high stresses at clay-clast aggregate contacts and at B-type gouge asperity contacts might determine the heat production and heat dissipation rates during friction experiments. The absence of any melting surface or interstitial glass within gouge layers (see III.C.1.2) indicates that the melting point of constitutive rock minerals is not reached during the experiments conducted at coseismic slip-rates, whatever initial moisture conditions. The presence of phyllosilicates, as a weaker component of fault gouge (see I.B.4), might play a key role in the development of the two particle dynamics, which accommodate the slip throughout the gouge layer and control heat production rate, i.e. the expended fracture energy  $E_f$  (assuming all frictional work converted into heat).

### 3.5. Energy expended in fracturing

The fracture energy expended during earthquakes has been estimated around  $0.5 \times 10^6$  N/m from dynamic modelling for the 1995 Kobe earthquake (Mizoguchi et al., 2007), and around  $11.6 \times 10^6$  N/m from waveform inversion method for the 1999 Chi-chi earthquake (Ma et al., 2005). Hence, in nature, the frictional strength of a fault reaches a steady-state value once the fault has consumed a fracture energy of  $10^6 - 10^7$  N/m (Mikumo & Fukuyama, 2006). The fracture energy expended in our friction experiments ranges from 2.2 to  $6.2 \times 10^6$  N/m (Table 4.4). This suggests a good reliability of our friction experiments with natural earthquakes.

It has been previously reported that the dramatic decrease in frictional strength of simulated fault gouges is controlled by gouge water content (see III.C.4). Similarly this chapter shows that the required  $d_c$  of a simulated fault to evolve from  $\mu_p$  to  $\mu_{ss}$  depends on gouge temperature rise, which is controlled by initial water content. It results that  $E_f$  is

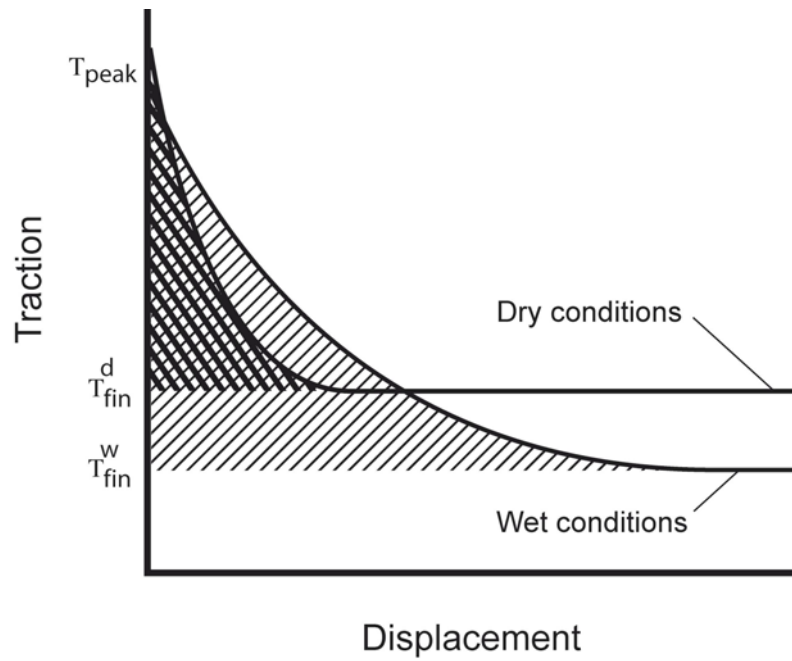


**Figure 4.10** - Typical mechanical behaviors and related fracture energy (shaded domains) of experimental gouge simulated faults at slip-rates of 0.9 or 1.3 m/s, for wet and dry initial conditions.  $T_{peak}$  corresponds to the peak shear stress,  $T_{fin}^d$  corresponds to the steady-state shear stress in dry conditions, and  $T_{fin}^w$  corresponds to the steady-state shear stress in wet conditions.

enlarged in wet initial conditions compare to dry initial conditions (Table 4.4; Fig. 4.10). These results indicate that water content is a relevant parameter that controls the expended fracture energy  $E_f$  of our friction experiments.

#### 4. Conclusions

Based on friction data obtained from laboratory experiments, modelling results suggest that heat generated by frictional sliding during *part I* (i.e. first meters of slip displacement) represents the major contribution to the total energy budget produced during the slip-weakening. Following temperature sequences (*part II* and *part III*) show the dominance of thermal diffusion rate on heat production rate up to  $d_c$ .

We suggest that the slip-weakening distance  $d_c$  might represent the necessary slip distance 1) to increase pore fluid pressure within the fault gouge by frictional heating, which reduces the effective normal stress and hence shear strength, 2) to produce and diffuse enough heat throughout the fault gouge layer to break liquid capillary bridge and to drain off completely pore water and adsorbed water at contact area of gouge particles.

The fracture energy necessary to produce this required heat in our friction experiments falls mid-way in the range of seismological reported data, and appears to be heightened in wet initial conditions. These results suggest that initial gouge water content might be a relevant parameter that controls the expended fracture energy  $E_f$  during coseismic events, which could explain the observed variations in consumed fracture energy of crustal events by seismologists.

Therefore, initial gouge water content is proposed to be a fundamental parameter for a slip-weakening constitutive law at high slip-rates.

## **CONCLUSIONS**



In order to determine the processes responsible of the efficiency of two thermally-activated slip-weakening mechanisms, field analyses and laboratory experiments have been conducted on a potentially active strike-slip fault: the Usukidani fault (Japan). The primary results of this research are exposed below.

Numerical modelling of thermal pressurization constrained by laboratory data, from hydrological and poroelastic properties measured on gouges and breccia of the Usukidani fault suggests that this thermally-activated slip-weakening mechanism is a viable process only as long as the rupture remains located in the central gouge zones or in mature splay fault gouge zones. Partial inhibition of thermal pressurization by propagation of the rupture into an adjacent fine breccia or into an immature splay fault may explain why seismologically determined coseismic stress drops do not generally reach zero. This implies that a complete investigation of the hydraulic behaviour of active faults should also include secondary or higher order faults, if the geological exposure conditions permit.

Based on friction data obtained from rotary-shear experiments conducted at coseismic slip-rates, modelling results of temperature rise on simulated fault suggest that heat generated by frictional sliding during the first meters of slip displacement represents the major contribution to the total energy budget produced during the slip-weakening. The experimental slip-weakening distance  $d_c$  is proposed to represent the necessary slip distance 1) to increase pore fluid pressure by frictional heating 2) to produce and diffuse enough heat throughout the fault gouge layer to break liquid capillary bridge and to drain off completely pore water and adsorbed water at contact area of gouge particles, that is the thermally-activated moisture-drained weakening mechanism

Detailed examination of gouge microstructures obtained at the residual friction stage of these experiments allow to define two cataclastic deformation regimes: a rolling regime with formation of *clay-clast aggregates*, and a sliding regime with formation of a *complex shear zone* localized at the gouge-granite interface. The observed slip-weakening behavior appears to be related to a decrease of the proportion of grain rolling to grain sliding with increasing displacement, which is favored by the development of clay-clast aggregates and controlled by water content and slip-velocity.

I suggest that the development of clay-clast aggregates, enhanced by an increase in initial gouge water content, reduces the heat production rate during the first meters of slip displacement, which impedes the efficiency of the thermally-activated moisture-drained weakening mechanism, leading to a larger fracture energy  $E_f$ . Therefore, to account for thermal mechanisms that govern the magnitude of the fault dynamic stress drop at high slip-

rates, initial gouge water content is proposed to be an additional specific state variable of the *Dieterich-Ruina's law*.



## **REFERENCES**



- Aagaard, B.T., Heaton T.H. & Hall, J. 2001. Dynamic earthquake ruptures in the presence of lithostatic normal stresses: Implications for friction models and heat production. *Bull. Seism. Soc. Amer.*, **91**, 1765-1796.
- Aisawa, Y. 2005. Estimation of Underground Porosity-Permeability Structures of Niigata basin and Katakai Fault Zone. *Master Thesis*, the Graduate School of Science, Kyoto University, 70 p.
- Andrews, D.J. 1976. Rupture propagation with finite stress in antiplane strain. *J. Geophys. Res.*, **81**, 3575-3582.
- Andrews, D.J. & Ben-Zion, Y. 1997. Wrinkle-like slip pulses on a fault between different materials. *J. Geophys. Res.*, **102**, 553-571.
- Andrews, D.J. 2002. A fault constitutive relation accounting for thermal pressurization of pore fluid. *J. Geophys. Res.*, **107**, doi:10.1029/2002JB001942.
- Archuleta, R. 1984. A faulting model for the 1979 Imperial Valley earthquake. *J. Geophys. Res.*, **89**, 4559-4585.
- Beeler, N.M, Tullis, T.E., Weeks, J.D. 1994. The roles of time and displacement in the evolution effect in rock friction. *Geophys. Res. Lett.*, **21**, 1987-1990.
- Ben-Zion, Y. & andrews, D.J. 1998. Properties and implications of dynamic rupture along a material interface. *Bull. Seism. Soc. Amer.*, **88**, 1085-1094.
- Bird, P. 1984. Hydration-phase diagrams and friction of montmorillonite under laboratory and geologic conditions, with implications for shale compction, slope instability, and the strength of fault gouge. *Tectonophysics*, **107**, 235-260.
- Blanpied, M.L., Lockner, D.A. & Byerlee, J.D. 1991. Fault stability inferred from granite sliding experiments at hydrothermal conditions. *Geophys. Res. Lett.*, **18**, 609-612.
- Blanpied, M.L., Lockner, D.A. & Byerlee, J.D. 1992. An earthquake mechanism based on rapid sealing of faults. *Nature*, **358**, 574-576.
- Blanpied, M.L., Tullis, T.E. & Weeks, J.D. 1998. Effects of slip, slip rate, and shear heating on the friction of granite. *J. Geophys. Res.*, **103**, 489-511.
- Bolton, A.J., Maltman, A.J. & Clennell, M.B. 1998. The importance of overpressure timing and permeability evolution in fine-grained sediments undergoing shear. *J. Struct. Geol.*, **20**, 1013-1022.
- Bos, B., Peach, C.J. & Spiers, C.J. 2000. Frictional-viscous flow of simulated fault gouge caused by the combined effects of phyllosilicates and pressure solution. *Tectonophysics*, **327**, 173-194.
- Bos, B. & Spiers, C. 2002. Fluid-assisted healing processes in gouge-bearing faults: Insights from experiments on a rock analogue system. *Pure Appl. Geophys.*, **159**, 2537-2566.

- Bouissou, S., Petit, J.P. & Barquins, M., 1998. Experimental evidence of contact loss during stick-slip: possible implications for seismic behaviour. *Tectonophysics*, **295**, 341-350.
- Boutareaud, S., Fabbri, O., Han, R., Buatier, M. & Shimamoto, T. 2006. Shear localization at seismic slip rates: first results from high-velocity experiments on the gouge of the Usukidani fault, southwest Japan. *Geophys. Res. Abstr.*, **8**, Abstract 01251, sref: 1607-7962/gra/EGU/06-A-01251.
- Boutareaud, S., Wibberley C.A.J., Fabbri, O. & Shimamoto, T. Permeability structure and co-seismic thermal pressurization on fault branches: insights from the Usukidani fault, Japan. In: Wibberley, C.A.J., Kruz, W., Imber, J., Collettini, C. & Holdsworth, R.E. (eds) *The internal structure of fault zones: Fluid flow and mechanical properties*. J. Geol. Soc. (Lond.), Sp. Publ., *in press*.
- Brace, W.F. & Byerlee, J.D. 1966. Stick slip as a mechanism for earthquakes. *Science*, **153**, 990-992.
- Brodsky, E.E. & Kanamori, H. 2001. Elastohydrodynamic lubrication of faults. *J. Geophys. Res.*, **106**, 16357-16374.
- Brune, J.N., Henyey, T.L. & Roy, R.F. 1969. Heat flow, stress, and rate of slip along the San Andreas fault, California. *J. Geophys. Res.*, **74**, 3821-3827.
- Brune, J.N., Brown, S. & Johnson, P.A. 1993. Rupture mechanism and interface separation in foam rubber models of earthquakes: A possible solution to the heat flow paradox and the paradox of large overthrusts. *Tectonophysics*, **218**, 59-67.
- Byerlee, J.D. 1978. Friction of rock. *Pure Appl. Geophys.*, **116**, 615-626
- Caine, J.S., Evans, J.P. & Forster, C.B. 1996. Fault zone architecture and permeability structure. *Geology*, **24**, 1025-1028.
- Calugaru, D.G. & Tromeur-Dervout, D. 2004. Non-overlapping domain decomposition methods to solve flow in heterogeneous porous media. Lecture notes in *Comput. Sci. Eng.*, **40**, 529-536.
- Calugaru, D.G. 2006. <http://www-math.univ-fcomte.fr/setmp>
- Cardwell, R.K., Chinn, D.S., Moore, G.F. & Turcotte, D.L. 1978. Frictional heating on a fault zone with finite thickness. *Geophys. J. R. Astron. Soc.*, **52**, 525-530.
- Carslaw, H.C. & Jaeger, J.C. 1959. Conduction of heat in solids. Oxford University Press, New York, 386 p.
- Chambon, G., Schmittbuhl, J. & Corfdir, A. 2006. Frictional response of a thick gouge sample: 2. Friction law and implications for faults. *J. Geophys. Res.*, **111**, B09309, doi:10.1029/2004JB003339.

- Chester, F.M. & Logan, J.M. 1986. Implications for mechanical properties of brittle faults from observations of the Punchbowl Fault zone, California *Pure Appl. Geophys.*, **124**, 79-106.
- Chester, F.M., Evans, J.P. & Biegel, R.L. 1993. Internal structure and weakening mechanisms of the San Andreas fault. *J. Geophys. Res.*, **98**, 771-786.
- Cox, S.F. 1995. Faulting processes at high fluid pressures: An example of fault valve behavior from the Wattle Gully Fault, Victoria, Australia. *J. Geophys. Res.*, **100**, 12841-12859.
- Crassous, J., Charlaix, E. & Loubet, J.B. 1994. Capillary condensation between high-energy surfaces: An experimental study with a surface force apparatus. *Europhys. Lett.*, **28**, 37-42.
- David, C., Wong, T.F., Zhu, W. & Zhang, J. 1994. Laboratory measurement of compaction-induced permeability change in porous rocks: implications for the generation and maintenance of pressure excess in the crust. *Pure Appl. Geophys.*, **143**, 425-456.
- de Gennes, P.G. 1999. Granular matter: A tentative view, *Rev. Mod. Phys.*, **71**, 374-382.
- Dehandschutter B., Gaviglio P., Sizun J.P., Sintubin M., Vandycke S., Vandenberghe N. & Wouters L. 2005. Volumetric matrix strain related to intraformational faulting in argillaceous sediments. *J. Geol. Soc. (Lond.)*, **162**, 801-813.
- De Las Cuevas, C. 1997. Pore characterization in rock salt. *Eng. Geol.*, **47**, 17-30.
- Dieterich, J.H. 1972. Time-dependence of rock friction. *J. Geophys. Res.*, **77**, 3690-3697.
- Dieterich, J.H. 1978. Time dependent friction and the mechanics of stick slip. *Pure Appl. Geophys.*, **116**, 790-806.
- Dieterich, J.H. 1981. Constitutive properties of faults with simulated gouge. *In: Carter, N.L., Friedman, M., Logan, J.M. & Sterns, D.W., (eds) Mechanical behavior of crustal rocks.* Am. Geophys. Union Monogr., **24**, 103-120. Washington, DC: Am. Geophys. Union.
- Dieterich, J.H. & Kilgore, B. 1994. Direct observation of frictional contacts: new insights for state-dependent properties. *Pure Appl. Geophys.*, **143**, 283-302.
- Dieterich, J.H. & Kilgore, B. 1996. Imaging surface contacts: Power law contact distributions and stresses in quartz, calcite, glass and acrylic plastic. *Tectonophysics*, **256**, 219-239.
- Di Toro, G., Goldsby, D.L. & Tullis, T.E. 2004. Friction falls towards zero in quartz rock as slip velocity approaches seismic rates. *Nature*, **427**, 436-439.
- Evans, J.P. & Chester, F.M. 1995. Fluid-rock interaction in faults of the San Andreas system. *J. Geophys. Res.*, **100**, 13007-13020.
- Evans, J.P., Forster, C.B. & Goddard, J.V. 1997. Permeability of fault-related rocks, and implications for hydraulic structure of fault zones. *J. Struc. Geol.*, **19**, 1393-1404.

- Fabbri, O., Iwamura, K., Matsunaga, S., Coromina, G. & Kanamori, Y. 2004. Distributed strike-slip faulting, block rotation and possible incrustal vertical decoupling in the convergent zone of SW Japan. *In: Grocott, J., McCaffrey, K. J. W., Taylor, G. & Tikoff, B. (eds) Vertical coupling and decoupling in the lithosphere.* J. Geol. Soc. (Lond.), Sp. Publ., **227**, 141-165.
- Faulkner, D.R. & Rutter, E.H. 1998. The gas-permeability of clay-bearing fault gouge at 20°C. *In: Jones, G., Fisher Q. & Knipe, R.J. (eds) Faulting, fault sealing and fluid-flow in hydrocarbon reservoirs.* J. Geol. Soc. (Lond.), Sp. Publ., **147**, 147-156.
- Faulkner, D.R. & Rutter, E.H. 2000. Comparison of water and argon permeability in natural clay-bearing fault gouge under high pressure at 20°C. *J. Geophys. Res.*, **105**, 16415-16426.
- Faulkner, D.R. & Rutter, E.H. 2001. Can the maintenance of overpressured fluids in large strike-slip fault zones explain their apparent weakness ? *Geology*, **29**, 503-506.
- Faulkner, D.R. 2004. A model for the variation in permeability of clay-bearing fault gouge with depth in the brittle crust. *Geophys. Res. Lett.*, **31**, L19611, doi:10.1029/2004GL020736.
- Favreau, P. & Archuleta, R. 2003. Direct seismic energy modeling and application to the 1979 Imperial Valley earthquake. *Geophys. Res. Lett.*, **30**, 1198, doi:10.1029/2002GL015968.
- Fialko, Y. & Khazan, Y. 2005. Fusion by earthquake fault friction: Stick or slip ? *J. Geophys. Res.*, **110**, 10.1029/2005JB003869.
- Fisher, D.M., Brantley, S.L., Everett, M. & Dzvonik, J. 1995. Cyclic fluid flow through a fracture network within the Kodiak accretionary prism. *J. Geophys. Res.*, **100**, 12881-12884.
- Frye, K. & Marone, C. 2002. Effect of humidity on granular friction at room temperature. *J. Geophys. Res.*, **107**, 2309, doi:10.1029/2001JB000654, ETG 11-1-11-13.
- Fukuyama, E., Ishida, M., Horiuchi, S., Inoue, H., Hori, S., Sekiguchi, S., Kubo, A., Kawai, H., Murakami, H. & Nonomura, K. 2000. NIED seismic moment tensor catalogue January-December 1997. *Technical Note of the National Research Institute for Earth Science and Disaster Prevention*, **205**, 35 p.
- Fukuyama, E., Ellsworth, W.L., Waldhauser, F. & Kubo, A. 2003a. Detailed fault structure of the 2000 western Tottori, Japan, earthquake sequence. *Bull. Seism. Soc. Am.*, **93**, 1468-1478.
- Fukuyama, E., Mikumo, T. & Olsen, B. 2003b. Estimation of the critical slip-weakening distance: Theoretical background. *Bull. Seism. Soc. Am.*, **93**, 1835-1840.
- Goddard, J.V. & Evans J.P. 1995. Fluid-rock interactions in faults of crystalline thrust sheets, northwestern Wyoming, U.S.A. Inferences from geochemistry of fault-related rocks. *J.*

- Struct. Geol.*, **17**, 533-549.
- Goldsby, D.L. & Tullis, T.E. 2002. Low frictional strength of quartz rocks at subseismic slip rates. *Geophys. Res. Lett.*, **29**, 1844, doi:10.1029/2002GL015240.
- Gregg, S.J. & Sing, K.S.W. 1982. Adsorption, surface area and porosity. Academic Press, New York, 303 p.
- Griffith, A.A. 1924. The theory of rupture. In: Biezeno, C.B. & Burgers, J.M., (eds) *Proc. 1st Int. Congr. Appl. Mech.* Delft: Tech. Boekhandel en Drukkerij J. Walter Jr., 54-63.
- Heaton, T. 1990. Evidence for and implications of self healing slip pulses in earthquake rupture. *Phys, Earth Planet. Inter.*, **64**, 1-20.
- Hickman, S., Sibson, R. & Bruhn, R. 1995. Introduction to special section: Mechanical involvement of fluids in faulting. *J. Geophys. Res.*, **100**, 12831-12840.
- Hirose, T. & Shimamoto, T. 2003. Fractal dimension of molten surfaces as a possible parameter to infer the slip-weakening distance of faults from natural pseudotachylytes. *J. Struct. Geol.*, **25**, 1569-1574.
- Hirose, T. & Shimamoto, T. 2005. Growth of molten zone as a mechanism of slip weakening of simulated faults in gabbro during frictional melting. *J. Geophys. Res.*, **110**, B05202, doi:10.1029/2004JB003207.
- Hirth, J.P. & Rice J.R. 1980. On the thermodynamics of adsorption at interfaces as it influences decohesion. *Metall. Trans.*, **11**, 1501-1511.
- Huzita, K. 1980. Role of the Median Tectonic Line in the Quaternary tectonics of the Japanese Islands. In: Ichikawa, K. (eds) *Median Tectonic Line of Southwest Japan*. Chishitsugaku ronshū, **18**, 129-153.
- Ichikawa, M. 1971. Reanalysis of mechanisms of earthquakes which occurred in and near Japan, and statistical studies on the nodal plane solutions obtained. *Geol. Mag.*, **35**, 207-274.
- Ide, S. & Takeo, M. 1997. Determination of constitutive relations of fault slip based on seismic wave analysis. *J. Geophys. Res.*, **102**, 27379-27391.
- Israelachvili, J.N., McGuiggan, P.M. & Homola, A.M. 1988. Dynamic properties of molecularly thin liquid films. *Science*, **240**, 189-191.
- Iwamatsu, M. & Horii, K. 1996. Capillary condensation and adhesion of two wetter surfaces. *J. Colloid Interface Sci.*, **182**, 400-406.
- Jaeger, H.M., Nagel, S.R. & Behringer R.P. 1996. Granular solids, liquids and gases. *Rev. Mod. Phys.*, **68**, 1259-1273.
- Jaeger, J.C., Cook, N.G.W. & Zimmerman R. 2007. Fundamentals of rocks mechanics, 4<sup>th</sup> edition. Blackwell Publishing Ltd, London, 475 p.

- Jeffreys, H., 1942. On the mechanics of faulting. *Geological Magazine*, **79**, 291-295.
- Jones, R, Pollock, H.M., Cleaver, J.A.S. & Hodges, C.S. 2002. Adhesion force between glass and silicon surface in air studied by AFM: Effects of relative humidity, particle, size, roughness, and surface treatment. *Langmuir*, **18**, 8045-8055.
- Kanamori, H. 1994. Mechanics of earthquakes. *Annu. Rev. Earth Planet. Sci.*, **22**, 207-237.
- Kanamori, H. & Heaton, T.H., 2000. Microscopic and Macroscopic Physics of Earthquakes. In: Rundle, J., Turcotte, D.L. & Klein, W., (eds.) *GeoComplexity and the Physics of Earthquakes*. Geophys. Res. Monogr. Series, **120**, 147-163. AGU, Washington.
- Kanaori, Y. 1990. Late Mesozoic-Cenozoic strike-slip and block rotation in the inner belt of Southwest Japan. *Tectonophysics*, **177**, 381-399.
- Kanaori, Y. 1997. Seismic risk assessment of active fault systems in the western Chugoku district of southwest Japan. *J. Nat. Disaster Sci.*, **19**, 9-29.
- Kanaori, Y. 1999. Reactivation of cataclastic belts and formation of fault gouge in the western Chugoku region. *Gekkan Chikyu (The Earth Monthly)*, **21**, 22-29.
- Kanaori, Y. 2005. *Active faults in Yamaguchi Prefecture: for the mitigation of earthquake disaster*. Kinmiraiisha Printing co., 122 p. (in Japanese).
- Kawamoto, E. & Shimamoto T. 1998. The strength profile for biminerale shear zones: an insight from high-temperature shearing experiments on calcite-halite mixtures. *Tectonophysics*, **295**, 1-14.
- Kübler, B. 1987. Cristallinité de l'illite, méthodes normalisées de préparation, méthodes normalisées de mesures. *Cahier Institut de Géologie de Neuchâtel Série ADX*.
- Klug, H.P. & Alexander, L. 1974. X-ray diffraction procedures for polycrystalline and Amorphous materials. New York, 200 p.
- Koizumi, Y., Nagahama, H., Otsuki, K., Takeuchi, H. & Nagahama, H. 2004. Frictional melting can terminate seismic slips: Experimental results of stick-slips. *Geophys. Res. Lett.*, **31**, 1-4.
- Lachenbruch, A.H. 1980. Frictional heating, fluid pressure, and the resistance to fault motion. *J. Geophys. Res.*, **85**, 6097-6112.
- Lawn, B.R. & Wilshaw, T.R. 1993. Fracture of brittle solids. Cambridge, Cambridge University Press, London, 378p.
- Lin, A. 2001. S-C fabrics developed in cataclastic rocks from the Nojima fault zone, Japan, and their implications for tectonic history. *J. Struc. Geol.*, **23**, 1167-1178.

- Lin, A., Shimamoto, T. and 7 others. 2001a. Comparative study of cataclastic rocks from a drill core and outcrops of the Nojima fault zone, on Awaji Island, Japan. *The Island Arc*, **10**, 368-380.
- Lin, A., Ouchi, T., Chen, C.F. & Maruyama, T. 2001b. Co-seismic displacements, folding and shortening structures along the Chelungpu surface rupture zone during the 1999 Chi-Chi (Taiwan) earthquake. *Tectonophysics*, **330**, 225-244.
- Lockner, D., Naka, H., Tanaka, H., Ito, H. & Ikeda, R., 1999. Permeability and strength of the Nojima core samples from the Nojima fault of the 1995 Kobe earthquake. In: Ito, H., Fujimoto, K., Tanaka, H., Lockner, D. (Eds.), Proceedings of the International Workshop on the Nojima Fault Core and Borehole Data Analysis. Preliminary Report, 147-152.
- Lupini, F., Skinner, A.E. & Vaughan, P.R., 1981. The drained residual strength of cohesive soils. *Géotechnique*, **31**, 181-213.
- Ma, K.F, Chan, C.H. & Stein, R.S. 2005. Response of seismicity to Coulomb stress triggers and shadows of the 1999 Mw=7.6 Chi-Chi, Taiwan, earthquake. *J. Geophys. Res.*, **110**, 1-16.
- Mair, K. & Marone, C. 1999. Friction of simulated fault gouge for a wide variety of velocities and normal stresses. *J. Geophys. Res.*, **104**, 28899-28914.
- Mair, K. & Marone, C. 2000. Shear heating in granular layers. *Pure Appl. Geophys*, **157**, 1847-1866.
- Mair, K., Frye, K. & Marone, C. 2002. Influence of grain characteristics on the friction of granular shear zones. *J. Geophys. Res.*, **107**, ECV 4-1-4-9.
- Mair, K., Renard, F. & Gundersen, O. 2006. Thermal imaging on simulated faults during frictional sliding. *Geophys. Res. Lett.*, **33**, L19301, doi:10.1029/2006GL027143.
- Mandl, G, de Jong, L.N.J. & Maltha, A. 1977. Shear zones in granular material. *Rock. Mech.*, **9**, 95-144.
- Marone, C. & Scholz, C. 1988. The depth of seismic faulting and the upper transition from stable to unstable slip regimes. *Geophys. Res. Lett.*, **15**, 621-624.
- Marone, C., Raleigh, C.B. & Scholz, C. 1990. Frictional behavior and constitutive modelling of simulated fault gouge. *J. Geophys. Res.*, **95**, 7007-7025.
- Marone, C. & Kilgore, B.D. 1993. Scaling of the critical slip distance for seismic faulting with shear strain in fault zones. *Nature*, **362**, 618-621.
- Marone, C. 1998a. The effect of loading rate on static friction and the rate of fault healing during the earthquake cycle. *Nature*, **391**, 69-72.
- Marone, C. 1998b. Laboratory-derived friction laws and their application to seismic faulting. *Annu. Rev. Earth Planet. Sci.*, **26**, 643-696.

- Mase, C.W. & Smith, L. 1985. Pore-fluid pressures and frictional heating on a fault surface. *Pure Appl. Geophys.*, **122**, 583-607.
- McKenzie, D. & Brune, J.N., 1972. Melting on fault planes during large earthquakes. *Geophys. J. R. Astron. Soc.*, **29**, 65-78.
- Melosh, J. 1979. Acoustic fluidization: a new geologic process ? *J. Geophys. Res.*, **84**, 7513-7520.
- Melosh, J. 1996. Dynamic weakening of faults by acoustic fluidization. *Nature*, **379**, 601-606.
- Micarelli, L, Benedicto A. & Wibberley, C.A.J. 2006. Structural evolution and permeability of normal fault zones in highly porous carbonate rocks. *J. Struct. Geol.*, **28**, 1214-1227.
- Michalske, T.A. & Fuller, E.R. 1985. Closure and repropagation of healed cracks in silicate glass. *J. Am. Ceram. Soc.*, **68**, 5586-5590.
- Mikumo, T., Olsen, K.B., Fukuyama, E. & Yagi, Y. 2003. Stress-breakdown time and slip-weakening distance inferred from slip-velocity functions on earthquake faults. *Bull. Seism. Soc. Am.*, **93**, 264-282.
- Mikumo, T. & Fukuyama, E. 2006. Near-source released energy in relation to fracture energy on earthquake faults. *Bull. Seismol. Soc. Am.*, **96**, 1177-1181.
- Mizoguchi, K, Hirose, T. & Shimamoto, T. 2000. Permeability structure of the Nojima fault at Funaki, Hokudan-Cho, Japan. *The Earth Monthly*, **31**, 58-65 (in Japanese).
- Mizoguchi, K. 2004. High-velocity frictional behaviour of Nojima fault gouge and its implications for seismogenic fault motion. *Doctoral Thesis*, the Graduate School of Science, Kyoto University, 80 p.
- Mizoguchi, K., Hirose, T., Shimamoto, T. & Fukuyama, E. 2006. Moisture-related weakening and strengthening of a fault activated at seismic slip rates. *Geophys. Res. Lett.*, **33**, L16319, doi: 10.1029/2006GL026980.
- Mizoguchi, K., Hirose, T., Shimamoto, T. & Fukuyama, E. 2007. Reconstruction of seismic faulting by high-velocity friction experiments: An example of the 1995 Kobe earthquake. *Geophys. Res. Lett.*, **33**, doi:10.1029/2006GL027931, *in press*.
- Moore, D.E., Summers, R. & Byerlee, J.D. 1986. The effects of sliding velocity on the frictional and physical properties of heated fault gouge. *Pure Appl. Geophys.*, **124**, 31-52.
- Moore, D.M. & Reynolds, R.C. 1989. X-ray diffraction and the identification and analysis of clay minerals, Oxford University Press, Oxford.

- Moore, D.E., Summers, R. & Byerlee, J.D. 1989 Sliding behaviour and deformation textures of heated illite gouge. *J. Struct. Geol.*, **11**, 329-342.
- Moore, D.E. & Lockner D.A. 2004a. Crystallographic controls on the frictional behavior of dry and water-saturated sheet structure minerals. *J. Geophys. Res.*, **109**, 1-16.
- Moore, D.E., & Lockner, D. 2004b. Interpreting the frictional behavior of the smectite clay montmorillonite, *EOS Trans. AGU*, **85**, 47, Fall Meet. Suppl., Abstract T41F-1306.
- Mora, P. & Place, D. 1999. The weakness of earthquake faults. *Geophys. Res. Lett.*, **26**, 123-126.
- Morrow, C.A., Shi., L.Q. & Byerlee J.D. 1984. Permeability of fault gouge under confining pressure and shear stress. *J. Geophys. Res.*, **89**, 3193-3200.
- Morrow, C.A. & Byerlee, J.D. 1989. Experimental studies of compaction and dilatancy during frictional sliding on faults containing gouge. *J. Struct. Geol.*, **11**, 815-825.
- Morrow, C.A., Radney, B. & Byerlee J.D. 1992. Frictional strength and the effective pressure law of montmorillonite and illite clays. *In: Evans, B. & Wong, T.F., (eds) Fault Mechanics and transport properties of rocks*. Academic Press, New York, 69-88.
- Morrow, C.A & Lockner, D.A. 1994. Permeability differences between surface-derived and deep drillhole core samples. *Geophys. Res. Lett.*, **21**, 2151-2154.
- Morrow, C.A., Moore, D.E. & Lockner, D.A. 2000. The effect of mineral bond strength and adsorbed water on fault gouge frictional strength. *Geophys. Res. Lett.*, **26**, 815-818.
- Mukoyoshi, H., Sakaguchi, A., Otsuki, K., Hirono, T. & Soh, W. 2006. Co-seismic frictional melting along an out-of-sequence thrust in the Shimanto accretionary complex. Implications on the tsunamigenic potential of splay faults in modern subduction zones. *Earth Planet. Sci. Lett.*, **245**, 330-343.
- Müller-Vonmoos, M. & Loken, T. 1989. The shearing behaviour of clays. *Appl. Clay Sci.*, **4**, 125-141.
- Nakatani, M. 1998. A new mechanism of slip weakening and strength recovery of friction associated with the mechanical consolidation of gouge. *J. Geophys. Res.*, **103**, 27,239-27,256.
- Noda, H. 2005. Fault constitutive properties at low and high slip rates and analysis of earthquake rupture propagation. *Master Thesis*, the Graduate School of Science, Kyoto University, 126 p.
- Noda, H., & Shimamoto, T. 2005. Thermal pressurization and slip-weakening distance of a fault: An example of the Hanaore fault, Southwest Japan. *Bull. Seism. Soc. Amer.*, **95**, 1224-1233.
- Okada, Y. 2004. Map of Japanese earthquakes. Tokyo Shoseki Co., 192 p. (in Japanese).

- Olson, R. 1974. Shearing strength of kaolinite, illite and montmorillonite. *J. Soil Mech. Found. Div., ASCE*, **100**, 1215-1229.
- O'Hara, K. 2005. Evaluation of asperity-scale temperature effects during seismic slip. *J. Struct. Geol.*, **27**, 1892-1898.
- O'Hara, K., Mizoguchi, K., Shimamoto, T. & Hower, J. 2006. Experimental frictional heating of coal gouge at seismic slip rates: Evidence for devolatilization and thermal pressurization of gouge fluids. *Tectonophysics*, **424**, 109-118.
- Ohnaka, M. & Shen, L.F. 1999. Scaling of the rupture process from nucleation to dynamic propagation: implications of geometric irregularity of the rupturing surfaces. *J. Geophys. Res.*, **104**, 817-844.
- Ordóñez, S., Fort, M. & Garcia del Cura, M.L. 1997. Pore size distribution and the durability of a porous limestone. *Q. J. Eng. Geol.*, **30**, 221-230.
- Otsuki, K., Monzawa, N. & Nagase, T. 2003. Fluidization and melting of fault gouge during seismic slip: Identification in the Nojima fault zone and implications for focal earthquake mechanisms. *J. Geophys. Res.*, **108**, B42192, doi:10.1029/2001JB001711.
- Perrin, G., Rice, J.R. & Zheng, G. 1995. Self-healing slip pulse on a frictional surface. *J. Mech. Phys. Solids*, **43**, 1461-1495.
- Poliakov, A.N.B., Dmowska, R. & Rice, J.R. 2002. Dynamic shear rupture interactions with fault bends and off-axis secondary faulting. *J. Geophys. Res.*, **107**, 2295, doi:10.1029/2001JB000572.
- Price, N.J. & Cosgrove, J.W., 1990. Analyses of geological structures. Cambridge University Press.
- Quin, H. 1990. Dynamic stress drop and rupture dynamics of the October 15, 1979 Imperial Valley California earthquake. *Tectonophysics*, **175**, 93-118.
- Rabinowicz, E. 1951. The nature of static and kinetic coefficient of friction. *J. Appl. Phys.*, **22**, 1373-1379.
- Rabinowicz, E. 1965. Friction and wear of materials, Wiley, New York.
- Rawling, G.C. & Goodwin, L.B. 2003. Cataclasis and particulate flow in faulted, poorly lithified sediments. *J. Struct. Geol.*, **25**, 317-331.
- Research Group for Active Faults of Japan 1991. *Active faults in Japan*. Sheet maps and inventories. Revised edition, Tokyo University Press, 442 p. (in Japanese with English abstract).
- Rice, J.R. 1976. Hydrogen and interfacial cohesion. In: Thompson, A.W. & Berstein, I.M., (eds) *Effect of hydrogen on behavior of materials*. Metall. Soc. of AIME, 455-466. New York.

- Rice, J.R. & Ruina, A. 1983. Stability of steady frictional sliding. *J. Appl. Mech.*, **105**, 343-349.
- Rice, J.R. 1992. Fault stress states, pore pressure distribution. *In*: Evans, B. & Wong, T.F., (eds) *Fault mechanics and transport properties in rocks*. A Festschrift in Honor of W.F. Brace, 475-503. Academic, San Diego, California.
- Rice, J.R. 1999. Flash heating at asperity contacts and rate-depend friction. *Eos Trans AGU*, **80(46)**, Fall Meet. Suppl., F681.
- Rice J.R., Lapusta, N. & Ranjith, K. 2001. Rate and state dependent friction and the stability of sliding between elastically deformable solids. *J. Mech. Phys. Solids*, **49**, 1865-1898.
- Rice, J.R. 2006. Heating and weakening of faults during earthquake slip. *J. Geophys. Res.*, **111**, 1-29.
- Rosenquist, I. 1962. The influence of physico-chemical factors upon the mechanical properties of clays. *Clays Clay Miner.*, **9**, 12-23.
- Rosenquist, I. 1984. The importance of pore water chemistry on mechanical and engineering properties of clay soils. *Philosophical Transactions of the Royal Society, Series A*, **311**, 369-383.
- Rutter, E.H., Maddock, R.H., Hall, S.H. & White, S.H. 1986. Comparative microstructures of natural and experimental produced clay-bearing fault gouges. *Pure Appl. Geophys.*, **124**, 3-30.
- Saffer, D.M. & Marone, C. 2003. Comparison of smectite- and illite-rich gouge frictional properties: application to the updip limit of the seismogenic zone along subduction megathrusts. *Earth Planet. Sci. Lett.*, **215**, 219-235.
- Sagiya, T., Nishimura, T., Hatanaka Y., Fukuyama, E. & Ellsworth, W.L. 2002. Crustal movements associated with the 2000 western Tottori earthquake and its fault model. *Jishin*, **54**, 523-534.
- Sammis, C.G., King, G. & Biegel, R. 1987. The kinematics of gouge deformation. *Pure Appl. Geophys.*, **125**, 777-812.
- Scholz, C.H. 1988a. The critical slip distance for seismic faulting. *Nature*, **336**, 761-763.
- Scholz, C.H. 1988b. The brittle-plastic transition and depth of seismic faulting. *Geol. Rundsch.*, **77**, 319-328.
- Scholz, C.H. 1990. The mechanics of earthquakes and faulting. Cambridge University Press, London, 439 p.
- Scholz, C.H. 1998. Earthquakes and friction laws. *Nature*, **391**, 37-42.
- Scholz, C.H. 2002. The mechanics of earthquakes and faulting, 2<sup>nd</sup> edition. Cambridge University Press, London, 471 p.

- Segall, P. & Rice J.R. 1995. Dilatancy, compaction, and slip instability of a fluid infiltrated fault. *J. Geophys. Res.*, **100**, 22155-22173.
- Semmane, F., Cotton, F. & Campillo, M. 2005. The Tottori earthquake: A shallow earthquake with no surface rupture and slip properties controlled by depth. *J. Geophys. Res.*, **110**, B03306, doi: 10.1029/2004JB003194.
- Seront, B., Wong, T.F. Caine, J.S., Forster, C.B., Bruhn, R.L. & Fredrich, J.T., 1998. Laboratory characterization of hydrodynamical properties of a seismogenic normal fault system. *J. Struct. Geol.*, **20**, 865-881.
- Shea, W.T., & Kronenberg, A.K. 1992. Rheology and deformation mechanisms of an isotopic micaschist. *J. Geophys. Res.*, **97**, 201-237.
- Shea, W.T.J. & Kronenberg, A.K. 1993. Strength and anisotropy of foliated rocks with varied mica contents. *J. Struct. Geol.*, **15**, 1097-1121.
- Shimamoto, T. & Tsutsumi, A., 1994. A new rotary-shear high-speed frictional testing machine: its basic design and scope of research. *Struct. Geol. (Japan)*, **39**, 79-84.
- Shimamoto, T. & Hirose, T. 2006. Reproducing low to high-velocity fault motion in fluid-rich environments: An experimental challenge and preliminary results. *Geophys. Res. Abstr.*, **8**, Abstract 09077, sref: 1607-7962/gra/EGU/06-A-09077.
- Sibson, R.H. 1973. Interactions between temperature and pore fluid pressure during earthquake faulting and a mechanism for partial or total stress relief. *Nature*, **243**, 66-68.
- Sibson, R.H. 1977. Fault rocks and fault mechanisms. *J. Geol. Soc. London*, **133**, 191-213.
- Sibson, R.H. 1980. Power dissipation and stress levels on faults in the upper crust. *J. Geophys. Res.*, **85**, 6239-6247.
- Sibson, R.H. 1981. Fluid flow accompanying faulting: field evidence and models. *Earthquake prediction: an international review*, 593-603.
- Sibson, R.H. 1982. Fault zone models, heat flow, and the depth distribution of earthquakes in the continental crust of the United States. *Seism. Soc. Amer. Bull.*, **72**, 151-163.
- Sibson, R.H. 1983. Continental fault structure and the shallow earthquake source, *J. Geol. Soc. London*, **140**, 741-767.
- Sibson, R.H. 1989. Earthquake faulting as a structural process. *J. Struct. Geol.*, **11**, 1-14.
- Sibson, R.H. 1990. Conditions for fault-valve behaviour. In: Knipe, R.J. & Rutter, E.H., (eds) *Deformation mechanisms, rheology and tectonics*, **54**. J. Geol. Soc. (Lond.), Sp. Publ., 15-28.

- Sibson, R.H. 1992. Implications of fault valve behaviour for rupture nucleation and recurrence. *Tectonophysics* **211**, 283-293
- Sibson, R.H. 2003. Thickness of the seismic slip zone. *Bull. Seism. Soc. Am.*, **93**, 1169-1178.
- Sleep, N.H. 1997. Application of a unified rate and state friction theory to the mechanics of fault zones with strain localization. *J. Geophys. Res.*, **102**, 2875-2895.
- Smith, L., Forster, C.B. & Evans, J.P. 1990. Interaction between fault zones, fluid flow and heat transfer at the basin scale. In: Newman, S.P. & Neretnieks, I. (eds) *International Association of Hydrologic Sciences Selected Papers in Hydrogeology*, **2**, 41-67.
- Sone, H. 2006. Structural description of cores from the Taiwan Chelungpu-fault drilling project and the fault weakening process inferred from frictional and transport properties of fault zone core samples. *Master Thesis*, the Graduate School of Science, Kyoto University, 101 p.
- Sowers, J.M., Unruh, J.R., Lettis, W.R. & Rubin, T.D. 1994. Relationship of the Kickapoo Fault to the Johnson Valley and Homestead Valley faults, San Bernardino County, California. *Bull. Seism. Soc. Am.*, **84**, 528-536.
- Spray, J.G. 1987. Artificial generation of pseudotachylyte using friction welding apparatus: Simulation of melting on a fault plane. *J. Struct. Geol.*, **9**, 49-60.
- Spray, J.G. 1992. A physical basis for the frictional melting of some rock-forming minerals. *Tectonophysics*, **204**, 205-221.
- Spray, J.G. 1995. Pseudotachylyte controversy: Fact or friction ? *Geology*, **23**, 1119-1122.
- Spray, J.G. 2005. Evidence for melt lubrication during large earthquakes. *Geophys. Res. Lett.*, **32**, L07301, doi:10.1029/2004GL022293.
- Stesky, R., Brace, W., Riley, D. & Robin P.Y. 1974. Friction in faulted rock at high temperature and pressure. *Tectonophysics*, **23** 177-203.
- Sulem, J., Vardoulakis, I., Ouffroukh, H., Boulon, M. & Hans J. 2004. Experimental characterisation of the thermo-poro-mechanical properties of the Aegion fault gouge. *Comptes Rendus - Geoscience*, **336**, 455-466.
- Swanson, M.T. 1992. Fault structure, wear mechanisms and rupture processes in pseudotachylyte generation. *Tectonophysics*, **204**, 223-242.
- Tsukahara, H. & Kobayashi, Y. 1991. Crustal stress field in central and southwest Japan. *Jishin*, **44**, 221-231.
- Tsutsumi, A., Shimamoto, T., 1997. High-velocity frictional properties of gabbro. *Geophys. Res. Lett.*, **24**, 699-702.

- Tsutsumi, A., Nishino, S., Mizoguchi, K., Hirose, T., Uehara, S., Sato, K., Tanikawa, W. & Shimamoto, T. 2004. Principal fault zone width and permeability of the active Neodani fault, Nobi fault system, Southwest Japan. *Tectonophysics*, **379**, 93-108.
- Uehara, S. & Shimamoto, T. 2004. Gas permeability evolution of cataclasite and fault gouge in triaxial compression and implications for changes in fault-zone permeability structure through the earthquake cycle. *Tectonophysics*, **378**, 183-195.
- Vannucchi, P., Maltman A., Bettelli G. & Clennell B. 2003. On the nature of scaly fabric and scaly clay. *J. Struct. Geol.*, **25**, 673-688.
- Vardoulakis, I. 2002. Steady shear and thermal run-away in clayey gouges. *Int. J. Solids Struct.*, **39**, 3831-3844.
- Veveakis, E., Vardoulakis, I. & Di Toro G. 2007. Thermo-poro-mechanics of creeping landslides: the 1963 Vaiont (Northern Italy) case. *J. Geophys. Res.*, *in press*.
- Vrolijk, P. & van der Pluijm B.A. 1999. Clay Gouge. *J. Struct. Geol.*, **21**, 1039-1048.
- Wang, C.Y., Mao, N.H. & Wu, F.T. 1980. Mechanical properties of clays at high pressures. *J. Geophys. Res.*, **85**, 1462-1468.
- Warr, L.N. & Cox, S.J. 2001. Clay mineral transformations and weakening mechanisms along the Alpine Fault, New Zealand. *In: Holdsworth, R.E., Strachan, R. A., Magloughlin, J.F. & Knipe, R.J. (eds) The nature and significance of fault zone weakening.* Geological Society, London, Special Publications, **186**, 85-101.
- Weertman, J. 1980. Unstable slippage across a fault that separates elastic media of different elastic constants. *J. Geophys. Res.*, **85**, 1455-1461.
- Wibberley, C.A.J. 2002. Hydraulic diffusivity of fault gouge zones and implications for thermal pressurization during seismic slip. *Earth Planets Space*, **54**, 1153-1171.
- Wibberley, C.A.J. & Shimamoto, T. 2003. Internal structure and permeability of major strike-slip fault zones: the Median Tectonic Line in Mie Prefecture, Southwest Japan. *J. Struct. Geol.*, **25**, 59-78.
- Wibberley, C.A.J. & Shimamoto, T. 2004. Hydrodynamical weakening of granular fault gouge during earthquake slip. *Geophys. Res. Abstr.*, **6**, Abstract 02051, sref: 1607-7962/gra/ EGU/04-A-02051.
- Wibberley, C.A.J. & Shimamoto, T. 2005. Earthquake slip weakening and asperities explained by thermal pressurization. *Nature*, **436**, 689-692.
- Wong, T.F., Gu, Y., Yanagidani, T. & Zhao, Y. 1992. Stabilization of faulting by cumulative slip. *In: Evans, B. & Wong, T.F., (eds) Fault Mechanics and Transport Properties of Rocks.* A Festschrift in Honor of W.F. Brace., 119-143. Academic, San Diego, California.

- Yamada, N., Higashimoto, S. & Mizuno, K. 1985. Hiroshima Map 1:200,000, **NI-53-33**. Geological Survey of Japan.
- Yue, Q.Z.Q., Shang, Y.J., Hu, R.L. & Tu, X.B. 2004. Five test methods for porosity of completely decomposed granite in Hong Kong. *Int. J. of Rock Mech. Min. Sci.*, **41**, 393-394.
- Yund, R.A., Blanpied, M.L, Tullis, T.E. & Weeks, J.D. 1990. Amorphous material in high strain experimental fault gouges. *J. Geophys. Res.*, **95**, 15589-15602.
- Zheng, G. & Rice, J.R. 1998. Conditions under which velocity-weakening friction allows a self-healing versus a cracklike mode of rupture. *Bull. Seism. Soc. Amer.*, **88**, 1466-1483.
- Zoback, M.D. 1987. New evidence on the state of stress of the San Andreas fault system. *Science*, **238**, 1105-1111.
- Zoback, M.L. & Zoback, M.D. 1997. Crustal stress and interplate deformation. *Geowissenschaften*, **15**, 112-116.



